

Ministry of Education and Science of the Russian Federation
Saint Petersburg National Research University of Information
Technologies, Mechanics, and Optics

NANOSYSTEMS:
PHYSICS, CHEMISTRY, MATHEMATICS

2019, volume 10(1)

Наносистемы: физика, химия, математика
2019, том 10, № 1



NANOSYSTEMS:

PHYSICS, CHEMISTRY, MATHEMATICS

ADVISORY BOARD MEMBERS

Chairman: V.N. Vasiliev (*St. Petersburg, Russia*),
V.M. Buznik (*Moscow, Russia*); V.M. Ievlev (*Voronezh, Russia*), P.S. Kop'ev (*St. Petersburg, Russia*), N.F. Morozov (*St. Petersburg, Russia*), V.N. Parmon (*Novosibirsk, Russia*),
A.I. Rusanov (*St. Petersburg, Russia*),

EDITORIAL BOARD

Editor-in-Chief: I.Yu. Popov (*St. Petersburg, Russia*)

Section Co-Editors:

Physics – V.M. Uzdin (*St. Petersburg, Russia*),
Chemistry, material science – V.V. Gusarov (*St. Petersburg, Russia*),
Mathematics – I.Yu. Popov (*St. Petersburg, Russia*).

Editorial Board Members:

V.M. Adamyan (*Odessa, Ukraine*); O.V. Al'myasheva (*St. Petersburg, Russia*);
A.P. Alodjants (*Vladimir, Russia*); S. Bechta (*Stockholm, Sweden*); J. Behrndt (*Graz, Austria*);
M.B. Belonenko (*Volgograd, Russia*); A. Chatterjee (*Hyderabad, India*); S.A. Chivilikhin
(*St. Petersburg, Russia*); A.V. Chizhov (*Dubna, Russia*); A.N. Enyashin (*Ekaterinburg, Russia*),
P.P. Fedorov (*Moscow, Russia*); E.A. Gudilin (*Moscow, Russia*); V.K. Ivanov
(*Moscow, Russia*), H. Jónsson (*Reykjavik, Iceland*); A.A. Kiselev (*Durham, USA*);
Yu.S. Kivshar (*Canberra, Australia*); S.A. Kozlov (*St. Petersburg, Russia*); P.A. Kurasov
(*Stockholm, Sweden*); A.V. Lukashin (*Moscow, Russia*); V.A. Margulis (*Saransk, Russia*);
I.V. Melikhov (*Moscow, Russia*); G.P. Miroshnichenko (*St. Petersburg, Russia*);
I.Ya. Mittova (*Voronezh, Russia*); H. Neidhardt (*Berlin, Germany*); V.V. Pankov (*Minsk, Belagus*);
K. Pankrashkin (*Orsay, France*); A.V. Ragulya (*Kiev, Ukraine*); V. Rajendran
(*Tamil Nadu, India*); A.A. Rempel (*Ekaterinburg, Russia*); V.Ya. Rudyak (*Novosibirsk, Russia*);
D Shoikhet (*Karmiel, Israel*); P Stovicek (*Prague, Czech Republic*); V.M. Talanov
(*Novocherkassk, Russia*); A.Ya. Vul' (*St. Petersburg, Russia*); A.V. Yakimansky
(*St. Petersburg, Russia*), V.A. Zagrebnov (*Marseille, France*).

Editors:

I.V. Blinova; A.I. Popov; A.I. Trifanov; E.S. Trifanova (*St. Petersburg, Russia*),
R. Simoneaux (*Philadelphia, Pennsylvania, USA*).

Address: University ITMO, Kronverkskiy pr., 49, St. Petersburg 197101, Russia.

Phone: +7(812)312-61-31, **Journal site:** <http://nanojournal.ifmo.ru/>,

E-mail: popov1955@gmail.com

AIM AND SCOPE

The scope of the journal includes all areas of nano-sciences. Papers devoted to basic problems of physics, chemistry, material science and mathematics inspired by nanosystems investigations are welcomed. Both theoretical and experimental works concerning the properties and behavior of nanosystems, problems of its creation and application, mathematical methods of nanosystem studies are considered.

The journal publishes scientific reviews (up to 30 journal pages), research papers (up to 15 pages) and letters (up to 5 pages). All manuscripts are peer-reviewed. Authors are informed about the referee opinion and the Editorial decision.

CONTENT

MATHEMATICS

- M.O. Smolkina, I.Y. Popov, I.V. Blinova, E. Milakis
On the metric graph model for flows in tubular nanostructures 6

PHYSICS

- S.V. Kidalov, M.V. Zamoryanskaya, V.A. Kravez,
L.V. Sharonova, F.M. Shakhov, E.B. Yudina,
T.O. Artamonova, M.A.Khodorkovskii, A.Ya. Vul'
**Photo- and cathodoluminescence spectra of diamond single crystals
formed by sintering of detonation nanodiamonds** 12

- S. Leble
**Heisenberg chain equations in terms of Fockian covariance with
electric field account and multiferroics in nanoscale** 18

- Jacob Katriel, H.E. Montgomery, Jr., A. Sarsa, E. Buendía,
F.J. Gálvez, K.D. Sen
**Hund's rule in open-shell states of two-electron systems: From free
through confined and screened atoms, to quantum dots** 31

- A.N. Kovalenko
Fractal characterization of nanostructured materials 42

- A. Chatterjee, M.O. Smolkina, I.Y. Popov
**Persistent current in a chain of two Holstein-Hubbard rings
in the presence of Rashba spin-orbit interaction** 50

CHEMISTRY AND MATERIAL SCIENCE

- S. Saravanan, R.S. Dubey
**Fabrication and characterization of TiO₂/SiO₂ multilayers using
sol-gel spin coating method** 63

- L.L. Larina, O.V. Alexeeva, O.V. Almjasheva, V.V. Gusarov,
S.S. Kozlov, A.B. Nikolskaia, M.F. Vildanova, O.I. Shevaleevskiy
**Very wide-bandgap nanostructured metal oxide materials
for perovskite solar cells** 70

- V.S. Molchanov, M.A. Efremova, T.Yu. Kiseleva, O.E. Philippova
Injectable ultra-soft hydrogel with natural nanoclay 76

- I.S. Popov, A.S. Vorokh, A.N. Enyashin
Effect of nitrogen impurities on ZnS polymorphism 86

A.L. Popov, A.M. Ermakov, T.O. Shekunova, A.B. Shcherbakov, O.N. Ermakova, O.S. Ivanova, N.R. Popova, A.Ye. Baranchikov, V.K. Ivanov PVP-stabilized tungsten oxide nanoparticles inhibit proliferation of NCTC L929 mouse fibroblasts via induction of intracellular oxidative stress	92
M.B. Shavelkina, R.H. Amirov Direct synthesis of hydrogenated graphene via hydrocarbon decomposition in plasmas	102
Information for authors	107



Obituary

Prof. Dr. Johannes Brasche

The Editorial Board regrettably announce that Professor Johannes Brasche, a member of the Editorial Board of the journal, suddenly and unexpectedly passed away on December 17, 2018.

Professor Brasche was an internationally known and respected mathematician. He was one of the pioneers of inverse spectral theory. His contributions to δ -shaped perturbations in operator theory have been groundbreaking and received much attention. He was a longtime employee at the Institute of Mathematics of the TU Clausthal.

Johannes Brasche was born in Frankfurt am Main in 1956 and studied mathematics and physics at the University of Bielefeld for teaching, but decided on a scientific career after the first state exam. He received his doctorate in 1988 at the University of Bielefeld based on his work "Perturbations of self-adjoint operators supported by null sets". He then worked as a research assistant at the Universities of Bielefeld, Bochum and Frankfurt before habilitation in 1996 in Bochum. The subject of his habilitation thesis was "On spectra of self-adjoint extensions and generalized Schrödinger operators".

After several professorial appointments at the University of Bonn, he was appointed in 2000 as a (tenured) associate professor at the Chalmers University of Technology in Gothenburg. For family reasons, in 2004 he moved to a position as a research associate at the Institute of Mathematics of the TU Clausthal, where he was appointed Privatdozent for Mathematics in 2015 and in April 2018 as an Associate Professor in the field of "Mathematical Modeling".

Professor Brasche has always worked with all his might for mathematics in Clausthal and for the students. He successfully held a variety of courses that, like his lectures, were always sophisticated and focused on the audience. He was very popular with students of all subjects and, because of his great commitment as a supervisor of numerous bachelor and master theses, was sought after. He was a pioneer in the video recording of mathematics lectures. He was a longtime member of the Editorial Board of the journal "Nanosystems: Physics, Chemistry, Mathematics".

Above all, however, he will be remembered for his assistance to those having research problems and kindness, his good temper and his open ear for all the difficulties. The loss of Johannes Brasche leaves a large gap in our community.

We would like to offer our sincere condolences to his family.

On the metric graph model for flows in tubular nanostructures

M. O. Smolkina¹, I. Y. Popov¹, I. V. Blinova¹, E. Milakis²

¹ITMO University, Kronverkskiy, 49, Saint Petersburg, 197101, Russia

²University of Cyprus, P.O.Box 20537, CY-1678 Nicosia, Cyprus

vega14@mail.ru, popov1955@gmail.com, irin-a@yandex.ru, emilakis@ucy.ac.cy

DOI 10.17586/2220-8054-2019-10-1-6-11

A metric graph model is suggested for the Stokes flow concentrated in the vicinity of a network embedded in \mathbb{R}^3 . As a basic problem, we consider the case corresponding to strong variation of the viscosity and density in a cylinder of small radius. An equation for the main term of the asymptotics is obtained. As for a graph structure, coupling conditions are assumed at the graph vertices.

Keywords: stokes flow, metric graph.

Received: 12 November 2018

Revised: 23 January 2019

1. Introduction

Many physical systems demonstrate flows concentrated near a network, e.g., flows through nanotubes [1–3] or biophysical flows [4–6]. Mentioned flow concentration near lines or surfaces may be caused by specific variation of viscosity. It is typical, for instance, for geophysical flows [7–10]. Narrowness of the domain means small ratio of width and length. It is worth noting that works concerning to viscous wires with free surface [11, 12] are related to glass and fiber technologies. The problems are complicated and it is of great relevance to construct models which allow simplification.

Concentration of a solution near lines or networks appears not only in fluid mechanics but also in other fields, e.g., in quantum theory. There is an effective and simple method for investigating such systems in quantum mechanics – the quantum graph model. This method was developed in the 1980's ([13, 14]) and now is a widely used approach (see, e.g., [15]). The model has some relevant features. On the one hand, it allows one to obtain explicit solutions of the model problem; in addition, it permits good approximation in many particular physical problems (see, e.g., [16–18]). This is one reason for seeking of a new field of application for such an effective instrument. In this paper, we make steps to the development of a model analogs to the quantum graph for fluid mechanics.

There are several ways to consider the hydrodynamic equations on a network (metric graph). One can deal with the 1D Navier–Stokes equation. For example, for compressible fluid of constant viscosity $\tilde{\eta}$ it takes the form:

$$\frac{\partial v}{\partial t} + v \frac{\partial v}{\partial x} - \tilde{\eta} \frac{\partial^2 v_x}{\partial x^2} = 0.$$

This is a nonlinear equation. To get the corresponding linear one we can linearize it in the vicinity of some solution or simply neglect the nonlinear inertial terms. It is possible to obtain the 1D Navier–Stokes equation by the asymptotic procedure for 3D or 2D Navier–Stokes equations in thin tubes (see, e.g., [19–22]). It is also possible to study linear 2D or 3D Stokes equations in a system of narrow tubes and to consider the limiting procedure for tubes having widths tending to zero. One observes an analogous situation for waveguides and thick quantum graphs (see, e.g., [23–25]). In the most popular model for the Stokes flow in a network one assumes that there is the Poiseuille flow in the tubes [26]). In our case the situation is more complicated (the flow is not localized inside tubes, the viscosity and the density varies essentially), and this model is not appropriate. We use the asymptotic approach. The first step was made in [27], where a metric graph model was constructed for 2D case. As a result, we obtain 1D problem on a metric graph for the main term of the asymptotic expansion. We called it the Stokes graph. In the present paper, we construct the model for 3D case.

2. Preliminaries

3D Stokes and continuity equation for the case of variable viscosity and density in cylindrical coordinates (r, φ, z) are as follows:

$$\begin{aligned}(\nabla \cdot \sigma)_r &= -\rho G_r, \\(\nabla \cdot \sigma)_\phi &= -\rho G_\phi, \\(\nabla \cdot \sigma)_z &= -\rho G_z,\end{aligned}\tag{1}$$

$$\nabla(\rho v) = 0.\tag{2}$$

Here σ is the stress tensor, ρ is the density, G is the external force, v is the flow velocity. In cylindrical coordinates the continuity equation (2) takes the form:

$$\frac{\rho v_r}{r} + \frac{\partial(\rho v_r)}{\partial r} + \frac{1}{r} \frac{\partial(\rho v_\phi)}{\partial \phi} + \frac{\partial(\rho v_z)}{\partial z} = 0\tag{3}$$

The divergence of a total stress tensor in cylindrical coordinates have the form:

$$\begin{aligned}(\nabla \cdot \sigma)_r &= \frac{\partial \sigma_{rr}}{\partial r} + \frac{\sigma_{rr} - \sigma_{\phi\phi}}{r} + \frac{1}{r} \frac{\partial \sigma_{\phi r}}{\partial \phi} + \frac{\partial \sigma_{zr}}{\partial z}, \\(\nabla \cdot \sigma)_\phi &= \frac{\partial \sigma_{r\phi}}{\partial r} + \frac{2\sigma_{r\phi}}{r} + \frac{1}{r} \frac{\partial \sigma_{\phi\phi}}{\partial \phi} + \frac{\partial \sigma_{z\phi}}{\partial z}, \\(\nabla \cdot \sigma)_z &= \frac{\partial \sigma_{rz}}{\partial r} + \frac{\sigma_{rz}}{r} + \frac{1}{r} \frac{\partial \sigma_{\phi z}}{\partial \phi} + \frac{\partial \sigma_{zz}}{\partial z}.\end{aligned}$$

Then equations (1) transform to the form:

$$\frac{\partial \tau_{rr}}{\partial r} + \frac{\tau_{rr} - \tau_{\phi\phi}}{r} + \frac{1}{r} \frac{\partial \tau_{r\phi}}{\partial \phi} + \frac{\partial \tau_{rz}}{\partial z} - \frac{\partial P}{\partial r} = -\rho G_r,\tag{4}$$

$$\frac{\partial \tau_{r\phi}}{\partial r} + \frac{2\tau_{r\phi}}{r} + \frac{1}{r} \frac{\partial \tau_{\phi\phi}}{\partial \phi} + \frac{\partial \tau_{\phi z}}{\partial z} - \frac{1}{r} \frac{\partial P}{\partial \phi} = -\rho G_\phi,\tag{5}$$

$$\frac{\partial \tau_{rz}}{\partial r} + \frac{\tau_{rz}}{r} + \frac{1}{r} \frac{\partial \tau_{\phi z}}{\partial \phi} + \frac{\partial \tau_{zz}}{\partial z} - \frac{\partial P}{\partial z} = -\rho G_z.\tag{6}$$

In cylindrical coordinates, the deviatoric stress tensor has the following components:

$$\begin{aligned}\tau_{rr} &= 2\eta \frac{\partial v_r}{\partial r}, \quad \tau_{\phi\phi} = 2\eta \left(\frac{1}{r} \frac{\partial v_\phi}{\partial \phi} + \frac{v_r}{r} \right), \quad \tau_{zz} = 2\eta \frac{\partial v_z}{\partial z}, \\ \tau_{r\phi} &= \eta \left(\frac{1}{r} \frac{\partial v_r}{\partial \phi} + \frac{\partial v_\phi}{\partial r} - \frac{v_\phi}{r} \right), \quad \tau_{rz} = \eta \left(\frac{\partial v_z}{\partial r} + \frac{\partial v_r}{\partial z} \right), \\ \tau_{\phi z} &= \eta \left(\frac{\partial v_\phi}{\partial z} + \frac{1}{r} \frac{\partial v_z}{\partial \phi} \right).\end{aligned}$$

In more detail, equations (4), (5), (6) take the form:

$$\begin{aligned}2 \frac{\partial \eta}{\partial r} \frac{\partial v_r}{\partial r} + 2\eta \frac{\partial^2 v_r}{\partial r^2} + 2\eta \frac{1}{r} \frac{\partial v_r}{\partial r} - 3\eta \frac{1}{r^2} \frac{\partial v_\phi}{\partial \phi} - 2\eta \frac{v_r}{r^2} + \frac{1}{r^2} \frac{\partial \eta}{\partial \phi} \frac{\partial v_r}{\partial \phi} + \\ \frac{1}{r} \frac{\partial \eta}{\partial \phi} \frac{\partial v_\phi}{\partial r} - \frac{\partial \eta}{\partial \phi} \frac{v_\phi}{r^2} + \eta \frac{1}{r^2} \frac{\partial^2 v_r}{\partial \phi^2} + \frac{1}{r} \eta \frac{\partial^2 v_\phi}{\partial \phi \partial r} + \\ + \frac{\partial \eta}{\partial z} \frac{\partial v_z}{\partial r} + \frac{\partial \eta}{\partial z} \frac{\partial v_r}{\partial z} + \eta \frac{\partial^2 v_z}{\partial z \partial r} + \eta \frac{\partial^2 v_r}{\partial z^2} - \frac{\partial P}{\partial r} = -\rho G_r,\end{aligned}\tag{7}$$

$$\begin{aligned}\frac{1}{r} \frac{\partial \eta}{\partial r} \frac{\partial v_r}{\partial \phi} + \frac{\partial \eta}{\partial r} \frac{\partial v_\phi}{\partial r} - \frac{1}{r} \frac{\partial \eta}{\partial r} v_\phi + \eta \frac{1}{r} \frac{\partial^2 v_r}{\partial r \partial \phi} + \eta \frac{\partial^2 v_\phi}{\partial r^2} + \\ 3\eta \frac{1}{r^2} \frac{\partial v_r}{\partial \phi} + \eta \frac{1}{r} \frac{\partial v_\phi}{\partial r} - \eta \frac{v_\phi}{r^2} + 2 \frac{1}{r^2} \frac{\partial \eta}{\partial \phi} \frac{\partial v_\phi}{\partial \phi} + 2 \frac{1}{r^2} \frac{\partial \eta}{\partial \phi} v_r + \\ 2\eta \frac{1}{r^2} \frac{\partial^2 v_\phi}{\partial \phi^2} + \frac{\partial \eta}{\partial z} \frac{\partial v_\phi}{\partial z} + \frac{1}{r} \frac{\partial \eta}{\partial z} \frac{\partial v_z}{\partial \phi} + \eta \frac{\partial^2 v_\phi}{\partial z^2} + \eta \frac{\partial^2 v_z}{\partial z \partial \phi} - \frac{1}{r} \frac{\partial P}{\partial \phi} = -\rho G_\phi,\end{aligned}\tag{8}$$

$$\begin{aligned}\frac{\partial \eta}{\partial r} \frac{\partial v_z}{\partial r} + \frac{\partial \eta}{\partial r} \frac{\partial v_r}{\partial z} + \eta \frac{\partial^2 v_z}{\partial r^2} + \eta \frac{\partial^2 v_r}{\partial r \partial z} + \eta \frac{1}{r} \frac{\partial v_z}{\partial r} + \eta \frac{1}{r} \frac{\partial v_r}{\partial z} + \frac{1}{r} \frac{\partial \eta}{\partial \phi} \frac{\partial v_\phi}{\partial z} \\ + \frac{1}{r^2} \frac{\partial \eta}{\partial \phi} \frac{\partial v_z}{\partial \phi} + \eta \frac{1}{r} \frac{\partial^2 v_\phi}{\partial \phi \partial z} + \eta \frac{1}{r^2} \frac{\partial^2 v_z}{\partial \phi^2} + 2\eta \frac{\partial^2 v_z}{\partial z^2} + 2 \frac{\partial \eta}{\partial z} \frac{\partial v_z}{\partial z} - \frac{\partial P}{\partial z} = -\rho G_z.\end{aligned}\tag{9}$$

3. Stokes graph model

We will consider the flow under some axisymmetric conditions. Keeping in mind future replacement of variables, we change notations. Namely, we equip all variables and parameters in equations (3), (7), (8), (9) by $\tilde{\cdot}$: $\tilde{r}, \tilde{\varphi}, \tilde{z}, \tilde{\eta}, \tilde{\rho}$. We will deal with the case when the values of the viscosity $\tilde{\eta}$ and the density $\tilde{\rho}$ are smooth and outside the cylinder $\{(\tilde{r}, \tilde{\varphi}, \tilde{z}) : \tilde{z} \in (-\infty, \infty), \tilde{r} \in (0, \varepsilon)\}$ are essentially greater than inside it ($(\tilde{r}, \tilde{\varphi}, \tilde{z})$ are the cylindrical coordinates):

$$\begin{aligned} \tilde{\eta}(\tilde{r}, \tilde{\varphi}, \tilde{z}) &= \eta(\tilde{z})\eta_2(\tilde{r}), & \tilde{\rho}(\tilde{r}, \tilde{\varphi}, \tilde{z}) &= \rho(\tilde{z})\rho_2(\tilde{r}), \\ \eta_2(\tilde{r}) &= \begin{cases} 1, & 0 \leq \tilde{r} \leq \varepsilon, \\ \eta_w, & \tilde{r} > 2\varepsilon, \end{cases} & \eta_w &\gg 1, \\ \rho_2(\tilde{r}) &= \begin{cases} 1, & 0 \leq \tilde{r} \leq \varepsilon, \\ \rho_w, & \tilde{r} > 2\varepsilon, \end{cases} & \rho_w &\gg 1. \end{aligned}$$

Here, ε is a small parameter. It means that the flow is essentially inside the cylinder. We will consider the flow inside the cylinder only. Let us introduce new coordinates: $z = \tilde{z}$, $r = \tilde{r}/\varepsilon$, $\varphi = \tilde{\varphi}$. We will consider an axisymmetric solution. Correspondingly, the flow velocity and the pressure do not depend on φ . Correspondingly, equation (8) becomes the identity. Equations (7), (9), (3) take the following form after the coordinate replacement:

$$\begin{aligned} 2\varepsilon^{-2} \frac{\partial \eta}{\partial r} \frac{\partial v_r}{\partial r} + 2\varepsilon^{-2} \eta \frac{\partial^2 v_r}{\partial r^2} + 2\varepsilon^{-2} \eta \frac{1}{r} \frac{\partial v_r}{\partial r} - 2\varepsilon^{-2} \eta \frac{v_r}{r^2} + \varepsilon^{-1} \frac{\partial \eta}{\partial z} \frac{\partial v_z}{\partial r} + \\ \varepsilon^{-1} \frac{\partial \eta}{\partial z} \frac{\partial v_r}{\partial z} + \varepsilon^{-1} \eta \frac{\partial^2 v_z}{\partial r \partial z} + \eta \frac{\partial^2 v_r}{\partial z^2} - \varepsilon^{-1} \frac{\partial P}{\partial r} = -\rho G_r, \end{aligned} \quad (10)$$

$$\begin{aligned} \varepsilon^{-2} \frac{\partial \eta}{\partial r} \frac{\partial v_z}{\partial r} + \varepsilon^{-1} \frac{\partial \eta}{\partial r} \frac{\partial v_r}{\partial z} + \varepsilon^{-2} \eta \frac{\partial^2 v_z}{\partial r^2} + \varepsilon^{-1} \eta \frac{\partial^2 v_r}{\partial z \partial r} + \varepsilon^{-2} \eta \frac{1}{r} \frac{\partial v_z}{\partial r} + \\ \varepsilon^{-1} \eta \frac{1}{r} \frac{\partial v_r}{\partial z} + 2\eta \frac{\partial^2 v_z}{\partial z^2} + 2 \frac{\partial \eta}{\partial z} \frac{\partial v_z}{\partial z} - \frac{\partial P}{\partial z} = -\rho G_z, \end{aligned} \quad (11)$$

$$\varepsilon^{-1} \frac{\rho}{r} v_r + \varepsilon^{-1} \frac{\partial \rho}{\partial r} v_r + \varepsilon^{-1} \rho \frac{\partial v_r}{\partial r} + \frac{\partial(\rho v_z)}{\partial z} = 0. \quad (12)$$

We will seek the solutions in the form of series in ε :

$$v_r = v_r^0 + v_r^1 \varepsilon + \dots, \quad v_z = v_z^0 + v_z^1 \varepsilon + \dots, \quad P = P^0 + P^1 \varepsilon + \dots$$

Let us insert the series (3) into equations (10), (11), (12) and collect terms of the same powers of ε . We obtain the chain of equations for the series coefficients. Terms of order ε^{-2} are in the Stokes equations (in new variables) only:

$$\eta \frac{\partial^2 v_r^0}{\partial r^2} + \frac{1}{r} \frac{\partial(r\eta)}{\partial r} \frac{\partial v_r^0}{\partial r} - \frac{\eta}{r^2} v_r^0 = 0, \quad (13)$$

$$\eta \frac{\partial^2 v_z^0}{\partial r^2} + \frac{1}{r} \frac{\partial(r\eta)}{\partial r} \frac{\partial v_z^0}{\partial r} = 0. \quad (14)$$

Equation (14) gives us:

$$v_z^0(r, z) = \frac{f(z)}{\eta(z)} \int \frac{dr}{r\eta_2(r)} = u(z) \int \frac{dr}{r\eta_2(r)}. \quad (15)$$

Here $u(z), f(z)$ are some functions of one variable. They should be determined later. Terms of order ε^{-1} are in three equations. The continuity equation gives us: $v_r^0 = g(z)/(r\rho)$. To avoid contradiction with (13), we conclude that $v_r^0 = 0$, i.e. the series for v_r starts from another power than for v_z . It is a conventional situation when one has different scales for different directions (see, e.g., [31]). The Stokes equations (10), (11) give us the following relations for the terms of this order:

$$\begin{aligned} \eta \frac{\partial^2 v_r^1}{\partial r^2} + \frac{1}{r} \frac{\partial}{\partial r} (r\eta) \frac{\partial v_r^1}{\partial r} - \frac{\eta}{r^2} v_r^1 = -\frac{\partial \eta}{\partial z} \frac{\partial v_z^0}{\partial r} - \eta \frac{\partial^2 v_z^0}{\partial r \partial z} + \frac{\partial P^0}{\partial r}, \\ \frac{\eta}{\partial r} \frac{\partial v_z^1}{\partial r} + \eta \frac{\partial^2 v_z^1}{\partial r^2} + \frac{1}{r} \frac{\partial v_z^1}{\partial r} = 0. \end{aligned}$$

These equations are solvable with respect to v_r^1, v_z^1 . The pressure term P^0 should be determined later.

Consider the terms of order ε^0 . The continuity equation (12) leads to the following equation for v_r^1 :

$$\frac{\partial \rho}{\partial r} v_r^1 + \frac{\rho}{r} v_r^1 + \rho \frac{\partial v_r^1}{\partial r} = -\frac{\partial \rho}{\partial z} v_z^0 - \rho \frac{\partial v_z^0}{\partial z}, \quad (16)$$

Equation (10) gives the relation:

$$\begin{aligned} & 2\eta \frac{\partial^2 v_r^2}{\partial r^2} + 2\frac{\partial\eta}{\partial r} \frac{\partial v_r^2}{\partial r} + 2\frac{\eta}{r} \frac{\partial v_r^2}{\partial r} - 2\eta \frac{v_r^2}{r^2} = \\ & -\frac{\partial\eta}{\partial z} \frac{\partial v_z^1}{\partial r} - \frac{\partial\eta}{\partial z} \frac{\partial v_r^1}{\partial z} - \eta \frac{\partial^2 v_z^1}{\partial z \partial r} + \frac{\partial P^1}{\partial r} - \rho G_r, \end{aligned} \quad (17)$$

Equation (11) produces the relation:

$$\begin{aligned} & \eta \frac{\partial^2 v_z^2}{\partial r^2} + \frac{\partial\eta}{\partial r} \frac{\partial v_z^2}{\partial r} + \frac{\eta}{r} \frac{\partial v_z^2}{\partial r} = \\ & -\frac{\partial\eta}{\partial r} \frac{\partial v_r^1}{\partial z} - \frac{\partial\eta}{\partial z} \frac{\partial v_z^0}{\partial z} - \eta \frac{\partial^2 v_r^1}{\partial z \partial r} - \frac{\eta}{r} \frac{\partial v_z^1}{\partial z} - 2\eta \frac{\partial^2 v_z^0}{\partial z^2} + \frac{\partial P^0}{\partial r z} - \rho G_z. \end{aligned} \quad (18)$$

The pressure is determined at the next stage (by taking into account the solvability condition $\left(\frac{\partial^2 P^0}{\partial r \partial z} = \frac{\partial P^0}{\partial z \partial r}\right)$ where the right hand side is obtained as a derivative with respect to r of the expression obtained from (18) and the left hand side – as a derivative in respect to z of the expression obtained from (17)). If we consider the first term of the asymptotic series for the velocity only, we obtain an interesting equation for v_z^0 from (18) and (16):

$$\frac{\partial^2 v_z^0}{\partial z^2} - \frac{\partial\eta}{\partial z} \frac{1}{\eta} \frac{\partial\rho}{\partial z} \frac{1}{\rho} v_z^0 = -\frac{\rho}{\eta} G_z + \frac{1}{\eta} \frac{\partial P^0}{\partial z}. \quad (19)$$

Taking into account the expressions for η, ρ, v_z^0 , one can see that it leads to the following equation for the function $u(z)$ in the homogeneous case $\left(G_x = 0, \frac{\partial P^0}{\partial z} = 0\right)$:

$$u'' - \frac{\eta'}{\eta} \frac{\rho'}{\rho} u = 0. \quad (20)$$

One can see that we have the 1D Schrödinger equation with a specific potential for the function $u(x)$ corresponding to zero energy (the similar problem for the quantum graph is known as the threshold resonance, see, e.g., [28]).

Thus, for the flow concentrated near a line (a thin cylinder) we have one-dimensional model. Correspondingly, more complicated case of flow concentrated near a network (system of coupled segments) can be reduced to the corresponding metric graph with the Schrödinger operator:

$$H = -\frac{d^2}{dx^2} + \frac{\eta' \rho'}{\eta \rho}$$

on the edges as the first approximation for the description of the flow. We call it the Stokes graph (Γ). It is necessary to determine boundary conditions at the graph vertices. Consider a vertex (let it be zero point) with n output edges. From physical conditions, one has:

$$\rho_1(0) = \rho_2(0) = \dots \rho_n(0) = \rho(0)$$

and

$$u_1'(+0) = u_2'(+0) = \dots u_n'(+0) = u'(0).$$

Here indices mark the edges (u_j is the value of u at j -th edge). The last condition is related to the pressure continuity (see, e.g., [26, 29, 30]). Here, $u_j'(+0)$ is the derivative in the outgoing direction at the vertex 0. The continuity equation gives us for this vertex:

$$\sum_{j=1}^n u_j = -\left(\frac{\rho(0)}{\sum_{j=1}^n \rho_j'(+0)}\right) u'(0). \quad (21)$$

It is similar to well-known δ' -coupling condition for the quantum graph [15]. The coupling constant is related to the density derivative.

We will consider the following case: $q = \frac{\eta' \rho'}{\eta \rho}$ is uniformly continuous on every edge of the graph Γ (we mark the set of its edges as E and the set of its vertices as V),

$$\theta = \frac{\rho(0)}{\sum_{j=1}^n \rho_j'(+0)}$$

is positive. We will deal with the following homogeneous equation:

$$(Hu)(x) = 0. \quad (22)$$

Here, operator H is defined as follows. At each edge it acts as:

$$(Hu)(x) = -\frac{d^2}{dx^2}u(x) + q(x)u(x), x \in E(\Gamma). \quad (23)$$

Elements from its domain belong to the Sobolev space H^2 at each edge. As for vertices, the following condition takes place (for a vertex x having n output edges):

$$u_1'(+x) = u_2'(+x) = \dots = u_n'(+x) = u'(x), x \in V(\Gamma), \quad (24)$$

$$\sum_{j=1}^n u_j(x) + \theta u'(x) = 0, x \in V(\Gamma), \theta > 0. \quad (25)$$

$$u(a) = 0, a \in \partial\Gamma. \quad (26)$$

One can see that we have constructed a metric graph model which coincides with that of the two-dimensional case [27]. Of course, the definition of the function u differs from that of the 2D case but the model operator is the same. Correspondingly, one can obtain the same result for ‘‘cylindrical’’ case. Namely, we obtain the following statement.

Definition. Operator H is denoted as sign preserving on the graph Γ if the inequality $u(x)u(x') > 0$ takes place for any nontrivial solution of equation (22). Here x, x' are arbitrary points of $\Gamma \setminus \partial\Gamma$.

The main result of the paper is the following inequality (27) that is analogous to the Harnack’s inequality for an elliptic operator on a manifold.

Main Theorem. Let H be sign preserving on graph Γ . Then there exists a constant γ , determined by the operator H and the structure of the graph Γ only, such that each non-negative on Γ solution $u(x)$ of inequality $Hu \geq 0$ satisfies the following inequality:

$$\max_{x \in \Gamma_0} u(x) \leq \gamma \min_{x \in \Gamma_0} u(x), \quad (27)$$

on any locally compact (in respect to Γ) subgraph Γ_0 , $\Gamma_0 \subset \Gamma$.

Acknowledgements

This work was partially financially supported by the Government of the Russian Federation (grant 08-08), by grant 16-11-10330 of Russian Science Foundation. E. Milakis was partially supported by Research Promotion Foundation (Cyprus) grant no Excellence/1216/0025.

References

- [1] Chivilikhin S.A., Gusarov V.V., Popov I.Y. Charge pumping in nanotube filled with electrolyte. *Chinese Journal of Physics*, 2018, **56**(5), P. 2531–2537.
- [2] Popov I.Yu., Kyzurova K.N. and Blinova I.V., Stokes flow driven by a Stokeslet in a cone. *Acta Mechanica*, 2014, **225**, P. 3115–3121.
- [3] Belonenko M.B., Chivilikhin S.A., Gusarov V.V., Popov I.Yu. and Rodygina O.A. Soliton-induced flow in carbon nanotube. *Europhys. Lett.*, 2013, **101**(6), P. 66001.
- [4] Sharan M. and Popel A.S. A two-phase model for flow of blood in narrow tubes with increased effective viscosity near the wall. *Biorheology*, 2001, **38**, P. 415–428.
- [5] Secomb T.W. and El-Kareh A.V. Models for slow blood flow in narrow tubes: effect of aggregation and sedimentation on flow resistance. *Biorheology*, 1995, **32**, P. 169–169.
- [6] Srivastava V.P. A theoretical model for blood flow in small vessels. *Int. J. Applications and Appl. Math.*, 2007, **2**(1), P. 51–65.
- [7] Gerya T. *Introduction to Numerical Geodynamic Modelling*. Cambridge, Cambridge University Press, 2010.
- [8] Ismail-Zadeh A., Tackley P. *Computational methods in Geodynamics*. Cambridge, Cambridge University Press, 2010.
- [9] Ribe N.M., et al. Buckling instabilities of subducted lithosphere beneath the transition zone. *Earth and Planetary Science Letters*, 2007, **254**, P. 173–179.
- [10] Griffiths R.W. The Dynamics of Lava Flows. *Annual Review of Fluid Mechanics*, 2000, **32**(1), P. 477–518.
- [11] Griffiths I.M., Howell P.D. The surfacetension-driven evolution of a two-dimensional annular viscous tube. *Journal of Fluid Mechanics*, 2007, **593**, P. 181–208.
- [12] Griffiths I.M., Howell P.D. Mathematical modelling of non-axisymmetric capillary tube drawing. *Journal of Fluid Mechanics*, 2008, **605**, P. 181–206.
- [13] Gerasimenko N., Pavlov B. Scattering problems on non-compact graph. *Theor. Math. Phys.*, 1988, **74**, P. 230–240.
- [14] Exner P. and Seba P. Free quantum motion on a branching graph. *Rep. Math. Phys.*, 1989, **28**, P. 7–26.
- [15] Berkolaiko G., Kuchment P., *Introduction to Quantum Graphs*. AMS, Providence, 2012.
- [16] Kostykin V., Schrader R. Laplacians on metric graphs: eigenvalues, resolvents and semigroups. Quantum graphs and their applications, 201–225, Contemp. Math., 415, Amer. Math. Soc., Providence, RI, 2006.
- [17] Popov I.Yu., Skorynina A.N., Blinova I.V. On the existence of point spectrum for branching strips quantum graph. *J. Math. Phys.*, 2014, **55**, P. 033504/1–20.
- [18] Eremin D.A., Grishanov E.N., Nikiforov D.S., Popov I.Y. Wave dynamics on time-depending graph with Aharonov-Bohm ring. *Nanosystems: Physics, Chemistry, Mathematics*, 2018, **9**(4), P. 457–463.

- [19] Panasenko G.P. Asymptotic expansion of the solution of Navier-Stokes equation in tube structure and partial asymptotic decomposition of the domain. *Applicable Analysis*, 2000, **76**(3), P. 363–381.
- [20] Panasenko G.P., Stavre R. Asymptotic analysis of a periodic flow in a thin channel with visco-elastic wall. *J. Math. Pures Appl.*, 2006, **85**, P. 558–579.
- [21] Panasenko G.P., Stavre R. Asymptotic analysis of the Stokes flow in a thin cylindrical elastic tube. *Applicable Analysis*, 2012, **91**(11), P. 1999–2027.
- [22] Melikhov I.F., Popov I.Y. Asymptotic analysis of thin viscous plate model. *Nanosystems: Physics, Chemistry, Mathematics*, 2018, **9**(4), P. 447–456.
- [23] Post O. Branching quantum waveguides with Dirichlet boundary conditions: the decoupling case. *J. Phys. A: Math. Gen.*, 2005, **38**, P. 4917–4931.
- [24] Molchanov S., Vainberg B. Scattering solutions in networks of thin fibers: small diameter asymptotics. *Comm. Math. Phys.*, 2007, **273**, P. 533–559.
- [25] Popov I.Yu., Eremin D.A., Ivanov D.A. Regular potential approximation for delta-perturbation supported by curve of the Laplace-Beltrami operator on the sphere. *Z. Anal. Anwen.*, 2012, **31**(2), P. 125–137.
- [26] Jivkov A.P., Hollis C., Etiese F., McDonald S.A., Withers P.J. A novel architecture for pore network modelling with applications to permeability of porous media. *J. Hydrology*, 2013, **486**, P. 246–258.
- [27] Kovaleva M.O., Popov I.Y. Harnack’s Inequality for Stokes Graph. *Zeitschrift für Analysis und ihre Anwendungen*, 2016, **35**(4), P. 383–396.
- [28] Cacciapuoti C. and Exner P. Nontrivial edge coupling from a Dirichlet network squeezing: the case of a bent waveguide. *J. Phys. A.*, 2007, **40**, P. F511–F523.
- [29] Gudzovski A.V. On the computation for hydraulic networks. *Doklady Akad. Nauk*, 1998, **358**, P. 765–767.
- [30] Pokornyi Yu.V., Penkin O.M., Pryadev V.L., Borovskikh A.V., Lazarev K.P. and Shabrov S.A. *Differential Equations on Geometrical Graphs*. Moscow, Fizmatlit, 2004.
- [31] Van Dyke M. *Perturbation Methods in Fluid Mechanics*. Stanford, Parabolic Press, 1975.

Photo- and cathodoluminescence spectra of diamond single crystals formed by sintering of detonation nanodiamond

S. V. Kidalov¹, M. V. Zamoryanskaya¹, V. A. Kravez¹, L. V. Sharonova¹, F. M. Shakhov¹, E. B. Yudina¹,
T. O. Artamonova², M. A. Khodorkovskii², A. Ya. Vul¹

¹Ioffe Institute, Polytechnicheskaya 26, St. Petersburg, 194021, Russia

²Peter the Great St. Petersburg Polytechnic University, Polytechnicheskaya 29, St. Petersburg, 195251, Russia
alexandervul@mail.ioffe.ru

PACS 68.55.Ln

DOI 10.17586/2220-8054-2019-10-1-12-17

The photo- and cathodoluminescence spectra (PL, CL) of diamond single crystals synthesized under high-pressure and at high-temperature (HPHT sintering) from detonation nanodiamonds (DND) particles with Gd and Eu ion-functionalized surfaces have been studied. The HPHT sintering was made under pressures ($P \cong 7$ GPa) and temperature ($T = 1300 - 1500$ °C). The DND particles have sizes of 4 – 5 nm, hydrocarbons and/or alcohols were used at the HPHT synthesis instead of traditional metal catalysts. The initial and synthesized crystals were characterized by X-ray microanalysis, mass-spectroscopy, scanning electron microscopy (SEM), PL and CL. Mass spectra confirmed that Gd and Eu atoms were inserted into the volume of diamond single crystals in the HPHT sintering. A significant conversion of the PL and CL spectra of synthesized diamond single crystals compared with HPHT diamond crystals were observed. Transformation of the point defect assemblies inherent to the diamond crystal can explain the observed spectra.

Keywords: detonation nanodiamond, surface modification, HPHT synthesis, diamond single crystal, photoluminescence of diamond, cathodoluminescence of diamond, defects in diamond, N-V centers, $3d-4f$ elements.

Received: 8 December 2018

Revised: 11 January 2019

1. Introduction

The recent increase of interest in nanodiamonds is related to their potential utility as nanoparticles in bio-imaging systems [1–3]. The idea is related to the usage of light emission from luminescent centers in diamond lattice. Currently-known centers are nitrogen-vacancy, silicon-vacancy color centers [4,5] and impurity of Eu ions in diamond lattice [6,7]. Gadolinium atoms are particularly attractive as a dopant in diamond lattice due to their potential use in nuclear magnetic resonance tomography [8].

Recently, we developed a method for producing of detonation nanodiamonds (DND) hydrosol with mean size of particles 4 – 5 nm [9,10] and submitted technological protocol for surface modification of DND particles by metal ions [11]. We also demonstrated an interesting effect of single diamond crystal formation from DND particles at high-pressure and high-temperature (HPHT) sintering [12].

It is readily obvious that it would be very attractive to study the possibility of metal ion encapsulation in diamond crystalline structure using DND surface modified particles as starting materials for HPHT sintering. This paper submits the first results from these studies.

2. Experimental

2.1. Samples

We studied following three types of samples. The first one was diamond single crystals (DSC) produced by sintering of DND powder at HPHT conditions in the presence of alcohols and/or hydrocarbons in a high-pressure chamber. The procedure of DND sintering is described in detail in [11,12]. The second type was DSC sintered at the same conditions from DND with surface modified with europium (Eu). The third type was DSC sintered at the same conditions from DND with surface modified with gadolinium (Gd).

The initial DND, with size of 4 – 5 nm, were purified and de-agglomerated in accordance with a procedure described in [9,10]. Surface modification of DND with $3d-4f$ elements (Eu, Gd) was carried out using ionic exchange in accordance to the procedure described in [13,14].

The synthesized DSC samples represent a powder of diamond single crystals ranging of up to 5 μm (see Fig. 1).

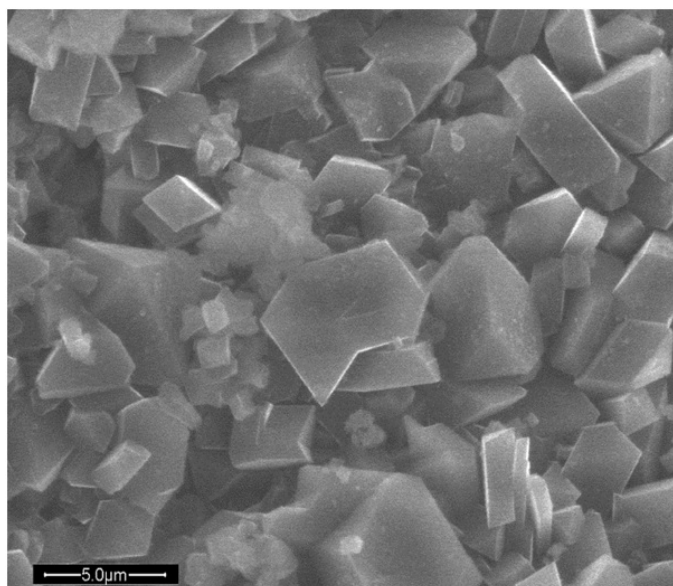


FIG. 1. SEM image of DSC obtained by HPHT sintering of DND modified with $3d-4f$ elements. Scale bar is 5 micron

2.2. Methods

The composition of the diamonds studied by energy-dispersive X-ray spectroscopy (EDX) using X-ray micro-analyzer CAMEBAX-MICROBEAM from CAMECA, equipped with four X-ray spectrometers with a set of crystal analyzers. Quantitative X-ray spectral microanalysis was carried out under the following conditions: accelerating voltage – 20 KV (electron energy 20 KeV), angle of X-ray selection – 40° , current of absorbed electrons – 10 – 50 nA. The detection limit of the rare-earth elements in the carbon matrix was under optimal conditions in the range 0.02 – 0.05 wt.%. As the concentration approaches this value, the microanalysis became semiquantitative, the relative error could reach 50 – 100 %. To obtain the average content of $3d-4f$ elements, the analysis have been performed with a defocused electron probe 50 μm in diameter.

Preparation of samples for mass-spectroscopy with laser evaporation consisted in gluing a portion of diamond powder to the target using a double-sided adhesive tape. Measurements performed using mass spectrometer with ion cyclotron resonance and Fourier transform (Model 902-MS MALDI Mass Spectrometer, Varian). The spectrometer was equipped with a superconducting magnet of 9.4 Tesla. Measurements were performed in the positive ion mode.

The laser evaporation of the samples performed using third harmonic of the Nd: YAG laser (355 nm), whose power can be widely changed. We used DPSS (Diode-pumped solid-state) Nd:YAG laser with titanyl potassium phosphate crystal (KTiOPO_4 , KTP) for frequency doubling. The accuracy of the measured monoisotopic mass after calibration was better than 5 ppm.

The PL study was carried out on spectrometer Ocean Optics Maya 2000 Pro in spectral range 200 – 1100 nm, using 532 nm laser for excitation. The resolution of the spectrometer was 0.45 nm.

Cathodoluminescence (CL) spectra were measured on samples of diamond powder pressed into indium and carbon film with a thickness of 100 nm deposited on diamonds. The spectra obtained at room temperature. Energy of incident electron beam was 15 KeV [15].

3. Results and discussion

According to EDX measurements, the europium and gadolinium content in DSC samples obtained by HPHT sintering of DND with modified surface was 0.01 – 0.02 at.% for both Gd and Eu samples.

Unfortunately, EDX technique is unable to distinguish $3d-4f$ atoms incorporated into crystal structure and deposited on the surface of diamond crystal. Thus, it is insufficient to give comprehensive evidence for presence of Gd or Eu inside DSC obtained by sintering of DND particles with modified surface.

3.1. Mass spectroscopy

Figure 2(a) presents mass spectrum of DSC obtained by sintering from initial DND without surface modification.

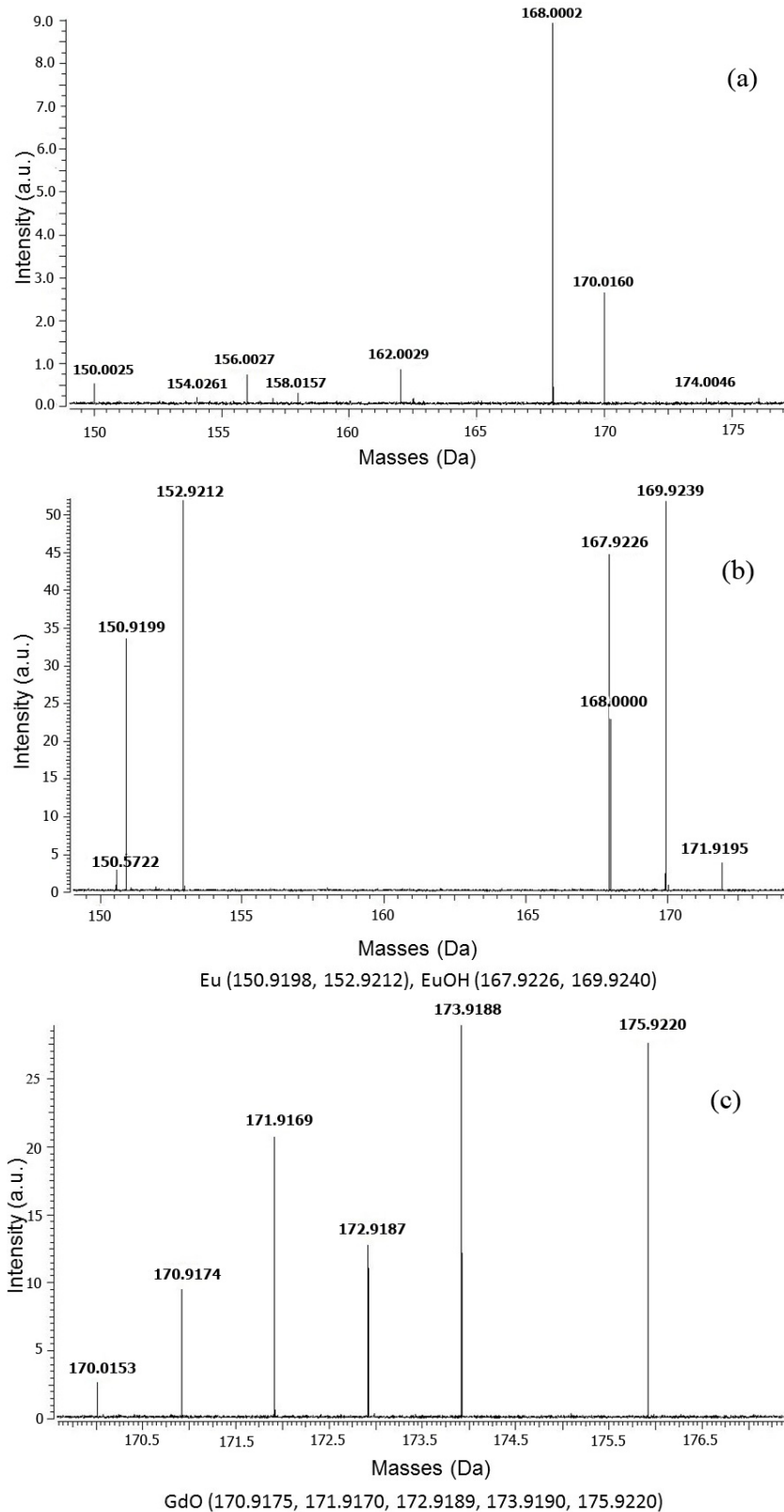


FIG. 2. Mass spectra of DSC samples obtained with use of laser evaporation: (a) from sample obtained by HPHT sintering of pure DND; (b) from sample obtained by HPHT sintering of DND with surface modified by Eu; (c) from sample obtained by HPHT sintering of DND with surface modified by Gd

The spectrum is measured using laser evaporation of diamond crystals. In the range of 150 – 175 AMU, it demonstrates a number of peaks corresponding to pure carbon atomic clusters (at 156.0027, 168.0002) and clusters containing nitrogen (158.0157, 170.0160), or both oxygen and nitrogen (150.0025, 162.0029, 174.046, 154.0261). The presence of oxygen and nitrogen is typical for surface of diamond crystals obtained by HPHT sintering. The same spectra demonstrate DSC samples prepared by sintering of DND modified by Eu as well as by Gd ions. At that, observed no lines that could attributed to Gd and Eu.

Figure 2(b) demonstrates mass spectrum at same band of masses of DSC sample produced by sintering DND modified by Eu. The spectrum measured at an order of magnitude increased compared to spectra in Fig. 2(a) power of evaporating laser. Along with prominent line of carbon clusters at mass 168.000, it demonstrates a series of intensive lines corresponding to europium isotopes (150.9198, 152.9212) and europium hydroxide EuOH (167.9226, 169.9240).

In Fig. 2(c), a mass spectrum of DSC sample produced by sintering DND modified by Gd is presented. In the band of masses 169.5 – 178.5, we observed noticeable line related to nitrogen-containing carbon clusters (170.0153). The observed series of intensive lines correspond to gadolinium oxide GdO (170.9175, 171.9170, 172.9189, 173.9190 and 175.9220). The fact that signals related to Eu and Gd appear only at increased intensity of evaporating laser irradiation suggests that corresponding atoms are situated not at the surface but inside the bulk of micron sized diamond particles.

3.2. Cathodeluminescence spectra

Figure 3 demonstrates the comparison of CL spectra measured on three types of samples: initial DND (curve 1), SDC sintered of initial DND (curve 2), SDC sintered of DND with surface modified by Eu ions (curve 3). Taking into account that the shape of CL spectra of diamond determined mainly by system of structural defects inside crystalline lattice of particles and contribution of surface [16], we can conclude that SDC conserve the system of defects inherited from the same of parental DND. The moderate shift to shorter wavelength range can be attributed to decrease of contribution of effective surface of diamond particles due to increase of crystalline size as a result of sintering process.

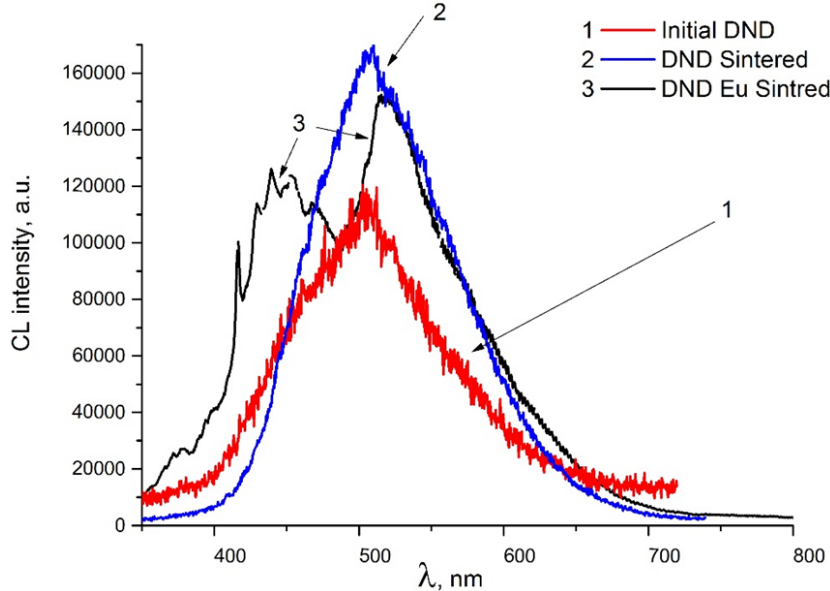


FIG. 3. Comparison of CL spectra from initial DND, DSC obtained from initial DND and DSC obtained from DND with surface modified by Eu ions

CL spectra of SDC obtained by sintering of DND with surface modified by Eu ions exhibit dramatic differences compared to the same spectra measured of SDC having no Eu. The presence of two peaks reveals significant transformation of bulk structure and increase of defects in crystalline structure of the SDC. The propagation of luminescence to short wavelength region can manifest formation the structural defects of diamond lattice obviously related to the difference between effective radius of carbon and europium atoms incorporated into diamond. Forming the breakdown in the middle of spectral range and corresponding longwave apex may be concerned to quenching the luminescence of nitrogen color centers at corresponding wavelengths due to distortion of diamond

crystalline lattice by intrusion of $3d-4f$ atoms. The observed dramatic transformation of CL spectra related to Eu atoms in structure of SDC samples under study suggests that structural modification of diamond lattice is most likely due to the presence of incorporated atoms in position far from crystal surface.

3.3. Photoluminescence spectra

Figure 4 demonstrates photoluminescence (PL) spectra for the three types of samples. The first spectrum measured on DSC sintered of initial DND containing no $3d-4f$ elements (curve 1). Second spectrum was measured on DSC sintered of DND modified by Gd (curve 2). The third spectrum corresponds to DSC sintered of DND modified by Eu (curve 3). The spectrum of DSC containing no $3d-4f$ elements is typical for diamond crystals obtained by sintering of DND in the presence of hydrocarbons at high pressure and temperature [17].

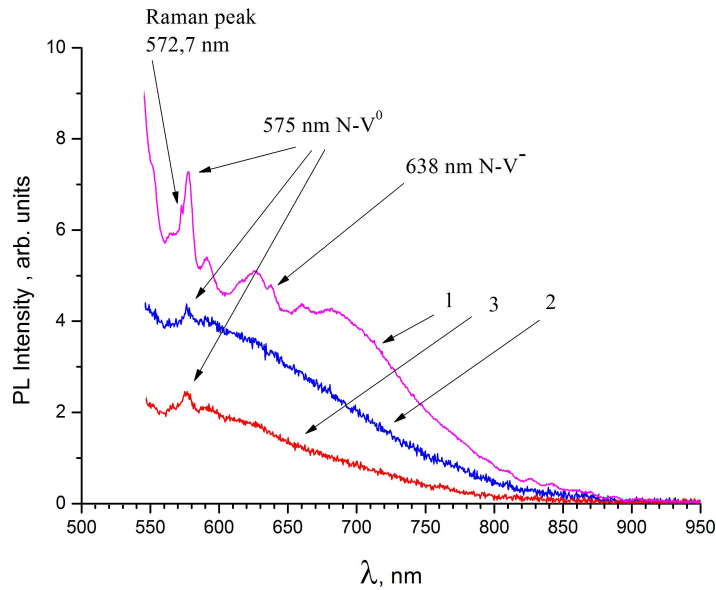


FIG. 4. PL spectra of diamond single crystals produced by HPHT sintering of DND: curve 1 – PL spectrum of diamond single crystals produced from pure DND curves 2 and 3 crystals produced from DND with surface modified by $3d-4f$ ions (Gd – curve 2, Eu – curve 3)

The spectrum demonstrates clearly visible lines of nitrogen-vacancy color centers and detectable feature attributed to Raman scattering (curve 1 in Fig. 4). Photoluminescence of DSC containing Gd and Eu exhibits noticeably smaller intensity and nearly complete absence of expressed lines from nitrogen centers. Most likely, it is related to additional distortion of diamond lattice due to incorporation of large sized and heavy $3d-4f$ atoms. The additional vacancies and distorted bond lengths promote quenching of luminescence of color centers in diamond lattice. Thus, comparison of PL spectra from samples of DSC sintered of DND with $3d-4f$ atoms on surface to spectra from DSC sintered of pure DND demonstrates successful incorporation of Eu and Gd into the lattice of diamond single crystals.

4. Conclusions

The results of experiments support the possibility of obtaining diamond crystals containing incorporated $3d-4f$ elements by sintering from DND particles with surface modified by corresponding ions.

We have successfully demonstrated incorporation of Eu and Gd atoms into structure of micron-sized diamond single crystals during sintering from DND particles. Analysis of mass spectra measured with help of laser ablation confirms the presence of Eu and Gd inside diamond crystals. The comparison of CL as well as PL spectra of diamond crystals, sintered from DND with and without surface modification by Eu or Gd reveals transformation of system of defects due to the insertion of large sized $3d-4f$ atoms inside diamond lattice.

Acknowledgements

The research was supported by the Russian Science Foundation (Project 14-13-00795). Mass spectrometry was carried out using scientific equipment of the Center of Shared Usage “The analytical center of nano- and biotechnologies of SPbPU”. Authors thanks to Dr. Artur Dideikin for very useful discussion and advices.

References

- [1] Guodong Xia, et al. Selective phase synthesis of a high luminescence $\text{Gd}_2\text{O}_3:\text{Eu}$ nanocrystal phosphor through direct solution combustion. *Nanotechnology*, 2010, **21**, 345601.
- [2] Antic B., et al. Optimization of photoluminescence of $\text{Y}_2\text{O}_3:\text{Eu}$ and $\text{Gd}_2\text{O}_3:\text{Eu}$ phosphors synthesized by thermolysis of 2,4-pentanedione complexes. *Nanotechnology*, 2010, **21**, 245702.
- [3] Aharonovich I. Engineering chromium-related single photon emitters in single crystal diamonds. *New Journal of Physics*, 2011, **13**, 045015.
- [4] Shenderova O.A., et al. Nitrogen control in nanodiamond produced by detonation shock-wave-assisted synthesis. *J. Phys. Chem. C*, 2011, **115**, P. 14014–14024.
- [5] Neu E., Steinmetz D., et al. Single photon emission from silicon-vacancy colour centres in chemical vapour deposition nano-diamonds on iridium. *New J. Phys.*, 2011, **13**, 025012.
- [6] Magyar A., Hu W., et al. Synthesis of luminescent europium defects in diamond. *Nature Communications*, 2014, **5**, 3523.
- [7] Sedov V.S., Kuznetsov S.V., et al. Diamond-EuF₃ nanocomposites with bright orange photoluminescence. *Diamond and Related Materials*, 2017, **72**, P. 47–52.
- [8] Nakamura T., Ohana T., et al. Simple Fabrication of Gd(III)-DTPA-Nanodiamond Particles by Chemical Modification for Use as Magnetic Resonance Imaging (MRI) Contrast Agent. *Applied Physics Express*, 2013, **6**, 0150016.
- [9] Aleksenskiy A.E., Eydelman E.D., Vul' A.Ya. Deagglomeration of detonation nanodiamonds. *Nanosci. Nanotech. Lett.*, 2011, **3**, P. 68–74.
- [10] Dideikin A.T., Aleksenskii A.E., et al. Rehybridization of carbon on facets of detonation diamond nanocrystals and forming hydrosols of individual particles. *Carbon*, 2017, **122**, P. 737–745.
- [11] Kidalov S.V., Shakhov F.M., et al. Growth of diamond microcrystals by the oriented attachment. *Tech. Phys. Lett.*, 2017, **43**, P. 53–56.
- [12] Dideikin A.T., Eidelman E.D., et al. Oriented-attachment growth of diamond single crystal from detonation nanodiamonds. *Diam. Relat. Mater.*, 2017, **75**, P. 85–90.
- [13] Aleksenskii A.E., Yagovkina M.A., Vul A.Ya. Intercalation of ultrafine-dispersed diamond in aqueous suspensions. *Physics of the Solid State*, 2004, **46**, P. 685–686.
- [14] Panich A.M., Shames A.I., et al. Magnetic Resonance Study of Gadolinium-Grafted Nanodiamonds. *The Journal of Physical Chemistry C*, 2016, **120**, P. 19804–19811.
- [15] Zamoryanskaya M.V., Konnikov S.G., Zamoryanskii A.N. A high-sensitivity system for cathodoluminescent studies with the Camebax Electron Probe Microanalyzer. *Instruments and Experimental Techniques*, 2004, **47**, P. 477–483.
- [16] Zaitsev A.M. *Optical properties of diamond*. Berlin, Heidelberg: Springer-Verlag, 2001.
- [17] Kidalov S.V., Shnitov V.V., et al. Chemical composition of surface and structure of defects in diamond single crystals produced from detonation nanodiamonds. *Nanosystems: Physics, Chemistry, Mathematics*, 2018, **9** (1), P. 21–24.

Heisenberg chain equations in terms of Fockian covariance with electric field account and multiferroics in nanoscale

S. Leble

Baltic Federal University, st. A.Nevskogo, 14, Kaliningrad, Russia, 236006

lebleu@mail.ru

DOI 10.17586/2220-8054-2019-10-1-18-30

Heitler–Heisenberg multispin states were studied via irreducible representations of the united symmetry with respect to permutations and space transformations group. The mean energy is given in explicit form in terms of the characters of the joint group irreducible representations. The system's Fockian covariance incorporates its exchange integral of the self-consistent states into the Heisenberg chain theory. External fields account is delivered in perturbation theory frame. Its application to statistical physics approach leads to the thermodynamic parameter evaluation. The nanotube example with space symmetry including rotations and translations, is studied. Its symmetry introduces basic closest neighbor exchange integrals that enter the statistical sum.

Keywords: multielectron states, permutation-space symmetry, mean energy, Gauss distribution, Heisenberg chain, Fockian symmetry, electric field, nanotube, multiferroics.

Received: 24 January 2019

Revised: 10 February 2019

1. Introduction

A quantum theory of a multielectron system bases on joint symmetry group of permutations and space symmetry. In the pioneer paper of Heisenberg [1] it was established, that Weiss model of ferro-magnetism is explained by electric interaction, which origin may be understood on base of theory of Heitler–London hydrogen molecule. It is naturally combined with Hartree–Fock theory [2] and its further self-consistent one-particle generalizations that provide better exchange integral evaluation including the system spectral properties [3].

The group theoretical foundation of [1] is based on multispin state via irreducible representations of the symmetry with respect to permutation group [4]. The problem of Hamiltonian spectrum parameters evaluation is expressed in terms of irreducible representations of symmetry group and exchange integrals, see also [5].

The next important step in the theory development taking into account the antisymmetry of the wave function of electrons and a more advanced extended symmetry, including space (geometry) symmetry of equivalent positions of atoms equilibrium. The magnetic properties of matter exist as a result of electrons spins and the antisymmetry of the wave function.

When a system is in an external electric or magnetic field, an additional terms in the Hamiltonian appear. Its microscopic origin is conventionally understand in terms of perturbation theory that gives deformation of wavefunctions and energy eigenvalues. The results in atomic physics are known as Stark and Zeeman effects.

A multiferroic control implies a manipulation of magnetic moment by electric field switching. General thermodynamic consideration, specified by Dzialoshinski, introduces the magnetoelectric constants, namely longitudinal and perpendicular dielectric constants, the magnetic susceptibilities, and the constants describing the magneto-electrical effect.

In this paper, a spectral and statistical theory in the Heisenberg spirit is developed. The application of statistical physics approach, formulated in [1] leads to the mentioned thermodynamic parameters evaluation with external magnetic and electric fields account. The ferro-magnetism appearance conditions are illustrated by plotting the dependence of closest neighbors number on exchange integral.

Applications to amorphous microwires and crystalline nanowires are discussed by example of a tube made of atoms which space positions form symmetrical configuration. The energy and distribution parameter modifications for nanotubes naturally introduce the closest neighbors exchange integrals defined by the nanostructure symmetry. It gives a model thermodynamic description based on a statistical sum modifications.

2. A joint symmetry group of multi-electron systems

Generally a wave function of a multi-electron system:

$$\Phi = \Phi \left(\vec{R}_1, \dots, \vec{R}_K, (\vec{r}_1, \sigma_1), \dots, (\vec{r}_N, \sigma_N) \right) \in \mathcal{H}, \quad (1)$$

depends on the variables $\vec{R}_j \in R^3, j = 1, \dots, K$, as on parameters, that are coordinates of ‘‘adiabatic’’ atoms positions, $\vec{r}_i \in R^3, i = 1, \dots, N$ are electron coordinates and $\sigma_1, \sigma_2, \dots, \sigma_N$ are spin variables of electrons. Since the electrons are fermions, the Pauli–Luders theorem states that the wave function must be antisymmetric in the variables of the electrons; this means that the function belongs the irreducible representation of the all-electrons permutation group.

A rotation in position space marked as $R(\alpha, \beta, \gamma)$, where the angles α, β, γ are Euler ones represents in a 1-electron spin space by a 2×2 matrix $u(\alpha, \beta, \gamma)$:

$$u(\alpha, \beta, \gamma) = D^{1/2}(\alpha, \beta, \gamma), \quad (2)$$

where $D^{1/2}$ is an unitary matrix of irreducible representation of rotation group [6]. This means that the wave function (1) transforms as direct product of the representations (2). To study the joint group table it is convenient to ‘‘jump’’ into the representation of the spinors Φ , because the permutations and rotations act also to the atoms positions. The actions in Hilbert space of states are for the permutations:

$$\begin{aligned} \mathcal{P}\Phi \left(\vec{R}_1, \dots, \vec{R}_K, (\vec{r}_1, \sigma_1), \dots, (\vec{r}_N, \sigma_N) \right) = \\ \Phi \left(\vec{R}_1, \dots, \vec{R}_K, (P\vec{r}_1, P\sigma_1), \dots, (P\vec{r}_N, P\sigma_N) \right) \end{aligned} \quad (3)$$

and

$$\begin{aligned} \mathcal{R}\Phi \left(\vec{R}_1, \dots, \vec{R}_K, (\vec{r}_1, \sigma_1), \dots, (\vec{r}_N, \sigma_N) \right) = \\ \mathcal{D}_{\sigma_1, \sigma'_1}^{1/2} \dots \mathcal{D}_{\sigma_N, \sigma'_N}^{1/2} \Phi \left(\vec{R}_1, \dots, \vec{R}_K, (R\vec{r}_1, \sigma'_1), \dots, (R\vec{r}_N, \sigma'_N) \right) \end{aligned} \quad (4)$$

for rotations. The operators \mathcal{P}, \mathcal{R} act in Hilbert space \mathcal{H} , while P, R act in position space R^3 .

A combination of the transformations (4) and (6):

$$\begin{aligned} \mathcal{P}\mathcal{R}\Phi \left(\vec{R}_1, \dots, \vec{R}_K, (\vec{r}_1, \sigma_1), \dots, (\vec{r}_N, \sigma_N) \right) = \\ \mathcal{D}_{P\sigma_1, \sigma'_1}^{1/2} \dots \mathcal{D}_{P\sigma_N, \sigma'_N}^{1/2} \Phi \left(\vec{R}_1, \dots, \vec{R}_K, (PR\vec{r}_1, \sigma'_1), \dots, (PR\vec{r}_N, \sigma'_N) \right), \end{aligned} \quad (5)$$

and, in opposite order,

$$\begin{aligned} \mathcal{R}\mathcal{P}\Phi \left(\vec{R}_1, \dots, \vec{R}_K, (\vec{r}_1, \sigma_1), \dots, (\vec{r}_N, \sigma_N) \right) = \\ \mathcal{D}_{\sigma_1, P\sigma_1}^{1/2} \dots \mathcal{D}_{\sigma_N, P\sigma_N}^{1/2} \Phi \left(\vec{R}_1, \dots, \vec{R}_K, (P\vec{r}_1, P\sigma_1), \dots, (RP\vec{r}_N, RP\sigma_N) \right). \end{aligned} \quad (6)$$

For the joint symmetry applications the Frobenius theorem is used. Let H be a subgroup of the group G and $\gamma^{(i)}$ is an irreducible representation of H . Then the representation Γ of G , induced by $\gamma^{(i)}$ contains each irreducible representation Γ^λ of G so many times as $\gamma^{(i)}$ contains in the representation of H given by matrices Γ^λ .

The characters of the symmetry group is evaluated by the formula from [7],

Let us give more details for simplest example of Hydrogen molecule. In the case of two-electron system the wave function is defined in six-dimensional position space with the coordinate set $\{x_1, y_1, z_1; x_2, y_2, z_2\}$ and with extra discrete spin variables σ_1, σ_2 , that runs numbers $-1, 1$. $\Phi = \Phi \left(\vec{R}_1, \vec{R}_2; \vec{r}_1, \sigma_1; \vec{r}_2, \sigma_2 \right)$. Suppose atom positions \vec{R}_1, \vec{R}_2 lie in the plane xy symmetrically to origin.

The permutation, in this case, acts in the direct product of space and spin variables as:

$$P\{x_1, y_1, z_1; x_2, y_2, z_2; \sigma_1, \sigma_2\} = \{x_2, y_2, z_2; x_1, y_1, z_1; \sigma_2, \sigma_1\}. \quad (7)$$

A rotation in xy plane:

$$R\{x_1, y_1, z_1; x_2, y_2, z_2\} = \{(\cos\pi)x_1, (\cos\pi)y_1, z_1; (\cos\pi)x_2, (\cos\pi)y_2, z_2\}. \quad (8)$$

is accompanied to a transformation in spin space $u(R) \in SU(2)$ so as, generally

$$uv_\sigma = \mathcal{D}_{\nu\sigma}^{1/2} v_\sigma. \quad (9)$$

The product of the actions is:

$$\begin{aligned} PR\{x_1, y_1, z_1; x_2, y_2, z_2; \sigma_1, \sigma_2\} = \\ P\{(\cos\pi)x_1, (\cos\pi)y_1, z_1; (\cos\pi)x_2, (\cos\pi)y_2, z_2\}, \end{aligned} \quad (10)$$

and, in inverse order:

$$RP\{x_1, y_1, z_1; x_2, y_2, z_2; \sigma_1, \sigma_2\} = R\{x_2, y_2, z_2; x_1, y_1, z_1; \sigma_2, \sigma_1\} \quad (11)$$

with rotation action by (8).

3. Born–Oppenheimer approximation. Hamiltonian of the system of electrons of a solid

In the Born–Oppenheimer approximation, in the problem for electrons, the nuclei of a solid are assumed to be static. The Hamiltonian is written for a system of N electrons, in the field of the nuclei:

$$\hat{H} = -\frac{\hbar^2}{2m} \sum_i \Delta_i - \sum_{J,i} \frac{Z_J e^2}{|\vec{r}_i - \vec{R}_J|} + \sum_{i,j \neq i} \frac{e^2}{|\vec{r}_i - \vec{r}_j|}. \quad (12)$$

In the expression (12), \sum_i is a sum over all electrons, i is the electron number; \sum_J is a sum over all nuclei, J is nucleus number; Z_J is the charge of the nucleus with number J , expressed in charges of an electron module $|e|$; \vec{R}_J is a position of the nucleus J , \vec{r}_i is a radius-vector for the electron number i .

The energy eigenvalue problem is formulated in terms of the equation:

$$\hat{H}\Phi = E\Phi, \quad (13)$$

where the eigenfunctions $\Phi = \Phi(\vec{R}_1, \dots, \vec{R}_K, (\vec{r}_1, \sigma_1), \dots, (\vec{r}_N, \sigma_N))$, are parametrized by the nuclei positions \vec{R}_j , $\sigma_1, \sigma_2, \dots, \sigma_N$ are electron spin variables. Since the electrons are fermions, the Pauli principle claims, that a wave function must be antisymmetric in the variables of the electrons, for example,

$$\Phi(\vec{R}_1, \dots, \vec{R}_K, (\vec{r}_1, \sigma_1), \dots, (\vec{r}_N, \sigma_N)) = -\Phi(\vec{R}_1, \dots, \vec{R}_K, (\vec{r}_N, \sigma_N), \dots, (\vec{r}_1, \sigma_1)).$$

For shorthand electrons are marked simply with their numbers, that is, we introduce the notation $i = (\vec{r}_i, \sigma_i)$. Then $\Phi = \Phi(\vec{R}_1, \dots, \vec{R}_K, 1, \dots, N)$, so further the summation by spin variable is implied.

A symmetry of the equation (13) is determined directly from Fock equations.

4. The Fock equations

Within the framework of the Hartree–Fock method, the wave function $\Phi = \Phi(\vec{R}_1, \dots, \vec{R}_K, 1, \dots, N)$ may be searched for in the form of automatically antisymmetric Slater determinant (see [2, 8]) composed of single-particle functions:

$$\Phi = \begin{vmatrix} \Psi_1(1) & \Psi_2(1) & \dots & \dots & \Psi_N(1) \\ \Psi_1(2) & \Psi_2(2) & \dots & \dots & \Psi_N(2) \\ \dots & \dots & \dots & \dots & \dots \\ \dots & \dots & \dots & \dots & \dots \\ \Psi_1(N) & \Psi_2(N) & \dots & \dots & \Psi_N(N) \end{vmatrix}$$

Here the functions $\Psi_j(i)$ are named as spin orbitals. From the variational principle ($\min \langle \Phi, \hat{H}\Phi \rangle$) the Fock equations for the spin-orbitals Ψ_i are derived. Let the set of variables “1,2” be marked as “ x, y ” as in [9] writing for shorthand:

$$\int dx = \sum_{\sigma} \int d\vec{r}. \quad (14)$$

The conventional form of the equations is:

$$\hat{F}_j \Psi_j(x) = \varepsilon_j \Psi_j(x), \quad (15)$$

and the \hat{F}_j are Fockians:

$$\hat{F}_j = \hat{h}_1 + \sum_{i=1}^{iN} (\hat{C}_i - \hat{J}_i) \quad (16)$$

where the Coulombian interaction operator is defined by: .

$$\hat{C}_i \Psi_j = \int \frac{\Psi_i^*(y) \Psi_i(y)}{r_{12}} dy \Psi_j(x) \quad (17)$$

where $r_{12} = |\vec{r}_1 - \vec{r}_2|$ and the exchange one is:

$$\hat{J}_i \Psi_j = \int \frac{\Psi_i^*(y) \Psi_j(y)}{r_{12}} dy \Psi_i(x) \quad (18)$$

and

$$\hat{h}_1 = -\frac{\hbar^2}{2m} \Delta_1 - \sum_J \frac{Z_J e^2}{|\vec{r}_1 - \vec{R}_J|}$$

A prime over summation sign means that a term with $i = j$ under the sum sign is skipped. The integration is carried out over the variables of particle 2, $r_{12} = |\vec{r}_1 - \vec{r}_2|$, $\Delta_1 = \frac{\partial^2}{\partial x_1^2} + \frac{\partial^2}{\partial y_1^2} + \frac{\partial^2}{\partial z_1^2}$, $\vec{r}_1 = (x_1, y_1, z_1)$. It is assumed that the functions Ψ_i are orthogonal: $\int \Psi_i^*(x) \Psi_k(x) dx = \delta_{ik}$.

A symmetry of the equation (15) is determined by the following.

5. Fock equation covariance

We base on **Fock Statement** [2]. Let L be a Hermitian operator, which is symmetric with respect to all the electrons, $\Omega = \alpha_1 \Psi_1 + \dots + \alpha_s \Psi_s$.

$$A = \frac{\int \bar{\Omega} L \Omega}{\int \bar{\Omega} \Omega}, \quad (19)$$

then the latter does not depend on coefficients $\alpha_1, \dots, \alpha_s$. If H is the energy operator, then, setting the variation of A to zero, one obtains the Schrödinger equation for the function Ω , to infer the Schrödinger equation from the variational principles, for any linear combination of functions. In particular the coefficients may be chosen as matrix elements of irreducible representation $D_{ik}^\nu(g)$ of the symmetry group $g \in G$, that defines action:

$$\Psi_i(gx) = \sum_k^s D_{ik}^\nu(g) \Psi_k, \quad (20)$$

A symmetry of the equation (13) is determined directly from Fock equations. Application of permutation transformation to the Fock equations system consist of

1) change the order of equations

2) the action of the operator T_g on exchange and Coulombian integrals includes action at $r_{12} = |x - y|$, that looks as $T_g|x - y| = |gx - y|$. After change of variables $y = gy'$ and application of irreducible representation matrices unitarity, we arrive at

$$\sum_i^s T_g \hat{J}_i \Psi_j = \sum_{k,p}^s D_{jp}^\nu(g) \int \frac{\Psi_k^*(y) \Psi_p(y)}{|g(x - y)|} dy \Psi_k(x) = \sum_{k,p}^s D_{jp}^\nu(g) \hat{J}_k \Psi_k, \quad (21)$$

and on the Coulomb one

$$\sum_i^s T_g \hat{C}_i \Psi_j = \sum_{k,p}^s D_{jk}^\nu(g) \int \frac{\Psi_p^*(y) \Psi_p(y)}{|g(x - y)|} dy \Psi_k = \sum_{k,p}^s \hat{C}_p D_{jk}^\nu(g) \Psi_k. \quad (22)$$

An account of symmetry with respect to the permutation group is studied in [4], where a determinant representation for the eigenfunctions was introduced. It explored by Fock in derivation of one-particle self-consistent equations via variational principle in terms of wave functions from irreducible subspaces [2]. The space transformation group action may be determined also via transformation of arguments.

A general symmetry transformations of the system of equations (15) is determined as in Sec. 2.

An irreducible representation basis is fixed by the projection operators P_{ik}^ν , numerated by indices ν, ik :

$$P_{ik}^\nu = \sum_G N_\nu D_{ik}^\nu(g) T_g, \quad (23)$$

normalized by N_ν .

The system of Fock equations then is rearranged under permutations action while the exchange integrals form the set J_g . The Coulombian and differential parts are invariant under permutations.

The eigenvalue problem of the exchange operators, numerated by the group elements g after summation by symmetry group is solved via:

$$\det\left[\sum_{g \in G} D_{ik}^\nu(g) J_g - \delta_{ik} E\right] = 0, \quad (24)$$

[4] that we take as the initial point of further investigation.

5.1. Heisenberg chain perturbation

Stark effect. A perturbation theory by the field $\epsilon = eE$ directed along x is applied to a solution ϕ of the perturbed Fockian:

$$H\phi = (H_F + \epsilon x)\phi, \quad (25)$$

reads as expansion by small parameter ϵ :

$$\phi = \phi_0 + \epsilon\phi^{(1)} + \dots \quad (26)$$

In the first order it gives the following expression for an eigen state:

$$\phi_n^{(1)} = \sum'_m \frac{(m|x|n)}{E_m - E_n} \phi_{0m}, \quad (27)$$

where $(m|x|n)$ are matrix elements of the Cartesian coordinate x in nonperturbed states. Plugging (26) into exchange integrals J_{ik} , defined for the electrons coupled to the centers i, k , by the expression (21):

$$J_{ik} = \frac{e^2}{2} \int \int \frac{\rho_{ik}(\vec{r}, \vec{r}')}{|\vec{r} - \vec{r}'|} d\vec{r} d\vec{r}', \quad (28)$$

where, in a spirit of Fock paper [10], it may include all interacting electrons of the closest neighbors, as:

$$\begin{aligned} \rho(\vec{r}, \vec{r}') &= \sum_p \phi_p^*(\vec{r}) \phi_p(\vec{r}') = \\ &= \sum_p (\phi_{0p}^*(\vec{r}) + \epsilon \phi_p^{(1)*}(\vec{r})) (\phi_{0p}(\vec{r}') + \epsilon \phi_p^{(1)}(\vec{r}')) = \\ &= \sum_p \phi_{0p}^*(\vec{r}) \phi_{0p}(\vec{r}') + \epsilon \sum_p [\phi_p^{(1)*}(\vec{r}) \phi_{0p}(\vec{r}') + \phi_{0p}^*(\vec{r}) \phi_p^{(1)}(\vec{r}')] + o(\epsilon^2) = \\ &= \rho_0(\vec{r}, \vec{r}') + \epsilon \rho_1(\vec{r}, \vec{r}') + \dots \end{aligned} \quad (29)$$

In the case of Stark effect:

$$J_{ik} = \frac{e^2}{2} \int \int \frac{\rho_0(\vec{r}, \vec{r}')}{|\vec{r} - \vec{r}'|} d\vec{r} d\vec{r}' + \epsilon \frac{e^2}{2} \int \int \frac{\rho_1(\vec{r}, \vec{r}')}{|\vec{r} - \vec{r}'|} d\vec{r} d\vec{r}' = J_{ik}^0 + eE J_{ik}^1, \quad (30)$$

we obtain the perturbed Heisenberg chain spin Hamiltonian [11]:

$$H = J_{ik}(\vec{S}_i, \vec{S}_k) = (J_{ik}^0 + eE J_{ik}^1)(\vec{S}_i, \vec{S}_k), \quad (31)$$

with obvious Ising case:

$$\begin{aligned} J_{ik}^1 &= \frac{e^2}{2} \int \int \frac{\rho_1(\vec{r}, \vec{r}')}{|\vec{r} - \vec{r}'|} d\vec{r} d\vec{r}' = \\ &= \frac{e^2}{2} \int \int \frac{\sum_p [\phi_p^{(1)*}(\vec{r}) \phi_{0p}(\vec{r}') + \phi_{0p}^*(\vec{r}) \phi_p^{(1)}(\vec{r}')] }{|\vec{r} - \vec{r}'|} d\vec{r} d\vec{r}'. \end{aligned} \quad (32)$$

Plugging (27) and using the shorthand $\int \int = \int$ yields:

$$\frac{e^2}{2} \int \frac{\sum'_{p,m} \phi_{0m}^*(\vec{r}) \frac{(n|x|m)}{E_m - E_n} \phi_{0p}(\vec{r}')}{|\vec{r} - \vec{r}'|} d\vec{r} d\vec{r}' + \frac{e^2}{2} \int \frac{\sum'_{p,m} \phi_{0p}^*(\vec{r}) \frac{(m|x|n)}{E_m - E_n} \phi_{0m}(\vec{r}')}{|\vec{r} - \vec{r}'|} d\vec{r} d\vec{r}', \quad (33)$$

or, in a bit more compact form:

$$\begin{aligned} &\frac{e^2}{2} \sum'_{p,m} \frac{(n|x|m)}{E_m - E_n} \int \frac{\phi_{0m}^*(\vec{r}) \phi_{0p}(\vec{r}')}{|\vec{r} - \vec{r}'|} d\vec{r} d\vec{r}' + \frac{e^2}{2} \sum'_{p,m} \frac{(m|x|n)}{E_m - E_n} \int \frac{\phi_{0p}^*(\vec{r}) \phi_{0m}(\vec{r}')}{|\vec{r} - \vec{r}'|} d\vec{r} d\vec{r}' \\ &= \frac{e^2}{2} \sum'_{p,m} \frac{(n|x|m)}{E_m - E_n} J_{mp}^0 + \frac{e^2}{2} \sum'_{p,m} \frac{(m|x|n)}{E_m - E_n} J_{pm}^0, \end{aligned} \quad (34)$$

$$= \frac{e^2}{2} \sum'_{p,m} \frac{(n|x|m)}{E_m - E_n} J_{mp}^0 + \frac{e^2}{2} \sum'_{p,m} \frac{(m|x|n)}{E_m - E_n} J_{pm}^0, \quad (35)$$

with the obvious notation for J_{pm}^0 .

Having the results of evaluation of the Fockian eigenfunction, one may calculate (35), otherwise we consider J_{ik}^1 as a parameter. Similarly, the Zeeman effect may be included on basis of the perturbation of Hamiltonian by

$$V = \vec{\mu} \vec{B}, \quad \vec{\mu} = \frac{\mu_B (g_L \vec{L} + g_S \vec{S})}{\hbar}.$$

6. The Heisenberg method of Gauss distribution parameter evaluation

6.1. On eigenvalues distribution

The basic eigenvalue equation written for multi-electron spin system for a given symmetry group $g \in G$ reads [1,4]:

$$\det\left[\sum_{g \in G} D_{ik}^\nu(g) J_g - \delta_{ik} E\right] = 0, \quad (36)$$

where ν is an irreducible representation number, J_g are exchange integrals. It defines the system of terms Γ_ν numerated by the irreducible representations of the symmetry group G , The Pauli principle yields: each value of the system spin corresponds to one system of terms:

$$2n = 2 + \dots + 2 + 1 + \dots + 1. \quad (37)$$

The mean energy is expressed as the sum of the roots $\sum E_i$ of the Eq. (36) as a coefficient by $E^{n_\nu-1}$:

$$E^\nu = \frac{1}{n_\nu} \sum_g \chi^\nu(g) J_g, \quad (38)$$

here $\chi^\nu(g) = D_{ii}^\nu(g)$ are chartacters of the group. The next term in the polynomial by $E^{n_\nu-2}$ gives:

$$\begin{aligned} \sum_{n>m} E_n E_m &= \sum_{i>k,g,g'} [D_{ii}^\nu(g) D_{kk}^\nu(g') - D_{ik}^\nu(g) D_{ki}^\nu(g')] J_g J_{g'} = \\ &= \frac{1}{2} \sum_{i,k,g,g'} [D_{ii}^\nu(g) D_{kk}^\nu(g') - D_{ik}^\nu(g) D_{ki}^\nu(g')] J_g J_{g'}. \end{aligned} \quad (39)$$

By the group property:

$$D_{ik}^\nu(g) D_{ks}^\nu(g') = D_{is}^\nu(gg'),$$

taking $D_{ii}^\nu(g) = \chi^\nu(g)$ into account:

$$\sum_{n>m} E_n E_m = \frac{1}{2} \sum_{g,g'} [\chi^\nu(g) \chi^\nu(g') - \chi^\nu(gg')] J_g J_{g'}. \quad (40)$$

Plugging $E_n = E^\nu + \Delta E_n$ yields:

$$\begin{aligned} \sum_{n>m} E_n E_m &= \sum_{n>m} (E^\nu + \Delta E_n)(E^\nu + \Delta E_m) = \\ &= \frac{n_\nu(n_\nu-1)}{2} (E^\nu)^2 + \sum_{n>m} \Delta E_n \Delta E_m. \end{aligned} \quad (41)$$

As $\sum \Delta E_n = 0$:

$$\sum_{n=1} (\Delta E_n)^2 = -2 \sum_{n>m} (\Delta E_n)(\Delta E_m). \quad (42)$$

From (38,40,41,42) and $\chi^\nu(e) = n_\nu$ we derive:

$$\sum_{n=1} (\Delta E_n)^2 = \frac{-1}{n_\nu} \sum_{g,g'} (\chi^\nu(g) \chi^\nu(g') - \chi^\nu(gg')) J_g J_{g'}. \quad (43)$$

Finally, the mean square deviation from the mean value E^ν

$$\overline{(\Delta E_n)^2} = \frac{1}{n_\nu^2} \sum_{g,g'} (\chi^\nu(gg') - \chi^\nu(g) \chi^\nu(g')) J_g J_{g'} \quad (44)$$

The characters of the symmetry group are evaluated by Frobenius theorem application. In the simplest case of the symmetry group as direct product of the permutation group and space symmetry group, the irreducible representations are all possible direct products of the irreducible representations of the subgroups. The characters in this case are simple products of the correspondent characters.

6.2. Perturbations of mean eigenvalues

The values of exchange integrals in external field (30) gives for (48):

$$E^\nu = \frac{1}{n_\nu} \sum_g \chi^\nu(g)(J_g^0 + eEJ_g^1) = E_0^\nu + eEE_1^\nu, \quad (45)$$

which demonstrates the Stark effect for the mean energy for a given IR of the symmetry group.

The mean square deviation from the mean value E^ν turns now becomes:

$$\begin{aligned} \overline{(\Delta E_n)^2} &= \frac{1}{n_\nu^2} \sum_{g,g'} (\chi^\nu(gg') - \chi^\nu(g)\chi^\nu(g'))(J_g^0 + eEJ_g^1)(J_{g'}^0 + eEJ_{g'}^1) \approx \\ &\quad \frac{1}{n_\nu^2} \sum_{g,g'} (\chi^\nu(gg') - \chi^\nu(g)\chi^\nu(g'))J_g^0J_{g'}^0 + \\ &\quad eE \frac{1}{n_\nu^2} \sum_{g,g'} (\chi^\nu(gg') - \chi^\nu(g)\chi^\nu(g'))(J_g^0J_{g'}^1 + J_{g'}^0J_g^1) = \\ &\quad \frac{1}{n_\nu^2} \sum_{g,g'} (\chi^\nu(gg') - \chi^\nu(g)\chi^\nu(g'))J_g^0J_{g'}^0 + 2eE \frac{1}{n_\nu^2} \sum_{g,g'} (\chi^\nu(gg') - \chi^\nu(g)\chi^\nu(g'))J_g^0J_{g'}^1, \end{aligned} \quad (46)$$

after summation rearranging. The magnetic field is accounted for similarly.

6.3. Permutation group characters

The permutation group characters are listed in [4], the nonzero ones ($P = e, P \in (12), (123), (12)(34)$) are:

$$\begin{aligned} \chi^\nu(e) &= n_\nu = \frac{(2n)!(2s+1)}{(n-s)!(n+s+1)}, \\ \chi^\nu(12) &= \frac{(2n-2)!2(2s+1)}{(n-s)!(n+s+1)}(s^2 + s + n^2 - 2n), \\ \chi^\nu(123) &= \chi^\nu(12)(34). \end{aligned} \quad (47)$$

For a specific case the result depends on J_g values. In a case of localized atomic states $J_{(12)}$ decays exponentially with distance. Therefore the main contribution arises from nearest neighbors. A number of the neighbors depends on atomic structure symmetry.

If to suppose that we account only the closest neighbors, taking for them $J_g = J$ and neglect by others the energy is:

$$E^\nu = \frac{1}{n_\nu} \sum_g \chi^\nu(g)J_g = -z \frac{s^2 + n^2}{2n} J + J_e. \quad (48)$$

For calculation of $\overline{(\Delta E_n)^2}$, we need:

$$A(g, g') = \frac{1}{n_\nu^2} (\chi_\nu(e)\chi^\nu(gg') - \chi^\nu(g)\chi^\nu(g'))J_gJ_{g'}. \quad (49)$$

Taking only the highest powers of n, s into account, we have:

$$\begin{aligned} 1. g = g' & \\ A_{(12)(12)} &= \frac{(n^2 - s^2)(3n^2 + s^2)}{4n^4}, \\ 2. g \text{ nad } g' \text{ have one joint element} & \\ A_{(12)(13)} &= \frac{(n^2 - s^2)(s^2)}{4n^4}, \\ 3. g \text{ nad } g' \text{ have no joint element} & \\ A_{(12)(34)} &= \frac{(s^2 - n^2)(s^2)}{2n^5}. \end{aligned} \quad (50)$$

If the atom has z neighbors, the type 1. we meet zn times, 2. - $z(z-1)$ times and 3. - $3 \frac{z^2 n^2}{2}$ times. Finally by (42), a deviation from E^ν is $\Delta E_\sigma \approx J\sqrt{n}$.

$$\overline{(\Delta E_n)^2} = J^2 z \frac{(n^2 - s^2)(3n^2 - s^2)}{4n^3}. \quad (51)$$

6.4. Nanotube example

The geometry of the nanoobject under consideration is shown at the Fig. 1, the positions of centers of adiabatic potentials, denoted in previous sections by \vec{R}_j are marked by boldface points. The axis of space symmetry of the figure is z , that is used as rotations $R \in S$ axis. The translations $t_a \in S$ are performed along this axis. The transversal Cartesian coordinates are xy . Let the symmetry group G be a direct product of space symmetry group S and the group of permutation \mathcal{P} , $G = S \odot \mathcal{P}$.

The permutation group characters (the nonzero ones $P = e, P \in (12), (123), (12)(34)$) are listed in [4],

As it was mentioned, for localized states account, the main contribution arises from nearest neighbors arriving at (48) and (51). The number of the neighbors depends on the material atoms positions.

For the whole symmetry group that is a direct product $G = S \otimes \mathcal{P}$, $s \in S, P \in \mathcal{P}$, $\dim G = \dim S \dim \mathcal{P}$, the characters are also products

$$\chi(g) = \chi(s)\chi(P) \quad (52)$$

and mean energy for the term corresponding to the irreducible representation ν of the whole G , yields, by the general (48)

$$E^\nu = \frac{1}{n_\nu} \sum_g \chi^\mu(s) \chi^{\nu_1}(P) J_g. \quad (53)$$

The index ν is a pair μ, ν_1 , where μ is the number of irreducible representation of the space group S , while ν_1 – of the permutation group \mathcal{P} .

For the tube of atoms at \vec{R}_i , see the Fig. 1, the group is described as follows [12].

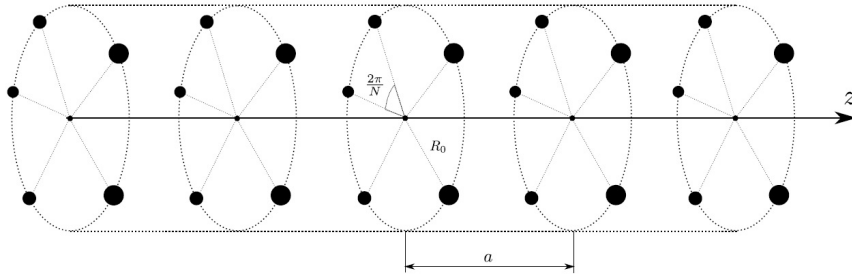


FIG. 1. The geometry of the tube centers positions

Let $A \in S$ be a group of the point-centers set symmetry and the finite group $R_j \in S_c \in S$ be a subgroup of rotations on angles $\phi_j = \frac{2\pi j}{N}$, $j = 0, \dots, N-1$ in a plane, orthogonal to the z -axis. Let also the translations along z -axis are denoted as t_{na} , $n = 0, \dots, M-1$ and form the discrete group $t_{na} \in G_T$, hence the group elements are the pairs $A = (R_j, t_{na})$. The particular case relates to the structure of the tube is described by the direct product:

$$S = S_c \otimes S_T. \quad (54)$$

Let the group is represented by transformations in the position space $\vec{r} \in R^3$. It is straightforward to see that A is equivalent to the combined operations of rotation:

$$R_j = \begin{pmatrix} \cos \theta_j & \sin \theta_j & 0 \\ -\sin \theta_j & \cos \theta_j & 0 \\ 0 & 0 & 1 \end{pmatrix} \quad (55)$$

and translation:

$$t_a \begin{pmatrix} x \\ y \\ z \end{pmatrix} = \begin{pmatrix} x \\ y \\ z + a \end{pmatrix}. \quad (56)$$

The representation of the elements A is written as:

$$A\vec{r} = R_j\vec{r} + t_a^n\vec{r} = \begin{pmatrix} \cos \theta_j x + \sin \theta_j y \\ -\sin \theta_j y + \cos \theta_j x \\ z + na \end{pmatrix}. \quad (57)$$

The transformations form an Abelian group, $R_j t_a = t_a R_j$. In a realistic geometry of the tube and using periodic von Karman conditions we restrict the positive n variable change so as $n \leq M$. The group element, or the transformation is parametrized by the vector $\vec{s} = \{s_1, s_2\} = \{\frac{2\pi j}{N}, na\}$. The transformation $A \in G$ is written as $A\vec{p} = \vec{p} + \vec{s}$.

For Abelian symmetry groups and cyclic subgroups, the IRs are one-dimensional. Conventionally choosing it as unitary, we write:

$$D^{\vec{\mu}}(s) = \exp[i(\vec{\mu}, \vec{s})], \quad (58)$$

where

$$\vec{\mu} = \{\mu_1, \mu_2\} = \{j_1, j_2\},$$

the integers, numerating irreducible representations run the values $j_1 = 1, \dots, N; j_2 = 1, \dots, M$. Hence:

$$D^{\vec{\mu}}(s) = \exp[i(j_1 \frac{2\pi j}{N} + \frac{2\pi n}{M} j_2)], \quad (59)$$

In such case, the sum that defines the mean energy is divided into two terms. One is “old”, corresponding the unit element of the space group and the second relates to combined transformations.

Note that the dimension of the IR n_ν of $S \otimes P$ is equal to dimension of the IR for the permutation group P because the dimension of it is unit:

$$E^\nu = \frac{1}{n_\nu} \sum_{\vec{s}} \sum_P \exp[i(\vec{\mu}, \vec{s})] \chi^{\nu_1}(P) J_{P_s}. \quad (60)$$

The summation may be rearranged as:

$$E^\nu = \frac{1}{n_\nu} \sum_P \chi^{\nu_1}(P) \sum_{\vec{s}} \exp[i(\vec{\mu}, \vec{s})] J_{P_s}. \quad (61)$$

In the model of equal exchange integrals the sum is proportional J. The characters of space group do not contribute:

$$\sum_s \chi^{\vec{\mu}}(s) = \sum_{j=0}^{N-1} \sum_{n=0}^{M-1} \exp[2\pi i(j_1 \frac{j}{N} + \frac{j_2}{M} n)]. \quad (62)$$

For nontrivial IR ($j_1 \neq 0, j_2 \neq 0$) the sum (62) is the sum of the geometric progression, that gives:

$$\sum_{j=0}^{N-1} \exp[2\pi i(j_1 \frac{j}{N})] = \frac{1 - \exp[2\pi i j_1]}{1 - \exp[2\pi i \frac{j_1}{N}]} = 0$$

For the trivial IR $D^0(s) = 1$, the sum is equal to NM . Generally, the sum in (61) depends on the model of J_{P_s} , that, for example, may depend on direction that link neighboring atoms. For the tube we study, the distance between neighbors along axis is a , while the neighbors at rings are at distance $b = 2R \sin \frac{\pi}{N}$. Generally $a \neq b$, hence we have two principal exchange integrals J_a, J_b . We divide the sum (58) into two terms:

$$E^\nu = \frac{1}{n_\nu} \left[\sum_P \chi^{\nu_1}(P) \sum_{\vec{s}} \exp[i(\vec{\mu}, \vec{s})] J_{P_s} + \sum_{P'} \chi^{\nu_1}(P') \sum_{\vec{s}} \exp[i(\vec{\mu}, \vec{s})] J_{P'_s} \right]. \quad (63)$$

The first contains permutations that are products of transpositions inside rings, while the second are built from transpositions along z axis. Other permutations are not taken into account as related to non-closest neighbors.

We calculate the first internal sum by the space group:

$$\begin{aligned} \sum_{\vec{s}} \exp[i(\vec{\mu}, \vec{s})] J_{P_s} &= \sum_{j=0}^{N-1} \sum_{n=0}^{M-1} \exp[2\pi i(j_1 \frac{j}{N} + \frac{j_2}{M} n)] J_{P_s} = \\ &= \sum_{n=0}^{M-1} \exp[2\pi i \frac{j_2}{M} n] \sum_{j=0}^{N-1} \exp[2\pi i j_1 \frac{j}{N}] J_b \end{aligned} \quad (64)$$

For nontrivial IR we have zero, for trivial $MN J_b$. The second one is:

$$\begin{aligned} \sum_{\vec{s}} \exp[i(\vec{\mu}, \vec{s})] J_{P'_s} &= \sum_{j=0}^{N-1} \sum_{n=0}^{M-1} \exp[2\pi i(j_1 \frac{j}{N} + \frac{j_2}{M} n)] J_{P'_s} = \\ &= \sum_{j=0}^{N-1} \exp[2\pi i j_1 \frac{j}{N}] \sum_{n=0}^{M-1} \exp[2\pi i \frac{j_2}{M} n] J_a \end{aligned} \quad (65)$$

with the same result, but for J_a . The nonzero sum (66) for $\nu = \{0, \nu_1\}$ hence is equal to:

$$E^\nu = \frac{MN}{n_\nu} \left[\sum_P \chi^{\nu_1}(P) J_b + \sum_{P'} \chi^{\nu_1}(P') J_a \right]. \quad (66)$$

The mean square deviation from the mean value E^ν , $\nu = \{0, \nu_1\}$ is also splits as follows

$$\overline{(\Delta E_n)^2} = \frac{1}{n_\nu^2} \sum_{g, g'} (\chi^\nu(gg') - \chi^\nu(g)\chi^\nu(g')) J_b^2 + \dots \quad (67)$$

in the first term the pair g, g' runs a ring set of atoms.

7. Statistics

7.1. Magnetic field

Let, following [1], the eigenvalues around the medium value are distributed by Gauss. As the number of terms, that belongs to a spin s is equal to n_ν , then, within the interval $E^\nu + \Delta E, E^\nu + \Delta E + d\Delta E$ one have for the number of terms

$$\frac{n_\nu}{\sqrt{2\pi(\Delta E_n)^2}} \exp\left\{-\frac{\Delta E^2}{2(\Delta E_n)^2}\right\} d\Delta E. \quad (68)$$

In the external magnetic field the additional energy of the system is:

$$E' = -\frac{eh}{2\pi\mu} H m \quad (69)$$

where $s \geq m \geq -s$, μ is electron mass.

The statistical sum of states:

$$\begin{aligned} \sum_{s=0}^n \sum_{m=-s}^s \int_{-\infty}^{\infty} d\Delta E \frac{n_\nu}{\sqrt{2\pi(\Delta E_n)^2}} \exp\left\{\alpha m + \beta \frac{s^2}{2n} - \frac{\Delta E}{kT} - \frac{\Delta E^2}{2(\Delta E_n)^2}\right\} = \\ \sum_{s=0}^n \sum_{m=-s}^s n_\nu \exp\left\{\alpha m + \beta \frac{s^2}{2n} + \frac{\Delta(E_n)^2}{2k^2 T^2}\right\} \end{aligned} \quad (70)$$

where:

$$\begin{aligned} \alpha &= \frac{eh}{2\pi\mu kT} H \\ \beta &= \frac{zJ}{kT} \end{aligned} \quad (71)$$

Plugging (51) gives:

$$Z = \sum_{s=0}^n \sum_{m=-s}^s n_\nu \exp\left\{\alpha m + \beta \frac{s^2}{2n} + \beta^2 \frac{s^2(4n^2 - s^2)}{8n^3 z}\right\}. \quad (72)$$

Denoting:

$$g(s) = \exp\left\{\frac{\beta s^2}{2n}\right\} \quad (73)$$

and taking into account:

$$n_\nu = \binom{2n}{n+s} - \binom{2n}{n+s+1}, \quad (74)$$

after reordering summation one obtains:

$$Z = \sum_{m=-n}^n \sum_{s=|m|}^n \exp\{\alpha m\} g(m) \left[\binom{2n}{n+s} - \binom{2n}{n+s+1} \right]. \quad (75)$$

After transformation similar to integrating by parts, we have:

$$Z = F \sum_{m=-n}^n \exp\{\alpha m\} g(m) \binom{2n}{n+m}. \quad (76)$$

One may show that the expression $\exp\{\alpha m\}g(m) \binom{2n}{n+m}$ has the sharp maximum at a point m_0 , hence the Taylor expansion in the vicinity of this point may be a good approximation in the exponent of $g(m)$. Approximately:

$$g(m) = \exp\left\{\frac{\beta n_0^2}{2n} + \beta \frac{m_0}{n}(m - m_0) - \frac{\beta^2}{8n^3 z} [4m_0^2 n^2 - m_0^4 + 8m_0 n^2(m - m_0) - 4m_0^3(m - m_0)]\right\}, \quad (77)$$

the statistical sum Z takes the form:

$$Z = F \sum_{m=-n}^n \exp\left\{\left(\alpha + \beta \frac{m_0}{n} - \beta^2 \frac{m_0^3}{2n^3 z}\right)m\right\} g(m) \binom{2n}{n+m} = F \left[2 \cosh\left(\frac{\alpha + \beta \frac{m_0}{n} - \beta^2 \frac{m_0^3}{2n^3 z}}{2}\right) \right]^{2n}. \quad (78)$$

The space symmetry account is based on modifications of the characters formula in expressions for energy (66) and the Gauss distribution parameter (67).

7.2. Electric field

The electric field perturbs the exchange integral as it is prescribed by (30)

$$\beta = \frac{z(J_0 + \epsilon J_1)}{kT} = \beta_0 + \epsilon \beta_1. \quad (79)$$

Plugging it into (85) yields:

$$\frac{Z}{F} = \left[2 \cosh\left(\frac{\alpha + (\beta_0 + \epsilon \beta_1) \frac{m_0}{n} - (\beta_0 + \epsilon \beta_1)^2 \frac{m_0}{nz} + (\beta_0 + \epsilon \beta_1)^2 \frac{m_0^3}{2n^3 z}}{2}\right) \right]^{2n} = \left[2 \cosh\left(\frac{\alpha + \beta_0 \frac{m_0}{n} - \beta_0^2 \frac{m_0}{nz} + \beta_0^2 \frac{m_0^3}{2n^3 z} + \epsilon \beta_1 \frac{m_0}{n} \left(1 - \frac{z}{z} + \frac{m_0^2}{2n^2 z}\right) + \dots}{2}\right) \right]^{2n}, \quad (80)$$

the quadratic terms in ϵ are not shown.

7.3. To thermodynamics

The most probable value of magnetic moment is determined as:

$$m_0 = \frac{\partial \ln Z}{\partial \alpha} = n \tanh \frac{\alpha + \beta \frac{m_0}{n} - \beta^2 \frac{m_0}{nz} + \beta^2 \frac{m_0^3}{2n^3 z}}{2}. \quad (81)$$

The neglected term with $\ln F$ is of order “1”. Further expansion of $\frac{m_0}{n}$ in power series of ϵ gives the coefficients in the equation of state [13]:

$$\frac{\partial m_0}{n \partial \epsilon} \Big|_{\epsilon=0} = \beta_1 \left(\frac{1}{2} - \frac{1}{z} + \frac{m_0^2}{2n^2 z} \right) \left(1 - \tanh^2 \frac{\alpha + \beta_0 \frac{m_0}{n} - \beta_0^2 \frac{m_0}{nz} + \beta_0^2 \frac{m_0^3}{2n^3 z}}{2} \right) \frac{m_0}{n}. \quad (82)$$

The derivative of $\ln Z$ by ϵ gives the polarization per atom:

$$\frac{p_0}{n} = \frac{\partial \ln Z}{n \partial \epsilon} = \beta_1 \frac{m_0}{n} \left(\frac{1}{2} - \frac{1}{z} + \frac{m_0^2}{2n^2 z} \right) \tanh \left(\frac{\alpha + \beta \frac{m_0}{n} - \beta^2 \frac{m_0}{nz} + \beta^2 \frac{m_0^3}{2n^3 z}}{2} \right), \quad (83)$$

which demonstrates electromagnetic effects. The energy (66) and the Gauss distribution parameter (67) modifications for nanotubes naturally introduce the closest neighbors exchange integrals defined by the nano-object symmetry. This gives a model thermodynamic description on base of a model of statistical sum.

7.4. Discussion

The expression (83) differs from Weiss formula by $\cot^{-1}x \rightarrow \tanh x$ because of two spin orientation and cubic term. Set:

$$\frac{m_0}{n} = y, \quad \frac{\alpha + \beta \frac{m_0}{n} - \beta^2 \frac{m_0}{nz} + \beta^2 \frac{m_0^3}{2n^3 z}}{2} = x, \quad (84)$$

arriving at the equations:

$$\begin{aligned} I. \quad & y = \tanh x \\ II. \quad & \alpha + \beta y - \beta^2 \frac{y}{z} + \beta^2 \frac{y^3}{2z} - 2x = 0. \end{aligned} \quad (85)$$

Plots Fig. 2, $\alpha = 0.2, \eta = 2, z = 8$, ferromagnetism condition (II curve inclination at $y = 0$ is less than one for I.)

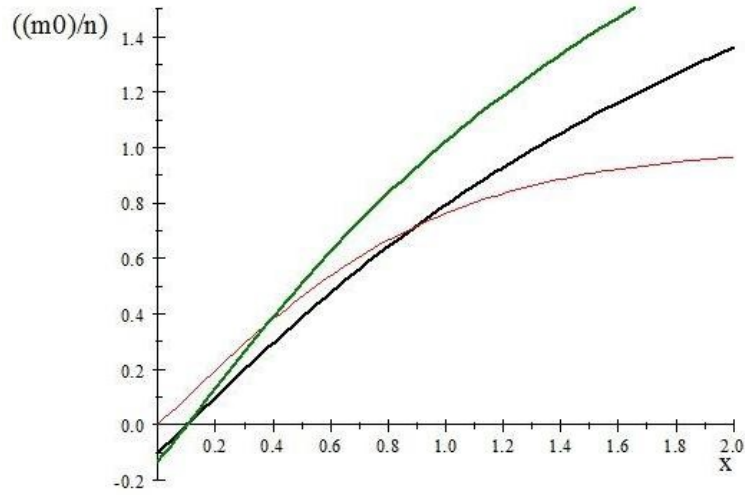


FIG. 2. Graphic solution of (85)

The next figure Fig. 3 presents number of closest neighbors as function J/kT .

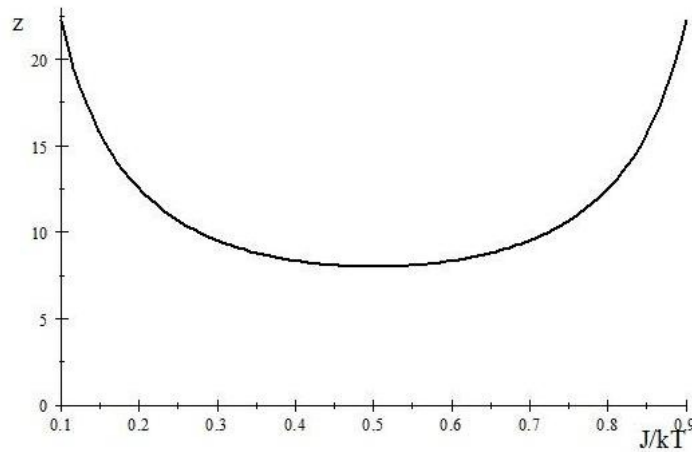


FIG. 3. The number of neighbors as function $\frac{J}{kT}$

$$\beta \left(1 - \frac{\beta}{z}\right) \geq 2, \quad (86)$$

maximum of the l.h.s. is $\beta_{max} = 1/2$, that yields

$$z \geq 8.$$

a good example is $z_{Fe} = 8$.

A small α allows the expansion ($thx \approx x - x^3/3 + \dots$), that gives the following dependence on β

$$y = \frac{\alpha}{2 - \beta + \frac{\beta^2}{z}} + \frac{\alpha^3}{\left(2 - \beta + \frac{\beta^2}{z}\right)^4} \left(\frac{\beta^2}{2z} - \frac{2}{3}\right), \quad (87)$$

The first term of the series gives the Weiss modification of Curie law

$$m_0 = \frac{1}{T - \Theta} \frac{T}{T \left(1 + \sqrt{1 - \frac{8}{z}}\right) - \Theta \left(1 - \sqrt{1 - \frac{8}{z}}\right)} \quad (88)$$

with the Curie point

$$\Theta = \frac{2J}{k \left(1 - \sqrt{1 - \frac{8}{z}}\right)}. \quad (89)$$

Within the concept suggested in this paper, the electric field account is introduced via its exchange integral perturbation by Stark effect (30).

8. Conclusion

The Zeeman energy we also can consider as a Zeeman effect, that add a perturbation to the exchange integral.

Both from microscopic (multipole expansion) and macroscopic (symmetry-based expansion of the free energy) points of view, with Dzialoshinski–Moryja interaction account see [14]. The great interest to the magnetoelectric effects is expressed in abundant publications [15].

An equivalence of the nonlinear Schrödinger equation and the equation of a Heisenberg ferromagnet [16] points out possible applications of the advanced NS equation perturbation theory.

The important perspective of more deep understanding of the chemical bonds contains in the Fock paper [9]; let us put here a citation: “...idea of a bond which is built by a pair of electrons assumes such strong interaction between the electrons with opposite spins that any description of this interaction by means of two one-electron functions is somewhat artificial and cannot be exact. It is much more natural to associate with each saturated bond its own two-electron function”. This also leads also to more natural notion and values of exchange integrals. The ideas of Heitler and Heisenberg are unified also with Floquet theory for non-localized eigenstates of Fock Hamiltonian and specified in the context of Wigner theorem [6].

References

- [1] Heisenberg W. Zur Theorie des Ferromagnetismus. *Zeitschrift für Physik*, 1928, **49**(9-10), P. 619–636.
- [2] Fock V.A. An Approximate Method for Solving the Quantum Many-Body Problem. Reported at the Session of the Russian Phys.-Chem. Soc. on 17 December 1929. Selected works. Quantum Mechanics and Quantum Field Theory. Ed. by L.D. Faddeev, L.A. Khalfin, I.V. Komarov. P. 137–164, CRC Press, 2004.
- [3] Popov I.Y., Melikhov I.F. The discrete spectrum of the multiparticle Hamiltonian in the framework of the Hartree-Fock approximation. *Journal of Physics: Conference Series*, 2014, **541**. P. 012099/1–4.
- [4] Heitler W. Zur Gruppentheorie der homopolaren chemischen Bindung. *Zs. Phys.*, 1928, **47**, P. 835–838.
- [5] Geyler V.A., Popov I.Yu. Group-theoretical analysis of lattice Hamiltonians with a magnetic field. *Phys. Lett. A.*, 1995, **201**, P. 359–364.
- [6] Wigner E. *Group Theory*. Academic Press, New York, London, 1959.
- [7] Petrashen M., Trifonov E. *Applications of Group Theory in Quantum Mechanics*. Dover publication, 2009.
- [8] Jens P. *Dahl: Introduction to The Quantum World of Atoms and Molecules*. World Scientific Publishing, Singapore, 2001.
- [9] Fock V.A. Application of Two-Electron Functions in the Theory of Chemical Bonds. Selected works. Quantum Mechanics and Quantum Field Theory. Ed. by L.D. Faddeev, L.A. Khalfin, I.V. Komarov. P. 519–524, CRC Press, 2004.
- [10] Fock V.A. *On Quantum Exchange Energy*. Selected works. Quantum Mechanics and Quantum Field Theory. Ed. by L.D. Faddeev, L.A. Khalfin, I.V. Komarov. P. 263–278, CRC Press, 2004.
- [11] Roberts J.A.G., Tompson C.J. Dynamics of the classical Heisenberg spin chain. *Journal of Physics A: Mathematical and General*, 1988, **21**(8), P. 1769–1780.
- [12] Leble S. Cyclic-periodic ZRP structures. Scattering problem for generalized Bloch functions and conductivity. *Nanosystems: physics, chemistry, mathematics*, 2018, **9**(2), P. 225–243.
- [13] Dzyaloshinskii I.E. On the magneto-electrical effect in antiferromagnets. *J. Exp. Theor. Phys.* (U.S.S.R.), 1959, **37**, P. 881–882.
- [14] Chandrashekar Radhakrishnan, Manikandan Parthasarathy, Segar Jambulingam and Tim Byrnes. Quantum coherence of the Heisenberg spin models with Dzyaloshinsky–Moriya interactions. *Scientific Reports*, 2017, **7**, P. 13865.
- [15] Spaldin, Nicola A., Fiebig, Manfred. The renaissance of magnetoelectric multiferroics. *Science*, 2005, **309**(5733), P. 391–392.
- [16] Zakharov V.E., Takhtajan L.A. Equivalence of the nonlinear Schrödinger equation and the equation of a Heisenberg ferromagnet. *Theor. Math. Phys.*, 1979, **38**, P. 17–23.
- [17] Heitler W. Störungsenergie und Austausch beim Mehrkörperproblem. *Zs. Phys.*, 1927, **46**, P. 47.

Hund's rule in open-shell states of two-electron systems: From free through confined and screened atoms, to quantum dots

Jacob Katriel¹, H. E. Montgomery², Jr., A. Sarsa³, E. Buendía⁴, F. J. Gálvez⁴, K. D. Sen⁵

¹Department of Chemistry, Technion - Israel Institute of Technology, Haifa, 32000 Israel

²Chemistry Program, Centre College, Danville, Kentucky 40422, USA

³Departamento de Física, Campus de Rabanales Edif. C2,
Universidad de Córdoba, E-14071 Córdoba, Spain

⁴Departamento de Física Atómica, Molecular y Nuclear, Facultad de Ciencias,
Universidad de Granada, E-18071 Granada, Spain

⁵School of Chemistry, University of Hyderabad, Hyderabad-500 046, India

jkatriel@technion.ac.il, ed.montgomery@centre.edu, fa1sarua@uco.es,
buendia@ugr.es, galvez@ugr.es, kds77@uohyd.ac.in

DOI 10.17586/2220-8054-2019-10-1-31-41

Singly-excited singlet-triplet pairs of states of two-electron spherically symmetric systems, that are degenerate in the absence of inter-electronic repulsion, are revisited. In addition to the obvious two-electron atom we consider the two-electron quantum dot confined by either a harmonic potential or by an infinite spherical well, the confined two-electron atom, and three variants of an atom immersed in a plasma, modeled by the screened Coulomb (Debye) potential. The validity of Hund's multiplicity rule is confirmed, and the contribution of the interparticle repulsion energy to the singlet-triplet splitting is examined. One feature that all these systems share is that the triplet wave function is contracted relative to that of the corresponding singlet. This feature, which is a consequence of the virial theorem, affects both the behavior of the outer electron ionization energies and the relative magnitudes of the inter-particle repulsion energies in the singlet vs. the triplet. Whereas in atomic highly positive ions the interelectronic repulsion is lower in the triplet than in the corresponding singlet state, this ordering is reversed in neutral atoms. Such reversal does not take place in quantum dots. Confined and screened systems exhibit more nuanced behavior. The analysis utilizes appropriate variants of the virial and Hellmann–Feynman theorems.

Keywords: two-electron quantum dots, confined two-electron atom, screened coulomb potential, Hund's multiplicity rule, Virial theorem, Hellmann-Feynman theorem.

Received: 25 January 2019

Revised: 19 February 2019

1. Introduction

The earliest theoretical framework allowing an interpretation of Hund's heuristic rules [1] concerning the energetic ordering of atomic open-shell multiplets, and examination of their validity, was developed by Slater [2]. A generalization of Hund's rules that is consistent with Slater's treatment was developed by Morgan and Kutzelnigg [3, 4]. Slater's treatment assumed that the different states to which each electronic configuration gives rise can be treated in terms of a common set of one-electron orbitals. Within this scheme, the differences among the energies of these different states is entirely due to the corresponding differences in the magnitudes of the interelectronic repulsions. Hence, the virial theorem is violated, with different states having a common kinetic energy but different total energies.

Going beyond this frozen orbital approximation, an intriguing feature is observed. While the splitting of the states within a common configuration is driven by the interelectronic repulsion term in the Hamiltonian, the order of the calculated expectation values of this term is sometimes reversed relative to the order of the total energies. This reversal was reported for the first time by Davidson [5], studying singly excited states of He within the Hartree–Fock framework, in which the orbitals are optimized for each term individually. Later Hartree–Fock calculations [6] confirmed that the interelectronic repulsion energy is higher in the ³P than in the ¹P state for all group II atoms (Be, Mg, Ca, Sr and Ra), where one of the two outermost *ns* electrons is excited into the *np* orbital. Similar observations had been reported in the late sixties and early seventies with respect to other atoms as well as to open shell molecules. An interpretation emphasizing the role of the virial theorem and of the interaction between inner and outer shells was presented in [7] and reviewed in [8]. It was argued that correlation (i.e., beyond Hartree–Fock features) does not play a qualitatively significant role in this context. Moreover, the absence of an inner shell in systems such as doubly excited He in which the two electrons are specified by means of the

same principal quantum number, was argued to exclude a reversal of the relative magnitudes of the interelectronic repulsion energy between states corresponding to common configurations of this type (such as $(2s2p)^1\ ^3P$ or $(2p)^2\ ^1D\ ^3P\ ^1S$). Some evidence supporting this claim was presented. Progress in the treatment of doubly excited states within the He isoelectronic sequence allowed, many years later, a study that suggested that correlation does play a significant qualitative role, yielding a reversal in the magnitudes of the interelectronic repulsion energies towards the low end of the isoelectronic sequence [9], despite the claim mentioned above. A comprehensive study of multiplets of neutral atoms within Hartree–Fock theory was undertaken by Koga and Koshida [10], establishing the rather universal validity of the reversal of the high- vs. low-multiplicity interelectronic repulsion in neutral atoms. Although positively charged atomic ions have not been studied nearly as extensively, we can conclude on sound theoretical grounds that the ordering of interelectronic repulsion energies must reverse into the “naively” expected one (the interelectronic repulsion is smaller in the lower energy state) upon increase of the nuclear charge, along isoelectronic sequences.

Application of the virial theorem suggested, rather early on, that reversal of the relative magnitudes of the interelectronic repulsion energies in different multiplicity states belonging to a common configuration is possible [7]. The proof that this reversal is inevitable was only proposed many years later [11].

During the last decade or two, growing interest in electrons “trapped” within nanoscale cavities in solids, referred to as “quantum dots”, has drawn attention to the spectroscopic properties of such systems. Evidence has been accumulating that these systems typically satisfy Hund’s rule, higher spin states tending to be lower in energy than corresponding lower spin states within a common configuration. However, unlike atoms, evidence has been presented indicating that these systems do not exhibit a reversal of the magnitudes of the interelectronic repulsion energies. Indeed, such reversal does not take place in the two-electron harmonically confined quantum dot [12, 13], a fact that could also be accounted for analytically [11].

The two-electron atom in a spherical cavity was recently explored, interpolating between the free atom and a pair of electrons in an infinite spherical well [14]. Atomic-like behavior (reversal of the singlet vs. triplet interelectronic repulsion energies) was observed at large cavity radii, where the Coulomb nuclear attraction regulates the extension of the wave function, whereas no such reversal takes place in smaller cavities.

This issue was also explored for open-shell screened atoms, in which the Coulomb potentials were replaced by Debye (Yukawa) type potentials [15]. Three variants of the two-electron Debye atom were considered:

1. The fully-screened (FS) two-electron Debye atom, whose Hamiltonian is:

$$\mathcal{H}_D = -\frac{1}{2}(\nabla_1^2 + \nabla_2^2) - Z\left(\frac{\exp(-\lambda r_1)}{r_1} + \frac{\exp(-\lambda r_2)}{r_2}\right) + \frac{\exp(-\lambda r_{12})}{r_{12}}, \quad (1)$$

where λ is the screening constant.

2. The screened nuclear attraction (SNA) Hamiltonian:

$$\mathcal{H}_d = -\frac{1}{2}(\nabla_1^2 + \nabla_2^2) - Z\left(\frac{\exp(-\lambda r_1)}{r_1} + \frac{\exp(-\lambda r_2)}{r_2}\right) + \frac{1}{r_{12}}, \quad (2)$$

3. The screened interelectronic repulsion (SIR) Hamiltonian:

$$\mathcal{H}_{int} = -\frac{1}{2}(\nabla_1^2 + \nabla_2^2) - Z\left(\frac{1}{r_1} + \frac{1}{r_2}\right) + \frac{\exp(-\lambda r_{12})}{r_{12}}. \quad (3)$$

The aim of the present article is to provide a synthetic overview of all these studies. We start by presenting rigorous relations between the interelectronic repulsion energy and derivatives of simple functions of the total energy, depending linearly on the latter. These relations follow by application of appropriate versions of the virial and the Hellmann–Feynman theorems. The linear dependence mentioned above means that the same relations hold for the energy differences between different states of the pertinent system. Homogeneous potentials are dealt with in Section 2, allowing the treatment of the free Coulomb atom and the harmonic quantum well as well as the infinite spherical well. Inhomogeneous potentials are treated in Section 3. These include the confined two-electron atom as well as the systems that involve Debye screening of the nuclear attraction, the interelectronic repulsion, or both. These relations are of particular interest for pairs of states for which the corresponding function of the energy difference is non-monotonic, yielding a vanishing first derivative (i.e., reversal in the sign of the difference of interelectronic repulsion energies) somewhere along the isoelectronic sequence. By considering the asymptotic behavior of the energy differences at both the high and low ends of the isoelectronic sequence, we show that such non-monotonicities generically arise within open-shell atomic isoelectronic sequences. On the other hand, confined few-electron systems (“quantum dots”), that remain bound in the weak attractive potential limit, do not give rise to such non-monotonicities. This provides a “kinematic” interpretation of the sign reversal of differences

of interelectronic repulsion energies, as opposed to the “dynamical” interpretations (right or wrong) that have been proposed. This analysis leaves open the possibility of reversal of interelectronic repulsion energies in the weak attractive potential limit of non-confining quantum dots, such as the Gaussian or finite spherical well, that exhibit analogues of a lower critical charge at which the system ceases to be bound.

Computational results for the various systems specified above are reviewed in Sections 4–8, confirming the analysis briefly reviewed above. For details of the computational procedures used we refer to the original publications.

Finally, we emphasize that the formal relations presented in sections 2 and 3 have a much broader relevance than the applications actually considered; the analysis of the He isoelectronic sequence is an illustration that can be extended to any open-shell, many-electron atomic isoelectronic sequence. Hence, our analysis establishes that the reversal of the relative magnitudes of the interelectronic repulsion energies in atomic multiplets corresponding to a common configuration is inevitable, while the absence of such reversal in many-electron quantum dots with confining potentials is equally universal.

2. The virial and Hellmann–Feynman theorems for homogeneous potentials

We consider the two-electron Hamiltonian:

$$\mathcal{H} = -\frac{1}{2} (\nabla_1^2 + \nabla_2^2) + \frac{1}{r_{12}} + \frac{1}{\nu} \left(\left(\frac{r_1}{R} \right)^\nu + \left(\frac{r_2}{R} \right)^\nu \right), \quad (4)$$

noting that the generalization to N electrons is straightforward. For an eigenstate Ψ the energy components are:

$$\begin{aligned} \text{The kinetic energy} & T = -\frac{1}{2} \langle \Psi | (\nabla_1^2 + \nabla_2^2) | \Psi \rangle, \\ \text{The one-body potential energy} & H = \frac{h}{\nu}, \quad \text{where } h = \langle \Psi | \left(\frac{r_1}{R} \right)^\nu + \left(\frac{r_2}{R} \right)^\nu | \Psi \rangle, \\ \text{The interelectronic repulsion energy} & C = \langle \Psi | \frac{1}{r_{12}} | \Psi \rangle. \end{aligned}$$

The total energy is:

$$E = \langle \Psi | \mathcal{H} | \Psi \rangle = T + C + H. \quad (5)$$

Coordinate scaling, followed by minimization of the energy with respect to the scaling parameter, yields the virial theorem in the form:

$$2T + C - h = 0. \quad (6)$$

The Hellmann–Feynman theorem, applied to the parameter R , yields:

$$h = -R \frac{dE}{dR}. \quad (7)$$

Combining (5), (6) and (7) we obtain:

$$C = 2E + \frac{\nu + 2}{\nu} R \frac{dE}{dR} = \frac{\nu + 2}{\nu} R^{\frac{2-\nu}{2+\nu}} \frac{d}{dR} \left(R^{\frac{2\nu}{\nu+2}} E \right). \quad (8)$$

We assume that ΔE , the difference between the energies of some pair of eigenstates of the Hamiltonian (4), is known as a function of the parameter R (in practice, this amounts to knowing it for a sufficiently dense set of values of R). Then, the differences between the interelectronic repulsion energies, ΔC , can be evaluated by applying (8) to ΔE . For a pair of related states whose difference of energies satisfies $\Delta E > 0$, if it can be shown that $\left(R^{\frac{2\nu}{\nu+2}} \Delta E \right)$ is non-monotonic as a function of R then the interelectronic repulsion difference reverses sign at the value of R at which $\left(R^{\frac{2\nu}{\nu+2}} \Delta E \right)$ is extremal.

We shall consider the following special cases:

2.1. The Coulomb potential, $\nu = -1$

In this case R can be identified with Z , the nuclear charge. We obtain:

$$\begin{aligned} T &= -E, \\ H &= Z \frac{dE}{dZ}, \\ &\text{and} \\ C &= -Z^3 \frac{d}{dZ} \left(\frac{E}{Z^2} \right). \end{aligned} \quad (9)$$

2.2. The harmonic potential, $\nu = 2$

In this case we relate R to the harmonic force constant k via $k = \frac{1}{R^2}$, and obtain

$$\begin{aligned} T &= 3k^{\frac{4}{3}} \frac{d}{dk} \left(\frac{E}{k^{\frac{1}{3}}} \right), \\ H &= -2k \frac{dE}{dk}, \\ &\text{and} \\ C &= -4k^{\frac{3}{2}} \frac{d}{dk} \left(\frac{E}{\sqrt{k}} \right). \end{aligned} \quad (10)$$

The expression for C , the expectation value of the interelectronic repulsion, can be written in terms of the frequency ω , related to the force constant via $k = \omega^2$. One obtains:

$$C = -2\omega^2 \frac{d}{d\omega} \left(\frac{E}{\omega} \right). \quad (11)$$

2.3. The infinite spherical well, $\nu = \infty$

Taking the limit $\nu \rightarrow \infty$ we obtain:

$$\begin{aligned} T &= -\frac{d}{dR} (RE), \\ H &= 0, \\ &\text{and} \\ C &= \frac{1}{R} \frac{d}{dR} (R^2 E). \end{aligned} \quad (12)$$

These expressions are consistent with $T + C = E$.

3. The virial and Hellmann–Feynman theorems for inhomogeneous potentials

3.1. Two-parameter Hellmann–Feynman systems

Consider the Hamiltonian:

$$\mathcal{H} = -\frac{1}{2} (\nabla_1^2 + \nabla_2^2) + \frac{1}{r_{12}} + \frac{1}{\nu_a} \left(\left(\frac{r_1}{R_a} \right)^{\nu_a} + \left(\frac{r_2}{R_a} \right)^{\nu_a} \right) + \frac{1}{\nu_b} \left(\left(\frac{r_1}{R_b} \right)^{\nu_b} + \left(\frac{r_2}{R_b} \right)^{\nu_b} \right). \quad (13)$$

Here, the potential is manifestly inhomogeneous.

The scaling argument yields the virial theorem in the form:

$$2T + C - h_a - h_b = 0.$$

T and C are the kinetic energy and the interelectronic repulsion energy, respectively, and

$$\begin{aligned} h_a &= \left\langle \Psi \left| \left(\frac{r_1}{R_a} \right)^{\nu_a} + \left(\frac{r_2}{R_a} \right)^{\nu_a} \right| \Psi \right\rangle, & H_a &= \frac{h_a}{\nu_a}, \\ h_b &= \left\langle \Psi \left| \left(\frac{r_1}{R_b} \right)^{\nu_b} + \left(\frac{r_2}{R_b} \right)^{\nu_b} \right| \Psi \right\rangle, & H_b &= \frac{h_b}{\nu_b}. \end{aligned}$$

The Hellmann–Feynman theorem can be applied to each of R_a , R_b individually, yielding:

$$\begin{aligned} h_a &= -R_a \frac{\partial E}{\partial R_a}, \\ h_b &= -R_b \frac{\partial E}{\partial R_b}. \end{aligned}$$

Using these relations we obtain:

$$C = 2E + \frac{\nu_a + 2}{\nu_a} R_a \frac{\partial E}{\partial R_a} + \frac{\nu_b + 2}{\nu_b} R_b \frac{\partial E}{\partial R_b}.$$

3.2. The confined two-electron atom

For particles in a Coulomb potential confined by an infinite spherical well of radius R [16] (and references therein) we have $\nu_a = -1$, $R_a = Z$ and $\nu_b \rightarrow \infty$, $R_b = R$. We obtain,

$$C = 2E - Z \frac{\partial E}{\partial Z} + R \frac{\partial E}{\partial R}, \quad (14)$$

or

$$C = -Z^{1-\mu_Z} \frac{\partial}{\partial Z} (Z^{\mu_Z} E) + R^{1-\mu_R} \frac{\partial}{\partial R} (R^{\mu_R} E),$$

where $\mu_R - \mu_Z = 2$.

Choosing $\mu_Z = 0$ we obtain:

$$C = -Z \frac{\partial E}{\partial Z} + \frac{1}{R} \frac{\partial}{\partial R} (R^2 E), \quad (15)$$

and choosing $\mu_R = 0$,

$$C = -Z^3 \frac{\partial}{\partial Z} \left(\frac{E}{Z^2} \right) + R \frac{\partial E}{\partial R}. \quad (16)$$

3.3. The one-electron Debye-screened atom

The one-electron Debye Hamiltonian is:

$$\mathfrak{h}_d = -\frac{1}{2} \nabla^2 - Z \frac{\exp(-\lambda r)}{r}. \quad (17)$$

Let ψ be an eigenfunction with eigenvalue e . Let:

$$\begin{aligned} t &= \left\langle -\frac{1}{2} \nabla^2 \right\rangle, \\ v &= -Z \left\langle \frac{\exp(-\lambda r)}{r} \right\rangle, \\ e &= t + v, \\ u &= \lambda Z \langle \exp(-\lambda r) \rangle, \end{aligned}$$

where $\langle \hat{O} \rangle \equiv \langle \psi | \hat{O} | \psi \rangle$. The virial theorem:

$$2t + v = 2e - v = u, \quad (18)$$

yields:

$$\begin{aligned} t &= -e + u, \\ v &= 2e - u. \end{aligned}$$

The Hellmann–Feynman theorem with respect to Z yields

$$Z \frac{\partial e}{\partial Z} = v,$$

and the Hellmann–Feynman theorem with respect to λ yields

$$\frac{\partial e}{\partial \lambda} = \frac{u}{\lambda}. \quad (19)$$

Using equations (18) and (19) we obtain:

$$2e - \lambda \frac{\partial e}{\partial \lambda} - Z \frac{\partial e}{\partial Z} = 0, \quad (20)$$

hence,

$$v = Z \frac{\partial e}{\partial Z} = 2e - \lambda \frac{\partial e}{\partial \lambda} = -\lambda^3 \frac{\partial}{\partial \lambda} \left(\frac{e}{\lambda^2} \right), \quad (21)$$

and

$$t = -e + \lambda \frac{\partial e}{\partial \lambda} = \lambda^2 \frac{\partial}{\partial \lambda} \left(\frac{e}{\lambda} \right).$$

3.4. The two-electron Debye screened atom

3.4.1. *Screened nuclear attraction Hamiltonian, \mathcal{H}_d .* Let Ψ be an eigenfunction of the two-electron Hamiltonian, equation (2).

E is the corresponding eigenvalue. Let:

$$\begin{aligned} T &= \left\langle -\frac{1}{2} (\nabla_1^2 + \nabla_2^2) \right\rangle, \\ L &= -Z \left\langle \frac{\exp(-\lambda r_1)}{r_1} + \frac{\exp(-\lambda r_2)}{r_2} \right\rangle, \\ C &= \left\langle \frac{1}{r_{12}} \right\rangle, \\ V &= L + C, \\ E &= T + L + C, \\ U &= \lambda Z \langle \exp(-\lambda r_1) + \exp(-\lambda r_2) \rangle. \end{aligned} \quad (22)$$

The virial theorem [17–19] yields:

$$\begin{aligned} T &= -E + U, \\ V &= 2E - U, \end{aligned} \quad (23)$$

the Z -Hellmann–Feynman theorem is

$$\frac{\partial E}{\partial Z} = \frac{L}{Z},$$

and the λ -Hellmann–Feynman theorem is:

$$\frac{\partial E}{\partial \lambda} = \frac{U}{\lambda}.$$

It follows that the two components of the potential energy are given by:

$$\begin{aligned} C &= 2E - \lambda \frac{\partial E}{\partial \lambda} - Z \frac{\partial E}{\partial Z}, \\ L &= Z \frac{\partial E}{\partial Z}. \end{aligned} \quad (24)$$

Subtracting (20) from (24) we obtain:

$$C = -2\epsilon + \lambda \frac{\partial \epsilon}{\partial \lambda} + Z \frac{\partial \epsilon}{\partial Z},$$

where $\epsilon = e - E$ is the first ionization energy of the two-electron system.

3.4.2. *Fully screened Debye atom, \mathcal{H}_D .* We follow the path described in the previous subsection, specifying only the expressions that require modification. The expectation value of the two-electron term becomes:

$$C = \left\langle \frac{\exp(-\lambda r_{12})}{r_{12}} \right\rangle.$$

Equation (22) should be replaced by:

$$U = \lambda \left\langle Z \left(\exp(-\lambda r_1) + \exp(-\lambda r_2) \right) - \exp(-\lambda r_{12}) \right\rangle.$$

3.4.3. *Screened interelectronic repulsion, \mathcal{H}_{int} .* In this case:

$$U = -\lambda \langle \exp(-\lambda r_{12}) \rangle.$$

4. The two-electron atom

4.1. The $(1s2p)^{1,3}P$ states of the He isoelectronic sequence

The energies calculated by Accad, Pekeris and Schiff [20] for $Z = 2, 3, \dots, 10$, along with the fact that the singlet-triplet energy difference vanishes at the critical charge $Z = 1$ [21] yield,

$$\Delta E \approx (Z - 1) \left(0.0344887 - \frac{0.0544423}{Z} + \frac{0.0081415}{Z^2} \right). \quad (25)$$

This expression resembles the $\frac{1}{Z}$ -perturbation expansion [22–25]

$$\Delta E = \frac{224}{6561} Z - 0.0840286 + \dots = 0.034141137Z - 0.0840286 + \dots$$

and the two leading coefficients crudely agree. Since, at large Z , ΔE grows linearly in Z , it follows that $\frac{\Delta E}{Z^2}$, which vanishes at $Z = 1$ (since ΔE does), also vanishes asymptotically as $Z \rightarrow \infty$. Hence, $\frac{\Delta E}{Z^2}$ must obtain a maximum, which is found to be at $Z \approx 3.78$. From (9) (applied to ΔE) it follows that ΔC is negative for $Z = 2, 3$, and positive but small at $Z = 4$.

Substituting (25) into (9), we obtain:

$$\Delta C \approx 0.0344887Z - 0.1778618 + \frac{0.1877513}{Z} - \frac{0.0325661}{Z^2}. \quad (26)$$

The differences between the *ab initio* values of the interelectronic repulsion energies in the 3P and the 1P states [20] are consistent with the values obtained by evaluating equation (26).

4.2. The $(1s2s)^{1,3}S$ states of the He isoelectronic sequence

In complete analogy with the treatment of the $(1s2p)^{1,3}P$ sequence in the previous section, we notice, using the energies calculated by Accad, Pekeris and Schiff [20] for $Z = 2, 3, \dots, 10$, that $\frac{\Delta E}{Z^2}$ obtains a maximum (at $Z \approx 2.6$), which implies, because of (9), that ΔC is negative for $Z = 2$. This is in agreement with the ΔC values obtained using the 21-order $\frac{1}{Z}$ variational perturbation theory expansion [26]. The value of ΔC at $Z = 2$ agrees with the *ab initio* value, -0.018514 [27].

5. The two-particle harmonic quantum dot: $(1s2p)^{1,3}P$ states

Using the relative-motion energies $\epsilon(n, \ell)$ evaluated by Prudente, Costa and Vianna [28] we note that the energies of the lowest $^{1,3}P$ pair, $(0, 1)_r(0, 0)_R^3P$ and $(0, 0)_r(0, 1)_R^1P$, are given by:

$$\begin{aligned} E(^3P) &= \epsilon_r(0, 1)(\omega) + \frac{3}{2}\omega, \\ E(^1P) &= \epsilon_r(0, 0)(\omega) + \frac{5}{2}\omega, \end{aligned}$$

respectively. Fitting the numerical values we obtain:

$$\frac{E(^1P) - E(^3P)}{\omega} \approx 1 + \sqrt{\omega} \left(0.00166828 - \frac{1.009793}{0.283907 + \sqrt{\omega}} \right),$$

in agreement with Hund's first rule, $E(^1P) > E(^3P)$. Obviously, $\lim_{\omega \rightarrow 0} (E(^1P) - E(^3P)) = 0$, as each energy individually vanishes in this (no confinement) limit. As expected, the calculated energies are consistent with $\lim_{\omega \rightarrow \infty} \frac{E(^1P)}{E(^3P)} = 1$. Using (11) we obtain the difference between the 1P and the 3P interelectronic repulsion energies. The ratio $\frac{\Delta E}{\omega}$ is clearly monotonically decreasing as a function of ω . Consequently, the interelectronic repulsion energy in the singlet is higher than that in the triplet for all the values of ω considered.

6. The two-particle infinite spherical well: the $1,3S$ states

The two-electron atom with nuclear charge Z , confined in a spherical well of radius R , interpolates between the free two-electron atom ($R \rightarrow \infty$) and the spherical quantum dot ($Z \rightarrow 0$) [14].

A careful analysis of the nodal structure of the various two-electron wave functions suggests that the lowest $3S$ state, which corresponds to the configuration $(1s2s)$, should be compared with the third $1S$ state, which corresponds to the same configuration. The lowest $1S$ state corresponds, in complete analogy with the He-like atoms and the two-electron Hooke's atom, to the ground configuration $1s^2$. However, in the present case the following $1S$ state corresponds to the $(2p)^2$ configuration.

Indeed, the 3^1S and the 1^3S states are rather close in energy (the latter being lower, in conformity with Hund's rule). The interelectronic repulsion energy is rather significantly lower in the latter than in the former state. Extrapolation yields: $\lim_{R \rightarrow 0} \frac{C(3^1S) - C(1^3S)}{E(3^1S) - E(1^3S)} = 1$. Over the range of values of R available, $R^2(E(3^1S) - E(1^3S))$, whose first derivative is related to $C(3^1S) - C(1^3S)$, is a monotonically increasing function of R , approaching zero in the limit $R \rightarrow 0$. This is consistent with $C(3^1S) - C(1^3S) > 0$.

7. The confined two-electron atom: the $(1s2p)^{1,3P}$ states

A principal distinction between the atomic isoelectronic sequence and the harmonic quantum dot is that in the former the singlet-triplet energy difference vanishes at some positive nuclear charge, below which the outermost electron is not bound. In view of the confining nature of the harmonic potential, the coincidence of the singlet and the triplet energies only takes place when the harmonic force constant vanishes. Since the infinite spherical well is even more remote from the Coulomb potential – more confining – than the harmonic well, it is safe to anticipate no reversal, as a function of the radius of the confining sphere, in the latter system as well.

To understand the transition between these two types of behaviour we consider confined open-shell many-electron atoms. The multiplet structure suggested by the single configuration – frozen orbitals treatment of the systems that we actually study agrees with that specified by Hund's rules. Furthermore, we deliberately avoid systems that exhibit asymptotic degeneracies as $\frac{1}{Z} \rightarrow 0$. We follow the behavior of pairs of states that correspond to a common configuration, say, the singlet and triplet states that correspond to the $(1s2p)$ configuration of the two-electron atom. In free space, the interelectronic repulsion is higher in the singlet for higher Z , and higher in the triplet for lower Z . Confining the system into a sphere of radius R and setting $Z = 0$ we still get a singlet-triplet pair, the triplet being lower in energy, but having a lower expectation value of the interelectronic repulsion, for all R . Our aim is to trace the transition between the case $R > 0, Z = 0$ and the case $R = \infty, Z > 1$.

For $R \rightarrow \infty$ ΔE is independent of R , so we obtain from (16):

$$\Delta C = -Z^3 \frac{\partial}{\partial Z} \left(\frac{\Delta E}{Z^2} \right). \quad (27)$$

Since $\frac{\Delta E}{Z^2}$ vanishes at $Z = Z_c$, the critical charge at which the outer electron ceases to be bound, as well as at $Z \rightarrow \infty$, and is positive in between, it must possess a maximum at some intermediate value Z_m . Hence, $\Delta C < 0$ for $Z_c < Z < Z_m$, and $\Delta C > 0$ for $Z > Z_m$.

For $Z = 0$ we obtain from (15):

$$\Delta C = \frac{1}{R} \cdot \frac{\partial}{\partial R} (R^2 \Delta E). \quad (28)$$

Near-Hartree-Fock wavefunctions and energies were obtained for the singly excited pair of states $(1s2p)^{1,3P}$, over a range of nuclear charges and confining radii. In all cases, the total energy is lower in the triplet than in the singlet. The most interesting aspect is that the difference between the expectation values of the interelectronic repulsion of the singlet and the corresponding triplet states. One notes that the interelectronic repulsion is higher in the singlet except at low Z and high R .

For low R the difference of the interelectronic repulsions between the singlet and the triplet is a decreasing function of Z . This is because when Z increases for a constant R the wavefunction contracts and the boundary becomes less significant. Since the singlet is more expanded, the boundary affects it more significantly, increasing the singlet-triplet difference of interelectronic repulsions. At high R , including the free atom ($R = \infty$), the difference of interelectronic repulsions increases with increasing Z . This is a trivial consequence of the fact that the difference of interelectronic repulsions is, asymptotically, equal to $2K[1s, 2p]Z$, where $K[1s, 2p]$ is the exchange integral. A minimum in the singlet-triplet difference of interelectronic repulsions as a function of Z is

noted at intermediate R . For Z above this minimum the high R behaviour is manifested, whereas for Z below the minimum one is in the low R regime. The location of the minimum shifts to lower Z upon increase of R . Noticing this trend helps understand what would otherwise look to be a suspicious sequence of interelectronic repulsion differences at $R = 5$. The difference of interelectronic repulsions is always a decreasing function of R , for constant Z . This trend is due to the fact that the confinement affects the singlet – that is more expanded – more than the triplet, increasing the singlet interelectronic repulsion upon lowering R .

8. The Debye-screened two-electron atom: the $(1s2s)^1,^3S$ states

Finally, we consider the fully-screened (FS) two-electron Debye atom, (1), the screened nuclear attraction (SNR) Hamiltonian (2), and the screened interelectronic repulsion (SIR) Hamiltonian (3) [15]. We refer to the term $\frac{\exp(-\lambda r_{12})}{r_{12}}$ either as the screened interelectronic repulsion or as the interparticle repulsion. The operator $\frac{1}{r_{12}}$ is referred to, as usual, as the interelectronic repulsion. We say “particle” to emphasize that the interaction is modified, although the properties (mass, spin, statistics) are those of an electron. The expectation values of these operators are referred to as the interparticle or interelectronic repulsion energies, respectively.

We find that the methodological standpoint taken by Lin *et al.* [29], allowing the effect of the Debye screening of the one- and the two-particle terms to be distinguished from one another, is helpful when dealing with the excited states as well. The fact that in \mathcal{H}_D both the one-electron and the two-electron potential energy terms are screened leads to unexpected trends in the behavior of the triplet *vs.* the singlet interparticle repulsion energies. We expect \mathcal{H}_d to behave more similarly to the confined two-electron atom. A complementary picture is offered by \mathcal{H}_{int} . Upon increasing the Debye screening the interelectronic repulsion is quenched and the system approaches two non-interacting hydrogen-like electrons in the $(1s2s)$ configuration, with the $\lambda \rightarrow \infty$ asymptotic energy $-Z^2 \left(\frac{1}{2} + \frac{1}{8} \right)$.

$$v = Z \frac{\partial e}{\partial Z} = 2e - \lambda \frac{\partial e}{\partial \lambda} = -\lambda^3 \frac{\partial}{\partial \lambda} \left(\frac{e}{\lambda^2} \right), \quad (29)$$

and

$$t = -e + \lambda \frac{\partial e}{\partial \lambda} = \lambda^2 \frac{\partial}{\partial \lambda} \left(\frac{e}{\lambda} \right).$$

The differences between the singlet and the triplet energies for the FS, the SNA and the SIR models have been examined as functions of $\frac{\lambda}{Z}$, for $Z = 2, 3, 4, 5$. The singlet is always higher than the corresponding triplet, the difference increasing with increasing Z . From the different versions of the λ -Hellmann–Feynman theorem it follows that the initial slopes of the singlet and the triplet energies, at $\frac{\lambda}{Z} = 0$, are equal. Hence, ΔE starts horizontally, with a vanishing slope.

For the SNA atom both the singlet and the triplet energies are higher (lower in absolute value) than those of the FS atom. This is due to the higher interparticle repulsion in the former systems. The singlet-triplet energy differences are smaller for the SNA atoms than for the FS atoms.

For the SIR atom the singlet-triplet energy difference increases at low $\frac{\lambda}{Z}$, because the triplet energy is lowered more rapidly by the enhanced interparticle screening. This energy difference reaches a maximum (roughly at $\frac{\lambda_m}{Z} \approx \frac{0.65}{\sqrt{Z}}$), vanishing asymptotically at $\frac{\lambda}{Z} \rightarrow \infty$.

8.1. The interparticle repulsion energies

For $Z = 2$ the interparticle repulsion energy is lower in the singlet over the whole range of values of the screening constant for both the FS atom and the SNA atom. For the SIR atom the difference between the singlet and the triplet interparticle repulsion energies rises, becoming positive above a certain screening constant. For $Z \geq 3$ the interparticle repulsion in the FS atom is lower in the triplet at low screening (up to $\lambda \approx 0.096$ at $Z = 3$, $\lambda \approx 0.17$ at $Z = 4$ and $\lambda \approx 0.208$ at $Z = 5$), but higher in the triplet for higher screening. This reversal takes place at lower values of the screening constants for the SNA atom. While the SIR singlet interparticle repulsion energy is always higher than that of the triplet, they both vanish, asymptotically, at $\frac{\lambda}{Z} \rightarrow \infty$, where the screening quenches the interparticle repulsion. Like the ionization energy, the triplet interparticle repulsion energy approaches the asymptotic value considerably more rapidly than the singlet.

Finally, Debye screening of the nuclear attraction enhances the reversal of the magnitudes of the singlet *vs.* the triplet interparticle repulsion energies by effectively lowering the nuclear charge, whereas Debye screening of the interparticle repulsion acts in the opposite direction. This behavior is due to the fact that the singlet wave function is more expanded, so that it samples the interparticle repulsion operator at higher values of r_{12} , at which the effect of the factor $\exp(-\lambda r_{12})$ is more pronounced.

9. Conclusions

The behavior of the interelectronic repulsion energy in two-electron systems with a range of one-body potentials was reviewed. Particular attention was paid to the relative magnitudes of the interelectronic repulsion energies within pairs of states which, in the limit of vanishing interelectronic repulsion, belong to a common electronic configuration. Expressions for these differences of interelectronic repulsion energies in terms of derivatives of simple expressions involving differences of corresponding total energies were derived, using appropriate versions of the virial and Hellmann–Feynman theorems. In the atomic case the expressions to be differentiated were shown to be non-monotonic by considering their behavior for both $Z \rightarrow \infty$ and for $Z \rightarrow Z_c$ (where Z_c is the critical charge below which the outermost electron is not bound). Hence, their derivatives yield an inevitable sign reversal in the difference of interelectronic repulsion energies, for some Z that satisfies $Z_c < Z < \infty$.

In the confined systems the behavior at the high correlation limit of the isoelectronic sequences (when $k \rightarrow 0$ for Hooke’s atom and when $R \rightarrow \infty$ for the infinite spherical well) implies a monotonic behavior of the energy-related quantities that need to be differentiated to obtain the corresponding difference of interelectronic repulsion energies. Hence, no sign reversal is expected. These conclusions are confirmed computationally, for appropriate pairs of states.

Careful analysis indicates that the ordering and structure of electronic configurations in Hooke’s atom, and even more so in the infinite spherical well, are sometimes very different from those in the atomic case, due to different degeneracies and configuration mixing. Such distinctions are important to keep in mind when trying to draw meaningful comparisons.

The lowest $^1,^3P$ pair exhibits remarkable robustness in the following sense: this is the only pair of states in which both members are lowest within the subspaces of their respective symmetry types, being reasonably well described by the $(1s2p)$ configuration. The $(1s2s)^1,^3S$ pair suffers from the fact that the singlet is not the lowest of its symmetry type, which makes a treatment in terms of a single configuration approximation somewhat delicate. The $^1,^3D$ states are even worse. They are nicely described in terms of the single configuration $(1s3d)$ in the atomic case, but each member of the pair belongs to a different limiting configuration (the singlet being $(2p)^2$ and the triplet $(1s3d)$) in the infinite spherical well. Even in Hooke’s atom the lowest 1D state involves a linear combination of two configurations that are mutually degenerate in the non-interacting limit. In view of this robustness of the $^1,^3P$ pair, the single most pertinent recommendation for further study is that this pair of states should be examined more carefully for spherically symmetric quantum dots with a range of shapes and strengths, including, in particular, non-confining potentials such as a finite well or a Gaussian potential. This is the context in which the least ambiguous results are likely to emerge.

The lowest energy pair of singly-excited states, $(1s2s)^1,^3S$, is investigated for three types of two-electron Debye Hamiltonians. The reversal in the relative magnitudes of the singlet *vs.* the triplet interparticle repulsions has been charted for the three models over a reasonably broad range of the pertinent parameters [15]. The overall behavior is in agreement with earlier results on the unscreened two-electron atom, showing interesting distinct features.

Singlet-triplet splitting was studied for two confined open-shell atomic systems as a function of the nuclear charge and of the radius of the confining sphere. In all the cases considered the total energy was confirmed to be lower in the triplet. The interelectronic repulsion was found to be lower in the singlet when the nuclear charge is low enough and the confining radius is large enough. The difference of interelectronic repulsions between the singlet and the triplet (denoted ΔC) was found to be a decreasing function of the radius of the confining sphere, at a constant nuclear charge. However, as a function of the nuclear charge at a constant confining radius, this difference increases for large confining spheres, and exhibits a minimum at intermediate confining spheres. For tightly confining spheres ΔC decreases with increasing nuclear charge in the two-electron $1s2p$ system, but increases with increasing nuclear charge in the four-electron $1s^2 2s2p$ system. This distinction can probably be understood as a consequence of the fact that the $1s$ and the $2p$ orbitals are very differently affected by the confining sphere, which is not the case for the $2s$ and $2p$ orbitals. While the contrast in the behavior of the difference between the singlet-triplet interelectronic repulsions in the free and in the confined atom follows from the analysis in [11], the transition between these two types of behavior is now clarified.

In both systems studied $\frac{\partial E}{\partial R} < 0$ (the energy decreases – increasing in absolute value – with increasing R). $\left| \frac{\partial E}{\partial R} \right|$ decreases with increasing R , vanishing at large R . More remarkably, it is higher in the singlet than in the triplet, due to the fact that the triplet wave function is more contracted, hence less affected by the confining sphere. Similarly, $\frac{\partial E}{\partial Z} < 0$. Like the absolute value of the derivative with respect to R , $\left| \frac{\partial E}{\partial Z} \right|$ decreases with increasing R , remaining finite at $R \rightarrow \infty$ where it is equal to the expectation value of $\sum_{i=1}^N \frac{1}{r_i}$, N being the number of electrons.

As a function of Z , $\left| \frac{\partial E}{\partial Z} \right|$ increases. This is obvious, at least at large R , reflecting the contraction of the wave function upon increasing Z . The contraction of the triplet wave function relative to the singlet is also reflected in the fact that $\left| \frac{\partial E}{\partial Z} \right|$ is larger in the former than in the latter.

Investigation of the effects of milder confining potentials, such as a finite spherical square-well or a Gaussian potential, are worth-while extensions of the present study.

References

- [1] Hund F., Zur deutung verwickelter spektren, insbesondere der elemente Scandium bis Nickel, *Z. Phys.*, 1925, **33**, P. 345–371.
- [2] Slater J.C. The theory of complex spectra. *Phys. Rev.*, 1929, **34**, P. 1293–1322.
- [3] Morgan III J.D., Kutzelnigg W. Hund's rules, the alternating rule, and symmetry holes. *J. Phys. Chem.*, 1993, **97**, P. 2425–2434.
- [4] Kutzelnigg W., Morgan III J.D. Hund's rules. *Z. Phys. D*, 1996, **36**, P. 197–214.
- [5] Davidson E.R. Single-configuration calculations on excited states of Helium. II. *J. Chem. Phys.*, 1965, **42**, P. 4199–4200.
- [6] Koga T., Matsuyama H., J. Molina Molina, Dehesa J.S. Electron-pair densities of group 2 atoms in their 1P and 3P terms. *Eur. Phys. J. D*, 1999, **7**, P. 17–23.
- [7] Katriel J. A study of the interpretation of Hund's rule. *Theoret. Chim. Acta*, 1972, **23**, P. 309–315. An interpretation of Hund's rule, *ibid.*, 1972, **26**, P. 163–170.
- [8] Katriel J. and Pauncz R., Theoretical interpretation of Hund's rule. *Adv. Quantum Chem.*, 1977, **10**, P. 143–185.
- [9] Katriel J. and Themelis S.I. Hund's rule in the doubly excited states of the Helium isoelectronic sequence. *Int. J. Quantum Chem.*, 2012, **112**, P. 2880–2893.
- [10] Koga T. and Koshida Y. Roles of nuclear attraction and electron repulsion energies in the relative stability of atomic LS terms. *J. Chem. Phys.*, 1999, **111**, P. 53–54.
- [11] Katriel J. and Montgomery Jr.H.E. Atomic vs. quantum dot open shell spectr. *J. Chem. Phys.*, 2017, **146**, P. 064104-(1-10).
- [12] Sako T., Paldus J., Ichimura A. and Diercksen G.H.F. Origin of the first Hund rule and the structure of Fermi holes in two-dimensional He-like atoms and two-electron quantum dots. *J. Phys. B*, 2012, **45**, P. 235001(1–13).
- [13] Katriel J. and Montgomery Jr.H.E., Hund's rule in the two-electron quantum dot. *Eur. Phys. J. B*, 2012, **85**, P. 394(1–4).
- [14] Sarsa A., Buendía E., Gálvez F.J. and Katriel J. Singlet vs. triplet interelectronic repulsion in confined atoms. *Chem. Phys. Letters*, 2018, **702**, P. 106–110.
- [15] Katriel J., Montgomery Jr.H.E. and Sen K.D. Hund's rule in the $(1s2s)^{1,3}S$ states of the two-electron Debye atom. *Phys. Plasmas*, 2018, **25**, P. 092111(1–6).
- [16] Pupyshv V.I. and Montgomery Jr.H.E. Spherically symmetric states of Hookium in a cavity, *Phys. Scr.*, 2015, **90**, P. 085401(1–8).
- [17] Ugalde J.M., Sarasola C. and Lopez X. Atomic and molecular bound ground states of the Yukawa potential. *Phys. Rev. A*, 1997, **56**, P. 1642–1645.
- [18] Mercero J.M., Fowler J.E., Sarasola C. and Ugalde J.M. Bound excited states of H^- and He^- in the statically screened Coulomb potential. *Phys. Rev. A*, 1998, **57**, P. 2550–2555.
- [19] Dai S.T., Solovyova A. and Winkler P. Calculations of properties of screened He-like systems using correlated wave functions. *Phys. Rev. E*, 2001, **64**, P. 016408(1–9).
- [20] Accad Y., Pekeris C.L. and Schiff B. S and P states of the Helium isoelectronic sequence up to $Z = 10$. *Phys. Rev. A*, 1971, **4**, P. 516–536.
- [21] Katriel J. The splitting of atomic orbitals with a common principal quantum number revisited: np vs. ns. *J. Chem. Phys.*, 2012, **136**, P. 144112(1–8).
- [22] Knight R.E. and Scherr C.W. Two-electron atoms II. A perturbation study of some excited states. *Rev. Mod. Phys.*, 1963, **35**, P. 431–436.
- [23] Sanders F.C. and Scherr C.W. Perturbation study of some excited states of two-electron atoms. *Phys. Rev.*, 1969, **181**, P. 84–97.
- [24] Blanchard P. Nonrelativistic-energy Z-expansion coefficients for singly excited S and P states of two-electron ions. *Phys. Rev. A*, 1976, **13**, P. 1698–1701.
- [25] Baker J.D., Freund D.E., Hill R.N. and Morgan III J.D. Radius of convergence and analytic behavior of the $1/Z$ expansion. *Phys. Rev. A*, 1990, **41**, P. 1247–1273.
- [26] Aashamar K., Lyslo G. and Midtdal J. Variational perturbation theory study of some excited states of two-electron atoms. *J. Chem. Phys.*, 1970, **52**, P. 3324–3336.
- [27] Thakkar A.J. and Smith Jr.V.H. Compact and accurate integral-transform wave functions. II. The 2^1S , 2^3S , 2^1P , and 2^3P states of the helium-like ions from He through Mg^{10+} . *Phys. Rev. A*, 1977, **15**, P. 16–22.
- [28] Prudente F.V., Costa L.S. and Vianna J.D.M. A study of two-electron quantum dot spectrum using discrete variable representation method. *J. Chem. Phys.*, 2005, **123**, P. 224701(1–11).
- [29] Lin Y.C., Fang T.K. and Ho Y.K. Quantum entanglement for helium atom in the Debye plasmas. *Phys. Plasmas*, 2015, **22**, P. 032113(1–8).

Fractal characterization of nanostructured materials

A. N. Kovalenko

Ioffe Institute, 26 Politekhnicheskaya, St. Petersburg 194021, Russia

ras-kan@mail.ru

PACS 81.05 U, 05.45.Df, 61.48.De, 81.20.Ka

DOI 10.17586/2220-8054-2019-10-1-42-49

The article presents a developed gradient-pixel method of fractal analysis and results of multifractal characterization of nano-structured materials with a high proportion of non-autonomous phases obtained from micrographs of their surface chips with high-resolution scanning microscopes. Compared with the black and white binarization option, the gray gradation improves the quality of multifractal analysis of nanostructured materials and expands its capabilities, in particular, the selection of multi-scale composite inclusions in the structure of the material and nano-objects on transparent or opaque basis. Establishing the characteristics of these dependencies permits linking the indicators of structural and phase nonuniformity in the development of new materials with changes in their physicochemical properties. In comparison with the fractal dimension of the Sierpinski carpet as a classic regular monofractal computed on the outlined basis, quite accurately coinciding with the known analytical value, the resulting spectrum of fractal dimensions of the synthesized chemical-catalytic and thermoelectric nanomaterials indicates the multifractal nature of their structural and phase nonuniformity according to the Rényi generalized equation.

Keywords: nanostructured materials, SEM micrographs of chips, fractal analysis, gradient-pixel method, spectrum of multifractal dimensions.

Received: 2 January 2019

Revised: 31 January 2019

1. Introduction

Studies of various processes for the synthesis of nanostructured materials with significantly different properties and composition from homogeneous model media show that fractal self-organization is a characteristic feature of their formation [1–3]. This causes the invariant metric-statistical self-similarity of multi-scale composite structures with a non-Euclidean (fractional) relationship between the rate of increase in the number of considered elements and the increase in the scale of their consideration [4, 5]. This is de facto valid for all technologies and methods for the synthesis of nanomaterials and is determined by the special role of the energy and entropy characteristics of the surface and interfacial layers, the correlation scale of the matter and energy transfer phenomena in different macro, micro and nanostructural blocks of the material, as well as the boundary tolerance factor of their partitioning [6–10]. This is clearly seen in materials with a high content of nanostructured non-autonomous phases of a substance. That is, the phases that are thermodynamically not existing in isolation from its macrovolumes and forming on their surface or interfaces under the conditions of spatial and mass restrictions [11, 12]. The high specific surface area of fractal aggregates of different nature explains the possibility of their active participation in condensation processes, sorption processes, chemical reactions of heterogeneous catalysis and inhibition, and other applied areas [13]. Establishing the characteristics of these dependencies allows us to link the indicators of structural and phase nonuniformity in the development of new materials with changes in their physicochemical properties, as well as predicting the effect of the size of the fractal object and the spatial scale of its consideration [14–20].

2. Methodology of fractal analysis

The calculation-experimental methods of fractal analysis, including the developed gradient-pixel method of characterization of the structural-phase nonuniformity of nanomaterials, are based on the general idea of Mandelbrot of the difference between the topological Euclidean dimension of such non-smooth objects and the geometric dimension. Mathematically, this manifests itself in the form of the dependence $M \sim \varepsilon^D$ between the rate of increase in the number of structural elements M under consideration and the increase in the spatial scale interval ε of their consideration with a fractional index of fractal dimension D . The similar pattern also takes place when considering the occurrence of fractal processes of deterministic chaos in time [21]. Here, the time series of the measured signal $U(\tau)$ is displayed in the phase space of the embedding $U' = f(U)$ in the form of an attracting set of unstable infinitely jagged phase trajectories, the so-called strange fractal dimension attractor, characterizing the effective number of degrees of freedom, forming a stochastic signal in a dynamic system. For real fractal objects, the self-similarity manifests itself in a certain scaling interval of natural scales of the considered elements size

$R_{\min} \leq \varepsilon \leq R_{\max}$, where R_{\min} is associated with the finite size of these elements, and R_{\max} – with the tendency of D to its final limit.

The practical assessment of the fractality of real objects (mass fractals, fractal cluster-aggregates, branched structures, fractal surfaces, fractal curves and fractal time series) is made by mathematical processing of experimental data to measure the abovementioned ε , M scale-structural parameters. The recognized methods of their “*in situ*” measurements for various powdered, porous, and composite polycrystalline materials, including nanostructured ones, are invasive mercury porosimetry, gas and liquid pycnometry, low-temperature nitrogen adsorption, calorimetry, inverse gas chromatography, small-angle neutron scattering, X-ray diffraction, transmission and scanning electron microscopy and some others [15,22–24]. Some of these methods are used to characterize not only material structure defects (pores, cracks, liquid, gas and solid inclusions), but also for dispersed systems of a different nature (emulsions, aerosols, etc.). In some cases, the identification of the dynamic characteristics of the processes taking place in time can be carried out simultaneously, for example, a topochemical measurement of the reaction rate [25–29]. It should be noted that the use of the outlined invasive methods is quite laborious, requiring high-precision measuring instruments along with special equipment, and is associated with a number of assumptions about the nature of the contact interaction of the substance being embedded with the material under study. In addition, many of the methods of “*in situ*” measurements of the fractal dimension were developed for a specific task. The use of radiation scattering methods (X-ray, neutron, light) by the fractal structure is sufficiently correct only in case when all the aggregates are characterized by the same size of primary particles and the same nature of their fractal growth.

One of the very common methods of express experimental study of the fractal nature of real nanoclusters in three-dimensional and two-dimensional space is the analysis of their electron microscopic images based on transmission and scanning electron microscopy. Despite the possibility of some subjective errors of the subsequent interpretation of images and a certain deformation of objects in preparation for the experiment, electron microscopy allows the required variation of the image scale and its spatial resolution. However, identical generally accepted algorithms for processing these images have not yet been developed, nor the general algorithms for processing the experimental data on the dynamics of fractal processes in real time. In all cases, the fractal indicator D for the measured M , ε parameters for spatial structures and for time processes of regular monofractal sets can be obtained geometrically in practice. In the first case, it can be done by the slope ratio of the line, approximating the graph of the above dependence $\ln M \sim D \ln \varepsilon$ in logarithmic coordinates as the limit $D = \lim_{\varepsilon \rightarrow 0} [\ln M / \ln \varepsilon]$. In the second case, the same can be achieved as the slope of the limit $D = \lim_{\varepsilon \rightarrow 0, K \rightarrow \infty} [\ln C(K, \varepsilon) / \ln \varepsilon]$ dependence

for the correlation integral (correlation sum) $C(K, \varepsilon) = K^{-2} \sum_{i,j}^K \theta [r - \rho(x_i x_j)]$, which characterizes the averaged

probability of proximity of fractal processes phase trajectories. Here, ε is the characteristic scale of consideration of the phase trajectory attractor elements, θ is the Heaviside function, $[r - \rho(x_i x_j)]$ is the distance function in the n -dimensional phase space, K is number points of the considered attractor in the correlation. The classical mathematical examples of the fractal analysis of ordered geometric models serve as illustrations of this approach: the infinitely jagged Koch curve (or snowflake) having no derivative in any point, the Cantor set or Cantor dust, the Sierpinski carpet, the Menger sponge, the Minkowski sausage. Their fractals are determined analytically and are respectively $D = \ln 4 / \ln 3 = 1.2618\dots$; $D = \ln 2 / \ln 3 = 0.6309\dots$; $D = \ln 8 / \ln 3 = 1.8928\dots$; $D = \ln 20 / \ln 3 = 2.7268\dots$; $D = \lim_{\varepsilon \rightarrow 0} [\ln(3/2\sqrt{\varepsilon}) / \ln \varepsilon] = 1/2$. A rare exception to the definition of fractals as objects with non-integer dimensions is the three-dimensional analogue model of the Sierpinski triangle with $D = \ln 4 / \ln 2 = 2$, the Peano and Hilbert plane curves with $D = 2$, the Fournier Universe with $D = 1$, and some others [30–32]. The difference between these examples reflects the fact of non-compactness (“friability”) of the fractal in the first case and the dense filling of the space it occupies in the second.

However, it should be noted that for an adequate description of the real unordered (nonuniform) natural fractals and many irregular model structures, using only one single value of the fractal dimension D is not enough. Along with the metric characteristics, it is necessary to determine their statistical properties, reflected by the full spectrum of fractal dimensions using the multifractal formalism [32]. The Rényi generalized dimensional equation [33] is its basis:

$$D_{Rq} = \lim_{\varepsilon \rightarrow 0} \lim_{\tau \rightarrow 0} \lim_{m \rightarrow \infty} \left[\frac{1}{q-1} \frac{\ln Z(q, \varepsilon)}{\ln(\varepsilon)} \right].$$

Here, $I_{Rq}(p, q) = [\ln Z(q, \varepsilon)] / (q - 1)$ is the Rényi generalized entropy of order q ; $Z(q, \varepsilon) = \sum_{i=1}^{N(\varepsilon)} p_i^q(\varepsilon)$ is the generalized statistical sum; $N(\varepsilon)$ is the minimum number of the “measuring” cubes with edge ε required to cover the attractor in n – dimensional phase space of embedding; $p_i(\varepsilon)$ is the probability of visiting the i -th cube by the phase trajectory in this phase space of embedding; m is the number of points used to estimate the dimension (or the number of measurements at time intervals τ). The well-known expressions for the Kolmogorov–Sinai entropy and the Kolmogorov–Hausdorff fractal dimension ($q = 0$), the Shannon–Gibbs entropy and the corresponding information dimension ($q = 1$), the correlation entropy and the correlation dimension ($q = 2$) are special cases of this equation with various values of q . Since the Rényi dimension is a steadily decreasing function of q , in order to display the attractor for larger q , a smaller dimension of the embedding space is required. An approximate analog of the Hausdorff dimension is the Minkowski dimension $D = \lim_{\varepsilon \rightarrow 0} [\ln M(\varepsilon) / \ln \varepsilon]$, which coincides with the Hausdorff dimension for the main classical fractals and many applied problems, but has a more efficient calculation algorithm.

For mathematical processing of the dynamic characteristics of the proceeding fractal processes with a limited sequence of the measured signal time series, the Takens theorem is used. According to it, the restoration of the missing coordinates of the attractor trajectories is carried out by using the data from the same series, taken with some delay [34].

3. Software implementation of the methodology

The main part of the research published on this base refers to the well-known software packages of fractal time series processing: the FracLab module of the MatLab package, the CDA program (by J. C. Sprott, G. Rowlands), the RQA program (by C. J. Webber, J. P. Zbilut), the TISEAN package (by R. Hegger, H. Kantz, T. Schreiber), the Fractan 4.4 package (by V. Sychev), the CorDimension application (Copyright © AIRES), etc. They were briefly reviewed in paper [35]. Less work is devoted to the software implementation of multifractal processing of disordered structures of materials (the MFDrom program by G. V. Vstovsky, the multifractal image analysis program by K. A. Kichigina, A. I. Degtyarev, D. M. Karavaev, etc. [15, 36]). Since fractal dimension is an invariant property with scale transformation, along with the standard method of physical change of the general scale of consideration of the object being analyzed, the method of digital zooming of its non-detailed elements (the size of “pixels”) forming a grid of the complete bitmap image can be used. At the same time, each pixel can be characterized only by one specific color or brightness, and also transparency. The latter possibility has not yet been taken into account. In the above-mentioned papers, either the change in the overall scale of the analyzed object was used, or a variant of black and white binarization of its pixel photographic images. To remove the limitations of this approach in the presence of different-scale composite inclusions in the structure of the material, the grid method of digital gradient pixelation of its micrographs by resizable cells is used as a method for changing the scale of consideration of details of the nanostructured nonuniformity in the algorithm developed below. As a method for identifying nonuniformities in these cells, including those on transparent or non-transparent basis, the gray level gradation of color and transparency of cell images is used.

The gray gradation, in contrast to the black-and-white one used in the above-mentioned works, improves the quality of the multifractal analysis of nanostructured materials and expands its capabilities, in particular, the selection of multi-scale composite inclusions and nano-objects on transparent or non-transparent basis. For each pixel partitioning, as a measure of the fractal spectrum of structural nonuniformity, the probability $p_i(\varepsilon) = n_i / N(\varepsilon)$ of the gray color distribution in the cells on the set digital scale of its gradation is used (for example, from 0 to 1), for the binary black and white gradation the probability of distribution is 0 or 1. Here, n_i is the fixed degree of color gradation in cell i ; $N(\varepsilon)$ is the total number of cells by size ε . Then, depending on the set size of ε_k cells,

the generalized correlation function is estimated (generalized statistical sum) $Z(q, \varepsilon) = \sum_{i=1}^{N(\varepsilon)} p_i^q(\varepsilon)$ for all cells,

characterized by the exponent q , which can take a value in the interval $-\infty < q < +\infty$. Then, the spectrum of the generalized Rényi fractal dimensions, which characterize the given distribution, is determined using the relation $D_q = \tau(q) / (q - 1)$ [32]. Here, the function $\tau(q) = (q - 1)D_q = \lim_{\varepsilon \rightarrow 0} [\ln Z(q, \varepsilon) / \ln \varepsilon]$ is defined as the slope

ratio of the approximate dependence $Z(q, \varepsilon) \approx \varepsilon^{\tau(q)}$ by the least squares method from the size ε of cells of the pixel division. The function of the multifractal spectrum is determined $f(\alpha) = q\alpha - \tau(q)$, where $\alpha = d\tau/dq =$

$-\lim_{\varepsilon \rightarrow 0} \left(\sum_{i=1}^{N(\varepsilon)} p_i^q \ln p_i \right) / \left(\sum_{i=1}^{N(\varepsilon)} p_i^q \ln \varepsilon \right)$ is the derivative of the function $\tau(q)$, note that $\alpha = d\tau/dq|_{q \rightarrow +\infty} =$

$D_{+\infty} = \alpha_{\min}$ and $\alpha = d\tau/dq|_{q \rightarrow -\infty} = D_{-\infty} = \alpha_{\max}$ [32]. Furthermore, the multifractal characteristics are found: with $q = 0$ the Hausdorff dimension is $D_0 = -\lim_{\varepsilon \rightarrow 0} [\ln N(\varepsilon)/\ln \varepsilon]$, where $\left(\sum_{i=1}^{N(\varepsilon)} p_i^{q=0}(\varepsilon)\right) \approx N(\varepsilon)$; with $q = 1$ the information dimension is $D_1 = \lim_{\varepsilon \rightarrow 0} \left(\sum_{i=1}^{N(\varepsilon)} p_i \ln p_i\right) / (\ln \varepsilon)$, where $\left(-\sum_{i=1}^{N(\varepsilon)} p_i \ln p_i\right) = S(\varepsilon)$ is the Shannon entropy; with $q = 2$ the correlation dimension is $D_2 = \lim_{\varepsilon \rightarrow 0} \left(\sum_{i=1}^{N(\varepsilon)} p_i^2\right) / (\ln \varepsilon)$, where $\left(\sum_{i=1}^{N(\varepsilon)} p_i^2\right) \approx C(K, \varepsilon)$ is the correlation integral (correlation sum).

The procedure of gradient gray pixelation with dividing the area of the processed image into a square grid with cells of a certain size ($\varepsilon_k \times \varepsilon_k$) can be included in the overall program using the size doubling algorithm $\varepsilon_k = 2^{n+1}$ ($n = 1, 2, 3, 4, 5, \dots$). This procedure can also be performed using the standard options of the Adobe Photoshop graphics editor [37], the standard PHP function of the ImageMagick command line utility in the Windows environment [38] and other graphics processing tools with the addition of the “*alpha channel*” program component in them to define the pixel image transparency.

Obvious criteria for the quality of digital “pixelation” are the ratio of the physical area of the processed image to the number of cells used by pixel partitioning, related to the size of the pixel itself, as well as the number of information units used to describe each pixel of the image.

4. Results and discussion

As an example, Fig. 1 shows the micrographs of samples of new model compounds with a high proportion of nanostructured non-autonomous phases for original functional materials for catalytic and thermoelectric purposes that were kindly provided by E. A. Tugova. The samples were synthesized at the Ioffe Institute of the Russian Academy of Sciences on the basis of layered oxides of different composition and structure using different technological methods. The micrographs were obtained using high resolution scanning (raster) electron microscopes JSM-5610 LV and CamScan MV2300 Quanta FEI 200 with direct magnification from 5000 to 300000 times and passport resolution of 2.5 nm for lines, 3.5 nm for points.

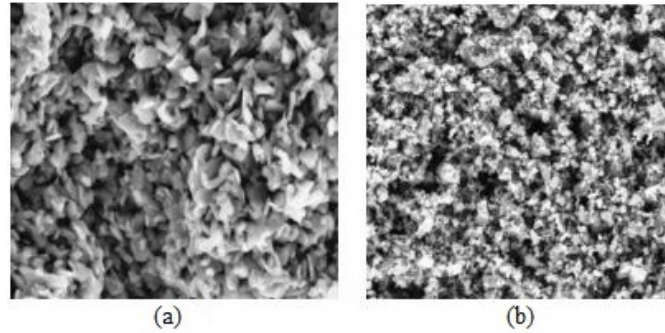


FIG. 1. Micrographs of the samples of $\text{Ca}_3\text{Co}_4\text{O}_9$ nanocrystalline compounds synthesized by the co-precipitation method with subsequent heat treatment (a) and the gas-flame combustion method of the glycine-nitrate gel precursor (b)

The sample of material according to Fig. 1(a) is characterized by multi-scale composite inclusions in its structure with an average crystallite size of 45 ± 5 nm according to X-ray diffraction data. The material was obtained by the method of co-precipitation of cobalt hydroxide $\text{Co}(\text{II})$ into CaCO_3 suspension with NaOH solution followed by the heat treatment. According to this method, synthesis reactions proceed in a diffusion mode, which is also characteristic of other traditional methods for producing nanodispersed materials based on solid-phase and sol-gel synthesis, hydrothermal and high-temperature processing. The use of the kinetic regime of gas-flame combustion of the glycine-nitrate gel precursor helps solving the problem of sintering the obtained $\text{Ca}_3\text{Co}_4\text{O}_9$ nanopowders with the size of coherent scattering regions of 40 ± 4 nm and approximates the properties of thermoelectric nanoceramics on their basis to the properties of single-crystal samples (Fig. 1(b)).

Examples of the results of partitioning the original electronic images Fig. 1 with square cells with pixel sizes of 4p, 8p, 16p and 32p, graded in 10 shades of gray, and their comparison with black and white binarization are shown in Fig. 2.

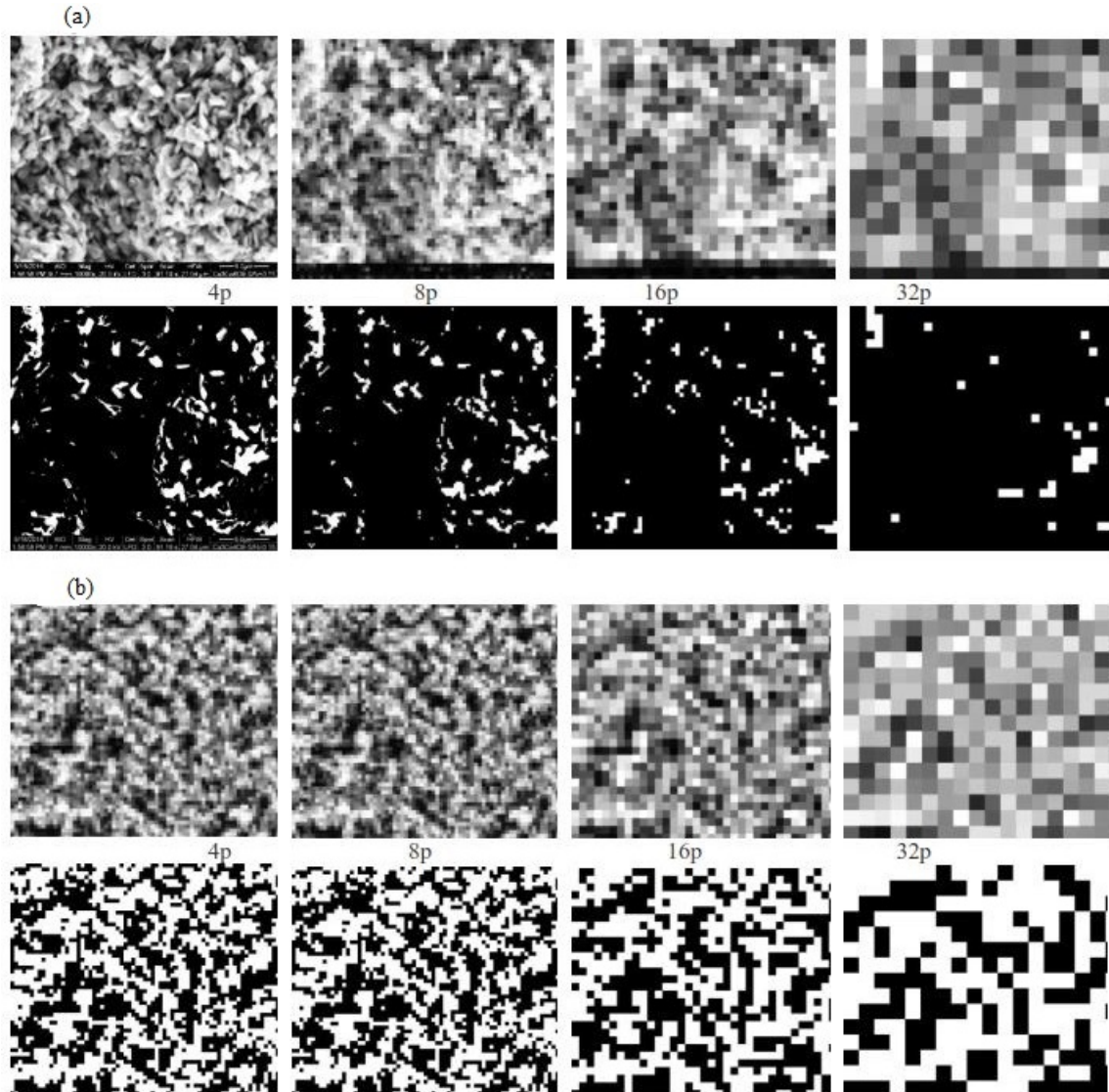


FIG. 2. Comparison of grid partitioning of the source micrographs of synthesized nanocomposite materials samples by cells with pixel sizes 4p, 8p, 16p and 32p: (a) for the image of the micrograph Fig. 1(a) in gradation of 10 shades of gray (cells 4p 8p, 16p and 32p - top row) and in the black and white binarization variant (cells 4p 8p, 16p and 32p - bottom row); (b) - same for the image of the micrograph of Fig. 1(b)

As can be seen, the variant of black and white binarization is associated with a significant loss of the information richness of the analyzed structures as compared to their gray gradation in the gradient pixelation method. The quality of the latter, if necessary, can be improved, for example, up to 256 shades (gradations) of gray color due to the transition to the gray scale widely used in a usual computer representation using 8 bits of information for each pixel of the image. More is possible when using the multibyte full color schemes of 16/24/30/36/48 bits and the transition to the full-color image. In this case, it becomes possible to add the program “*alpha channel*”, which sets the transparency of the image for each pixel [33,34].

For comparison, Fig. 3 shows an example of the gradient pixelation of the classical model image of the Sierpinski carpet as a planar analogue of the regular monofractal Cantor set constructed in the MATLAB-SIMULINK simulation environment [39]. For its construction the method of random iterations was used with the number

of repeated partitionings of 2^3 with exclusion of the middle thirds by removing the central squares from all the fragments formed by successive division of the sides of the carpet and all its remaining fractions into 3 equal parts.

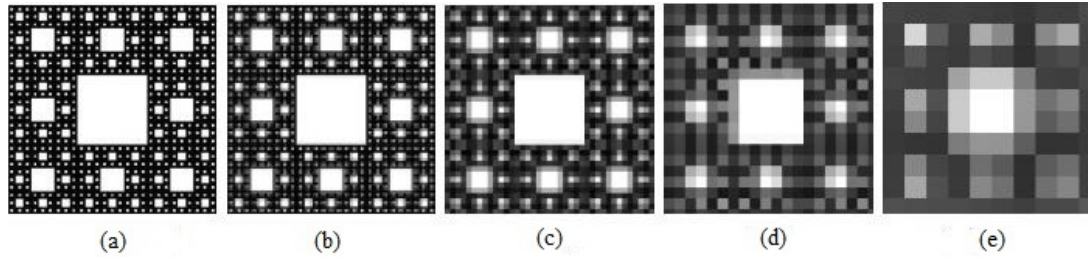


FIG. 3. The Sierpinski carpet (a), constructed by random iteration with exclusion of middle thirds, and its grid partitionings by gradient cells with pixel sizes of 4p (b), 8p (c), 16p (g) and 32p (d)

The results of the fractal analysis of the aforementioned model nanostructures based on the developed approach are shown in Fig. 4 in the form of the $D_q(q)$ dependence. Thus, Fig. 4(a) shows the fractal dimension of the Sierpinski square carpet model, obtained from its black and white binarized and gradient pixelized images in Fig. 3 and Fig. 4(b) shows the dependence $D_q(q)$ obtained from micrographs of the surface chip of a nanocomposite material samples synthesized by different methods on the basis of layered calcium cobaltite $\text{Ca}_3\text{Co}_4\text{O}_9$ (see Fig. 1). Fig. 4(c) shows the dependence of the function multifractal spectrum $f(\alpha) = q\alpha - \tau(q)$ on the synthesized nanocomposite material from factor q and synthesis method. For calculations, we used a square fragment, maximum in area, with initial resolution from (1024×768) to (1920×1080) pixels with different cell sizes of their “digital” pixelation, graded by 10 shades of gray, examples of which were shown in Fig. 2.

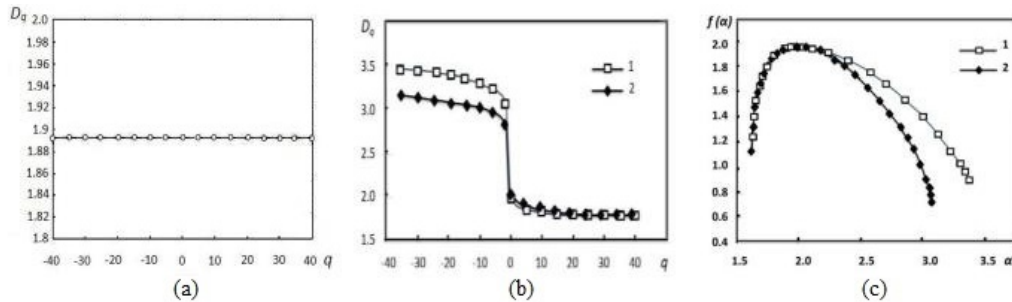


FIG. 4. Comparison of the calculated fractal dimension from the factor q for the Sierpinski carpet model (a) and for the nanocomposite material (b) synthesized by the co-precipitation method with subsequent heat treatment (1) and the gas-flame combustion method of the glycine-nitrate gel precursor (2) with their function of the multifractal spectrum (c)

As can be seen, the resulting fractal dimension of the Sierpinski carpet as a regular monofractal does not depend on q and with sufficient accuracy coincides with the known analytical value $D = \ln 8 / \ln 3 = 1.8928\dots$. At the same time, the obtained spectrum of the generalized fractal dimensions of the synthesized nanocomposite material depends non-linearly on q , indicating the multifractal nature of its structural-phase nonuniformity depending on the synthesis method.

5. Conclusion

Fractal self-organization is a characteristic feature of the nanostructured materials formation with significantly different properties and composition from homogeneous model media for virtually all technologies and methods of synthesis. This is manifested in the invariant metric-statistical self-similarity of multi-scale nanocomposite structures with non-Euclidean (fractional) dependence between the rate of increase in the number of elements under consideration and the increase in the scale of their consideration. The value of the fractal dimension of such structures is potentially related to the resulting material properties. This is especially evident when there is a high content of nanostructured non-autonomous phases in the material, that is, the phases that do not exist thermodynamically in isolation from the macrovolumes of the substance and are formed on their surface or

interfaces under conditions of spatial and mass restrictions. Energy-entropy characteristics and the correlation scale of transfer phenomena in different-sized macro, micro and nanostructural blocks of the material, as well as the boundary tolerance factor can be the key in establishing the relationship between the indicators of structural-phase nonuniformity and the influence of the object's fractal dimensionality on them during the development of new materials with variable physicochemical properties.

Along with *in situ* measurements of fractal dimensions by invasive methods (mercury porosimetry, gas and liquid pycnometry, low-temperature nitrogen adsorption, calorimetry, inversion gas chromatography) and methods of radiation scattering (X-ray, neutron, light), the analysis of electron microscopic images of nanostructured materials based on the transmission and scanning electron microscopy is very common. Since the fractal dimension is an invariant property in the scale transformation, along with the standard technique of the "physical" changing the overall scale of consideration of the object being analyzed, the method of the "digital" zooming of its non-detailed elements (pixel size) forming a comprehensive raster image can be used. The paper proposes the gray-gradient (if necessary expanded to full-color) pixel method of fractal characterization of nanostructured materials from micrographs of their surface chips using high-resolution scanning (raster) electron microscopes without changing the scale of the processed micrograph itself. Compared with the black and white binarization option, the gray gradation improves the quality of multifractal analysis of nanostructured materials and expands its capabilities, in particular, the selection of multi-scale composite inclusions in the structure of the material and nano-objects on transparent or opaque basis. Obvious quality criteria for such digital "pixelation" are the ratio of the physical area of the image being processed to the number of cells used by pixel partitioning, related to the dimensions of the pixel itself, as well as the number of information units used to describe each pixel of the image.

The obtained results of using this method for characterizing the synthesized samples of new nanostructured materials of chemical-catalytic and thermoelectric purposes with a high proportion of non-autonomous phases in comparison with the classic example of Sierpinsky monofractal model of the carpet indicate the multifractal nature of their structural-phase nonuniformity with a whole range of fractal dimensions according to the generalized Rényi equation.

References

- [1] Kohler M., Fritzsche W. *Nanotechnology: An Introduction to Nanostructuring Techniques*. Wiley, John & Sons, Incorporated, 2004, 284 pp.
- [2] Zhabrev V.A., Kalinnikov V.T., Margolin V.I., Nikolaev A.I., Tupik V.A. *Physico-chemical processes of nanoscale objects synthesis*. St. Petersburg: Elmor Publishing House, 2012 (in Russian).
- [3] Ivanov V.K., Kopitsa G.P., Ivanova O.S., Baranchikov A.Ye., Pranzas K., Grigoriev S.V. Complete inheritance of fractal properties during first-order phase transition. *Journal of Physics and Chemistry of Solids*, 2014, **75**(2), P. 296–299.
- [4] Jens Feder. *Fractals*. Plenum Press. New York and London, 1988, 284 pp.
- [5] Mandelbrot B.B. *The fractal geometry of nature*. San Francisco, Freeman, 1982.
- [6] Roldughin V.I. Self-assembly of nanoparticles at interfaces. *Russian Chemical Reviews*, 2004, **73**(2), P. 115–145.
- [7] Krasilin A.A., Almjasheva O.V., Gusarov V.V. Effect of the structure of precursors on the formation of nanotubular magnesium hydrosilicate. *Inorganic Materials*, 2011, **47**(10), P. 1111–1115.
- [8] Ivanov V.K., Kopitsa G.P., Baranchikov A.E., Grigoriev S.V., Runov V.V., Garamus V. Hydrothermal growth of ceria nanoparticles. *Russian Journal of Inorganic Chemistry*, 2009, **54**(12), P. 1939–1943.
- [9] Vasilevskaya A., Almjasheva O.V., Gusarov V.V. Peculiarities of Structural Transformations in Zirconia Nanocrystals. *Journal of Nanoparticle Research*, 2016, **18**(188), P. 1–11.
- [10] Korytkova E.N., Pivovarova L.N., Drosdova I.A., Gusarov V.V. Hydrothermal synthesis of nanotubular Co-Mg hydrosilicates with the chrysotile structure. *Russ. J. Gen. Chem.*, 2017, **77**(10), P. 1669–1676.
- [11] Prigogine I., Defay R. *Chemical thermodynamics*. Longman Green and Co. London-New York - Toronto, 1954.
- [12] Kovalenko A.N., Tugova E.A. Thermodynamics and kinetics of non-autonomous phases formation in nanostructured materials with variable functional properties. *Nanosystems: physics, chemistry, mathematics*, 2018, **9**(5), P. 641–662.
- [13] Emets E.P., Novoselova A.E., Poluektov P.P. In situdetermination of the fractal dimensions of aerosol aggregates. *Physics-Uspexhi* (Advances in Physical Sciences), 1994, **37**(9), P. 881–887.
- [14] Swapna M.S., Sankararaman S. Fractal analysis - a surrogate technique for material characterization. *Nanosystems: physics, chemistry, mathematics*, 2017, **8**(6), P. 809–815.
- [15] Stryapunina K.A., Makarova L.E., Degtyarev A.I., Karavayev D.M., Matyullina E.V., Sirotenko L.D. The multifractal analysis of the composite material on the basis of thermoexpanded graphite. *Izvestia of Samara Scientific Center of the Russian Academy of Sciences*, 2014, **16**(2), P. 552–556.
- [16] Lomanova N.A., Tomkovich M.V., Ugolkov V.L., Volkov M.P., Pleshakov I.V., Panchuk V.V., Semenov V.G. Formation mechanism, thermal and magnetic properties of $(\text{Bi}_{1-x}\text{Sr}_x)_{m+1}\text{Fe}_{m-3}\text{Ti}_3\text{O}_{3(m+1)-\delta}$ ($m=4-7$) ceramics. *Nanosystems: physics, chemistry, mathematics*, 2018, **9**(5), P. 676–687.
- [17] Oksengendler B.L., Ashurov N.R., Maksimov S.E., Uralov I.Z., Karpova O.V. Fractal structures in perovskite-based solar cells. *Nanosystems: physics, chemistry, mathematics*, 2017, **8**(1), P. 92–98.
- [18] Ivanov V.K., Baranov A.N., Oleinikov N.N., Tretyakov Yu.D. Fractal surfaces of ZrO_2 , WO_3 , and CeO_2 powders. *Inorganic Materials*, 2002, **38**(12), P. 1224–1227.

- [19] Ivanov V.K., Baranov A.N., Oleinikov N.N., Tretyakov Yu.D. Synthesis of iron(III) oxide with controlled surface fractality. *Russian Journal of Inorganic Chemistry*, 2002, **47**(12), P. 1769–1772.
- [20] Krivolapova L.I., Kravtsova O.A., Sokolov S.V. Fractal dimension - an estimated quality measure of a surface of metal rolling. *Proceedings of Tomsk State University of Control Systems and Radioelectronics*, 2015, **1**(35), P. 147.
- [21] Schuster H.G. *Deterministic Chaos. An Introduction*. Weinheim, Physik&Verlag, 1984.
- [22] J.Rouquerol, D.Avnir, C.W.Fairbridge et al. Recommendations for the characterisation of porous solids (Technical report). *Pure and Applied Chemistry*, 1994, **66**, P. 1739–1758.
- [23] Ivanov V.K., Polezhaeva O.S., Kopitsa G.P., Baranchikov A.E., Tretyakov Yu.D. Fractal structure of ceria nanopowders. *Inorganic Materials*, 2008, **44**(3), P. 272–277.
- [24] Yashkin S.N., Svetlov A.A. Study of geometrical heterogeneity of surface of carbon adsorbents with inverse gas chromatography. *Russian journal of chemistry and chemical technology*, 2009, **52**(9), P. 144(70-77).
- [25] Ivanov V.K., Oleinikov N.N., Yuri D. Tretyakov Yu.D. Effect of CeO₂ surface fractality on the reaction kinetics of ceria with barium nitrate. *Russian Journal of Inorganic Chemistry*, 2003, **48**(4), P. 455–458.
- [26] Farin D., Avnir D. Thermal analysis and self-similarity law in particle size distribution of powder samples. Part 4. *Thermochimica Acta*, 1993, **220**, P. 191–201.
- [27] Pfeifer P., Avnir D., Farin D. Scaling behavior of surface irregularity in the molecular domain: from absorption studies to fractal catalysis. *J. Stat. Phys.*, 1984, **36**, P. 699–716.
- [28] Schmalzried H. *Chemical kinetics of solids*. Weinheim, VCH, 1995, P. 433.
- [29] Schmidt P.W. *Use of scattering to determine the fractal dimension. Fractal Approach to Heterogeneous Chemistry*. Ed. D. Avnir. N.Y.: John Wiley&Sons, 1989.
- [30] Crowover R.M. *Introduction to Fractals and Chaos*. Published by Jones and Bartlett Publishers, Boston and London, 1995.
- [31] Falconer K. *Fractal Geometry: Mathematical Foundations and Applications*, John Wiley & Sons, New York, 1990.
- [32] Bozhokin S.V., Parshin D.A. *Fractals and multifractals*. Moscow – Izhevsk, Regular and chaotic dynamics, 2001, P. 128.
- [33] Renyi A. On a new axiomatic theory of probability. *Acta Mathematica Hungaria*, 1955, **6**, P. 285–335.
- [34] Takens F. Strange Attractors in Turbulence. *Dynamical Systems and Turbulence. Lecture Notes in Mathematics*. Berlin, Springer-Verlag, 1981, 898, P. 366.
- [35] Zakharov A.I., Zagaynov A.I. Multifractal mathematical modeling of processes of chaotic origin. *Proceedings of the Mozhaisky Military Space Academy*. Mozhaisky MAA, 2015, **648**, P. 241.
- [36] Vstovsky G.V., Kolmakov A.G., Bunin I.Z. *Introduction to Multifractal Parameterization of Material Structures*. Izhevsk. Regular and Chaotic Dynamics, 2001. P. 116.
- [37] URL: <https://www.adobe.com/>.
- [38] URL: <https://www.microsoft.com/>.
- [39] URL: <https://www.mathworks.com/products/matlab.html/>.

Persistent current in a chain of two Holstein–Hubbard rings in the presence of Rashba spin-orbit interaction

A. Chatterjee², M. O. Smolkina¹, I. Y. Popov¹

¹ITMO University, Kronverkskiy, 49, St. Petersburg, 197101, Russia

²University of Hyderabad, Hyderabad-500046, India

acsp@uohyd.ernet.in, vega14@mail.ru, popov1955@gmail.com

DOI 10.17586/2220-8054-2019-10-1-50-62

The persistent current in a chain of two quantum rings threaded by an Aharonov–Bohm flux is studied in the presence of electron-phonon interactions and Rashba spin-orbit coupling. The chain is modeled by the Holstein–Hubbard–Rashba Hamiltonian, the phonon’s degrees of freedom were eliminated by the conventional Lang–Firsov transformation, the effective electronic Hamiltonian was diagonalized by using the Hartree–Fock approximation. The equations for ground state energy, persistent current and Drude weight were also obtained. The persistent current was calculated by differentiating the GS energy. The dependence of ground state energy, persistent current and Drude weight as a functions of flux for different values of Rashba spin-orbit interaction was numerically shown. The effects of Aharonov–Bohm flux, temperature, chemical potential spin-orbit interaction and electron-phonon interaction on the persistent current were also investigated.

Keywords: spin-orbit interaction, persistent current.

Received: 2 January 2019

Revised: 10 February 2019

1. Introduction

A normal metal ring threaded by a magnetic flux can sustain a loss-less current, commonly referred to as the persistent current, because of the quantum mechanical phase coherence effect. This novel effect was first predicted by Buttiker, Imry and Landauer [1] and later quite a few other aspects of this problem were reported by several other investigators [2]. For example, it was proposed that the persistent current would be periodic in flux. Several experiments [3] have established quite unequivocally that persistent current can exist in a semiconductor quantum ring and it is indeed periodic in nature. The Hubbard model turns out to be a suitable model to investigate the persistent current in a quantum ring consisting of discrete sites [4]. The effects of spin-orbit interactions [5] are also found to be pronounced in quantum rings. Recently the effect of electron-phonon interaction on the persistent current in a correlated quantum ring in the presence of Rashba spin-orbit interaction has been studied by Monisha et al. [6] using the one-dimensional Holstein–Hubbard model. Using of quantum rings is rather popular in nanoscience (see, e.g., [7, 8]). The advantage with the Rashba interaction is that it can be manipulated by tuning the external magnetic field and concomitantly the persistent current can be controlled. This is one of the main principles on which spintronics is based.

In the present work, we study the effect of Rashba spin-orbit interaction on persistent current in a chain of two Holstein–Hubbard rings threaded by an Aharonov–Bohm flux. We consider the magnetic flux going through the quantum rings in such a way that the magnetic field is zero at the radii of the rings. It is a quantum mechanical phenomenon which can be observed in small metallic rings whose size is comparable to the electron coherence length. The energy spectrum is periodic in flux and consequently, the persistent current which is the change in ground state energy with respect to the magnetic flux is also periodic in flux.

2. Model of two Holstein–Hubbard rings in the presence of Rashba spin-orbit interaction

The chain of two Holstein–Hubbard rings considered in this work is shown in Fig. 1. Both of the rings consist of discrete lattice sites and the electrons can hop from one site to another.

The Hamiltonian for a chain of two Holstein–Hubbard rings threaded by a magnetic flux is written in the presence of Rashba spin-orbit interaction as:

$$H = H_{el} + H_p + H_{ep} + H_{so} \quad (1)$$

with

$$H_{el} = \varepsilon_0 \sum_i c_i^\dagger c_i + \varepsilon_0 \sum_k c_k^\dagger c_k - t e^{\gamma\theta} \sum_{\langle i,j \rangle} (c_i^\dagger c_j + h.c.) - \frac{t}{2} e^{\gamma\theta} \sum_{\langle k,l \rangle} (c_k^\dagger c_l + h.c.) + U \sum_i n_{i\uparrow} n_{i\downarrow} + U \sum_k n_{k\uparrow} n_{k\downarrow}, \quad (2)$$

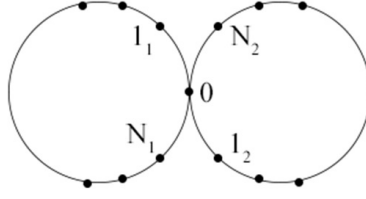


FIG. 1. Chain of two Holstein–Hubbard rings. The intersection point is 0, points 1_1 , N_1 , 1_2 , N_2 are its nearest neighbors

$$H_p = \hbar\omega_0 \sum_i \left(b_i^\dagger b_i + \frac{1}{2} \right) + \hbar\omega_0 \sum_k \left(b_k^\dagger b_k + \frac{1}{2} \right), \quad (3)$$

$$H_{ep} = g_1 \sum_i n_i (b_i + b_i^\dagger) + g_1 \sum_k n_k (b_k + b_k^\dagger) + g_2 \sum_{\langle i,j \rangle} n_i (b_j + b_j^\dagger) + \frac{g_2}{2} \sum_{\langle k,l \rangle} n_k (b_l + b_l^\dagger), \quad (4)$$

$$H_{so} = -t \sum_{\langle i,j \rangle} (c_i^\dagger t_{so} e^{\gamma\theta} c_j + h.c.) - \frac{t}{2} \sum_{\langle k,l \rangle} (c_k^\dagger t_{so} e^{\gamma\theta} c_l + h.c.), \quad (5)$$

where $\langle i, j \rangle$ is any pair of two nearest neighbors on the ring, except at the point of intersection and its nearest neighbors. Pairs $\langle k, l \rangle$ include the point of intersection and its nearest neighbors. H_{el} , given by Eq. (2), is the electronic Hamiltonian which consists of six terms. The first two terms stand for the site energies of the two rings, ε_0 referring to the on-site energy, $c_i = \begin{pmatrix} c_{i\uparrow} \\ c_{i\downarrow} \end{pmatrix}$, $c_{i\sigma}^\dagger (c_{i\sigma})$ denoting the creation (annihilation) operator for an electron at site i with spin σ , i taking values $1, 2, 3, 4, \dots, N$, where N is the total number of sites in each ring except the point of intersection and its nearest neighbors, k is the number of point of intersection and its nearest neighbors (points $0, 1_1, 1_2, N_1, N_2$ on Fig. 1). Next two terms describe the kinetic energies, t being the hopping integral and $\theta = (2\pi\Phi/n)$ the Aharonov–Bohm phase arising from the quantized magnetic flux $\Phi = m\Phi_0$ where m is an integer and $\Phi_0 = hc/e$ is the elementary flux quantum. The last two terms represent the onsite Coulomb repulsion with U measuring the strength of the repulsion and $n_{i\sigma} = c_{i\sigma}^\dagger c_{i\sigma}$ refers to the operator corresponding to the electron number at site i with spin σ . H_p , given by Eq. (3), is the sum of the Hamiltonians for non-interacting phonons in the two rings, $b_i^\dagger (b_i)$ being the phonon creation (annihilation) operator at site i and ω_0 the phonon frequency which is assumed to be dispersionless. H_{ep} , given by Eq. (4), describes the on-site and nearest-neighbor electron-phonon interactions with g_1, g_2 denoting the corresponding coupling strengths. We assume that g_2 is smaller than g_1 by an order of magnitude or so. Finally, Eq. (5) represents the Rashba spin-orbit interaction with t_{so} as the spin-orbit coupling constant given by: $t_{so} = i\alpha(\sigma_x \cos \varphi_{ij} + \sigma_y \sin \varphi_{ij})$ where σ_m is the m -th component of the Pauli matrix $\boldsymbol{\sigma}$, $\varphi_{ij} = (\varphi_i + \varphi_j)/2$ with $\varphi_i = 2\pi(i-1)/N$, i being the site index along the azimuthal direction of the ring.

3. Analytical results

To eliminate the phonons we carry out the celebrated Lang–Firsov transformation [7,9] on the Hamiltonian (1) with the generator:

$$R = \frac{1}{\hbar\omega_0} \left(g_1 \sum_{i\sigma} n_{i\sigma} (b_i^\dagger - b_i) + g_1 \sum_{k\sigma} n_{k\sigma} (b_k^\dagger - b_k) + g_2 \sum_{\langle i,j \rangle\sigma} n_{i\sigma} (b_j^\dagger - b_j) + \frac{g_2}{2} \sum_{\langle k,l \rangle\sigma} n_{k\sigma} (b_l^\dagger - b_l) \right). \quad (6)$$

The transformed Hamiltonian is given by:

$$\begin{aligned}
\tilde{H} &= e^R H e^{-R} = H + [R, H] + \frac{1}{2!}[R, [R, H]] + \dots = \\
& -\frac{1}{\hbar\omega_0}(g_1^2 + z g_2^2) \sum_{i\sigma} n_{i\sigma} - t e^{i\theta} \sum_{\langle i,j \rangle \sigma} e^{(Y_i - Y_j)} c_{i\sigma}^+ c_{j\sigma} - \iota e^{i\theta} \sum_{\langle i,j \rangle \sigma} \begin{bmatrix} 0 & P \\ Q & 0 \end{bmatrix} e^{(Y_i - Y_j)} c_{i\sigma}^+ c_{j\sigma} + \\
& + (U - \frac{2}{\hbar\omega_0}(g_1^2 + z g_2^2)) \sum_i n_{i\uparrow} n_{i\downarrow} - \frac{g_2^2}{\hbar\omega_0} \sum_{i\Delta\sigma\sigma'} n_{i\sigma} n_{i+\Delta\sigma'} - \frac{2}{\hbar\omega_0} g_2 g_1 \sum_{\langle i,j \rangle \sigma\sigma'} n_{i\sigma} n_{j\sigma'} + \hbar\omega_0 \sum_i \left(b_i^+ b_i + \frac{1}{2} \right) - \\
& - \frac{1}{\hbar\omega_0} \sum_{k\sigma} (g_1^2 + \frac{z_{k\sigma}}{4} g_2^2) n_{k\sigma} - \frac{t}{2} e^{i\theta} \sum_{\langle k,l \rangle \sigma} e^{(Y_k - Y_l)} c_{k\sigma}^+ c_{l\sigma} - \frac{\iota}{2} e^{i\theta} \sum_{\langle k,l \rangle} \begin{bmatrix} 0 & P \\ Q & 0 \end{bmatrix} e^{(Y_k - Y_l)} c_k^+ c_l + \\
& + \sum_k (U - \frac{2}{\hbar\omega_0}(g_1^2 + \frac{z_1}{4} g_2^2)) n_{k\uparrow} n_{k\downarrow} - \frac{g_2^2}{2\hbar\omega_0} \sum_{\langle k,l \rangle \sigma\sigma', k,l \neq 0} n_{k\sigma} n_{l\sigma'} + \frac{1}{\hbar\omega_0} g_2 g_1 \sum_{\langle k,l \rangle \sigma\sigma'} n_{k\sigma} n_{l\sigma'} + \\
& + \hbar\omega_0 \sum_k \left(b_k^+ b_k + \frac{1}{2} \right).
\end{aligned} \tag{7}$$

The effective electronic Hamiltonian can be obtained by taking the zero-phonon averaging:

$$H_{eff} = \langle 0 | e^R H e^{-R} | 0 \rangle = \langle 0 | \tilde{H} | 0 \rangle. \tag{8}$$

It is easy to see that $[Y_i, Y_j] = 0$, $[Y_k, Y_l] = 0$ and

$$\langle 0 | e^{Y_i - Y_j} | 0 \rangle = e^{-\left(\frac{1}{\hbar\omega_0}\right)^2 [(g_1 - g_2)^2 + (z-1)g_2^2]}, \quad \langle 0 | e^{Y_k - Y_l} | 0 \rangle = e^{-\left(\frac{1}{\hbar\omega_0}\right)^2 [(g_1 - g_2)^2 + (z_k - 1)g_2^2]}.$$

Using these results, we can write the effective electronic Hamiltonian in a simplified form as:

$$\begin{aligned}
H_{eff} &= \epsilon_0^e \sum_{i\sigma} n_{i\sigma} - t_e e^{i\theta} \sum_{\langle i,j \rangle \sigma} c_{i\sigma}^+ c_{j\sigma} - t_{SO-e}^{ij} e^{i\theta} \sum_{\langle i,j \rangle \sigma} c_{i\sigma}^+ c_{j\sigma} + U_e \sum_i n_{i\uparrow} n_{i\downarrow} + \\
& + \sum_{k\sigma} \epsilon_{0k}^e n_{k\sigma} - \frac{e^{i\theta}}{2} \sum_{\langle k,l \rangle \sigma} t_{ek} c_{k\sigma}^+ c_{l\sigma} - \frac{e^{i\theta}}{2} \sum_{\langle k,l \rangle \sigma} t_{SO-ek}^{kl} c_{k\sigma}^+ c_{l\sigma} + \sum_k U_{ek} n_{k\uparrow} n_{k\downarrow},
\end{aligned}$$

where $\epsilon_0^e = -\frac{(g_1^2 + z g_2^2)}{\hbar\omega_0}$, z is the number of nearest neighbors (for all the sites except the point of intersection and its nearest neighbors), $\epsilon_{0k}^e = -\frac{(g_1^2 + \frac{z_k}{4} g_2^2)}{\hbar\omega_0}$, z_k - number of nearest neighbors (for the point of intersection and its nearest neighbors),

$$t_e = t e^{-\left(\frac{1}{\hbar\omega_0}\right)^2 [(g_1 - g_2)^2 + (z-1)g_2^2]}, \quad t_{ek} = t e^{-\left(\frac{1}{\hbar\omega_0}\right)^2 [(g_1 - g_2)^2 + (z_k - 1)g_2^2]},$$

$$t_{SO-e}^{ij} = \iota A e^{-\left(\frac{1}{\hbar\omega_0}\right)^2 [(g_1 - g_2)^2 + (z-1)g_2^2]}, \quad t_{SO-ek}^{ij} = \iota A_k e^{-\left(\frac{1}{\hbar\omega_0}\right)^2 [(g_1 - g_2)^2 + (z_k - 1)g_2^2]},$$

$$A = \begin{bmatrix} 0 & P \\ Q & 0 \end{bmatrix} = \begin{bmatrix} 0 & \alpha e^{-\iota\phi_{ij}} \\ \alpha e^{\iota\phi_{ij}} & 0 \end{bmatrix}, \quad A_k = \begin{bmatrix} 0 & P \\ Q & 0 \end{bmatrix} = \begin{bmatrix} 0 & \alpha e^{-\iota\phi_{kl}} \\ \alpha e^{\iota\phi_{kl}} & 0 \end{bmatrix},$$

$$U_e = U - \frac{2}{\hbar\omega_0} (g_1^2 + z g_2^2), \quad U_{ek} = U - \frac{2}{\hbar\omega_0} \left(g_1^2 + \frac{z_k}{4} g_2^2 \right).$$

Next, we perform the unitary transformation on the effective Hamiltonian H_{eff} with the matrix:

$$U_m = \frac{1}{\sqrt{2}} \begin{bmatrix} 1 & -1 \\ e^{\frac{2\pi\iota}{N}(m-\frac{1}{2})} & e^{\frac{2\pi\iota}{N}(m-\frac{1}{2})} \end{bmatrix}.$$

This transformation helps us to eliminate the index dependence of the spin-orbit interaction coefficients t_{SO-e}^{ij} , t_{SO-ek}^{ij} and transforms the old operators c_i, c_k to a new set of operators $\tilde{c}_i = U_i^+ c_i$, $\tilde{c}_k = U_k^+ c_k$. The transformed effective Hamiltonian is given by:

$$\begin{aligned}
 H_e = & \epsilon_0^e \sum_{i\sigma} \tilde{n}_{i\sigma} - \frac{1}{2} e^{i\theta} \sum_{\langle i,j \rangle \sigma} c_{i\sigma}^+ [t_e + i\alpha_e] B c_{j\sigma} + U_e \sum_i \tilde{n}_{i\uparrow} \tilde{n}_{i\downarrow} + \sum_{k\sigma} \epsilon_{0k}^e \tilde{n}_{k\sigma} - \frac{1}{4} e^{i\theta} \sum_{\langle k,l \rangle \sigma} c_{k\sigma}^+ [t_{ek} + i\alpha_{ek}] B c_{l\sigma} + \\
 & + \sum_k U_{ek} \tilde{n}_{k\uparrow} \tilde{n}_{k\downarrow} + \frac{\tilde{n}_i \left[c_{i\uparrow}^\dagger \tilde{c}_{i\downarrow} + c_{i\downarrow}^\dagger \tilde{c}_{i\uparrow} \right]}{4} - \frac{\left[c_{i\uparrow}^\dagger \tilde{c}_{i\downarrow} + c_{i\downarrow}^\dagger \tilde{c}_{i\uparrow} \right] \tilde{n}_i}{4} + \frac{\tilde{n}_k \left[c_{k\uparrow}^\dagger \tilde{c}_{k\downarrow} + c_{k\downarrow}^\dagger \tilde{c}_{k\uparrow} \right]}{4} - \frac{\left[c_{k\uparrow}^\dagger \tilde{c}_{k\downarrow} + c_{k\downarrow}^\dagger \tilde{c}_{k\uparrow} \right] \tilde{n}_k}{4},
 \end{aligned}$$

where

$$\begin{aligned}
 \alpha_e = & \alpha e^{-\left(\frac{1}{\hbar\omega_0}\right)^2 [(g_1 - g_2)^2 + (z-1)g_2^2]}, \quad \alpha_{ek} = \alpha e^{-\left(\frac{1}{\hbar\omega_0}\right)^2 [(g_1 - g_2)^2 + (z_k - 1)g_2^2]}, \\
 B = & \begin{bmatrix} 1 + e^{\frac{2\pi i}{N}} & -1 + e^{\frac{2\pi i}{N}} \\ -1 + e^{\frac{2\pi i}{N}} & 1 + e^{\frac{2\pi i}{N}} \end{bmatrix}.
 \end{aligned}$$

Next, we use the mean-field approximation to linearize the quadratic terms in H_e (see equation (9)). In 1D systems, for a half filled band the electron-phonon interaction can cause the distortion of the lattice leading to dimerization with the unit cell getting doubled.

To proceed further, we divide the lattice into two sublattices: even numbered sites-A, and odd numbered sites-B. Using some algebraic simplifications following Cabib and Callen [10] we obtain:

$$\begin{aligned}
 H_e^m = & \sum_{i=1}^N \tilde{c}_i^+ [C + (-1)^i D] \tilde{c}_i - e^{i(\theta + \frac{\pi}{N})} \sum_{\langle ij \rangle \sigma, i, j \neq 0} \tilde{c}_{i\sigma}^+ [t_e E + i\alpha_e F] \tilde{c}_{j\sigma} + K_1 + \\
 & \sum_{k=0}^N \tilde{c}_k^+ [C_k + (-1)^k D_k] \tilde{c}_k - e^{i(\theta + \frac{\pi}{N})} \sum_{\langle kl \rangle \sigma} \tilde{c}_{k\sigma}^+ [t_{ek} E + i\alpha_{ek} F] \tilde{c}_{l\sigma} + K_2.
 \end{aligned}$$

where

$$\begin{aligned}
 C = & \begin{bmatrix} \varepsilon_{AB\uparrow}^+ & 0 \\ 0 & \varepsilon_{AB\downarrow}^+ \end{bmatrix}, \quad C_k = \begin{bmatrix} \varepsilon_{AB\uparrow k}^+ & 0 \\ 0 & \varepsilon_{AB\downarrow k}^+ \end{bmatrix}, \\
 \varepsilon_{AB\uparrow}^+ = & \frac{\varepsilon_{A\uparrow} + \varepsilon_{B\uparrow}}{2}, \quad \varepsilon_{AB\downarrow}^+ = \frac{\varepsilon_{A\downarrow} + \varepsilon_{B\downarrow}}{2}, \quad \varepsilon_{AB\uparrow k}^+ = \frac{\varepsilon_{A\uparrow k} + \varepsilon_{B\uparrow k}}{2}, \quad \varepsilon_{AB\downarrow k}^+ = \frac{\varepsilon_{A\downarrow k} + \varepsilon_{B\downarrow k}}{2}, \\
 D = & \begin{bmatrix} \varepsilon_{AB\uparrow}^- & 0 \\ 0 & \varepsilon_{AB\downarrow}^- \end{bmatrix}, \quad D_k = \begin{bmatrix} \varepsilon_{AB\uparrow k}^- & 0 \\ 0 & \varepsilon_{AB\downarrow k}^- \end{bmatrix}, \\
 \varepsilon_{AB\uparrow}^- = & \frac{\varepsilon_{A\uparrow} - \varepsilon_{B\uparrow}}{2}, \quad \varepsilon_{AB\downarrow}^- = \frac{\varepsilon_{A\downarrow} - \varepsilon_{B\downarrow}}{2}, \quad \varepsilon_{AB\uparrow k}^- = \frac{\varepsilon_{A\uparrow k} - \varepsilon_{B\uparrow k}}{2}, \quad \varepsilon_{AB\downarrow k}^- = \frac{\varepsilon_{A\downarrow k} - \varepsilon_{B\downarrow k}}{2}, \\
 \varepsilon_{A\uparrow} = & \varepsilon_0^e + \frac{U_e(c-s)}{2}, \quad \varepsilon_{B\uparrow} = \varepsilon_0^e - \frac{U_e(c-s)}{2}, \quad \varepsilon_{A\downarrow} = \varepsilon_0^e + \frac{U_e(c+s)}{2}, \quad \varepsilon_{B\downarrow} = \varepsilon_0^e - \frac{U_e(c+s)}{2}, \\
 \varepsilon_{A\uparrow k} = & \varepsilon_{0k}^e + \frac{U_{ek}(c-s)}{2}, \quad \varepsilon_{B\uparrow k} = \varepsilon_{0k}^e - \frac{U_{ek}(c-s)}{2}, \quad \varepsilon_{A\downarrow k} = \varepsilon_{0k}^e + \frac{U_{ek}(c+s)}{2}, \quad \varepsilon_{B\downarrow k} = \varepsilon_{0k}^e - \frac{U_{ek}(c+s)}{2}, \\
 E = & \begin{bmatrix} \cos\left(\frac{\pi}{N}\right) & \iota \sin\left(\frac{\pi}{N}\right) \\ \iota \sin\left(\frac{\pi}{N}\right) & \cos\left(\frac{\pi}{N}\right) \end{bmatrix}, \quad F = \begin{bmatrix} \cos\left(\frac{\pi}{N}\right) & \iota \sin\left(\frac{\pi}{N}\right) \\ -\iota \sin\left(\frac{\pi}{N}\right) & -\cos\left(\frac{\pi}{N}\right) \end{bmatrix} \\
 K_1 = & \frac{NU_e(n^2 - c^2 + s^2)}{4}, \quad K_2 = \frac{NU_{ek}(n^2 - c^2 + s^2)}{4}, \\
 n = & \frac{[(n_{A\uparrow} + n_{A\downarrow}) + (n_{B\uparrow} + n_{B\downarrow})]}{2}, \\
 c = & \frac{[(n_{A\uparrow} + n_{A\downarrow}) - (n_{B\uparrow} + n_{B\downarrow})]}{2}, \\
 s = & \frac{[(n_{A\uparrow} - n_{A\downarrow}) - (n_{B\uparrow} - n_{B\downarrow})]}{2},
 \end{aligned}$$

where n is the electron concentration, c is the charge density wave order parameter, and s is the spin density wave order parameter. Performing the Fourier transformation:

$$\tilde{c}_{m\sigma} = \frac{1}{\sqrt{N}} \sum_{\xi} e^{i\xi ma} \tilde{c}_{\xi\sigma},$$

where a is the lattice spacing and making the redefinitions: $\tilde{c}_{i\sigma}(\tilde{c}_{i\sigma}^+)$ as $c_{i\sigma}(c_{i\sigma}^+)$ and $\tilde{c}_{k\sigma}(\tilde{c}_{k\sigma}^+)$ as $c_{k\sigma}(c_{k\sigma}^+)$ and using the following identities:

$$\sum_{m=1}^{\frac{N}{2}} c_{2m}^+ c_{2m} = \frac{1}{2} \sum_{\xi} c_{\xi}^+ c_{\xi} + \frac{1}{2} \sum_{\xi} c_{\xi}^+ c_{\xi+\frac{\pi}{a}}, \text{ for even sites,}$$

$$\sum_{m=1}^{\frac{N}{2}} c_{2m-1}^+ c_{2m-1} = \frac{1}{2} \sum_{\xi} c_{\xi}^+ c_{\xi} - \frac{1}{2} \sum_{\xi} c_{\xi}^+ c_{\xi+\frac{\pi}{a}}, \text{ for odd sites, we can separate the Hamiltonian into even and}$$

odd sited terms to get the effective mean-field Hamiltonian as:

$$H_e^M = 2 \sum_{\xi=-\pi/a, \xi \neq 0}^{\pi/a} c_{\xi}^+ G c_{\xi} + 2 \sum_{\xi=-\pi/a, \xi \neq 0, \xi+(\pi/a) \neq 0}^{\pi/a} c_{\xi}^+ D c_{\xi+(\pi/a)} + c_0^+ G_0 c_0 + c_0^+ D_0 c_{\pi/a} + 2K_1 + K_0, \quad (9)$$

where

$$G = \begin{bmatrix} \varepsilon_{AB\uparrow}^+ + \alpha_{11} & \alpha_{12} \\ \alpha_{21} & \varepsilon_{AB\downarrow}^+ + \alpha_{22} \end{bmatrix}, \quad D = \begin{bmatrix} \varepsilon_{AB\uparrow}^- & 0 \\ 0 & \varepsilon_{AB\downarrow}^- \end{bmatrix},$$

$$G_0 = \begin{bmatrix} \varepsilon_{AB\uparrow}^- - \varepsilon_{AB\uparrow}^+ + \frac{1}{2}[\varepsilon_{AB\uparrow 0}^+ - \varepsilon_{AB\uparrow 0}^-] + \alpha_{11,0} & \alpha_{12,0} \\ \alpha_{21,0} & \varepsilon_{AB\downarrow}^- - \varepsilon_{AB\downarrow}^+ + \frac{1}{2}[\varepsilon_{AB\downarrow 0}^+ - \varepsilon_{AB\downarrow 0}^-] + \alpha_{22,0} \end{bmatrix},$$

$$D_0 = \begin{bmatrix} \varepsilon_{AB\uparrow}^+ - \varepsilon_{AB\uparrow}^- - \frac{1}{2}[\varepsilon_{AB\uparrow 0}^+ - \varepsilon_{AB\uparrow 0}^-] & 0 \\ 0 & \varepsilon_{AB\downarrow}^+ - \varepsilon_{AB\downarrow}^- - \frac{1}{2}[\varepsilon_{AB\downarrow 0}^+ - \varepsilon_{AB\downarrow 0}^-] \end{bmatrix},$$

$$\begin{aligned} \alpha_{11} &= -2t_e \cos(\pi/N) \cos(\xi a + \theta + \pi/N) + 2\alpha_e \cos(\pi/N) \sin(\xi a + \theta + \pi/N), \\ \alpha_{12} &= 2t_e \sin(\pi/N) \sin(\xi a + \theta + \pi/N) + 2\alpha_e \sin(\pi/N) \cos(\xi a + \theta + \pi/N), \\ \alpha_{21} &= 2t_e \sin(\pi/N) \sin(\xi a + \theta + \pi/N) - 2\alpha_e \sin(\pi/N) \cos(\xi a + \theta + \pi/N), \\ \alpha_{22} &= -2t_e \cos(\pi/N) \cos(\xi a + \theta + \pi/N) - 2\alpha_e \cos(\pi/N) \sin(\xi a + \theta + \pi/N), \end{aligned}$$

$$\begin{aligned} \alpha_{11,0} &= 2[2t_e - t_{e0}] \cos(\pi/N) \cos(\theta + \pi/N) - 2[2\alpha_e + \alpha_{e0}] \cos(\pi/N) \sin(\theta + \pi/N), \\ \alpha_{12,0} &= 2[-2t_e + t_{e0}] \sin(\pi/N) \sin(\theta + \pi/N) - 2[2\alpha_e - \alpha_{e0}] \sin(\pi/N) \cos(\theta + \pi/N), \\ \alpha_{21,0} &= 2[-2t_e + t_{e0}] \sin(\pi/N) \sin(\theta + \pi/N) - 2[-2\alpha_e + \alpha_{e0}] \sin(\pi/N) \cos(\theta + \pi/N), \\ \alpha_{22,0} &= 2[2t_e - t_{e0}] \cos(\pi/N) \cos(\theta + \pi/N) + 2[+2\alpha_e + \alpha_{e0}] \cos(\pi/N) \sin(\theta + \pi/N). \end{aligned}$$

It is convenient to work in the reduced zone scheme and so we choose the domain of ξ as: $-\pi/2a$. The matrix elements then satisfy the equation: $\alpha_{ij}(\xi + \pi/a) = -\alpha_{ij}(\xi)$. The effective Hamiltonian is finally given in the mean-field approximation by:

$$H_e^M = 2 \sum_{\xi=0}^{\pi} (c_{k\uparrow}^+ c_{k\downarrow}^+ c_{k+\pi,\uparrow}^+ c_{k+\pi,\downarrow}^+) W \begin{pmatrix} c_{k\uparrow} \\ c_{k\downarrow} \\ c_{k+\pi,\uparrow} \\ c_{k+\pi,\downarrow} \end{pmatrix} + (c_0^+ c_0^+ c_{\pi,\uparrow}^+ c_{\pi,\downarrow}^+) W_0 \begin{pmatrix} c_{0\uparrow} \\ c_{0\downarrow} \\ c_{\pi,\uparrow} \\ c_{\pi,\downarrow} \end{pmatrix}, \quad (10)$$

where

$$W = \begin{bmatrix} \varepsilon_{AB\uparrow}^+ + \alpha_{11} & \alpha_{12} & \varepsilon_{AB\uparrow}^- & 0 \\ \alpha_{21} & \varepsilon_{AB\downarrow}^+ + \alpha_{22} & 0 & \varepsilon_{AB\downarrow}^- \\ \varepsilon_{AB\uparrow}^- & 0 & \varepsilon_{AB\uparrow}^+ - \alpha_{11} & -\alpha_{12} \\ 0 & \varepsilon_{AB\downarrow}^- & -\alpha_{21} & \varepsilon_{AB\downarrow}^+ - \alpha_{22} \end{bmatrix},$$

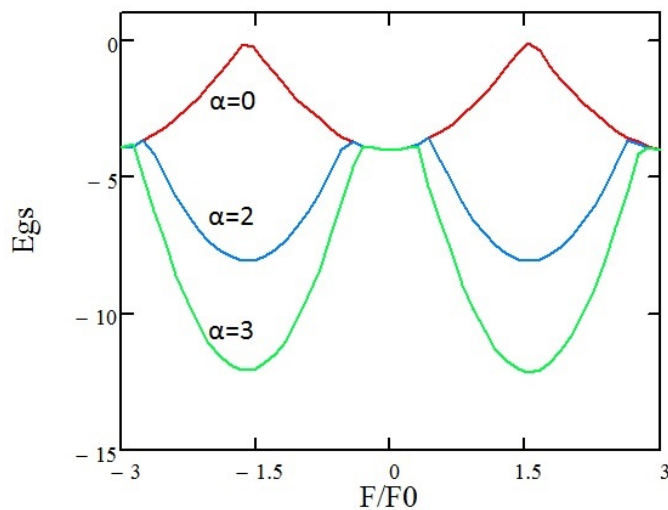


FIG. 2. The ground state energy E_{GS} as a function of the flux Φ for different α

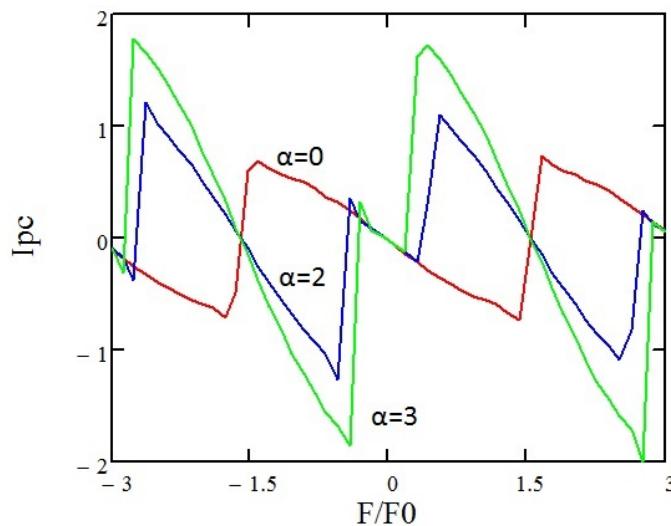


FIG. 3. The persistent current I_{pc} as a function of the flux Φ for different α

electrons experience a larger onsite repulsion and find it more difficult to hop from one site to another and this reduces the persistent current.

Next, we explore the effects of on-site electron-phonon interaction. We set $t = 1$, $K_B T = 0.1$, $\alpha = 0$, $U = g_2 = 0$ and measure the persistent current (see Fig. 8) for different values of g_1 ($g_1 = 0.1$, $g_1 = 0.5$, $g_1 = 0.9$). The function for $g_1 = 0$ is similar to function $g_1 = 0.1$ with the difference that could be neglected. It is evident that persistent current decreases when g_1 increases. The increase of g_1 leads to deepening of the self-trapping polarization potential causing localization which will inhibit conduction.

The variation of persistent current for different values of g_1 with $\alpha = 0$, $\alpha = 2$ on Fig. 9 shows the effects of g_1 on persistent current with and without Rashba spin-orbit interaction. When there is no Rashba spin-orbit interaction, the I_{pc} decreases as g_1 increases. The gradient of the curve vanishes monotonically. When there is a Rashba spin-orbit interaction ($\alpha = 2$) there seem to exist a critical value g_{1c} . The I_{pc} decreases when $g_1 > g_{1c}$ increases.

Next, to study the NN electron-phonon interaction, we set $t = 1$, $K_B T = 0.1$, $\alpha = 0$, $U = g_1 = 0$ and measure the persistent current (see Fig. 10) for different values of g_2 ($g_2 = 0.1$, $g_2 = 0.3$, $g_2 = 0.6$). The function of I_{pc} for $g_2 = 0$ is similar to function $g_2 = 0.1$ with the difference that could be neglected. The behavior of g_2 is similar for that of g_1 but the effect of g_2 on persistent current is stronger. The periodicity of I_{pc} decreases when g_2 increases.

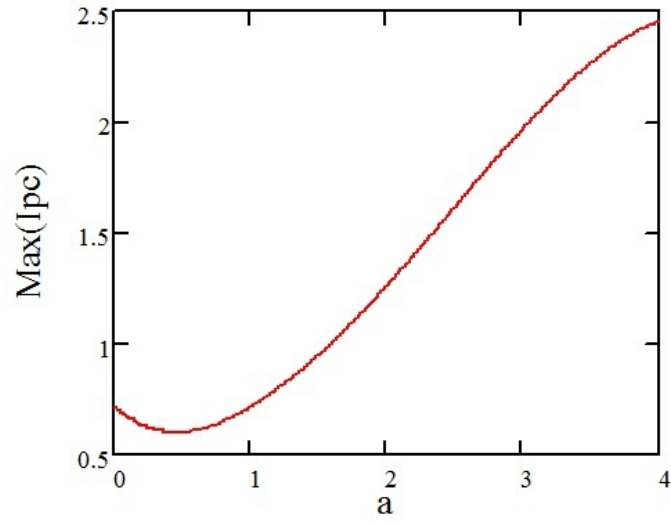


FIG. 4. Variation of I_{pc} as a function of α

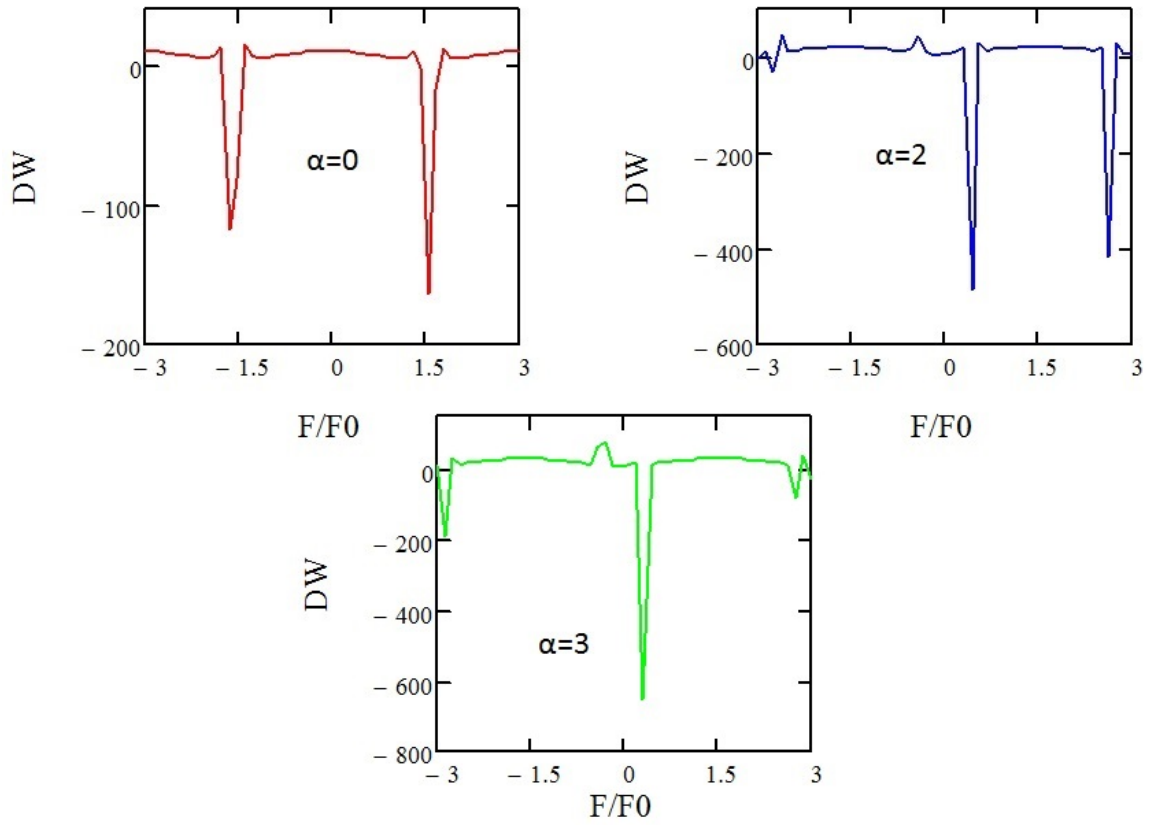
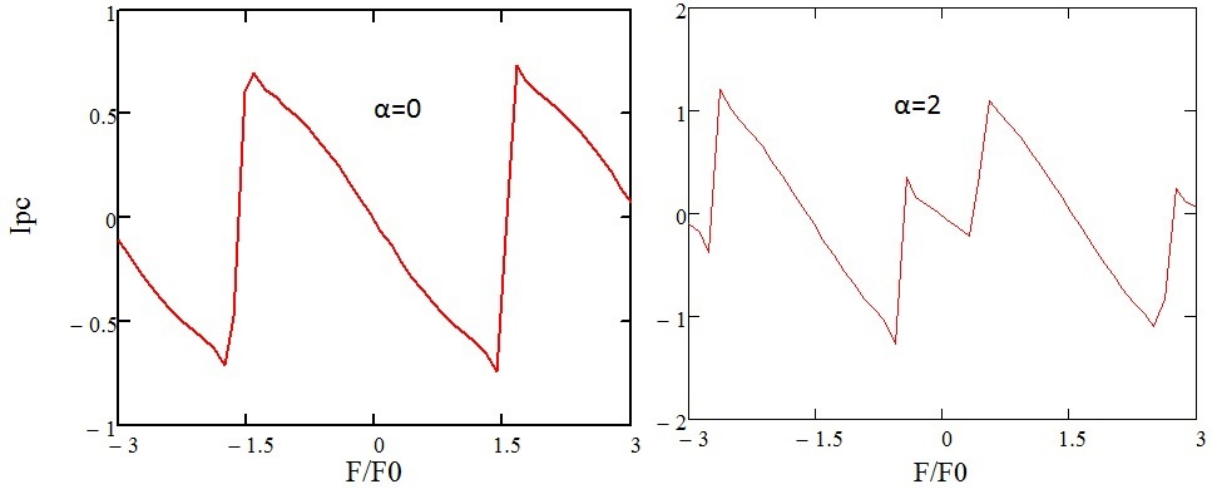
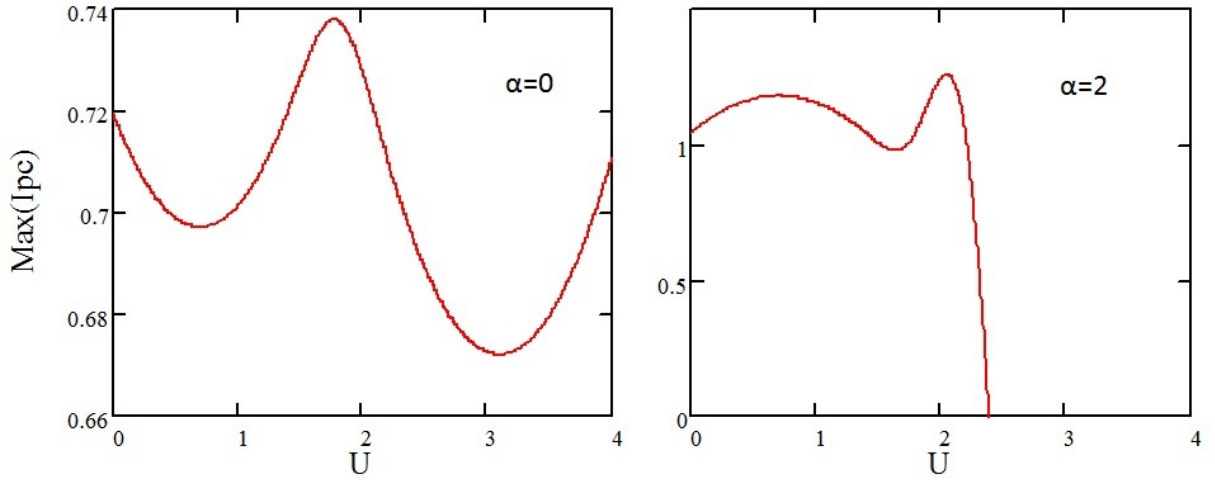
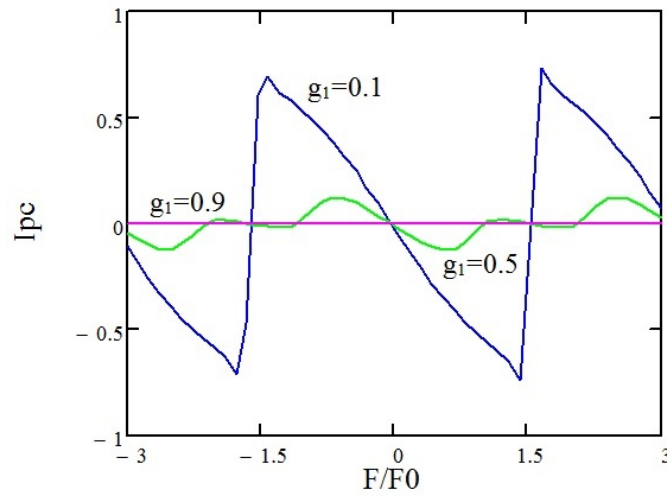
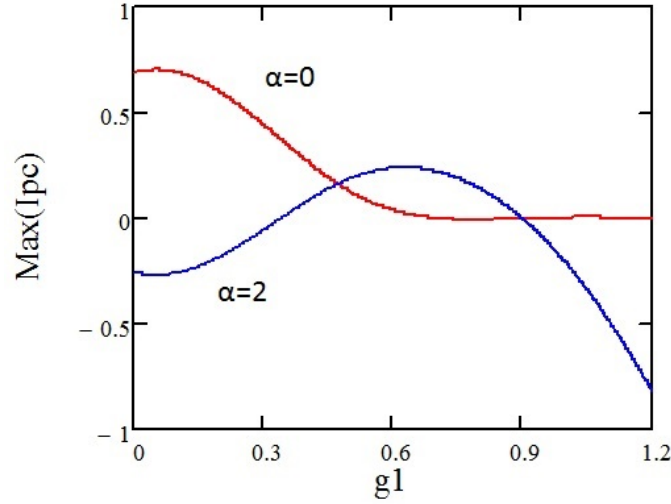
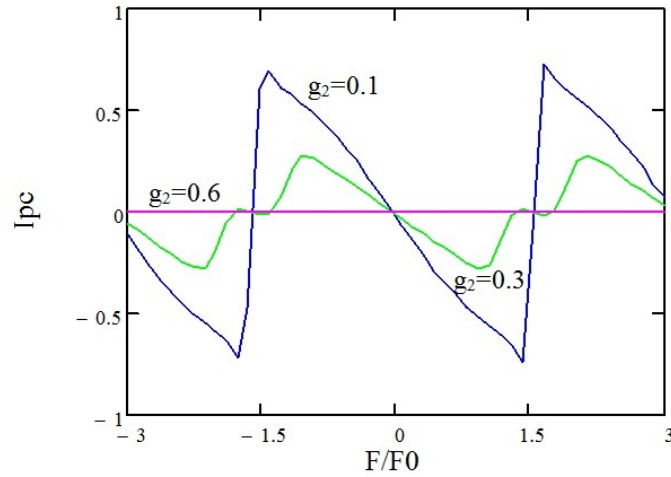


FIG. 5. The Drude weight as a function of flux Φ for different α

FIG. 6. Persistent current I_{pc} for different values of U with $\alpha = 0, 2$ FIG. 7. Variation of persistent current I_{pc} for different values of U with $\alpha = 0, 2$ FIG. 8. Persistent current I_{pc} for different values of g_1 with $\alpha = 0$


 FIG. 9. Variation of persistent current I_{pc} for different values of g_1 with $\alpha = 0$, $\alpha = 2$

 FIG. 10. Persistent current I_{pc} for different values of g_2 with $\alpha = 0$

In Fig. 11 we show the dependence of persistent current I_{pc} on g_2 with $\alpha = 2$, $g_1 = 0.9$ in the presence of on-site electron-phonon interaction. The periodicity of I_{pc} also decreases.

The next important step is to study the effects of temperature on persistent current. We set $t = 1$, $\alpha = 0$, $U = 0$, $g_1 = g_2 = 0$ and measure the persistent current (see Fig. 12) for different values of $K_B T$ ($K_B T = 0.1$, $K_B T = 0.24$, $g_2 = 0.46$, $K_B T = 0.71$) and for $\alpha = 2$ (see Fig. 13).

Both Fig. 12,13 show that persistent current decreases as temperature increases. According the Fig. 14, there appears to exist a critical value $(k_B T)_c$, and when $k_B T > (k_B T)_c$, the persistent current decreases.

In the presence of Rasba spin-orbit interaction we plot the variation of persistent current I_{pc} for different values of $k_B T$ with $\alpha = 2$, $g_1 = 0.5$ and compare it with the variation for $\alpha = 2$, $g_1 = 0$. The persistent current also decreases when temperature increases (Fig. 15).

Finally, we will study the effect of chemical potential on persistent current. On Fig. 16 the dependence of persistent current on Φ for different values of chemical potential μ is shown. We set $t = 1$, $K_B T = 0.1$, $\alpha = 0$, $U = 0$, $g_1 = g_2 = 0$ and measure the persistent current for different values of μ ($\mu = 0$, $\mu = 0.01$, $\mu = 0.03$, $\mu = 0.05$) and $\alpha = 2$. One can see that the resulted figures are quite similar. So the changes of magnitude and phase of persistent current with μ are small. This result is different from what is presented in [6] for similar quantum ring.

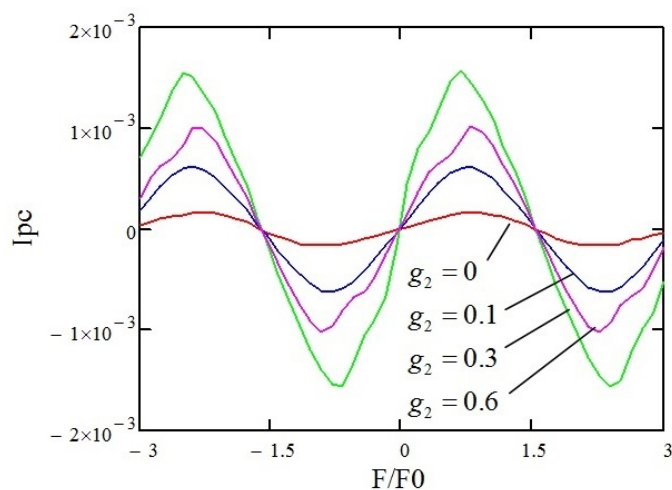


FIG. 11. Persistent current I_{pc} for different values of g_2 with $\alpha = 2, g_1 = 0.9$

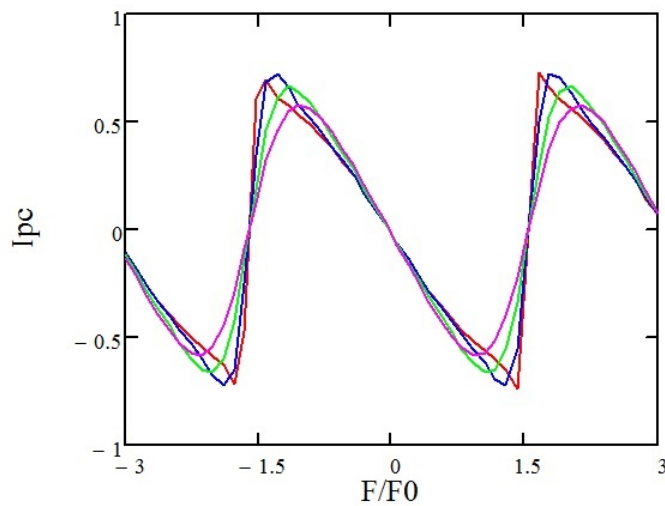


FIG. 12. Persistent current I_{pc} for different values of $k_B T$ with $\alpha = 0$

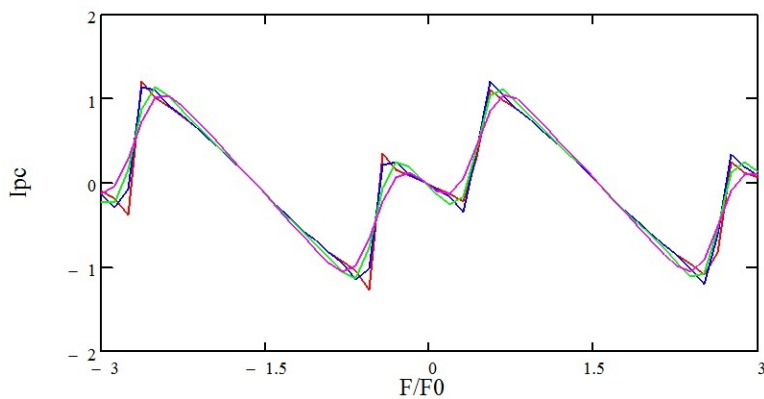


FIG. 13. Persistent current I_{pc} for different values of $k_B T$ with $\alpha = 2$

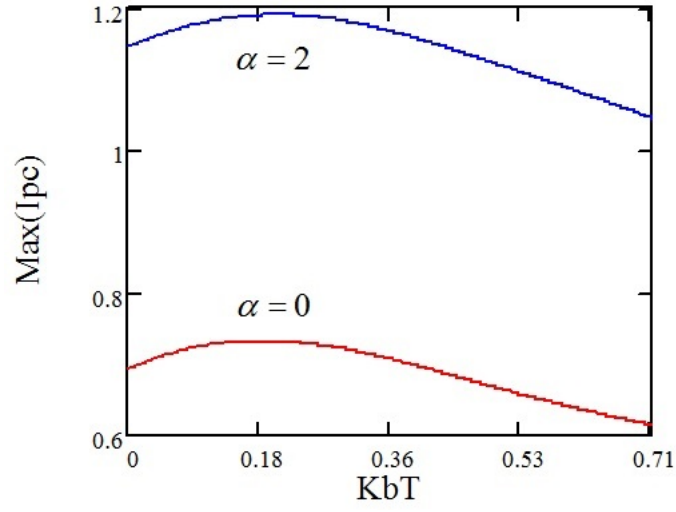


FIG. 14. Variation of persistent current I_{pc} for different values of $k_B T$ with $\alpha = 0, 2$

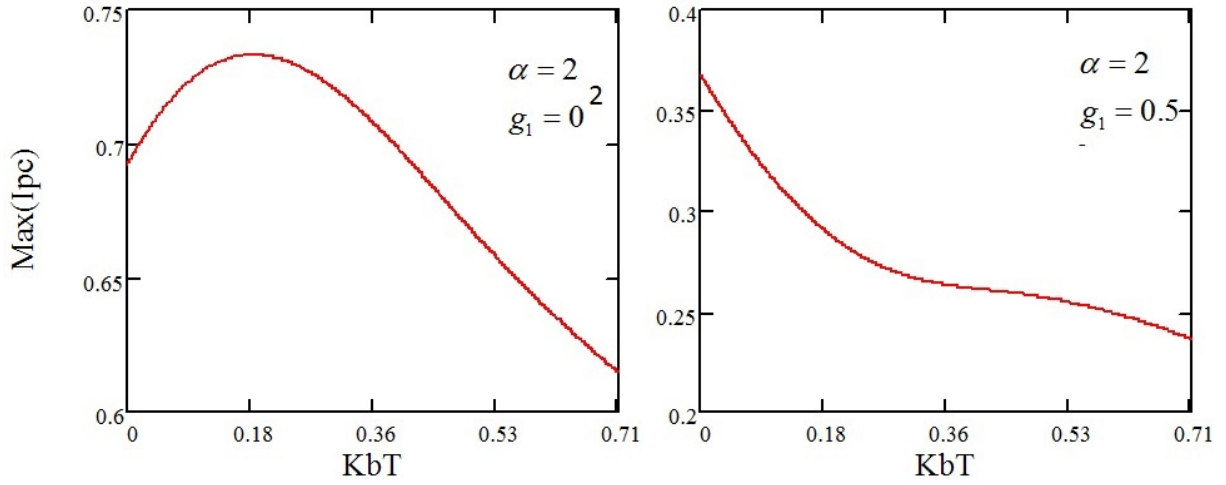


FIG. 15. Variation of persistent current I_{pc} for different values of $k_B T$ with $\alpha = 2, g_1 = 0,$
 $\alpha = 2, g_1 = 0.5$

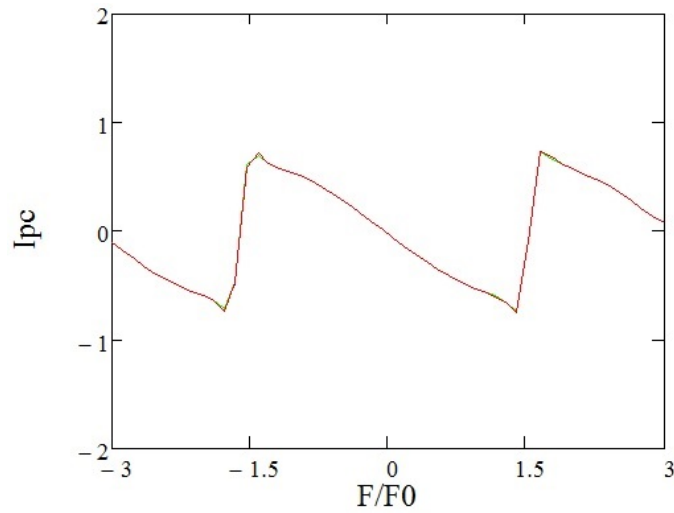


FIG. 16. Persistent current I_{pc} as a function of flux Φ for different values of $\mu, \alpha = 0$

The variation of persistent current I_{pc} for different values of μ in the presence ($\alpha = 2$) and absence ($\alpha = 0$) of Rashba spin-orbit interaction is shown in Fig. 17. In both cases there seem to exist a critical value μ_c such that when $\mu > \mu_c$ the persistent current decreases.

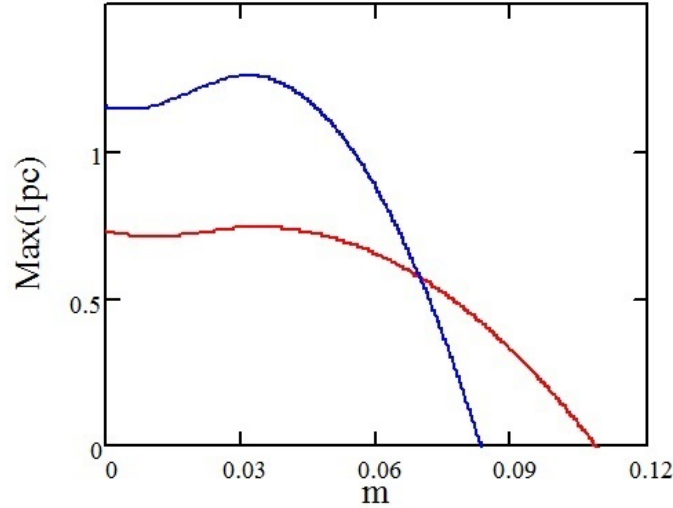


FIG. 17. Variation of persistent current I_{pc} for different values of μ , $\alpha = 0, 2$

5. Conclusions

Thus during the work, the model of two chained Holstein–Hubbard rings in the presence of Rashba spin-orbit interaction and the effect of Rashba spin-orbit interaction were obtained. First, the phonons degrees of freedom were eliminated by the conventional Lang–Firsov transformation and then the spin-dependence was removed by performing the unitary transformation, the effective electronic Hamiltonian was diagonalized by using the Hartree–Fock approximation. The equations for ground state energy, persistent current and Drude weight were also obtained. The persistent current was calculated by differentiating the GS energy. The dependence of ground state energy, persistent current and Drude weight as a functions of flux for different values of Rashba spin-orbit interaction was numerically shown. Next, the effects of Aharonov–Bohm flux, temperature, chemical potential spin-orbit interaction and electron-phonon interaction on the persistent current were also investigated.

Acknowledgements

This work was partially financially supported by the Government of the Russian Federation (grant 08-08), by grant 16-11-10330 of Russian Science Foundation. The authors thank Prof. R. Figari and Prof. W. Florek for interesting discussion.

References

- [1] Buttiker M., Imry Y. and Landauer R. Josephson behavior in small normal one-dimensional rings. *Phys. Lett. A*, 1983, **96**, P. 365–267.
- [2] Cheung H.-F., Gefen Y., Riedel E.K. and Shih W.-H. Persistent current in small one-dimensional metal rings. *Phys. Rev. B*, 1988, **37**, P. 6050–6062
- [3] Takada Y. and Chatterjee A. Possibility of a metallic phase in the charge-density-wave-spin-density-wave crossover region in the one-dimensional Hubbard–Holstein model at half filling. *Phys. Rev. B*, 2003, **67**, P. 081102.
- [4] Sil S., Maiti S.K. and Chakrabarti A. Interplay of magnetic field and geometry in magneto-transport of mesoscopic loops with Rashba and Dresselhaus spin-orbit interactions. *J. Appl. Phys.*, 2012, **112**, P. 024321.
- [5] Manolescu A., Daday C., Gudmundsson V. Coulomb effects on the spin polarization of quantum ring. *Nanosystems Phys. Chem. Math.*, 2011, **2**(3), P. 29–36.
- [6] Monisha P.J., Sankar I.V., Sil S. and Chatterjee A. Persistent current in a correlated quantum ring with electron-phonon interaction in the presence of Rashba interaction and Aharonov–Bohm flux. *Scientific Reports*, 2016, **6**, P. 20056.
- [7] Voda A. *Micro, Nanosystems and Systems on Chips: Modeling, Control, and Estimation*. New York, John Wiley & Sons, 2013.
- [8] Eremin D.A., Grishanov E.N., Nikiforov D.S., Popov I.Y. Wave dynamics on time-depending graph with Aharonov–Bohm ring. *Nanosystems: Physics, Chemistry, Mathematics*, 2018, **9**(4), P. 457–463.
- [9] Lang I. and Firsov Y.A. Kinetic theory of semiconductors with low mobility. *Sov. Phys. JETP*, 1963, **16**(5), P. 1301–1312.
- [10] Cabib D. and Callen E. Charge order and antiferromagnetic order in the Hubbard model with nearest neighbor Coulomb interaction: Weak coupling. *Phys. Rev. B*, 1975, **12**, P. 5249–5254.

Fabrication and characterization of TiO₂/SiO₂ multilayers using sol-gel spin coating method

S. Saravanan, R. S. Dubey

Department of Nanotechnology, Swarnandhra College of Engineering and Technology,
Seetharampuram, Narsapur-534280, (A.P), India

shasa86@gmail.com

DOI 10.17586/2220-8054-2019-10-1-63-69

The TiO₂/SiO₂ alternating multilayers of one-dimensional photonic crystals (1DPCs) was fabricated by the sol-gel process and a spin coating method. This study investigated the possibility of creating a better solar cell back reflector by introducing maximum and broader reflection towards longer wavelength spectral region with effect of optimal thin films. After the fabrication of 1DPCs, the optical properties were investigated by Raman spectroscopy, Fourier infrared spectroscopy (FTIR), UV-visible spectroscopy (UV-vis) and scanning electron microscopy (SEM). From the results, the Raman spectra exhibited notable peaks and indicates the presence of anatase TiO₂ and SiO₂ layered structures. Furthermore, the highest reflectance was observed in the visible region and shifting into the longer wavelength spectral region due to the increment of alternative layers (stacks). These structural and morphological results are encouraging for the realization of TiO₂ and SiO₂ materials for various applications, including LED and photovoltaics.

Keywords: multilayers, sol-gel, spin coating, back reflector, anatase.

Received: 25 January 2019

1. Introduction

Currently, TiO₂ has great attention due to its various applications and correlating research associated with nanomaterials that are environment-friendly. Y. Y. Liu et al. reported that the addition of SiO₂ onto TiO₂ films enhanced photon induction [1]. The fabrication of dielectric multilayers can be accomplished using various techniques such as ion-assisted-deposition (IAD), sol-gel, dip-coating, spin-coating, sputtering, etc [2–5]. Sol-gel is an appropriate method for the synthesis of TiO₂/SiO₂ thin films with enhanced electrical and optical performance in industrial applications because of large refractive index contrast. This is one of the significant features of one-dimensional photonic crystals (or multilayers) and existing photonic band gap (PBG) with high (n₁) and low (n₂) refractive index contrast. The alternative layers (stacks) of TiO₂/SiO₂ coatings mainly focusing on various applications such as antireflection coating, photocatalysis, light emitting diodes (LEDs), solar cells, optical filter, dental implants, sensor and thermal applications [6–12]. Dubey and Ganesan have studied the optical properties of SiO₂/TiO₂ multilayers by using sol-gel spin coating method. They have obtained maximum ~78% reflection with the combination of six alternative low (SiO₂) and high (TiO₂) refractive indices of the films. For the corresponding fabricated multilayer structure, it was observed that when the number of stacks was increased, the reflectance was also enhanced. Furthermore, the film thickness (230 and 70 nm), refractive index (1.43 and 2.0) along with surface topography (AFM) were discussed [13]. Ding et al. have demonstrated the improvement of reflectance and efficiency of the light emitting diodes (LEDs) with the integration of aluminium film and double (16 stacks) distributed Bragg reflectors (TiO₂/SiO₂). They have also reported the light output power of LED with double distributed Bragg reflector (DBR) was ~3.7% greater than single (8 stacks) DBR stacks [14]. Pana et al. have reported the design and fabrication of seven stacks TiO₂/SiO₂ multilayers by using optical modeling and RF magnetron sputtering. The RF magnetron sputtering used for the thermal solar collector consists of an optical filter comprising TiO₂/SiO₂ alternative layers. They have demonstrated colored glazing showing significant reflectivity ~54% at 574 nm and integrated total transmittance was ~80.3%. The yellow and green glaze had the best mechanical and thermal stability for thermal solar collectors [15]. Ilinykh and Matyushkin have fabricated 1DPCs using a sol-gel process and spin coating method. They have found minimum transmittance (~7%) between the photonic band gaps (450–600 nm). Also, the band gap varied with respect to the viscosity of the prepared solution and the thickness of the layers also changed [16]. Jena et al. have investigated design and fabrication of 1DPCs (TiO₂/SiO₂) using an asymmetric bipolar pulse DC magnetron sputtering technique. They have proved both theoretical and experimental works were congruent by measured photonic band gap (PBG) in the visible spectral region [17]. Hegmann et al. have prepared SiO₂-TiO₂ scattering layers using sol-gel process and a dip-coating method. They improved thin film solar cells with the addition of aluminium doped ZnO and a-Si:H/ μ c-Si:H by vapor phase deposition. Further, the electrical properties and performance have been studied by different

characterizations. They have implemented sol-gel based scattering thin films for light trapping mechanism with two different concepts for solar cell application [18]. In this present work, highly reflective $\text{TiO}_2/\text{SiO}_2$ multilayers were prepared using sol-gel spin coater techniques and characterized their optical performance. Section 2 explains the experimental works of sol-gel process and spin-coating techniques. After calcination, the thin films analysis results are discussed in section 3 and conclude the paper in section 4.

2. Experimental approach

An experimental technique for the synthesis of the $\text{TiO}_2/\text{SiO}_2$ multilayer structure was a spin coating of SiO_2 sol and TiO_2 sol on a glass substrate in which the prepared solution was used in a sol-gel technique at room temperature. Fig. 1 shows the schematic diagram of the preparation of $\text{TiO}_2/\text{SiO}_2$ thin films.

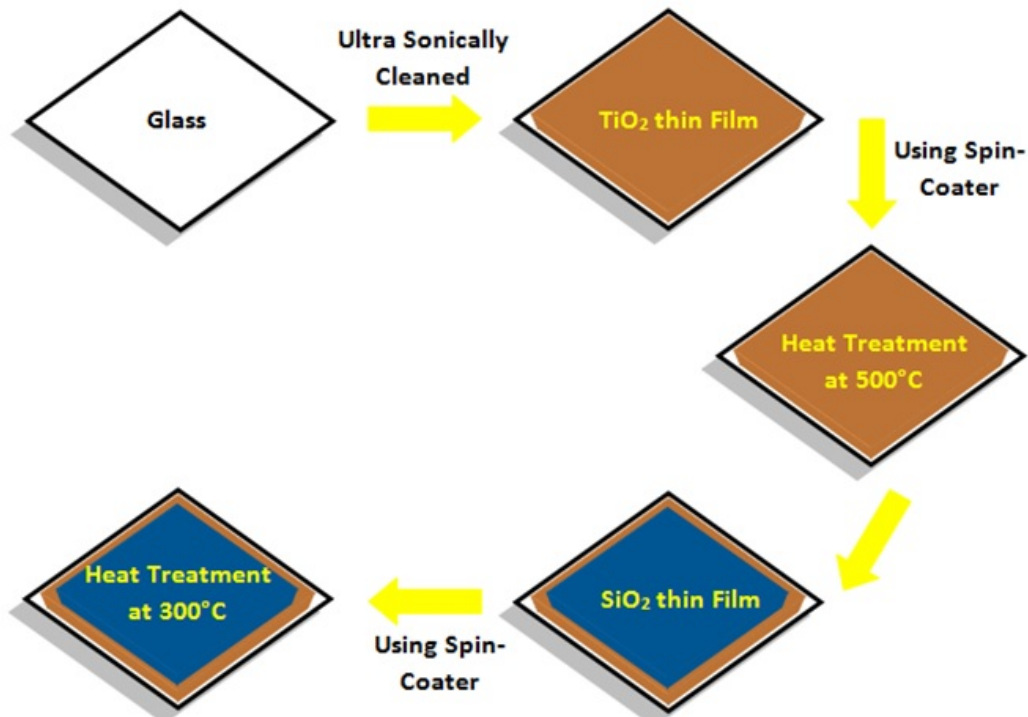
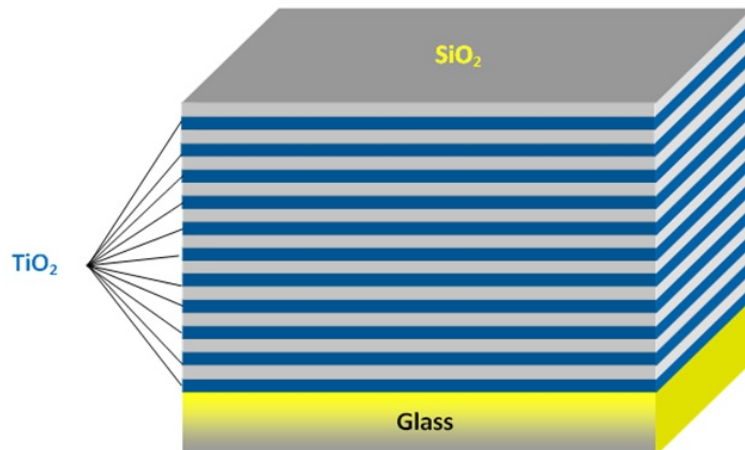
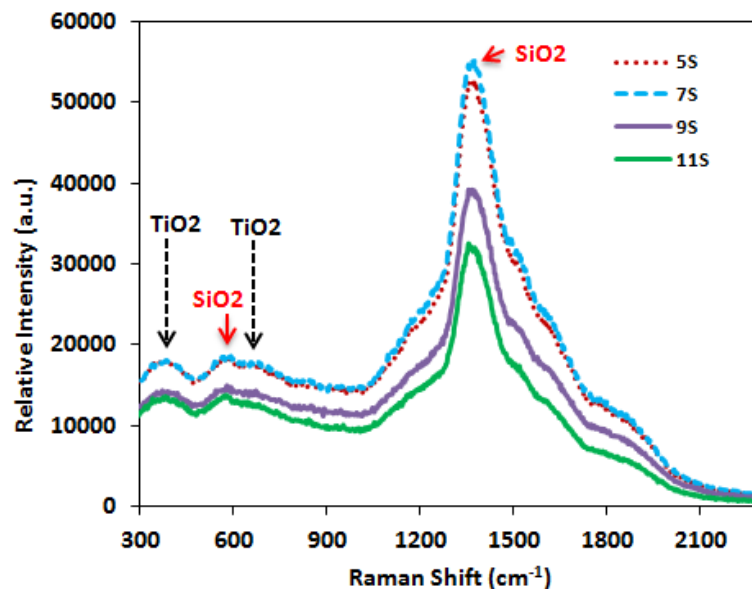


FIG. 1. The schematic diagram of the preparation steps of $\text{TiO}_2/\text{SiO}_2$ thin films

Prior to coating, the glass substrates were cleaned using ultra sonication process in distilled water, acetone, ethanol respectively. First, SiO_2 and TiO_2 solutions were prepared independently. The TiO_2 solution was prepared by adding 1.7 mL CH_3COOH (acetic acid) in 20 mL CH_3OH (methanol) and to this mixture 1.2 mL of $\text{C}_{16}\text{H}_{36}\text{O}_4\text{Ti}$ (TBOT) was added dropwise and stirred for 30 minutes. After magnetic stirring, the TiO_2 solution was deposited on the glass substrate with the rotation speed of 3000 rpm for the 30s. Then, the coated glass substrates were annealed at 500°C for 1 hour. Next, a solution of $\text{SiC}_8\text{H}_{20}\text{O}_4$ (TEOS-1.5ml), $\text{C}_2\text{H}_6\text{O}$ (ethanol-20ml) and CH_3COOH (Acetic Acid-2.3ml) was first prepared and stirred for 90 minutes at room temperature. Then, SiO_2 solution coated on a TiO_2 coated glass substrate by the spin-coater technique with the 3000 rpm for the 30s. The coated glass substrates were dried at room temperature and then heat-treatment (300°C) for 1 hour. Both the final stirred solution was aged in a closed glass container at room temperature for one day and then used for coating. Simultaneously, we prepared the 5, 7, 9 and 11 stacks of alternating TiO_2 and SiO_2 layers. Fig. 2 shows the schematic diagram of final multilayer stacks of $\text{TiO}_2/\text{SiO}_2$.

3. Results and discussion

The Raman spectroscopic technique was employed to study the presence of different frequency modes. Fig. 3 shows the comparison of Raman scattering spectra at various $\text{TiO}_2/\text{SiO}_2$ stacks. The relevant positions of the bands are also indicated and calculated band range from 300 to 2300 cm^{-1} .

FIG. 2. The schematic diagram of the fabricated $\text{TiO}_2/\text{SiO}_2$ FIG. 3. Raman spectra of anatase $\text{TiO}_2/\text{SiO}_2$ multilayer thin films grown on a glass substrate

First, the anatase phase TiO_2 thin films were successfully observed on glass substrates using Raman spectroscopy. The Raman bands of the anatase phase noticed on 5, 7, 9 and 11 stacks at 393 and 640 cm^{-1} , which can be indicated B1g and Eg modes. These broader and low-intensity peaks the presence of a poorly-defined anatase phase [19,20]. The characteristics recorded in our studies were similar to those obtained in previous studies. Further, the deposition conditions such as solution viscosity, the deposition period and calcination temperature are significant for obtaining a better anatase TiO_2 phase. For SiO_2 deposited on TiO_2 , we characterized and observed broad peak at higher frequencies such as 600 cm^{-1} and 1369 cm^{-1} . Here, the first peak was assigned to breathing modes of oxygen atoms [21,22]. The SiO_2 grown layers on TiO_2 has higher peaks at 1369 cm^{-1} as seen in Fig. 3. Compared to the TiO_2 spectrum, the SiO_2 is so broad and strong spectral curve. Fig. 4 shows typical infrared transmittance spectrum of various stacks (5S, 7S, 9S & 11S) of $\text{TiO}_2/\text{SiO}_2$ layers. The strong peaks at 3400 cm^{-1} and 1644 cm^{-1} are attributed to OH stretching bands due to water adsorbed by TiO_2 layers. The absorption band at 1089 cm^{-1} confirmed the presence of Si–O–Si stretching vibration [23]. The characteristic of Ti–O vibration bending mode shows the presence of metal oxide at $686\text{--}742\text{ cm}^{-1}$ [24]. We have observed that the peak intensity increasing at lower wavelength range for the case of 5S and 7S while it is decreases for the 9S and 11S samples.

Figure 5 shows the reflectance spectrum of 5S, 7S, 9S and 11S stacks of $\text{TiO}_2/\text{SiO}_2$ prepared by spin coating process. The partial reflection wave of each layer produces maximum reflections and the many reflected waves

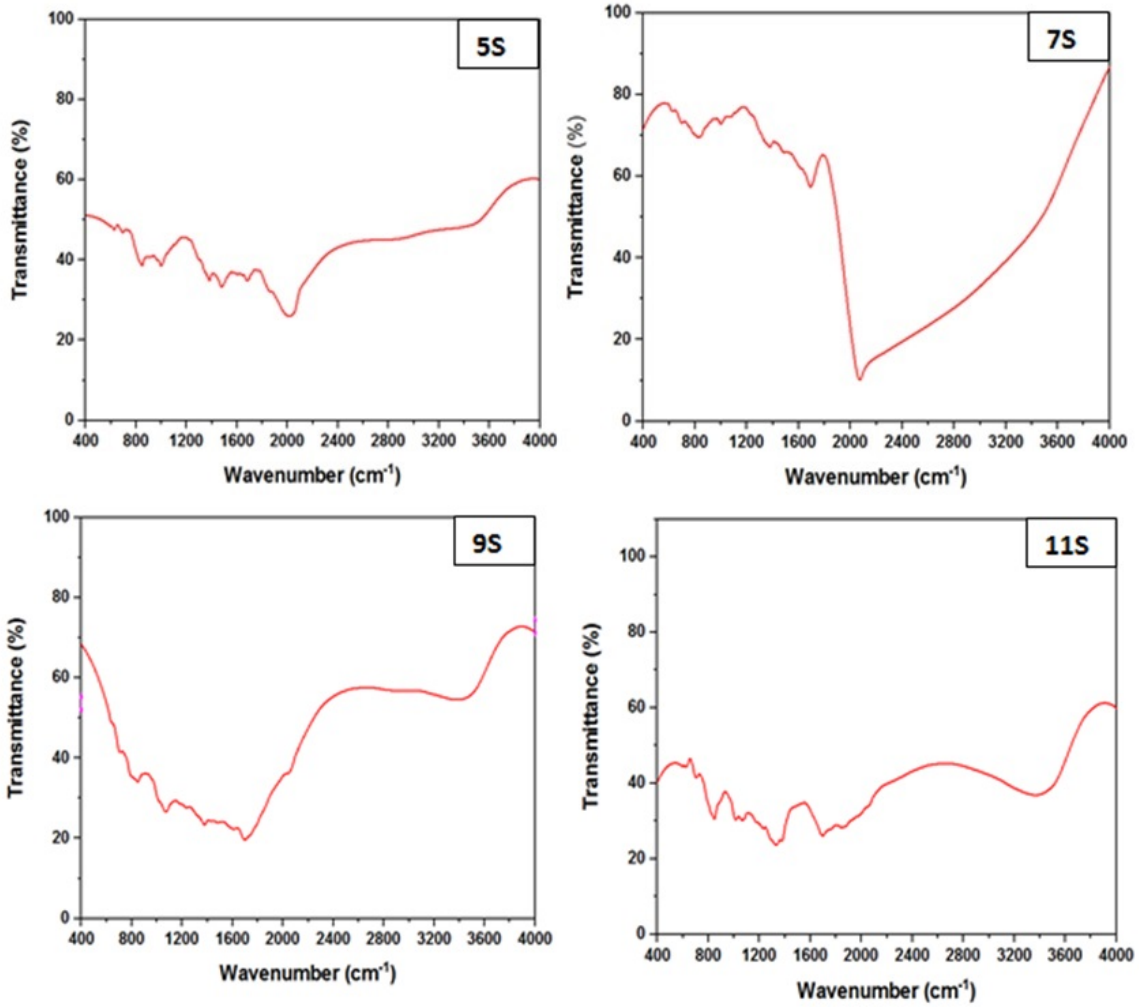


FIG. 4. FTIR spectrum of $\text{TiO}_2/\text{SiO}_2$ multilayer films deposited on glass with 3000 rpm at room temperature

creating high-quality back reflectors. This reflected wavelength range is called distributed Bragg reflector (DBR) and referred as photonic band gap (PBG). The band gaps (full width at half maximum-FWHM) of DBR changing with respect to refractive index contrast between the layered structures. This can be expressed in the terms of frequency by using the following equation [25,26]:

$$\Delta\omega = \frac{4\omega_{max}}{\pi} \sin^{-1} \left(\frac{|n_h - n_l|}{n_h + n_l} \right),$$

here, $\omega_{max} = 2\pi c/\lambda_{max}$, n_h and n_l are the high and low refractive index. Overall, the reflectance peaks achieved maximum (> 99 %) level and shift can be verified. When increasing the number (N) of alternating layers from 5 to 11 stacks, the enhanced reflection shifts significantly and broadening towards higher wavelength region which will be optimized.

Figure 6 shows the enhanced reflectance FWHM with increased number of stacks, it is dominant for the case of 11S sample with its reflectance FWHM 270 nm. Particularly, the reflectance is mainly dependent on the optical thickness and surface structure of the layers also called first-order center wavelength:

$$\lambda_{max} = 2(n_h d_h + n_l d_l)$$

where λ_{max} is the reflected wavelength, d is the thickness of the layers. The bright and dark color (interference) shows the illuminated light yields a good reflectance band at desired wavelength region. These films exhibit bright colors when the stop band fell in the visible spectral region. By controlling the optical thickness, thin film color can be varied across both the visible and infrared spectral region [27,28].

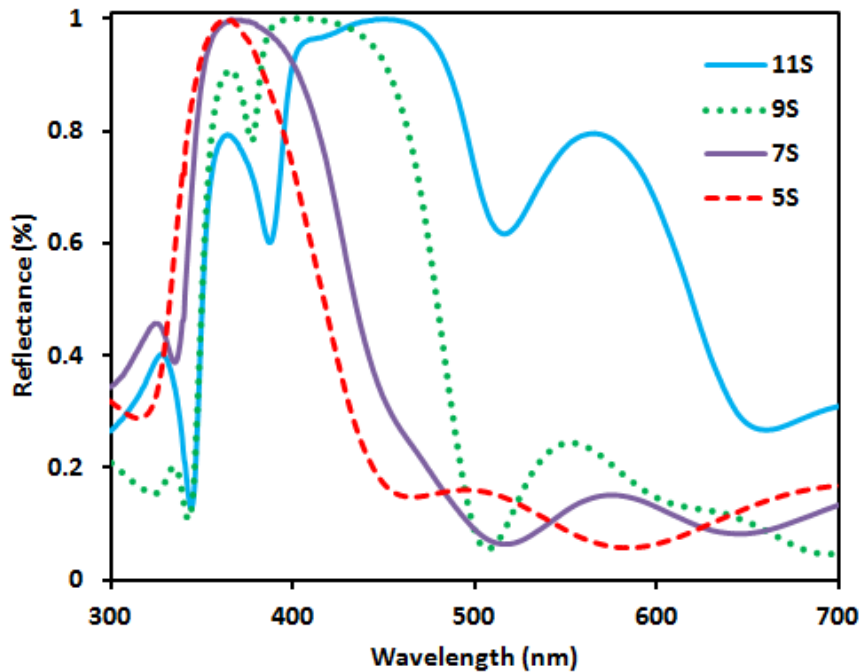
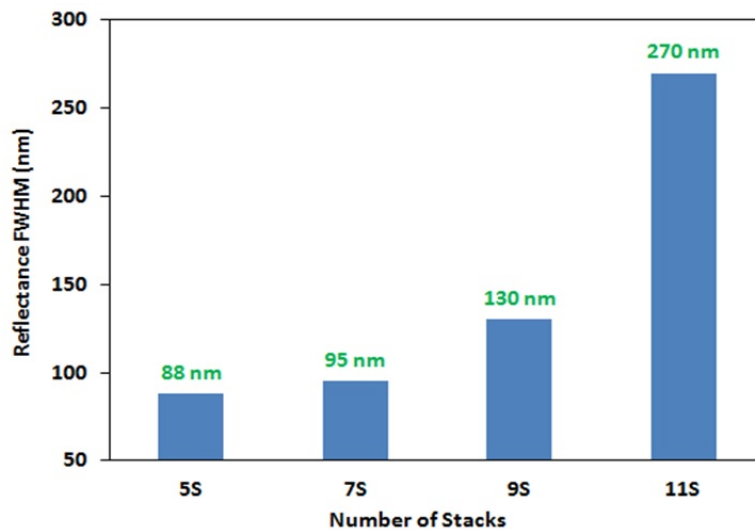
FIG. 5. The reflectance spectra of different stacks of TiO₂/SiO₂ layers

FIG. 6. The bar diagram of the reflectance of FWHM vs a number of stacks

Cross-sectional TiO₂/SiO₂ multilayer (11 stacks) thin films were characterized by the field emission scanning electron microscopy (FESEM) as depicted in Fig. 7. From the cross-sectional image of the alternating dielectric layers, we can find some of the borders and remaining are merged with each other. The structural defect was achieved by multiplying the layers of TiO₂ and SiO₂ embedded in which the light bands correspond to titanium dioxide and dark bands are silicon dioxide layers. The cross-sectional image indicates that the film thickness is 1 μ m TiO₂/SiO₂ multilayer film and confirms the heterogeneous structure.

4. Conclusion

In this paper, TiO₂/SiO₂ multilayers were fabricated and studied. TiO₂ nantase phase and amorphous SiO₂ were confirmed by the Raman Study. The back-side light reflecting structures of alternating high-index and low-index multilayers of 11 stacks had shown maximum reflection in the visible spectral region. The reflectance center

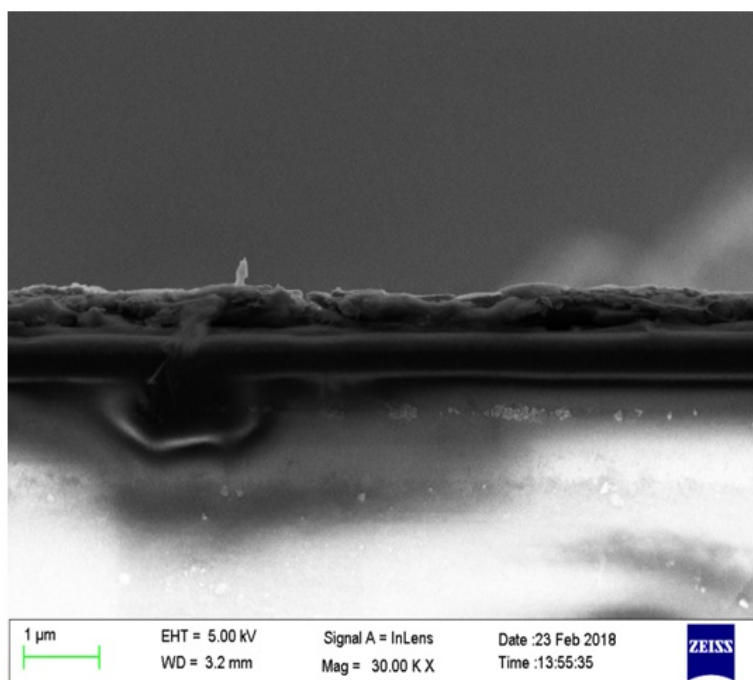


FIG. 7. The cross-sectional image of FESEM representative $\text{TiO}_2/\text{SiO}_2$ multilayers

wavelength noticed at 362, 365, 404 and 450 nm corresponding to the sample 5S, 7S, 9S and 11S upon increasing the number of stacks the reflection bands were found shifted towards the longer wavelength with enhanced reflectivity. The FESEM showed the formation of alternative layers of light (TiO_2) and dark (SiO_2) strips with their one-dimensional periodicity. The morphological and optical measurement confirmed the changes in thin films and surface roughness are attributed to the better backside reflector for the photovoltaic device. Further, the work optimization is required to enhance optical behavior.

References

- [1] Liu Y.Y., Qian L.Q., Guo C., Jia X., Wang J.W., Tang, W.H. Natural superhydrophilic $\text{TiO}_2/\text{SiO}_2$ composite thin films deposited by radio frequency magnetron sputtering. *J Alloys Compd*, 2009, **479**(1-2), P. 532–535.
- [2] Bin Fan, Masahiro Suzuki and Ken Tang. Ion-assisted deposition of $\text{TiO}_2/\text{SiO}_2$ multilayers for mass production. *Appl Opt.*, 2006, **45**(7), P. 1461–1463.
- [3] Li D., Wan D., Zhu X., Wang Y., Han Z., Han S., Shan Y., Huang F. Broadband antireflection $\text{TiO}_2\text{-SiO}_2$ stack coatings with refractive-index-grade structure and their applications to Cu(In,Ga)Se_2 solar cells. *Sol. Energy Mater Sol. Cells*, 2014, **130**, P. 505–512.
- [4] Dubey R.S., Ganesan V. Fabrication and characterization of $\text{TiO}_2/\text{SiO}_2$ based Bragg reflectors for light trapping applications. *Results Phys*, 2017, **7**, P. 2271–2276.
- [5] Yamaguchi T., Tamura H., Taga S., Tsuchiya S. Interfacial optical absorption in $\text{TiO}_2\text{-SiO}_2$ multilayer coatings prepared by RF magnetron sputtering. *Appl Opt.*, 1986, **25**(16), P. 2703–2706.
- [6] Liu Z., Zhang X., Murakami T., Fujishima A. Sol-Gel $\text{SiO}_2/\text{TiO}_2$ bilayer films with self-cleaning and antireflection properties. *Sol. Energy Mater Sol. Cells*, 2008, **92**(11), P. 1434–1438.
- [7] Liu C., Yang D., Jiao Y., Tian Y., Wang Y., Jiang Z. Biomimetic synthesis of $\text{TiO}_2\text{-SiO}_2\text{-Ag}$ nanocomposites with enhanced visible-light photocatalytic activity. *ACS Appl. Mater. Interfaces*, 2013, **5**(9), P. 3824–3832.
- [8] Lin C.H., Lai C.F., Ko T.S., Huang H.W., Kuo H.C., Hung Y.Y., Leung K.M., Yu C.C., Tsai R.J., Lee C.K., Lu T.C., Wang S.C. Enhancement of InGaN-GaN indium-tin-oxide flip-chip light-emitting diodes with $\text{TiO}_2\text{-SiO}_2$ multilayer stack omnidirectional reflector. *IEEE Photonics Technol.*, 2006, **18**(19), P. 2050–2052.
- [9] Mbakop F.K., Djongyang N., Raidandi D. One-dimensional $\text{TiO}_2/\text{SiO}_2$ photonic crystal filter for thermophotovoltaic applications. *Journal of the European Optical Society-Rapid Publications*, 2016, **12**(23), P. 1–9.
- [10] C.M. Pecnik, D. Muff and R. Sailer. Color evaluation of a dielectric mirror coating using porcine tissue and prosthetic gingival material: a comparison of two models. *Clin Oral Implan Res.*, 2015, **27**(2), P. 139–148.
- [11] Hopman W.C.L., Pottier P., Yudistira D., Van Lith J., Lambeck P.V., De La Rue R.M., Driessen A., Hoekstra H.J.W.M., de Ridder R.M. Quasi-one-dimensional photonic crystal as a compact building-block for refractometric optical sensors. *IEEE J. Sel. Top. Quantum Electron.*, 2005, **11**(1), P. 11–16.
- [12] Pavlichenko I., Exner A.T., Lugli P., Scarpa G., Lotsch B.V. Tunable thermoresponsive $\text{TiO}_2/\text{SiO}_2$ Bragg stacks based on sol-gel fabrication methods. *J. Intell. Material Syst. Struct.*, 2012, **24**(18), P. 2204–2214.

- [13] Dubey R.S., Ganesan V. Reflectance modulation using SiO₂/TiO₂ multilayer structures prepared by sol-gel spin coating process for optical applications. *Superlattices and Microstruct.*, 2017, **111**, P. 1099–1103.
- [14] Ding X., Gui C., Hu H., Liu M., Liu, X., Lv J., Zhou S. Reflectance bandwidth and efficiency improvement of light emitting diodes with double distributed Bragg reflectors. *Applied Physics*, 2017, **56**(15), P. 4375–43810.
- [15] Pana I., Vitelaru C., Kiss A., Zoita N.C., Dinu M. Design, fabrication and characterization of TiO₂-SiO₂ multilayer with tailored color glazing for thermal solar collectors. *Mater. Des.*, 2017, **130**, P. 275–284.
- [16] Ilinykh V.A., Matyushkin B. Fabrication of One-Dimensional Photonic Crystals by Sol-Gel Method. *IEEE*, 2016, P. 47–50.
- [17] Jena S., Tokas R.B., Sarkar P., Haque S.M., Misal J.S., Rao K.D., Thakur S., Sahoo N.K. achieving omnidirectional photonic band gap in sputter deposited tio₂/sio₂ one dimensional photonic crystal. *AIP Conf. Proc.*, 2015, **1665**, P. 060018-1-3.
- [18] Hegmann J., Jahn R., Schonau S., Sommer N., Lobmann P. SiO₂-TiO₂ scattering layers prepared by sol-gel processing for light management in thin film solar cells. *J. Sol gel Sci Technol.*, 2015, P. 1–9.
- [19] Vernardou D., Spanakis E., Vlachou K., Kalogerrakis G., Costello J., Koudoumas E., Katsarakis N. , Pemble M.E. A Comparative study of the photoinduced of TiO₂/SiO₂ and TiO₂/ZnO/SiO₂ layers prepared by chemical routes. *ECS Trans.*, 2009, **25**(8), P. 73–80.
- [20] Vijayalakshmy S., Subramanian B. Enhanced Performance of dye-sensitized solar cells with TiO₂ blocking layers and Pt counter electrodes prepared by physical vapor deposition (PVD). *Electrochim. Acta*, 2014, **116**, P. 334–342.
- [21] Narasimha Rao Mavilla, Chetan Singh Solanki and Juzer Vasi. Raman spectroscopy of silicon-nanocrystals fabricated by inductively coupled plasma chemical vapor deposition. *Physica E*, 2013, **52**, P. 59–64.
- [22] Galeener F. Planar rings in glasses. *Solid State Communications*, 1982, **44**(7), P. 1037–1040.
- [23] Hecht E. *Optics*, 4th edn, Pearson Inc. San Francisco, California, USA, 2002.
- [24] Puzzo D.P., Bonifacio L.D., Oreopoulos J., Yip C.M., Manners I., Ozin G.A. Color from colorless nanomaterials: Bragg reflectors made of nanoparticles *J. Mater. Chem.*, 2009, **19**, P. 3500–3506.
- [25] Joannopoulos J.D., Johnson S.G., Winn J.N., Meade R.D. *Photonic Crystals: Molding the Flow of Light*, 2008, 2-nd edn, Princeton University Press, Princeton, New Jersey, USA, 2008.
- [26] Wu Z., Lee D., Rubner M.F., Cohen R.E. Structural color in porous, superhydrophilic, and self-cleaning SiO₂/TiO₂ Bragg stacks. *Small*, 2007, **3**(8), P. 1445–1451.
- [27] Madani M., Omri K., Fattah N., Ghorbal A., Portier X. Influence of silica ratio on structural and optical properties of SiO₂/TiO₂ nanocomposites prepared by simple solid phase reaction. *J. Mater. Sci. Mater. Electron.*, 2017, P. 5–7.
- [28] Suwarakar M.B., Dhabbe R.S., Kadam A.N., Garadkar K.M. Enhanced photocatalytic activity of Ag doped TiO₂ nanoparticles synthesized by a microwave assisted method, *Ceram Int.*, 2014, **40**, P. 5489–5496.

Very wide-bandgap nanostructured metal oxide materials for perovskite solar cellsL. L. Larina¹, O. V. Alexeeva¹, O. V. Almjasheva², V. V. Gusarov³, S. S. Kozlov¹,
A. B. Nikolskaia¹, M. F. Vildanova¹, O. I. Shevaleevskiy¹¹Department of Solar Photovoltaics, Institute of Biochemical Physics RAS,
Kosygin St. 4, Moscow, 119334, Russia²St. Petersburg Electrotechnical University “LETI”, Professora Popova St. 5, Saint Petersburg, 197376, Russia³Ioffe Physical-Technical Institute RAS, Politekhnicheskaya St. 26, Saint Petersburg, 194021, Russia
shevale2006@yahoo.com, almjasheva@mail.ru, victor.v.gusarov@gmail.com**PACS 73.63.Bd****DOI 10.17586/2220-8054-2019-10-1-70-75**

Very wide-bandgap undoped and Y₂O₃-doped ZrO₂ nanoparticles were synthesized and their structural, optical, morphological and energy characteristics were investigated. It was found that the bandgap value in ZrO₂ decreases with Y₂O₃ doping. The developed materials were used for fabrication of nanostructured photoelectrodes for perovskite solar cells (PSCs) with the architecture of glass/FTO/ZrO₂–Y₂O₃/CH₃NH₃PbI₃/spiro-MeOTAD/Au. The power conversion efficiency in the PSCs based on ZrO₂–Y₂O₃ photoelectrodes was significantly higher than that for undoped ZrO₂ photoelectrodes. We have found that nanostructured layers, based on very wide-bandgap materials could efficiently transfer the injected electrons via a hopping transport mechanism.

Keywords: nanostructures, ZrO₂, thin films, semiconductors, solar photovoltaics, perovskite solar cells.*Received: 10 November 2018**Revised: 18 January 2019***1. Introduction**

Nanostructured materials are widely used for the development of next-generation solar cells (SCs) since they enable fabrication of high efficiency and low-cost devices which are promising for mass production of photovoltaic technologies [1, 2]. Recently, a considerable interest is focused on inorganic–organic metal halide perovskite solar cells (PSCs) in which the record power conversion efficiency (PCE) exceeded 22 % [3] and reached 27.3 % in perovskite-silicon tandem solar cell [4]. PSC’s architecture comprises a mesoscopic layer of metal-oxide nanoparticles on a conductive substrate, which plays a role of the electron-conductive photoelectrode, a perovskite (CH₃NH₃PbI₃) layer deposited on top of the photoelectrode, a hole-conductive layer and a metallic counter electrode [5, 6].

One of the key components of the PSC is an electron-conductive photoelectrode, which consists of metal oxide semiconductor nanoparticles organized in a mesoscopic architecture. Nanostructured layers of titanium dioxide (TiO₂) with the band gap (E_g) of 3.0 – 3.2 eV are generally used as photoelectrodes in PSCs [7, 8]. At the same time, some other wide-bandgap materials were also successfully used in photoelectrodes [9]. The application of a very wide-bandgap metal oxide, such as ZrO₂ with $E_g \sim 5.7$ eV, is of special interest for this purpose [10]. Condensed layers of wide-bandgap materials are dielectrics with insulator type conductivity behavior and can’t be used as a conductive medium. However, their analogs with nanostructured morphology demonstrate high electron-conductive abilities, due to the large concentration of the nanoparticle surface defects. A number of publications confirmed that in nanostructured systems with $E_g > 5$ eV, the effective transfer of the injected electrons was observed, while the density of the electrons in the conduction band was negligible [9]. Charge transport through the nanostructured layer can be realized on the basis of a hopping conduction mechanism through localized states within forbidden zone [10].

The formation of crystal phase and morphology in ZrO₂ as well as optical and electrical properties of ZrO₂ nanoparticles strongly depend on the synthesis conditions [11]. A significant advantage of ZrO₂ material is its ability to be doped with yttrium oxide (Y₂O₃), which allows one to vary the optoelectronic characteristics of ZrO₂–Y₂O₃-based nanostructured systems. Doping with rare-earth metals or niobium (Nb) allows to significantly improve the transport characteristics of the photoelectrode and to increase the PCE of the PSCs [12, 13]. Previously reports of PSCs fabricated using undoped ZrO₂-based photoelectrode have been made [14]. In this work, we have synthesized ZrO₂ nanoparticles and yttrium oxide doped ZrO₂–Y₂O₃ systems which were used for fabrication of the nanostructured electron-conductive photoelectrodes for PSCs. Using the developed ZrO₂–Y₂O₃-based photoelectrodes, we have prepared a series of PSCs and provided comparative measurements of the main photovoltaic parameters.

2. Experimental

2.1. Materials and samples preparation

Nanocrystalline zirconium dioxide was prepared by hydrothermal treatment of zirconium oxyhydroxide precipitated from a solution of $ZrOCl_2$ (chemical pure grade) with concentrated aqueous NH_4OH . Hydrothermal treatment was performed at $T = 250$ °C and $P = 70$ MPa over 4 h. The Y_2O_3 -doped ZrO_2 nanoparticles were obtained by hydrothermal treatment of co-precipitated zirconium and yttrium hydroxides from solutions of the corresponding metal salts. The conditions of hydrothermal treatment were chosen according to the data in [11] and corresponded to complete dehydration of zirconium hydroxide.

To fabricate a nanostructured photoelectrode based on ZrO_2 - Y_2O_3 system, we utilized a known technique; pastes from ZrO_2 and ZrO_2 - Y_2O_3 nanopowders were prepared in organic solvent [6]. The photoelectrodes were formed by depositing the pastes on the glass substrates with a conductive FTO coating. The ZrO_2 and ZrO_2 - Y_2O_3 layers with a thickness of about 200 nm were deposited using spin-coating method, followed by sintering at 500 °C for 30 min.

The PSC fabrication process was provided under ambient conditions with high humidity ($\sim 50 - 60$ %) using a one-step method described previously [15]. During the fabrication process, ZrO_2 -based photoelectrodes were first coated with a photosensitive perovskite ($CH_3NH_3PbI_3$) layer, obtained from lead iodide and methylammonium iodide precursor solutions, followed by depositing a layer of spiro-MeO-TAD as a hole-transporting material [7,14]. The PSC fabrication process was completed by thermal evaporation of conductive Au contacts with a thickness of 50 nm using vacuum system VUP-4. As a result, we have prepared PSCs with a device architecture of glass/FTO/ ZrO_2 - Y_2O_3 / $CH_3NH_3PbI_3$ /spiro-MeOTAD/Au, in which the doping content of Y_2O_3 was varied from 0 % (undoped system) to 3 and 10 mol.%.

2.2. Characterization studies

The structure and composition of nanostructured ZrO_2 - Y_2O_3 system were determined by X-ray diffraction (XRD) analysis in the $13 - 65$ ° range (Cu $K\alpha$ radiation) using Rigaku Corporation SmartLab 3 diffractometer. The optical properties were investigated using UV-vis double-beam spectrophotometer Shimadzu 3600 with an integrating sphere ISR-3100 (Shimadzu, Japan), followed by an analysis of diffuse reflection spectra over a wavelength range 200 – 900 nm. The morphology of the films was investigated using dual-beam scanning electron microscope (SEM) Helios NanoLab 660 (FEI, USA).

The measurements of the photovoltaic parameters for PSCs were provided under standard illumination conditions (AM1.5G) with $P_{IN} = 1000$ W/m² by recording the current-voltage characteristics (J-V) using Abet Technologies Solar Simulator (Abet, USA) as a light source and Keithley 4200-SCS Parameter Analyzer (USA) for recording the current-voltage characteristics (J-V). The PCE (η) of the PSC was calculated from the J-V data using the known formula:

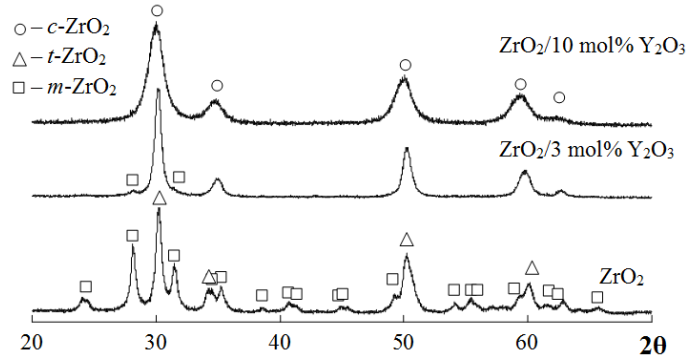
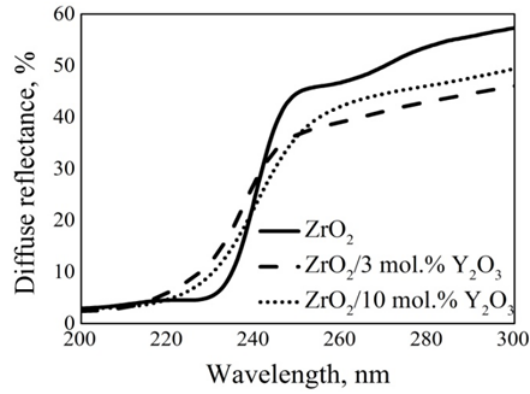
$$\eta = \frac{J_{SC} \cdot V_{OC} \cdot FF}{P_{IN}} \cdot 100 \%, \quad (1)$$

where J_{SC} – short-circuit current density, V_{OC} – open-circuit voltage, FF – fill factor and P_{IN} – light intensity of solar radiation.

3. Results and discussion

In Fig. 1, we present comparative data of XRD patterns for the powders of undoped ZrO_2 nanoparticles and for ZrO_2 - Y_2O_3 system with Y_2O_3 doping level of 3 and 10 mol.%. XRD results for the samples, obtained using hydrothermal processing of co-precipitated zirconium and yttrium, reveal the co-existence of tetragonal (~ 53 %) and monoclinic (~ 47 %) phases in ZrO_2 nanoparticles. The addition of 3 mol.% Y_2O_3 to ZrO_2 leads to the formation of a predominantly pseudo-cubic modification of ZrO_2 (c - ZrO_2) and a trace amount of the monoclinic modification of m - ZrO_2 (up to 5 %), the addition of 10 mol.% Y_2O_3 leads to the complete disappearance of m - ZrO_2 . The crystallite size of zirconia phases, determined by the X-ray line broadening method using the Scherrer equation, was found to be 16 and 14 nm for m - ZrO_2 and t - ZrO_2 , respectively. The obtained results shows that 3 mol.% Y_2O_3 additive does not affect the crystallite size. The addition of 10 mol.% Y_2O_3 decreases the crystallite size down to 5 nm, which can be explained by the formation of the “core-shell” structure in which the shell is enriched with yttria [16].

Figure 2 shows the dependence of the diffuse reflection spectra for the powders of undoped ZrO_2 and ZrO_2 - Y_2O_3 system with Y_2O_3 content of 3 and 10 mol.%. XRD data have shown that yttria doping stabilizes the high-temperature tetragonal ZrO_2 phase. This result revealed that ZrO_2 - Y_2O_3 samples have a monophase structure and, thus, the semiconductor properties of these materials could be characterized by a direct transition from the

FIG. 1. XRD patterns for ZrO_2 nanoparticles with a varied Y_2O_3 contentFIG. 2. Diffuse reflectance spectra for the powders of undoped ZrO_2 and $\text{ZrO}_2\text{-Y}_2\text{O}_3$ system

valence to the conduction band. Following the Kubelka–Munk theory, the value of the optical energy bandgap (E_g) for direct transitions can be determined from the Tauc plots [17]:

$$\alpha(h\nu) = C \frac{(h\nu - E_g)^{1/2}}{h\nu}, \quad (2)$$

where a – optical absorption coefficient, C – constant, $h\nu$ – photon energy.

The E_g values for ZrO_2 and $\text{ZrO}_2\text{-Y}_2\text{O}_3$ system were defined with linear extrapolation of $(\alpha h\nu)^2$ plots with the photon energy axis (Fig. 3). The results obtained showed that E_g value also enhances with the increase of doping concentration from 5.74 eV in ZrO_2 to 5.63 eV in $\text{ZrO}_2\text{-Y}_2\text{O}_3$ (3 %). However, in $\text{ZrO}_2\text{-Y}_2\text{O}_3$ (10 %), the E_g value was found to be 5.45 eV, which can be explained by a significant decrease of the nanoparticle size for that particular sample, to about 5 nm.

Typical scanning electron microscopy (SEM) surface image of the undoped ZrO_2 nanostructured layer deposited on a conductive glass substrate (Fig. 4) indicates the agglomeration of ZrO_2 sphere-like crystallites. SEM results show that the average particle size was approximately 30 – 40 nm. Fig. 5 presents the cross-sectional SEM image of the undoped ZrO_2 electron transport layer spin-coated on FTO glass substrate. It is seen that FTO conductive layer is covered with ~ 200 nm uniform ZrO_2 -based mesoscopic layer. Fig. 6 presents J–V characteristics, recorded for PSCs under standard illumination AM 1.5G. Photovoltaic parameters for all the investigated PSCs are summarized in Table 1. Comparative studies of the PSCs based on undoped and Y_2O_3 -doped ZrO_2 photoelectrodes showed that doping leads to the increase of the short-circuit current values and improves the fill factor of the devices, resulting in the increase of total PCE values. The best performance of 11.4 % was obtained for the PSC with $\text{ZrO}_2\text{-Y}_2\text{O}_3$ (10 %) photoelectrode that significantly exceeds the corresponding value of 5.9 % for PSC based on undoped ZrO_2 photoelectrode.

The performance of ZrO_2 -based PSCs developed in this study was higher than that in TiO_2 based PSCs with much higher observed V_{OC} . The major difference between the above mentioned configurations of PSCs concerns the different charge transport mechanisms at the perovskite/photoelectrode interface for ZrO_2 and TiO_2 electrodes. Fig. 7 presents schematic energy band diagrams demonstrating the energy band structure for PSCs

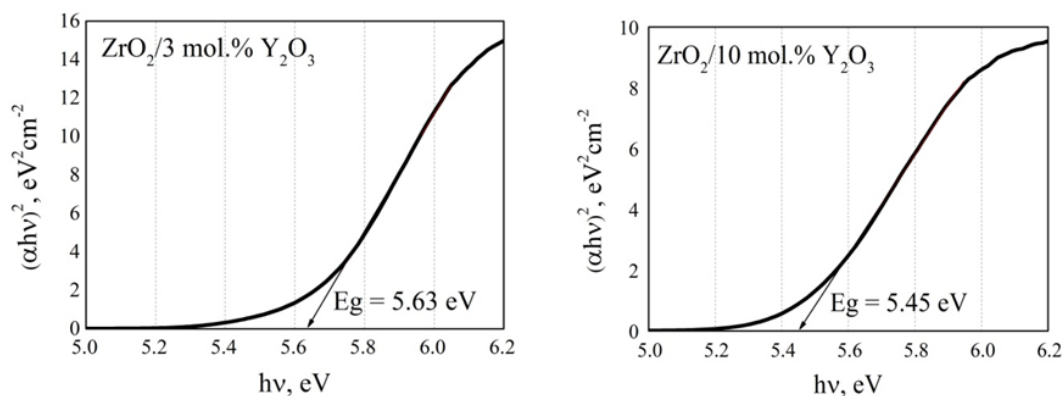


FIG. 3. E_g values for ZrO_2 - Y_2O_3 system extracted from $(\alpha h\nu)^2$ vs. photon energy graphics

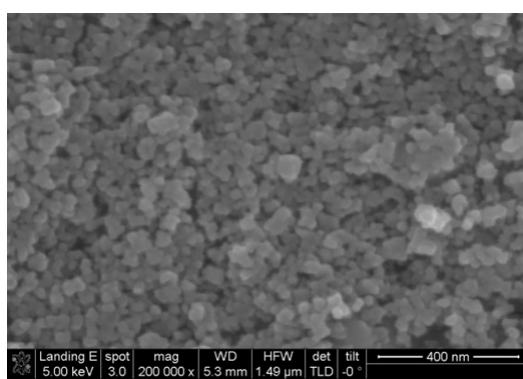


FIG. 4. SEM image of undoped ZrO_2 nanostructured layer spin-coated on a conductive glass substrate

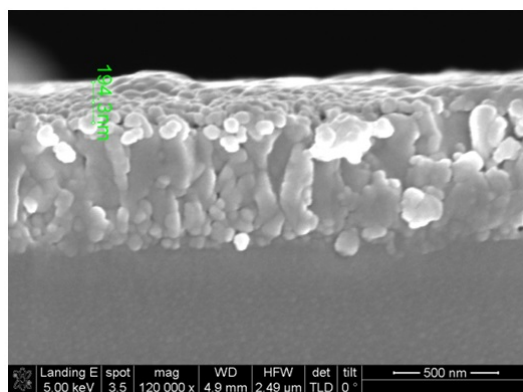


FIG. 5. Cross-sectional SEM image of the ZrO_2 -based photoelectrode

TABLE 1. Photovoltaic characteristics of ZrO_2 - Y_2O_3 based PSCs

PCE parameters	Photoelectrode		
	ZrO_2	$ZrO_2/3 \text{ mol.}\% Y_2O_3$	$ZrO_2/10 \text{ mol.}\% Y_2O_3$
V_{OC} , V	0.94	1.0	1.0
J_{SC} , m/m^2	10.9	13.6	15.4
FF , a.u.	0.58	0.69	0.74
η , %	5.9	9.4	11.4

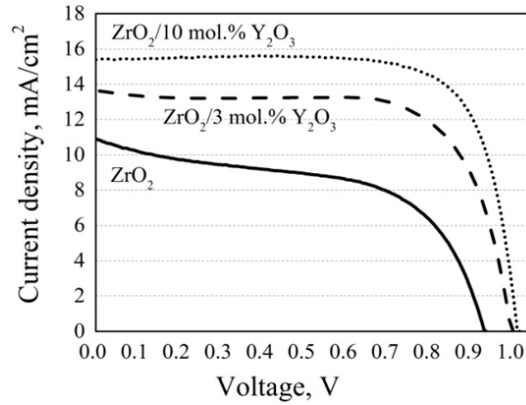


FIG. 6. J–V characteristics of the PSCs based on $\text{ZrO}_2\text{-Y}_2\text{O}_3$ photoelectrodes under simulated AM 1.5G (1000 W/m^2) irradiance

based on a ZrO_2 photoelectrode (Fig. 7(a)) and on traditional TiO_2 photoelectrode (Fig. 7(b)). The band diagram in Fig. 7(b) demonstrates that the conduction band edge of perovskite has the energy above the conduction band edge of TiO_2 [18] that enables a classic photoexcited electron transfer from the perovskite layer to the TiO_2 photoelectrode. Unlike the previously described situation, the conduction band edge of ZrO_2 has much higher energy (Fig. 7(a)), leaving the conduction band edge of perovskite far below, which makes it impossible to transfer the electrons from the perovskite to ZrO_2 in terms of the classical charge transfer mechanism. It is also known that under ambient temperature, ZrO_2 is an insulator with poor carrier transport characteristics and its practical applicability as a charge carrier transporting material is questionable. However, several publications confirmed that the mechanism of charge transport in nanostructured wide-bandgap electrodes, being of primary physical and technical significance, is different from that in the bulk materials [19]. It was also shown that rare earth oxide doping initiates the creation of core-shell structures and results in a high concentration of surface defects [16] that significantly improves the transport characteristics of the mesoscopic photoelectrodes and increases the efficiency of the solar cells [20,21]. The latter is possible due the large concentration of the nanoparticle surface defects. A number of publications confirmed that in nanostructured systems with $E_g > 5 \text{ eV}$, the effective transfer of the injected electrons was observed, while the density of the electrons in the conduction band was negligible [19]. In our study, we observed the effective electron conduction through the nanostructured ZrO_2 layer that can be explained on the basis of the hopping conduction mechanism through localized states within forbidden zone of ZrO_2 [10].

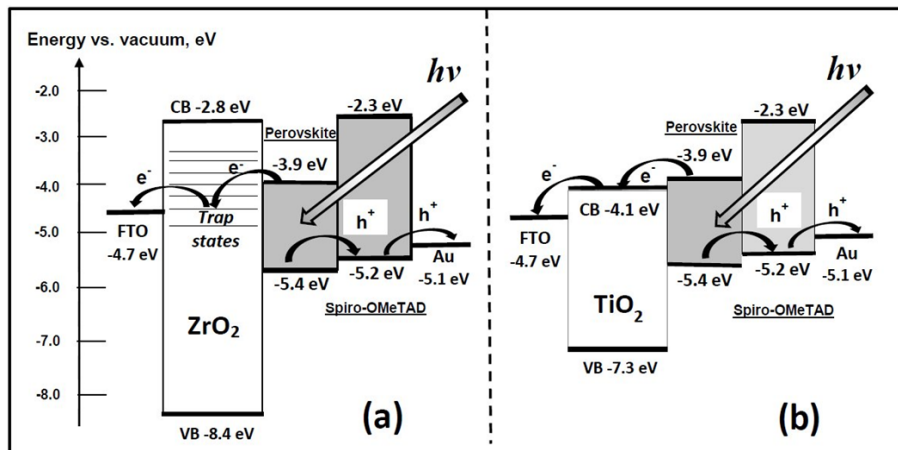


FIG. 7. Schematic energy band diagrams comparing the energy band structures for PSCs based on ZrO_2 (a) and TiO_2 photoelectrodes (b)

4. Conclusions

As a result, we have developed the technology and provided synthesis of both undoped and Y_2O_3 -doped ZrO_2 nanoparticles for which the structural, optical and energy characteristics were investigated. It was found that the band-gap value in ZrO_2 decreases with increased Y_2O_3 doping. The developed materials were used for fabrication of nanostructured thin film photoelectrodes for constructing and providing a comparative study of the PSCs with the architecture of glass/FTO/ ZrO_2 - Y_2O_3 / $CH_3NH_3PbI_3$ /spiro-MeOTAD/Au. The power conversion efficiency in the PSCs based on ZrO_2 - Y_2O_3 photoelectrodes was shown to be significantly higher than that for undoped ZrO_2 photoelectrodes. We have found that nanostructured layer, based on very wide-bandgap ZrO_2 nanoparticles, could efficiently transfer the injected electrons to the back contact through the hopping transport mechanism via trap states in the forbidden zone of ZrO_2 . The obtained results demonstrate the possibility of using a very wide-bandgap oxide nanostructured materials with E_g values exceeding 5 eV for fabrication electron-conductive layers, including their successful application as mesoscopic photoelectrodes for perovskite solar cells.

Acknowledgements

This work was supported by the Russian Science Foundation under grant No. 17-19-01776.

References

- [1] Shevaleevskiy O. The future of solar photovoltaics: from physics to chemistry. *Pure Appl. Chem.*, 2008, **80**, P. 2079–2089.
- [2] Kuznetsov S.V., Morozov O.A., et al. $Ca_{1-x-y}Yb_xPr_yF_{2+x+y}$ solid solution powders as a promising materials for crystalline silicon solar energetics. *Nanosystems: Phys. Chem. Math.*, 2018, **9** (2), P. 259–262.
- [3] Shi Z., Jayatissa A.H. Perovskite solar cells: from the atomic level to film quality and device performance. *Materials*, 2018, **57** (10), P. 2554–2569.
- [4] Ho-Baillie A. Perovskites cover silicon textures. *Nat. Energy*, 2018, **17**, P. 751–752.
- [5] Marinova N., Tress W., et al. Light harvesting and charge recombination in $CH_3NH_3PbI_3$ perovskite solar cells studied by hole transport layer thickness variation. *ACS Nano*, 2015, **9**, P. 4200–4209.
- [6] Vildanova M.F., Kozlov S.S., et al. Niobium-doped titanium dioxide nanoparticles for electron transport layers in perovskite solar cells. *Nanosystems: Phys. Chem. Math.*, 2017, **8** (4), P. 540–545.
- [7] Vildanova M.F., Nikolskaia A.B., et al. Novel types of dye-sensitized and perovskite-based tandem solar cells with a common counter electrode. *Tech. Phys. Lett.*, 2018, **44** (2), P. 126–129.
- [8] Kozlov D.A., Lebedev V.A., et al. The microstructure effect on the Au/TiO₂ and Ag/TiO₂ nanocomposites photocatalytic activity. *Nanosystems: Phys. Chem. Math.*, 2018, **9** (2), P. 266–278.
- [9] Ganguly A., Nath S.S., Gope G., Choudhury M. CdS quantum dot sensitized zinc oxide based solar cell with aluminum counter electrode. *Nanosystems: Phys. Chem. Math.*, 2017, **8** (6), P. 782–786.
- [10] Rath M.S., Ramakrishna G., Mukherjee T., Ghosh H.N. Electron injection into the surface states of ZrO_2 nanoparticles from photoexcited quinizarin and its derivatives: effect of surface modification. *J. Phys. Chem. B*, 2005, **109**, P. 20485–20492.
- [11] Bugrov A.N., Almjasheva O.V. Effect of hydrothermal synthesis conditions on the morphology of ZrO_2 nanoparticles. *Nanosystems: Phys. Chem. Math.*, 2013, **4**, P. 810–815.
- [12] Almjasheva O.V., Krasilin A.A., Gusarov V.V. Formation mechanism of core-shell nanocrystals obtained via dehydration of coprecipitated hydroxides at hydrothermal conditions. *Nanosystems: Phys. Chem. Math.*, 2018, **9** (4), P. 568–572.
- [13] Kolesnik I.V., Lebedev V.A., Garshev A.V. Optical Properties and photocatalytic activity of nanocrystalline TiO₂ doped by 3d-metal ions. *Nanosystems: Phys. Chem. Math.*, 2018, **9** (3), P. 401–409.
- [14] Bi D., Moon S.J., et al. Using a two-step deposition technique to prepare perovskite ($CH_3NH_3PbI_3$) for thin film solar cells based on ZrO_2 and TiO₂ mesostructures. *RSC Advances*, 2013, **3** (41), P. 18762–18766.
- [15] Shevaleevskiy O.I., Nikolskaia A.B., et al. Nanostructured TiO₂ Films with a Mixed Phase for Perovskite Solar Cells. *Russ. J. Phys. Chem.*, 2018, **12** (4), P. 663–669.
- [16] Almjasheva O.V., Smirnov A.V., et al. Structural features of ZrO_2 - Y_2O_3 and ZrO_2 - Gd_2O_3 nanoparticles formed under hydrothermal conditions. *Russ. J. Gen. Chem.*, 2014, **84** (5), P. 804–809.
- [17] Tauc J., Grigorovici R., Vancu A. Optical properties and electronic structure of amorphous germanium. *Phys. St. Sol.*, 1966, **15**, P. 627–637.
- [18] Kim H.-S., Lee C.-R., et al. Lead iodide perovskites all-solid-state submicron thin film mesoscopic solar cell with efficiency exceeding 9%. *Sci. Rep.*, 2012, **2**, 591.
- [19] Oum K., Lohse P.W., et al. Photoinduced ultrafast dynamics of the triphenylamine-based organic sensitizer D35 on TiO₂, ZrO₂ and in acetonitrile. *Phys. Chem. Chem. Phys.*, 2013, **15**, P. 3906–3916.
- [20] Nikolay T., Larina L., Shevaleevskiy O., Ahn B.T., Electronic structure study of lightly Nb-doped TiO₂ electrode for dye-sensitized solar cells. *Energ. Environ. Sci.*, 2011, **4**, P. 1480–1486.
- [21] Kozlov S., Nikolskaia A., et al. Rare-earth and Nb doping of TiO₂ nanocrystalline mesoscopic layers for high-efficiency dye-sensitized solar cells. *Phys. St. Sol. A*, 2016, **213**, P. 1801–1806.

Injectable ultra soft hydrogel with natural nanoclay

V. S. Molchanov, M. A. Efremova, T. Yu. Kiseleva, O. E. Philippova

Department of Physics, Lomonosov Moscow State University, Leninskie Gory, 1, bld. 2, Moscow, 119991, Russia
molchan@polly.phys.msu.ru

PACS 82.70.Uv. 82.70.Dd

DOI 10.17586/2220-8054-2019-10-1-76-85

Soft hydrogels based on a transient network of wormlike surfactant micelles containing bentonite nanoclay tactoids as physical cross-links were developed. The network was composed of mixed micelles of nontoxic zwitterionic surfactant oleylamidopropyltrimethylcarboxybetaine and an anionic surfactant sodium dodecyl sulfate. It was demonstrated that before nanoclay addition the solution has pronounced viscoelastic properties with zero-shear viscosity of 100 Pa s and plateau modulus around 7 Pa, which were attributed to the formation of an entangled micellar network. The solution demonstrated pronounced shear thinning behavior provided by the elongation of wormlike micellar chains in flow direction. Upon addition of non-exfoliated nanoclay particles, the zero-shear viscosity increases by an order of magnitude, while the useful property of shear-induced thinning is retained. Oscillation amplitude tests show that viscoelastic fluid becomes hydrogel upon addition of nanoclay, because elastic response was observed even at large stress amplitudes. This behavior was attributed to the formation of nanoclay-wormlike micelles junctions. Prepared soft hydrogel is a promising candidate for injection applications, because of its self-assembled structure providing pronounced shear-thinning behavior and fast recovery of rheological properties at rest. In this nanocomposite material, nanoclay tactoids strengthen the hydrogels and can serve as reservoirs for the delivery of various substances.

Keywords: surfactant, wormlike micelles, rheology, nanoclay, bentonite, hydrogel.

Received: 15 November 2018

Revised: 29 January 2019

1. Introduction

Injectable nanocomposite hydrogels represent an ever-growing class of nanomaterials possessing a unique combination of physical and chemical properties. For injection applications, the hydrogels should demonstrate a shear-thinning behavior resulting in a significant decrease in viscosity when subjected to shear strain and a fast recovery of the initial state, when the deformation is no longer applied. Such hydrogels can be used as control delivery systems since they can be delivered in a minimally *invasive* manner because the final form and shape are defined by the space into which they are injected.

Injectable hydrogels can be based either on polymer network or on self-assembled network of wormlike surfactant micelles (WLMs). Polymer hydrogels are classically defined as three-dimensional, water-swollen polymer networks formed as a result of physical or chemical cross-linking [1,2]. For injectable hydrogels application physically cross-linked polymer networks are preferred. They are disrupted under shear deformation during injection and then reassembled at rest due to recovery of noncovalent cross-links between the macromolecules. To provide additional functionality to the matrix the hydrogels can contain delivery vehicle components, for instance, nanoclay tactoids, which make them very promising for drug delivery and tissue engineering applications [3–5].

Another type of injectable hydrogels is based on WLMs [6–9]. Such micelles are often compared with polymers and have even been given the name of living polymers [10–12], because they incessantly break and recombine. With increasing surfactant concentration, solutions of WLMs become viscoelastic and at certain conditions, a transient network of entangled micellar chains is formed. Such a network possesses gel-like properties. In particular, its rheological properties demonstrate plateau modulus, low values of loss factor and pronounced shear- or stress-thinning behavior. At the same time, under high deformation, the micellar chains are disrupted, which induces a much more pronounced drop of viscosity than the disruption of physical cross-links in polymer gels [12, 13], which is advantageous for injection applications. The disrupted micellar chains are completely recovered due to restoration of non-covalent bonds between surfactant molecules within the micelles [12]. Thus, WLM-based hydrogels are promising candidates for the preparation of injectable systems.

Properties of the WLM network can be modified by nanoparticles. Until now, only spherical inorganic particles were dispersed within WLM network [14–20]. It was shown that these particles can significantly increase the rheological properties. For instance, near the overlap concentration of WLMs silica nanoparticles incorporated within similarly charged WLM solutions [15] induced liquid to viscoelastic fluid transition. This was explained by the formation of micelle-nanoparticle junctions as a result of binding of the WLMs to the layer of surfactant adsorbed on the particle's surface [15]. It was suggested that the WLMs are connected to surfactant layer on the

particle surface by their end-caps because these parts are energetically less favorable in comparison with cylindrical central parts of the micelles. Similar results were obtained for silica nanoparticles oppositely charged with respect to WLMs [14,18]. At the same time, addition of particles into dense WLM network either decreased rheological properties or did not significantly alter them [14,18].

In addition to silica nanoparticles, some functional nanoparticles were incorporated into WLM networks including pyroelectric [16] and magnetic particles [17,19,20]. Introduction of pyroelectric particles made the hydrogel sensitive to temperature variation. Heating increased the charge on the surface of particles thereby strengthening their interaction with oppositely charged surfactant micelles and enhancing the rheological properties [16]. In their turn, magnetic particles imparted magnetoresponsive properties to WLM hydrogel [17,19,20]. The aggregation of particles into chain-like/column structures because of magnetization resulted in a solid-like behavior even in rather low magnetic fields and at small volume fraction of particles, indicating the weak restrictions imposed by the matrix on the reorganization of particles in the field, which can be due to the self-assembled structure of the micellar network [19].

Thus, many types of particles were incorporated within WLM network but such systems were never tested for injection purposes. This gap is filled in the present paper. Moreover, instead of spherical particles we use plate-like particles of natural nanoclay bentonite. We suggest that large surface area of such particles will additionally stimulate the formation of WLM-particles junctions acting as cross-links in the network. Also, the interior volume of these particles is quite promising for the incorporation and further delivery of different substances [21,22].

For the preparation of the WLM hydrogel, the nontoxic zwitterionic surfactant oleylamidopropyldimethylcarboxybetaine (OB) was used. This surfactant can make transient network of long WLMs, as was shown recently [23,24]. Betaines demonstrate a strong synergism when mixed with anionic surfactant [25], in particular, sodium dodecyl sulfate (SDS) [26]. For this reason, in the present paper, a small amount of SDS is added to OB. Zwitterionic surfactants are the most eco-friendly and biocompatible type of the surfactants widely applied in different cosmetic products. To the best of our knowledge, soft nanocomposites based on the zwitterionic surfactant were not previously investigated.

Thus, the present paper is devoted to the preparation and study of soft nanocomposite hydrogels based on network of WLMs composed of zwitterionic and anionic surfactants with embedded plate-like bentonite nanoclay particles. It is shown that nanoparticles significantly enhance the rheological properties of WLM hydrogel, acting as physical cross-links between micellar chains. It was demonstrated that the prepared nanocomposite hydrogels possess promising properties for injection applications.

2. Experimental section

2.1. Materials

Zwitterionic surfactant OB (Fig. 1) with molar mass 450.5 g/mol and density of 1.1 g/cm³ was purchased from SPF NIIPAV (Russia) as a solution containing 29.0 wt. % OB, 0.5 wt. % oleylamidopropyldimethylamine, 4.0 wt. % sodium chloride, 17.0 wt. % isopropanol, and 49.5 wt. % water. To recover the solids the solvents were removed by lyophilization. The complete removal of isopropanol was confirmed by ¹H NMR spectroscopy. The resulting dried solid contained 85.0 wt. % OB (surfactant), 1.44 wt. % oleylamidopropyldimethylamine, and 13.56 wt. % sodium chloride. The carboxylic group of OB has pK = 2 [27], at the pH range under study (pH = 11÷11.5) it is always charged and therefore the OB molecules are in the zwitterionic form. The ratio between sodium chloride and OB is stoichiometric, since sodium and chloride ions are counterions of the charged groups of the surfactant. The third component of the mixture – oleylamidopropyldimethylamine is a byproduct of the synthesis OB. Note that the molar ratio between oleylamidopropyldimethylamine and OB surfactant is very small (1:51), and at the experimental conditions (pH = 11÷11.5) the amine is uncharged, therefore it cannot appreciably affect the behavior of the OB surfactant.

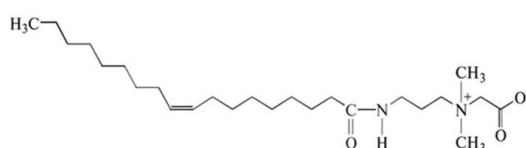


FIG. 1. Chemical structure of zwitterionic surfactant oleylamidopropyldimethylcarboxybetaine (OB)

The anionic surfactant SDS, with molar mass of 265 g/mol and density of 1.0 g/cm³ was purchased from Helicon. Bentonite nanoclay with density of 2.4 g/cm³ was provided by Sigma-Aldrich. Its specific surface area is 63 m²/g [28]. The surface of bentonite nanoclay platelets contains Al–OH, Mg–OH and Si–OH functional groups [29]. At pH range under study (pH = 11 – 11.5), the clay carries negative charge both on the face and at the edge of a platelet [30]. Sodium hydroxide with purity 85 % and molar mass 56.11 g/mol was purchased from Riedel-de Haen. Double distilled water purified on Milli-Q Millipore Waters was used as a solvent.

2.2. Organoclay preparation

It is well known [31–34] that clay can adsorb ionic surfactants both on the external surface and into the interlayer region of tactoids (stacks of parallel clay platelets). As a result, the exchangeable ions can be transferred from the tactoids to the solution. Therefore, when clay is added to a solution of WLMs, the effective concentration of a surfactant in the solution can decrease, whereas the concentration of ions can increase. To prevent these effects, we prepared organoclay saturated with the surfactant, thus ensuring that the clay will not adsorb more surfactant from the solution.

Three different types of organoclays were prepared: (i) clay saturated with only SDS (anionic organoclay), (ii) clay saturated with only OB (zwitterionic organoclay), and (iii) clay saturated with both these surfactants (mixed organoclay). To prepare each type of clay, the bentonite (4 wt. %) was added to water containing an excess of surfactant (0.6 wt. %). The resulting dispersions were stirred with a magnetic stirrer for two days for complete intercalation of surfactant into the clay. Then saturated clay was separated from the surfactant solution by centrifugation (10 min at a speed of 5000 rpm) and rinsed several times with distilled water. As was demonstrated previously [31–34], after these operations the intercalated surfactant remains between the clay platelets. The saturated organoclay thus prepared was dried for 3 days at 50 °C and then ground in an agate mortar. As was demonstrated previously [34], after these operations the intercalated surfactant remains between the clay platelets.

2.3. Characterization methods

2.3.1. Transmission electron microscopy (TEM). TEM experiments were performed on transmission electron microscope LEO912 AB OMEGA. To prepare samples for TEM examination, a drop of 0.01 wt. % aqueous dispersion of clay was deposited on the grid and dried.

2.3.2. X-ray diffraction. Powder X-ray diffraction patterns were recorded on a Empyrean PANalytical diffractometer in θ - 2θ geometry using CuK α radiation ($\lambda_{k\alpha}(\text{Cu}) = 0.15406$ nm). Patterns were processed using HighScore software and structure database JSPDS.

2.3.3. Elemental analysis. CHN elemental analysis of the modified nanoclay samples was performed with Vario Micro Cube Elementar Analyzer (Germany). The technique is based on the quantitative flash combustion method. In the combustion process (at ca. 1000 °C), carbon is converted to carbon dioxide; hydrogen to water; nitrogen to nitrogen gas/oxides of nitrogen. The gases are then passed through the absorbent traps in order to leave only carbon dioxide, water, nitrogen and then analyze them.

2.3.4. Rheology. Experiments were performed on rheometer Anton Paar Physica MCR301 at 25 °C. Steady shear measurements were carried out by setting shear stress σ and measuring shear rate $\dot{\gamma}$. Oscillation amplitude tests were carried out at a fixed frequency of 1 rad/s. Recovery test was carried out at fixed frequency of 6 rad/s and step-like amplitudes of 0.1 and 20 Pa, which correspond respectively to linear and non-linear regimes. In the last case, the amplitude was so high that the network should be disrupted.

In all experiments, the cone-plane measuring cell CP50-1 with diameter 49.973 mm, angle 10 and sample volume 0.78 ml was used.

3. Results and discussion

3.1. Clay and organoclay characterization

The nanoclay particles were visualized by TEM. The image of bentonite is presented on Fig. 2. Similar TEM images were obtained for three different types of organoclay. They show that the average size of clay platelets is around 100 nm (Fig. 2, left). The platelets are aggregated in tactoids (Fig. 2, right) that is the interaction with surfactants does not induce a full exfoliation of clay layers. This suggests rather weak adsorption of the surfactants by the clay.

To estimate the amount of the adsorbed surfactants, elemental analysis was employed. The estimation was made taking into account that all surfactants have carbon atoms, while clay itself does not contain them. In addition, among the surfactants under study, the zwitterionic surfactant has nitrogen. The results of estimation

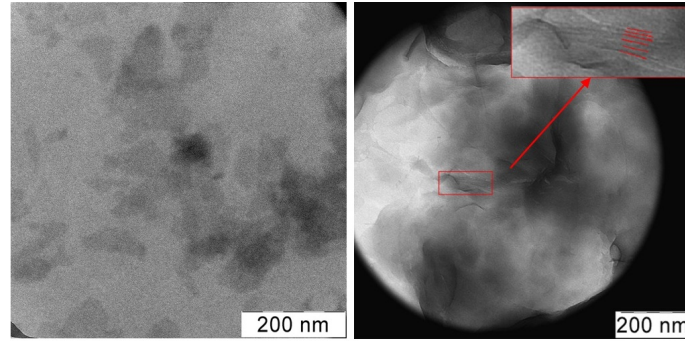


FIG. 2. TEM micrographs of bentonite. Magnified image (inset) demonstrates an inner structure of clay tactoid

TABLE 1. Characteristics of the clay samples

Clay	Interlayer space d_{001} , nm	Amount of adsorbed surfactant	
		in mmol/g	in % of CEC
Bentonite	1.301	0	0
Organoclay with anionic surfactant	1.437	0.08	1.6
Organoclay with zwitterionic surfactant	1.459	0.27	8.0
Organoclay with mixed anionic and zwitterionic surfactants	1.356	0.03	0.7

are given in Table 1. The obtained values represent the total amount of the surfactant molecules intercalated within tactoids and adsorbed on their surface. It is seen that among the surfactants under study, the zwitterionic surfactant is more effectively adsorbed by the clay. Its adsorption is provided by electrostatic and hydrophobic interactions [31,32]. However, even in this case, the amount of the adsorbed surfactant is much smaller than the cation exchange capacity (CEC) of bentonite equal to 90 – 110 mmol/100 g [29,34] usually characterizing the amount of intercalated surfactant molecules which can exfoliate tactoids as a result of the removal of all exchangeable ions [31,34]. This value can be achieved by cationic surfactants, which strongly bind on oppositely charged clay surfaces. As seen from Table 1, the adsorption of zwitterionic surfactant reaches only 8 % of CEC. As to anionic surfactant, its adsorption is even smaller (1.6 % of CEC), which may be attributed to electrostatic repulsion with similarly charged clay surface. Some amount of anionic surfactant adsorption, which is still occurs on the clay, may be due to hydrophobic interactions. By contrast, in the case of zwitterionic surfactant, the electrostatic attraction should also contribute to the adsorption resulting in the increase of the adsorption capacity. From Table 1, one can see that mixed organoclay contains the lowest amount of surfactant. Probably, this pair of surfactants prefers to form mixed micelles in the solution rather than to intercalate into the clay.

With the surfactant intercalation, the space between the clay layers increases due to the large size of the surfactant molecules [32]. To measure the gap between the clay platelets, X-ray diffraction (XRD) analysis was performed. XRD patterns of bentonite and three types of organoclay: anionic, zwitterionic and mixed are presented in Fig. 3. Analysis of the peaks using the database for clays JSPDS shows that the closest structure, which describes the position of the diffraction peaks is montmorillonite, the main component of bentonite. The diffraction patterns show that the positions of these peaks are similar for bentonite and organobentonite. Reflection peak (001) at the lowest angle corresponds to a distance between the platelets. Other peaks correspond to the inner crystalline structure of the platelets, and their position does not depend on the presence of surfactant molecules between the platelets. As to the (001) peak, in organoclays it is shifted towards lower angles (Fig. 3), pointing to an increase in the interlayer distances d , which can be estimated from the formula $d = \frac{\lambda}{2 \sin \theta}$, where $\lambda = 0.154$ nm is the wavelength of $K\alpha$ -radiation of copper.

The interlayer distance d values are summarized in Table 1. It is seen that for unmodified bentonite, the distance d is 1.301 nm, and it increases for organoclays, which suggests the intercalation of surfactants in the interlayer space of the clay. From Table 1, one can see that the most pronounced increase of d_{001} is observed

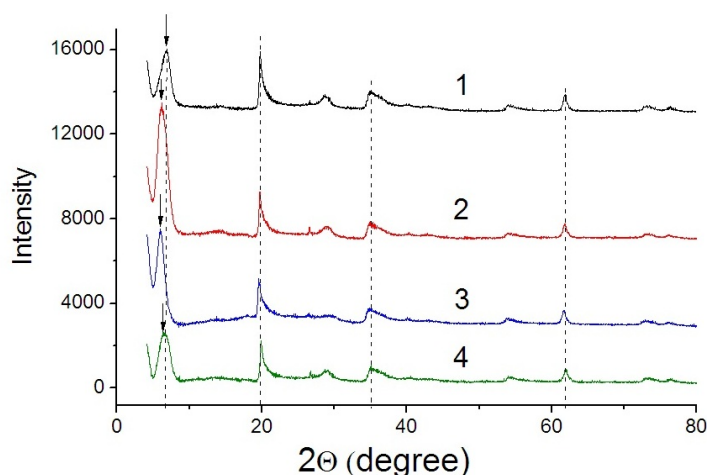


FIG. 3. XRD patterns of bentonite (top curve 1) and different organoclays: anionic (2), zwitterionic (3) and mixed (4). For clarity the intensity of the curves 1, 2, 3 was multiplied by 40, 20 and 10, respectively

for zwitterionic organoclay, which is more saturated with surfactant than other organoclays. Mixed organoclay contains the lowest amount of surfactant and the gap between platelets is increased only slightly. As to anionic clay, surprisingly its interlayer distance is increased significantly compared to untreated bentonite, whereas the amount of adsorbed surfactant is rather low. This may be due to the electrostatic repulsion between the clay and the intercalated surfactant.

It is important to note that in all types of organoclay, the intercalation of surfactant does not lead to exfoliation, as the peak corresponding to periodic packing of platelets in tactoids saves its shape. Most of the observed tactoids are composed of 6 – 10 clay platelets, therefore, the height of the tactoids is nearly 10 – 15 nm. Their axial ratio is about 1:8, because the average size of the clay platelets is around 100 nm.

Thus, it was shown that anionic and zwitterionic surfactants intercalate into the clay tactoids, but in small amounts, so that exfoliation does not occur. It suggests that the organoclay, which is used as a nanofiller of WLM network, retains the useful properties of the initial clay and it can serve e.g. as delivery vehicle for various substances embedded between the platelets.

3.2. Viscoelasticity of WLM networks with embedded nanoclay particles

Stable suspensions of mixed organoclay in viscoelastic surfactant solutions were prepared. For this purpose, 0.1 wt. % organoclay saturated with mixed surfactant was added to an aqueous solution of the same surfactant mixture (2 wt. % of zwitterionic surfactant OB and 0.1 wt. % SDS), which was used for the preparation of the organoclay. The concentration of organoclay under study was much less than the percolation threshold of the clay platelets (around 3 – 5 wt. %). At 0.1 wt.% content of the nanoclay, the sample was homogeneous and stable for a long period of time (for at least 6 months).

Before the addition of the organoclay, the surfactant solutions represented viscoelastic fluids. It should be noted that the 2 wt. % OB solution, even without SDS, possesses viscoelastic properties indicating to the presence of WLMs [23,24]. At the same time, the solution of 0.1 wt. % of SDS behaves as Newtonian liquid with very low viscosity close to pure water because at this concentration SDS forms only spherical micelles. The rheological properties of the mixed OB–SDS surfactant system suggest the presence of network of entangled WLMs (Figs. 4,5), since the zero-shear viscosity is several orders of magnitude higher than that of water and the dynamic rheological data demonstrate a large region of predominantly elastic response, where the storage modulus exceeds the loss modulus $G' > G''$ [35].

The influence of organoclay on the rheological properties of mixed WLMs of surfactants was studied. Fig. 4(a) shows the viscosity as a function of shear stress before and after the addition of nanoclay particles. At low stress, for both systems, one can see a plateau corresponding to zero-shear viscosity. Above a critical shear stress value (2 Pa), the viscosity of pure surfactant system sharply drops by 5 orders of magnitude, approaching the viscosity of pure water. So pronounced shear-thinning behavior is typical for the network of entangled WLMs. It was explained by shear-induced elongation of wormlike micellar chains in flow direction [36,37].

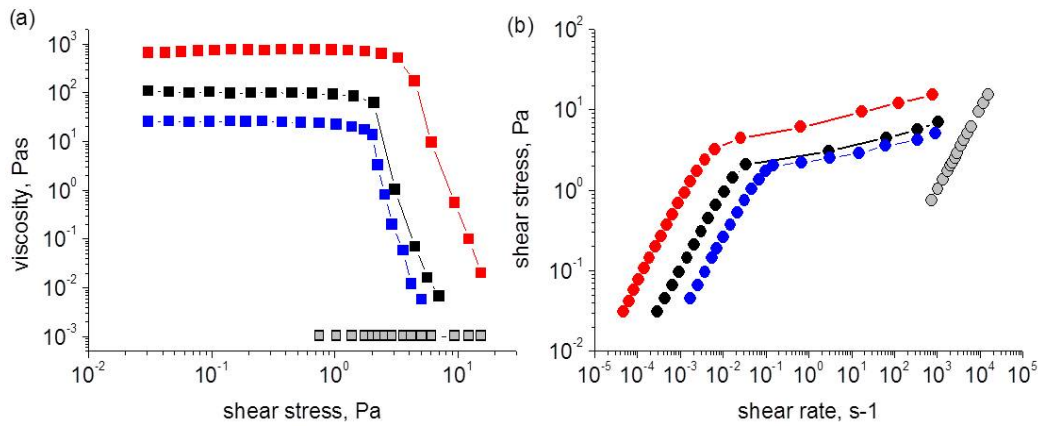


FIG. 4. Viscosity as a function of shear stress (a) and shear stress as a function of shear rate (b) for solutions of 2 wt.% zwitterionic OB (blue), 0.1 wt.% anionic SDS (grey), 2 wt.% zwitterionic OB surfactant and 0.1 wt.% anionic SDS surfactant before (black) and after (red) the addition of 0.1 wt.% bentonite

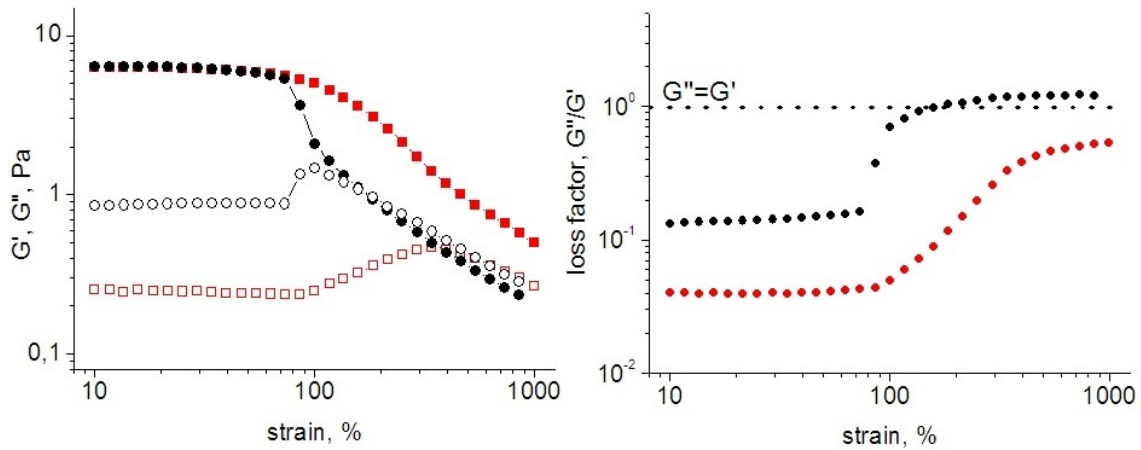


FIG. 5. Storage (filled symbols) and loss moduli (open symbols) as a function of oscillation amplitude at 1 rad/s (a) and the corresponding dependence of the loss factor for solution of 2 wt.% zwitterionic OB surfactant and 0.1 wt.% anionic SDS surfactant before (black) and after (red) the addition of 0.1 wt.% bentonite

In the presence of nanoclay particles, the overall behavior is still the same with a huge viscosity drop, but the zero-shear viscosity rises by one order of magnitude and the shear-thinning region starts from higher stress (Fig. 4(a)). The effect of nanoclay can be explained by the formation of nanoclay-WLM junctions. The particles covered by surfactant can act as physical cross-links of the WLM network similar to spherical inorganic particles [15, 17]. When organoclay is added into the surfactant network, the end-caps of WLMs as the most unfavorable parts of the micellar chains can fuse with surfactant aggregates on the particles. One can suggest that the point of the junction can slide along the nanoclay particles surface to get additional gain in entropy.

Figure 4(b) shows the shear stress as a function of shear rate before and after the addition of nanoclay particles. It is seen that very high shear rates can be achieved if we will overcome initial linear region. This is significant for the application of these gels as an injectable system. Fig. 4(b) demonstrates that in the presence of nanoclay, higher values of stresses are required to obtain the high shear rates that indicates the impact of nanoclay cross-links on the flow of the sample.

To determine the elastic response of both pure surfactant network and the nanocomposite network the oscillation stress was applied to the samples. At an angular frequency of 1 rad/s the storage G' and loss G'' moduli were measured as a function of the deformation amplitude (Fig. 5(a)). From Fig. 5(a) it is seen that at small amplitudes until 70 % in the absence of the nanoclay the storage modulus is higher than the loss modulus almost by one

order of magnitude pointing out to a gel-like behavior. The entanglements of the WLMs make three-dimensional network demonstrating such elastic response (Fig. 6 left). Moreover, these moduli do not depend on the amplitude, indicating that it is the region of linear viscoelasticity. Out of this region (i.e. at higher amplitudes), the storage modulus drops and becomes even lower than the loss modulus suggesting the transition to viscous flow state. This indicates that the number of entanglements in the WLM network decreases under action of high amplitude shear stresses.

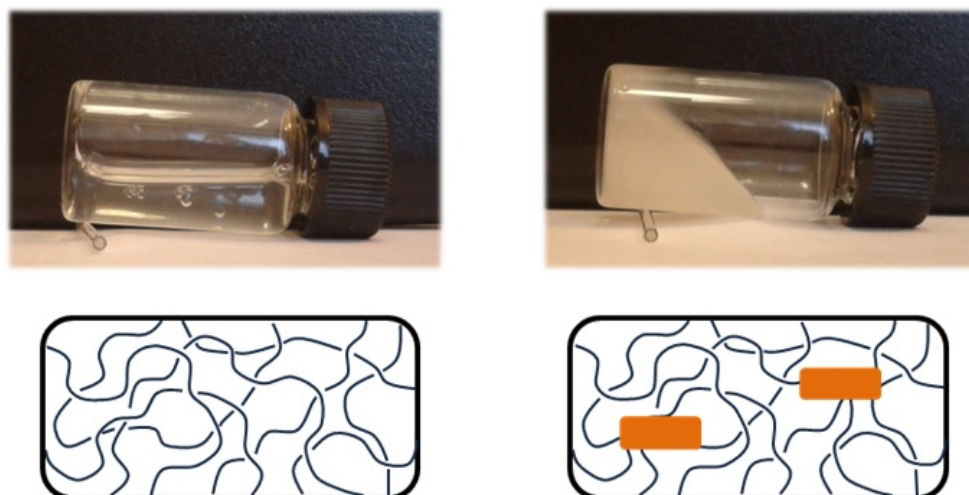


FIG. 6. Solution of 2 wt.% zwitterionic OB surfactant and 0.1 wt.% anionic SDS surfactant before (left) and after addition of 0.1 wt.% bentonite (right). The structure of the corresponding systems is shown on the schematic representations below the photos. Before the addition of nanoclay the solution contains entangled WLMs (left); after the addition of nanoclay the solution contains two types of cross-links: entanglements of WLMs and WLM/nanoclay junctions (right)

In the presence of nanoclay particles, at small amplitudes, the storage modulus retains its values, whereas the loss modulus drops significantly (Fig. 5(a)). This means that dissipated part of the response corresponding to WLM reptation motion supplemented by breaking and recombination processes becomes lower. This can be explained by the formation of additional bonds in the network due to cross-linking of the WLMs by nanoclay particles. At higher amplitudes the storage modulus decreases, but remains always higher than G'' up to as large amplitudes of deformation as 1000 %. We assume that at high amplitudes, the network partly disrupts: the number of the entanglements between the WLMs decreases, whereas the links between nanoclay and WLMs are strong enough so that the WLM/nanoclay junctions remain undisrupted providing predominantly elastic response ($G' > G''$) of the system. Thus, at low amplitudes, there are two types of cross-links in the network: entanglements between WLMs and WLM/nanoclay junctions (Fig. 6 right). With increasing amplitude, some of the entanglements disappear (since storage modulus for neat WLM network decreases), but the elastic response of the nanoclay containing network remains up to much higher amplitudes indicating that the strength of WLM/nanoclay junctions is higher than that of WLMs entanglements. Thus, nanoclay junctions in WLM network convert WLM viscoelastic fluid into soft WLM nanocomposite hydrogel.

Surprisingly, a maximum of loss modulus is observed at some oscillation amplitude both for pure surfactant and for nanocomposite networks (Fig. 5(a)). According to literature [38,39], it can be due to the interactions between the WLMs opposing their alignment induced by the strain. For instance, similar maximum was obtained for CTAB micelles with embedded hydrotrope ions [39]. This was attributed to the formation of connections between WLMs as a result of penetration of hydrotrope into two neighboring micellar chains. The same behavior is observed in the present system without any hydrotrope ions indicating that the WLMs can interact with each other in the absence of hydrotrope salt. When clay particles are added, the maximum of loss modulus becomes more pronounced and shifts toward large amplitudes indicating to stronger links between subchains in the nanocomposite network in comparison with the pure WLM network, thus pointing out to the cross-linking of WLMs by clay particles.

Figure 5(b) shows the loss factor (G''/G') as a function of amplitude of deformation for pure WLM and nanofilled systems. The value of loss factor lower than 1 ($G''/G' < 1$) indicates gel-like state, while higher values ($G''/G' > 1$) are inherent for viscous flow state for the samples. From Fig. 5(b), it is seen that with increasing

amplitude, a gel-to-liquid transition takes place in the absence of nanoclay, whereas when nanoclay is present, a gel-like state is observed in the whole range of deformation amplitudes up to 1000 %.

Thus, bentonite nanoclay particles can be incorporated into similarly charged WLM network and induce pronounced reinforcement of the structure (Fig. 6). The observed enhancement of rheological properties indicates to the formation of particles-WML physical junctions.

3.3. Recovery test

The oscillation recovery tests were carried out both at small (0.1 Pa) and high (20 Pa) stress amplitudes at fixed angular frequency (6 rad/s) to study breaking and recovery of the nanocomposite WLM network. Fig. 7(a) shows the storage and the loss moduli as a function of time under periodic change from low (0.1 Pa) to high (20 Pa) stress amplitude actions. It is seen that initially at low stress (cycle 1) $G' > G''$ indicating to the gel state of the system, but under high stress (cycle 2) storage modulus drops by almost 3 orders of magnitude and becomes lower than the loss modulus $G' < G''$ (liquid-like state). This suggests that at high amplitudes, the network disrupts because the cross-links and wormlike subchains themselves are formed by relatively weak physical interactions. At the same time, at further switching to low stress (cycle 3) the system rapidly turns back to the gel state $G' > G''$, which can be attributed to the reassembly of the nanocomposite surfactant network. From Fig. 7(a), it is seen that the disruption of the network is faster than the recovery. Gradual growth of the storage modulus takes tens of the seconds that is close to the typical relaxation time for the WLM networks [20,25]. Such restoring rate is comparable to the restoring rate of various injectable systems for wound healing application [5]. Fig. 7(b) demonstrates the variation of the loss factor under the same periodical action. It is seen that the loss factor jumps by 2 orders of magnitude from gel state ($G''/G' < 1$) into liquid state ($G''/G' > 1$). These high changes are more pronounced than those obtained for polymer-nanoclay hydrogel physically cross-linked by ions [5], where only cross-links are disrupted under high stress amplitudes, whereas the polymer chains remain intact. WLM-based network is more responsive to shear stress because not only cross-links, but also subchains can be disrupted under the stress. Thus, the WLM-based hydrogel have demonstrated high responsiveness to shear actions that makes it promising as an injectable system.

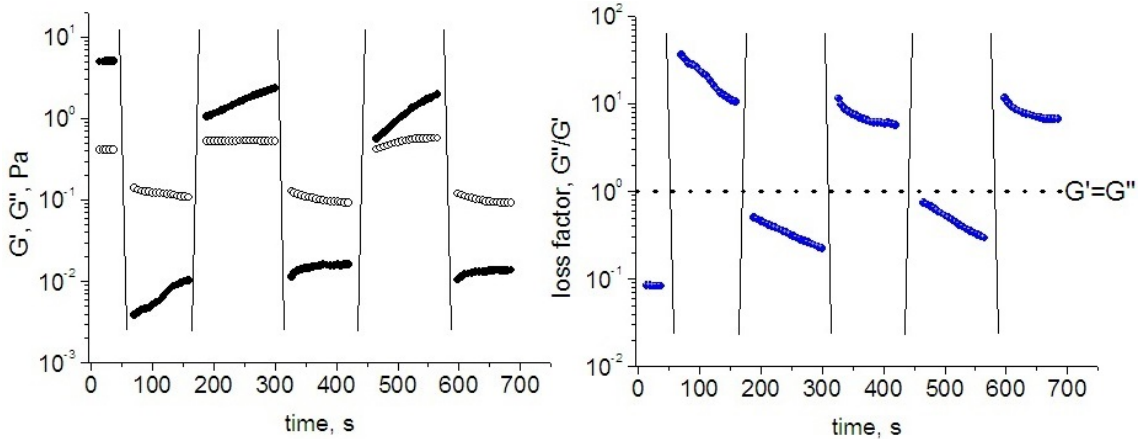


FIG. 7. Storage (filled symbols) and loss moduli (open symbols) as a function of time under periodic change of stress amplitude from 0.1 to 20 Pa at angular frequency of 6 rad/s (a) and the corresponding dependence of the loss factor (b) for solution of 2 wt.% zwitterionic OB surfactant and 0.1 wt.% anionic SDS surfactant containing 0.1 wt.% bentonite

4. Conclusions

The nanocomposite WLM-based soft hydrogels containing tactoid particles of bentonite organoclay are developed. It was found that the mixture of zwitterionic and anionic surfactant molecules adsorb only moderately on nanoclay tactoids and in much smaller amounts than the surfactant molecules taken separately. The adsorption of the surfactant molecules did not exfoliate nanoclay tactoids. A pronounced enhancement of rheological properties of transient WLM network induced by nanoclay was observed. It was explained by the formation of particle-WLM physical junctions reinforcing the network.

High zero-shear viscosity and plateau modulus of the nanoclay-WLM hydrogels at moderate stress and shear were detected, whereas significant shear- and amplitude-thinning effect at high stress was demonstrated. Shear-induced disruption of the hydrogel and further recovery were explained by reassembly of non-covalent links in WLM micelles and in nanoparticle-WLMs junctions.

The changes of rheological properties of WLM-based hydrogels induced by shear are more significant in comparison with polymer-based physical nanocomposite hydrogels. This was explained by subchain disruption of the WLM network under shear action in contrast to only cross-links disruption of polymer-based system. The observed properties make WLM-based nanocomposite hydrogels promising candidates for injectable applications, where nanoclay tactoids can be useful as delivery vehicles.

Acknowledgements

This work was supported by the Russian Science Foundation (project No. 17-13-01535).

References

- [1] Philippova O.E., Khokhlov A.R. Polymer gels. In *Polymer Science: A Comprehensive reference*, vol. 1, Elsevier B.V., USA, 2012, P. 339–366.
- [2] Philippova O.E., Chtcheglova L.A., Karybians N.S., Khokhlov A.R. Two mechanisms of gel/surfactant binding. *Polymer Gels and Networks*, 1998, **6**, P. 409–421.
- [3] Sharifi S., Blanquer S.B.G., Van Kooten T.G., Grijpma D.W. Biodegradable nanocomposite hydrogel structures with enhanced mechanical properties prepared by photo-crosslinking solutions of poly(trimethylene carbonate)-poly(ethylene glycol)-poly(trimethylene carbonate) macromonomers and nanoclay particles. *Acta Biomater.*, 2012, **8** (12), P. 4233–4243.
- [4] Li C., Shi G. Functional gels based on chemically modified graphenes. *Advanced Materials*, 2014, **26** (24), P. 3992–4012.
- [5] Lokhande G., Carrow J.K., et al. Nanoengineered injectable hydrogels from kappa-carrageenan and two-dimensional nanosilicates for wound healing application. *Acta Biomater.*, 2018, **70** (1), P. 35–47.
- [6] Rehage H., Hoffmann H. Rheological properties of viscoelastic surfactant systems. *J. Phys. Chem.*, 1988, **92** (16), P. 4712–4719.
- [7] Granek R., Cates M.E. Stress relaxation in living polymers: Results from a Poisson renewal model. *J. Chem. Phys.*, 1992, **96** (6), P. 4758–4767.
- [8] Philippova O.E. Self-assembled networks formed by wormlike micelles and nanoparticles. In *Wormlike Micelles: Advances in Systems, Characterisation and Applications*, Soft Matter Series, 2017, **6**, P. 103–120.
- [9] Shibaev A.V., Philippova O.E. Viscoelastic properties of new mixed wormlike micelles formed by a fatty acid salt and alkyipyridinium surfactant. *Nanosystems: Physics, Chemistry, Mathematics*, 2017, **8** (6), P. 732–739.
- [10] Berret J.-F., Appell J., Porte G. Linear rheology of entangled wormlike micelles. *Langmuir*, 1993, **9** (11), P. 2851–2854.
- [11] Dreiss C.A. Wormlike micelles: Where do we stand? Recent developments, linear rheology and scattering techniques. *Soft Matter*, 2007, **3** (8), P. 956–970.
- [12] Chu Z., Dreiss C.A., Feng Y. Smart wormlike micelles. *Chem. Soc. Rev.*, 2013, **42** (17), P. 7174–7203.
- [13] Khatory A., Lequeux F., Kern F., Candau S.J. Linear and nonlinear viscoelasticity of semidilute solutions of wormlike micelles at high salt content. *Langmuir*, 1993, **9** (6), P. 1456–1464.
- [14] Bandyopadhyay R., Sood A.K. Effect of silica colloids on the rheology of viscoelastic gels formed by the surfactant cetyl trimethylammonium tosylate. *J. Colloid Interface Sci.*, 2005, **283**, P. 585–591.
- [15] Helgeson M.E., Hodgdon T.K., Kaler E.W., Wagner N.J. Formation and rheology of viscoelastic “double networks” in wormlike micelle-nanoparticle mixtures. *Langmuir*, 2010, **26** (11), P. 8049–8060.
- [16] Luo M., Jia Z., et al. Rheological behavior and microstructure of an anionic surfactant micelle solution with pyroelectric nanoparticle. *Colloids and Surfaces A: Physicochem. Eng. Aspects*, 2012, **395**, P. 267–275.
- [17] Pletneva V.A., Molchanov V.S., Philippova O.E. Viscoelasticity of smart fluids wormlike micelles and oppositely charged magnetic particles. *Langmuir*, 2015, **31**, P. 110–119.
- [18] Fan Q., Li W., et al. Nanoparticles induced micellar growth in sodium oleate wormlike micelles solutions. *Colloid. Polym. Sci.*, 2015, **293** (9), P. 2507–2513.
- [19] Molchanov V.S., Pletneva V.A., et al. Soft magnetic nanocomposites based on adaptive matrix of wormlike surfactant micelles. *RSC Adv.*, 2018, **8** (21), P. 11589–11597.
- [20] Molchanov V.S., Klepikov I.A., Razumovskaya I.V., Philippova O.E. Magnetically tunable viscoelastic response of soft magnetic nanocomposites with wormlike surfactant micellar matrix. *Nanosystems: Physics, Chemistry, Mathematics*, 2018, **9** (3), P. 335–341.
- [21] Hosseini F., Hosseini F., Jafari S.M., Taheri A. Bentonite nanoclay-based drug-delivery systems for treating melanoma. *Clay Minerals*, 2018, **53** (1), P. 53–63.
- [22] Zhang Y., Peng M.L., et al. Emerging integrated nanoclay-facilitated drug delivery system for papillary thyroid cancer therapy. *Scientific Reports*, 2016, **6**, AN33335.
- [23] Kelleppan V.T., Moore J.E., et al. Self-Assembly of long-chain betaine surfactants: effect of tail group structure on wormlike micelle formation. *Langmuir*, 2018, **34** (3), P. 970–977.
- [24] McCoy T.M., King J.P., et al. The effects of small molecule organic additives on the self-assembly and rheology of betaine wormlike micellar fluids. *J. Colloid Interface Sci.*, 2019, **534**, P. 518–532.
- [25] Kuryashov D.A., Philippova O.E., et al. Temperature effect on the viscoelastic properties of solutions of cylindrical mixed micelles of zwitterionic and anionic surfactants. *Colloid J.*, 2010, **72**, P. 230–235.
- [26] Christov N.C., Denkov N.D., et al. Synergistic sphere-to-rod micelle transition in mixed solutions of sodium dodecyl sulfate and cocoamidopropyl betaine. *Langmuir*, 2004, **20**, P. 565–571.

- [27] Weers J.G, Rathman J.F., et al. Effect of the intramolecular charge separation distance on the solution properties of betaines and sulfobetaines. *Langmuir*, 1991, **7**, P. 854–867.
- [28] Tayebee R., Mazruy V. Acid-thermal activated nanobentonite as an economic industrial adsorbent for malachite green from aqueous solutions. Optimization, isotherm, and thermodynamic studies. *J. Water Environ. Nanotechnol.*, 2018, **3** (1), P. 40–50.
- [29] Baik M.H., Lee S.Y. Colloidal stability of bentonite clay considering surface charge properties as a function of pH and ionic strength. *J. Ind. Eng. Chem.*, 2010, **16**, P. 837–841.
- [30] Yao M., Zhang X., Lei L. Removal of reactive Blue 13 from dyeing wastewater by self-assembled organobentonite in a one-step process. *J. Chem. Eng. Data*, 2012, **57** (7), P. 1915–1922.
- [31] Zhu J., Qing Y., et al. Preparation and characterization of zwitterionic surfactant-modified montmorillonites. *J. Colloid Interface Sci.*, 2011, **360** (2), P. 386–392.
- [32] Belova V., Mohwald H., Shchukin D.G. Ultrasonic intercalation of gold nanoparticles into a clay matrix in the presence of surface-active materials. Part II: negative sodium dodecylsulfate and positive cetyltrimethylammonium bromide. *J. Phys. Chem.*, 2009, **113**, P. 6721–6760.
- [33] Yalçın T., Alemdar A., Ece Ö.I., Güngör N. The viscosity and zeta potential of bentonite dispersions in presence of anionic surfactants. *Materials Letters*, 2002, **57**, P. 420–424.
- [34] Kooli F. Exfoliation properties of acid-activated montmorillonites and their resulting organoclay. *Langmuir*, 2009, **25** (2), P. 724–730.
- [35] Molchanov V.S., Shashkina Y.A., Philippova O.E., Khokhlov A.R. Viscoelastic properties of aqueous anionic surfactant (potassium oleate) solutions. *Colloid J.*, 2005, **67** (5), P. 606–609.
- [36] Lerouge S., Berret J.-F. Shear-induced transitions and instabilities in surfactant wormlike micelles. *Adv. Polym. Sci.*, 2009, **230**, P. 1–71.
- [37] Molchanov V.S., Philippova O.E. Dominant role of wormlike micelles in temperature-responsive viscoelastic properties of their mixtures with polymeric chains. *J. Colloid Interface Sci.*, 2013, **394**, P. 353–359.
- [38] Hyun K., Kim S.H., Ahn K.H., Lee S.J. Large amplitude oscillatory shear as a way to classify the complex fluids. *J. Non-Newtonian Fluid Mech.*, 2005, **107**, P. 51–65.
- [39] Zhao Y. Rheological characterizations of wormlike micellar solutions containing cationic surfactant and anionic hydrotropic salt. *J. Rheology*, 2015, **59** (5), P. 1229–1259.

Effect of nitrogen impurities on ZnS polymorphism

I. S. Popov, A. S. Vorokh, A. N. Enyashin

Institute of Solid State Chemistry UB RAS, Ekaterinburg, Russia

popov@ihim.uran.ru

PACS 61.72.Vv, 61.72.Bb, 31.15.E-

DOI 10.17586/2220-8054-2019-10-1-86-91

The ZnS polymorphs – sphalerite and wurtzite – have the very close formation energies, setting their coexistence in nature. Moreover, numerous cases of a disordered phase formation based on these polymorphs have been registered. However, sphalerite is a common mineral, while wurtzite is rare. Perhaps the wider distribution of sphalerite can be explained by means of stabilizing effect from impurities. In this paper, the most stable form and the localization of nitrogen impurities in both ZnS polymorphs is screened using the methods of quantum chemistry. The influence of impurity on polymorphic wurtzite-sphalerite equilibrium is disclosed. According to the obtained results, the introduction of nitrogen impurities facilitates the domination of sphalerite over wurtzite.

Keywords: nitrogen impurity, ZnS polymorphism, polymorphic equilibria, ZnS nitridation, MD simulations.

Received: 27 December 2018

Revised: 19 January 2019

1. Introduction

In natural deposits, zinc sulfide occurs in the form of two polymorphs: sphalerite and wurtzite. Sphalerite is a more common mineral, while wurtzite is less frequent. Sphalerite is also predominant in ZnS of biogenic origin [1,2]. Wurtzite is a high-temperature phase formed from sphalerite when heated to 1020 °C [3]. The phase transition temperature can be significantly reduced by reducing the size of ZnS samples to nanoscale [4] or bringing sphalerite nanoparticles into contact with wurtzite-like ZnO nanoparticles [5]. According to theoretical estimations, the difference in the formation energies between wurtzite and sphalerite ZnS is negligibly small (~ 3.25 meV/atom) [6]. Both phases can be obtained with different degree of phase purity in the lab, depending on the conditions of synthesis [7–9]. In addition, there are examples of the formation of numerous intermediate polytypes and disordered structures, which can be derived from the wurtzite and sphalerite polymorphs [10]. The structures of disordered phases can be described as violations of the ZnS layers' alternation along the c direction of the hexagonal wurtzite lattice. The phase of wurtzite corresponds to the layers' alternation A–B–A–B–A–B along vector c , while sphalerite is formed by alternating A–B–C–A–B–C.

All factors affecting the formation of a particular ZnS phase in a solvent medium have not been fully identified, yet. The addition of the tetrabutylammonium hydroxide modifier to the alcohol solution leads to the formation of wurtzite, whereas sphalerite was mainly formed without the modifier [9]. This result was attributed by the authors [9] to the higher modifier adsorption energy on the crystal seed of the wurtzite phase. A mechanism for the ZnS crystal seed formation in water was proposed, relying on the molecular mechanics calculations and suggesting a higher stability of sphalerite seeds [11]. Other molecular dynamics studies show that wurtzite ZnS in vacuum is more stable in a nanoscale form [12], while wetting the surface with water leads to stabilization of sphalerite. A previous study [2] assumes that the interaction between the surface of biogenic ZnS nanoparticles with some peptides may contribute to the formation of a crystal with fewer defects due to a decrease in the polarity of the ZnS crystal surface. All these facts indicate a significant role of surface interactions in the formation of a ZnS crystalline structure of one or another type.

Impurities within the bulk are another factor that may have a significant impact on the stacking order of the ZnS layers. It was assumed in the past that under normal conditions another ZnS polymorph (matraite) could form in addition to sphalerite and wurtzite [13]. Currently, the matraite is identified as (111)-twined sphalerite [14], which twinning is likely forced by the admixtures of Fe, Mn, Cu, and In – the elements prone to accumulation in (111) plane of growing sphalerite. The role of Cu and In admixtures in ZnS was investigated [15]. It was shown that the concentration of these elements is higher in sphalerite than in wurtzite. Presumably, a higher concentration of Cu and In in the cubic lattice of sphalerite is associated with a greater symmetry similarity between the sphalerite and the CuInS₂ structure. Meanwhile, GaN has a structure similar to ZnS and is stable in the wurtzite phase. It was previously shown that the appearance of the sphalerite phase fragments within wurtzite GaN arose as a result of the introduction of a Zn impurity [16].

ZnS ores contain a large amount of various impurities. Namely, the traces of the following elements were found in samples of sphalerite: As, Sb, Bi, Sn, Ge, In, Mo, Pb, Cd, Fe, Mn, Cu, Hg, Ni, Co, Ag, Tl [17, 18]. Often, the mineral ZnS is accompanied by sulfides of iron, copper, lead and cadmium, which can both lower and increase the concentrations of individual impurity elements due to their redistribution [15, 17]. An impurity of N and C attributed to peptides was found in the biogenic samples of ZnS [19]. Many attempts have been undertaken to introduce a variety of dopants into synthetic ZnS: Mo [20], Ni [21], Sn [22], Cu [23, 24], Mn [23], N [25, 26], C [25], etc. The effect of these impurities on the formation of the ZnS crystal lattice remains often unknown and requires further research.

We have previously demonstrated that the O impurity replacing the S atoms has no significant effect on the mutual thermodynamic stability of the wurtzite and sphalerite phases, as well as of their mixed polytypes [27]. Here, the quantum chemistry method is employed to perform a comparative analysis of the chemical form, localization, and energy difference of the N impurity hosted at sphalerite and wurtzite lattices.

2. Computational details

The self-consistent-charge density-functional tight-binding method (DFTB) was used [28, 29]. This is an approximate method based on the density functional theory (DFT), enabling one to simulate the considerably large supercells. Hence, a low content of impurity within a periodic crystal can be studied, eliminating any spurious interaction between mirror images of the impurity atoms. A complete relaxation of the atomic positions and the optimization of lattice parameters were carried out, employing the periodic boundary conditions in Γ -point approximation as implemented in deMon program [30]. The 3OB-3-1 parametrization set of Slater-Koster parameters for description of all interatomic interactions was employed [31, 32]. In addition, the main conclusions of our study were confirmed by calculations on the DFT-GGA level using the SIESTA software package [33].

Extended $3a \times 3a \times 3a$ sphalerite and $3a \times 3\sqrt{3}a \times 3c$ wurtzite cells consisting of 216 atoms were used as the basic models. The admixture of nitrogen was introduced into these cells after complete optimization of their geometry. Nitrogen was represented as one of three chemical species: an atom impurity N, molecular ammonia NH_3 or ionic ammonium NH_4 . An impurity was hosted instead of the Zn or S single atoms as well as at the tetrahedral interstitial voids formed by four Zn or four S atoms. The octahedral voids in wurtzite were also considered. Different dispositions of the H atoms in the complex impurities (NH_3 and NH_4) relative to a ZnS crystal lattice were also taken into account. In a number of models, the possibility of a Zn or S vacancy near an impurity was considered as well as the introduction of additional H atoms with the formation of SH groups near an impurity. Hereafter, the only relaxation of atomic positions in the designed models of defective crystals was carried out, while the values of translation vectors were maintained the same as for the pristine model of ZnS. The thermodynamic stability of the models and the study of their electronic properties were performed after optimizing the model geometry.

Molecular dynamics (MD) simulations at the same DFTB level were used to confirm the kinetic stability of the most thermodynamically stable impurity defects. MD simulations have been performed using deMon code as for canonical ensembles (NVT). The annealing temperature was set to 100 K or 300 K. In all simulations, the temperature was controlled by global Berendsen thermostat with the time constant 100 fs. The MD trajectories were collected during the time interval of ~ 25 ps with the time step 0.1 fs.

Rendering of atomic structures and MD trajectories was performed using VMD software [34].

3. Results and discussion

3.1. Thermodynamic stability

According to the results obtained by DFTB, sphalerite is slightly more stable than wurtzite by only 0.2 meV/atom. DFT calculations indicate a larger difference in energies (1.3 meV/atom), which is closer to the result 3.25 meV/atom in [6]. In any case, such tiny differences may be attributed to a numerical error during computations.

An estimation of the thermodynamic stability of nitrogen impurity defects was performed according to the formation energies of nitrogen impurity defects in sphalerite or wurtzite (E_f , eV). The latter was calculated on the basis of DFTB simulations with respect to the pristine sphalerite crystal and the molecular species S_8 , N_2 , NH_3 and H_2 according to the following formula:

$$E_f = E_{mod} \cdot N - E_{ZnS} \cdot 2N_{Zn} - E_{NH3} \cdot 4N_N - E_{S8} \cdot (N_S - N_{Zn}) - E_{H2} \cdot (N_H - 3N_N),$$

where E_{mod} is the total energy of a model with a defect (eV/atom); N is the total number of atoms in a model; E_{ZnS} , E_{NH_3} , E_{S_8} , E_{H_2} are the total energies of sphalerite, NH_3 , S_8 , and H_2 , respectively, given in the eV/atom; N_{Zn} , N_S , N_N , N_H are the numbers of Zn, S, N and H atoms that make up the model ($N = N_{Zn} + N_S + N_N + N_H$).

The four types of the most stable nitrogen impurity defects in ZnS are listed in Table 1 and their consequence turns out to be similar for both sphalerite and wurtzite. The fifth possible defect in the rank is different: in sphalerite it is the introduction of NH_3 into the tetrahedral void formed by Zn atoms, while in wurtzite it is the introduction of NH_3 into the octahedral void formed by S atoms. The most stable state of nitrogen in both ZnS polymorphs is the substitution of one ZnS unit by NH_4SH unit. Its formation energy in sphalerite is found to be 0.54 eV lower, than in wurtzite. All the following defects in Table 1 demonstrate the same pattern: the appearance of nitrogen impurity in sphalerite is energetically more beneficial than in wurtzite. However, the relative difference between the same types of defects in the ZnS polymorphs increases, approaching 1 eV.

TABLE 1. The rank of the most thermodynamically stable models of nitrogen impurity defects in ZnS crystals. DFTB calculations

No.	Defect description	Defect formation energy, eV	
		sphalerite	wurtzite
I	replacement of a ZnS unit on NH_4HS unit	-0.19	+0.35
II	substitution of a Zn atom on NH_4	+0.72	+1.75
III	replacement of a ZnS unit on single NH_3 molecule	+1.82	+2.86
IV	substitution of a Zn atom on molecular NH_3	+1.82	+2.88

The difference between the formation energies of the same nitrogen impurity defects either in sphalerite or in wurtzite was confirmed by additional DFT calculations of the models I (Table 1) distinguished as the most stable defect type. The difference between the total energies of single defect in these models was estimated as 0.34 eV according to the DFT results, which is well comparable to 0.54 eV after DFTB calculation.

The simple substitution of an atom in a ZnS crystal for a single N atom impurity appears as the most unstable defect; e.g., the most stable model among these variants is the substitution of S atom by N with E_f 6.33 and 7.35 eV for sphalerite and wurtzite, respectively. The appearance of vacancies near an atomic N impurity leads only to further destabilization of the sphalerite and wurtzite lattices.

3.2. Kinetic stability

Molecular dynamics (MD) simulations were used to study the kinetic stability of three types of defects (I–III, Table 1) hosted in both sphalerite and wurtzite. The collection of the main results can be viewed at the links [35].

MD simulation of the model I from Table 1 was carried out at 300 K for sphalerite and at 100 and 300 K for wurtzite. This defect in the sphalerite crystal undergoes reversible changes: the NH_4 group decomposes to NH_3 molecule and H that forms the secondary SH group. The resulting NH_3 molecule is coordinated on the nearest Zn atom. Afterwards, the ammonium recombines. The same defect in the wurtzite crystal undergoes similar processes at 300 K, but ammonium recombination is not observed (Fig. 1). The defect is stable only at 100 K, where the decay of NH_4 is not observed.

Model II from Table 1 was investigated at 100 and 300 K for sphalerite and at 100 K for wurtzite. The defect in sphalerite is subject to reversible decomposition into NH_3 and SH at 100 K and irreversible decomposition at 300 K. Released NH_3 molecule binds to one of the Zn atoms. Hence, the initial structure of this defect is kinetically unstable. This defect in wurtzite also disintegrates already at 100 K.

MD simulations of model III from Table 1 at $T = 300$ K in both sphalerite and wurtzite demonstrate its kinetic stability. Molecular ammonia coordinates alternately at neighboring Zn atoms with dangling bonds.

Thus, single-type defects in wurtzite and sphalerite crystals exhibit similar kinetic stability. Replacement of a ZnS unit by a NH_4HS unit or by a single NH_3 molecule leads to the formation of a kinetically stable defect. The defect in which the Zn atom is replaced by single ammonium is kinetically unstable and prone to decomposition into NH_3 molecule and H joining the S atom.

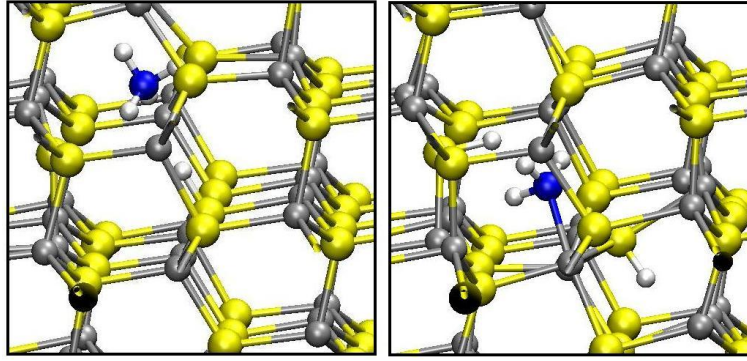


FIG. 1. Optimized model of the most thermodynamically stable nitrogen impurity defect (replacement of a ZnS unit on NH_4HS unit) in wurtzite (on the left) and the results of its MD simulation at $T = 300$ K (on the right, see also the supplementary movies 1 and 2 [35]). Atom color coding: Zn – gray, S – yellow, N – blue, H – white

3.3. Electronic properties

The electronic properties of sphalerite and wurtzite ZnS pristine crystals, as well as crystals containing various nitrogen impurity defects, were investigated using the DFTB method. The plots of the electron densities of states (DOS) for wurtzite crystals are given in Fig. 2. DOSs of sphalerite crystal with similar types of defects have the same appearance.

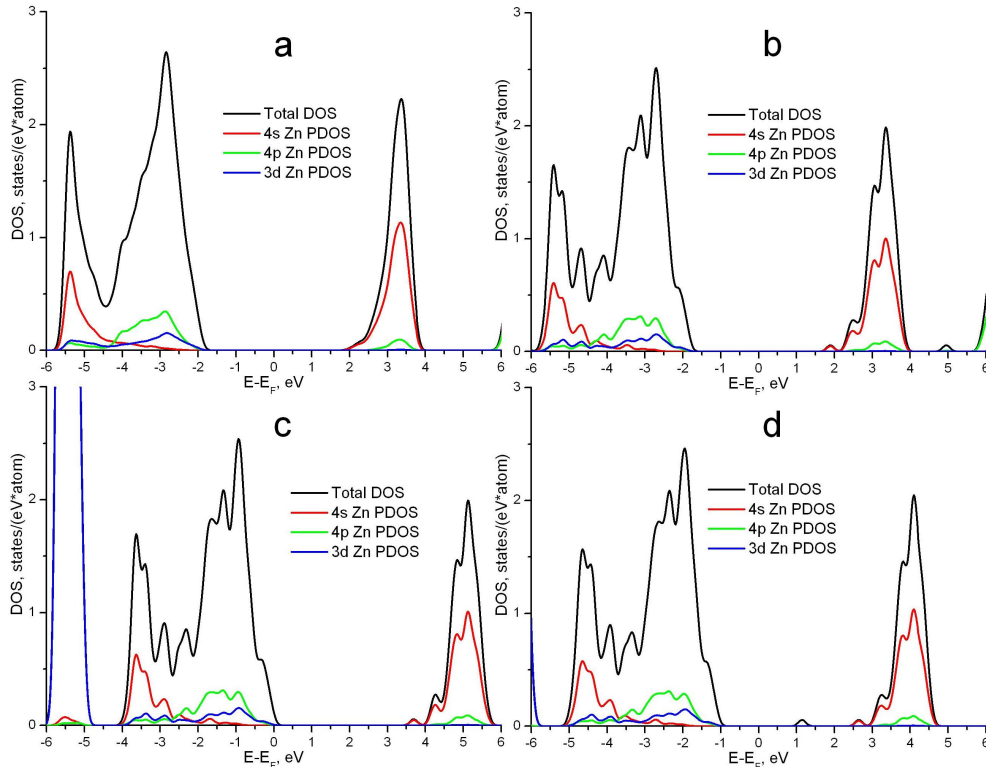


FIG. 2. Total and partial densities of states (DOS) for the wurtzite ZnS perfect crystal (a) and for the wurtzite ZnS crystal with different defects: replacement of a ZnS unit on NH_4HS unit (b), substitution of a Zn atom on NH_4 (c) substitution of a Zn atom on molecular NH_3 (d) (models I, II and IV in Table 1, respectively)

The sphalerite and wurtzite are semiconductors with the fundamental band gaps (E_g) equal to 3.73 and 3.80 eV, respectively (Fig. 2(a)). These values are in good agreement with the experimental data of 3.68 and 3.91 eV [36].

The valence band of both crystals is formed predominantly by $S3p$ states, and the bottom of conduction band by $Zn4s$ states.

Replacement of single ZnS unit by NH_4HS (model I, Table 1) leads to the splitting of a part of the localized $Zn4s$ states from the bottom of conduction band (Fig. 2(b)). Similar changes in DOS occur for the introduction of the NH_3 molecule at the tetrahedral void formed by four Zn and for the substitution of a ZnS unit on single NH_3 molecule (model III, Table 1).

Substitution of a Zn atom on NH_4 (model II from Table 1) leads to a shift of the Fermi level (E_F) to the edge of the valence band (Fig. 2(c)), which is characteristic for a p -type semiconductor. DOS near E_F are formed predominantly by $S3p$ states. Similar changes in DOS can be observed for other unstable defect – the replacement of one atom S by atom N which agrees with the earlier DFT study [37].

Substitution of a Zn atom on NH_3 molecule leads to a new state located within the fundamental band gap (Fig. 2(d)). This state is formed mainly by $S3p$ and $N2p$ orbitals. Orbitals' visualization of the electron wave function isosurfaces reveals that this state is strongly localized (Fig. 3), hence, it cannot lead to a decrease of the value E_g .

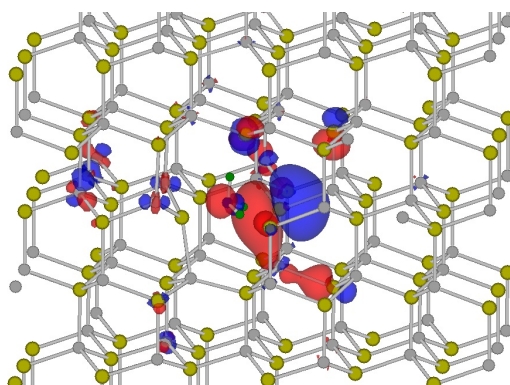


FIG. 3. Orbitals visualization of the electron wave function isosurface for the states located within the fundamental band gap of the model IV (Table 1). Color coding: Zn – gray, S – yellow, N – blue, H – green

4. Summary

A comparative analysis of the most stable form and the localization of nitrogen impurities in sphalerite and wurtzite ZnS crystals has been carried out using DFTB method. The effect of impurities on polymorphic equilibrium in ZnS is considered. It was found that the most stable type of N impurity, irrespective of the ZnS polymorph, is the substitution of one ZnS unit on NH_4SH . However, the thermodynamic stability of this defect depends on the ZnS polymorphism. The rise of this defect in the ZnS lattice leads to the removal of enthalpy degeneracy of wurtzite and sphalerite in favor of the latter. Perhaps, this effect may also be caused by other impurities, which would explain the wider distribution of sphalerite in nature.

Various types of N impurities modify differently the band gap of ZnS polymorphs. The most stable substitutional defect – the NH_4SH unit – may lead to a slight narrowing of the band gap.

Acknowledgements

The work was financially supported by the Russian Science Foundation (Grant No. 17-79-20165).

References

- [1] Posfai M., Dunin-Borkowski R.E. Sulfides in Biosystems. *Rev. Mineral. Geochem.*, 2006, **61**, P. 679–714.
- [2] Xu J., Murayama M., et al. Highly-defective nanocrystals of ZnS formed via dissimilatory bacterial sulfate reduction: A comparative study with their abiogenic analogues. *Geochim. Cosmochim. Acta*, 2016, **180**, P. 1–14.
- [3] Zhang H., Huang F., Gilbert B., Banfield J.F. Molecular Dynamics Simulations, Thermodynamic Analysis, and Experimental Study of Phase Stability of Zinc Sulfide Nanoparticles. *J. Phys. Chem. B*, 2003, **107**, P. 13051-13060.
- [4] Qadri S.B., Skelton E.F., et al. Size-induced transition-temperature reduction in nanoparticles of ZnS . *Phys. Rev. B*, 1999, **60** (13), P. 9191-9193.
- [5] Lin P.-C., Hua C.C., Lee T.-C. Low-temperature phase transition of ZnS : The critical role of ZnO . *J. Solid Chem.*, 2012, **194**, P. 282–285.
- [6] Boutaiba F., Belabbes A., Ferhat M., Bechstedt F. Polytypism in ZnS , $ZnSe$, and $ZnTe$: First-principles study. *Phys. Rev. B*, 2014, **89**, 245308.

- [7] Zhao Y., Zhang Y., et al. Low-Temperature Synthesis of Hexagonal (Wurtzite) ZnS Nanocrystals. *J. Am. Chem. Soc.*, 2004, **126**, P. 6874–6875.
- [8] Yin L.W., Bando Y., et al. Self-assembled highly faceted wurtzite-type ZnS single-crystalline nanotubes with hexagonal cross-sections. *Adv. Mater.*, 2005, **17**, P. 1972–1977.
- [9] La Porta F.A., Andres J., et al. Sphalerite versus wurtzite ZnS nanoparticles: control of the phase and optical properties by tetrabutylammonium hydroxide. *Phys. Chem. Chem. Phys.*, 2014, **16**, P. 20127–20137.
- [10] Huang F., Zhang H., Banfield J.F. The Role of Oriented Attachment in Crystal Growth in Hydrothermal Coarsening of Nanocrystalline ZnS. *J. Phys. Chem. B*, 2003, **107** (38), P. 10470–10475.
- [11] Luther G.W., Theberge S.M., Rickard D.T. Evidence for aqueous clusters as intermediates during zinc sulfide formation. *Geochim. Cosmochim. Acta*, 1999, **63**, P. 3159–3169.
- [12] Zhang H., Huang F., Gilbert B., Banfield J.F. Molecular Dynamics Simulations, Thermodynamic Analysis, and Experimental Study of Phase Stability of Zinc Sulfide Nanoparticles. *J. Phys. Chem. B*, 2003, **107**, P. 13051–13060.
- [13] Vasil'ev V.I. New data on the composition of metacinnabar and Hg-sphalerite with an isomorphous Cd admixture. *Russian Geology and Geophysics*, 2011, **52**, P. 701–708.
- [14] Nitta E., Kimata M., et al. Crystal chemistry of ZnS minerals formed as high-temperature volcanic sublimates: matraite identical with sphalerite. *J. Mineral. Petrol. Sci.*, 2008, **103**, P. 145–151.
- [15] Chaplygin I.V., Mozgova N.N., et al. Minerals of the system ZnS–CdS from fumaroles of the Kudriavyy volcano, Iturup Island, Kuriles, Russia. *Can. Mineral.*, 2007, **45**, P. 709–722.
- [16] Yang B., Liu B., et al. Zn-dopant dependent defect evolution in GaN nanowires. *Nanoscale*, 2015, **7**, P. 16237–16245.
- [17] George L.L., Cook N.J., Ciobanu C.L. Partitioning of trace elements in co-crystallized sphalerite–galena–chalcopyrite hydrothermal ores. *Ore Geol. Rev.*, 2016, **77**, P. 97–116.
- [18] Pfaff K., Koenig A., et al. Trace and minor element variations and sulfur isotopes in crystalline and colloidal ZnS: Incorporation mechanisms and implications for their genesis. *Chem. Geol.*, 2011, **286**, P. 118–134.
- [19] Moreau J.W., Weber P.K., et al. Extracellular Proteins Limit the Dispersal of Biogenic Nanoparticles. *Science*, 2007, **316**, P. 1600–1603.
- [20] Zhang R., Du B., et al. Molybdenum-doped ZnS sheets with dominant {111} facets for enhanced visible light photocatalytic activities. *J. Colloid Interface Sci.*, 2017, **507**, P. 200–208.
- [21] Kudo A., Sekizawa M. Photocatalytic H₂ evolution under visible light irradiation on Ni-doped ZnS photocatalyst. *Chem. Commun.*, 2000, **15**, P. 1371–1372.
- [22] Kumar K.C., Rao N.M., Kaleemulla S., Rao G.V. Structural, optical and magnetic properties of Sn doped ZnS nano powders prepared by solid state reaction. *Physica B: Condens. Matter*, 2017, **522**, P. 75–80.
- [23] Patel P.C., Ghosh S., Srivastava P.C. Effect of impurity concentration on optical and magnetic properties in ZnS: Cu nanoparticles. *Physica E: Low-dimens. Syst. Nanostruct.*, 2017, **93**, P. 148–152.
- [24] Al-Jawad S.M.H., Ismail M.M. Characterization of Mn, Cu, and (Mn, Cu) co-doped ZnS nanoparticles. *J. Opt. Techn.*, 2017, **84**, P. 495–499.
- [25] Muruganandham M., Kusumoto Y. Synthesis of N, C codoped hierarchical porous microsphere ZnS as a visible light-responsive photocatalyst. *J. Phys. Chem. C*, 2009, **113**, P. 16144–16150.
- [26] Popov I.S., Kozhevnikova N.S., et al. Nitrogen-doped ZnS nanoparticles: Soft-chemical synthesis, EPR statement and quantum-chemical characterization. *Mater. Chem. Phys.*, 2018, **215**, P. 176–182.
- [27] Popov I.S., Vorokh A.S., Enyashin A.N. Stability and electronic properties of oxygen-doped ZnS polytypes: DFTB study. *Chem. Phys.*, 2018, **510**, P. 70–76.
- [28] Seifert G. Tight-binding density functional theory: an approximate Kohn–Sham DFT scheme. *J. Phys. Chem. A*, 2007, **111**, P. 5609–5613.
- [29] Frauenheim T., Seifert G., et al. A Self-consistent charge density-functional based tight-binding method for predictive materials simulations in physics, chemistry and biology. *Phys. Status Solidi B*, 2000, **217**, P. 41–62.
- [30] Koster A.M., Flores R., et al. Program deMon (version 1.1.0). National Research Council, Ottawa, Canada, 2003.
- [31] Gaus M., Lu X., Elstner M., Cui Q. Parameterization of DFTB3/3OB for sulfur and phosphorus for chemical and biological applications. *J. Chem. Theory Comput.*, 2014, **10**, P. 1518–1537.
- [32] Lu X., Gaus M., Elstner M., Cui Q. Parameterization of DFTB3/3OB for magnesium and zinc for chemical and biological applications. *J. Phys. Chem. B*, 2015, **119**, P. 1062–1082.
- [33] Soler J.M., Artacho E., et al. The SIESTA method for ab initio order-N materials simulation. *J. Phys. Condens. Matter*, 2002, **14** (11), P. 2745–2779.
- [34] Humphrey W., Dalke A., Schulten K. VMD: Visual molecular dynamics. *J. Mol. Graphics*, 1996, **14**, P. 33–38.
- [35] Videolinks: (Movie 1) Defect model I in wurtzite. URL: <https://youtu.be/mr9ZP15Pj8Y>. (Movie 2) Defect model I in sphalerite. URL: https://youtu.be/dEy_K7hbN3c. (Movie 3) Defect model II in wurtzite. URL: <https://youtu.be/7yHPp6EEhA>. (Movie 4) Defect model II in sphalerite. URL: <https://youtu.be/q-HVyrS8QeQ>. (Movie 5) Defect model III in wurtzite. URL: <https://youtu.be/04-pDu1IruE>. (Movie 6) Defect model III in sphalerite. URL: https://youtu.be/_OHRE-Pfh3g.
- [36] Derek W.P. The semiconductors-information web-site. URL: <http://www.semiconductors.co.uk/propriivi5410.htm> (on the date 05.12.2018).
- [37] Long R., English N.J. Magnetic properties of first-row element-doped ZnS semiconductors: A density functional theory investigation. *Phys. Rev. B*, 2009, **80**, 115212.

PVP-stabilized tungsten oxide nanoparticles inhibit proliferation of NCTC L929 mouse fibroblasts *via* induction of intracellular oxidative stress

A. L. Popov¹, A. M. Ermakov¹, T. O. Shekunova^{2,4}, A. B. Shcherbakov³, O. N. Ermakova¹, O. S. Ivanova⁴,
N. R. Popova¹, A. Ye. Baranchikov⁴, V. K. Ivanov^{4,*}

¹Institute of Theoretical and Experimental Biophysics, Russian Academy of Sciences,
Pushchino, Moscow region, 142290, Russia

²Lomonosov Moscow State University, Moscow, 119991, Russia

³Zabolotny Institute of Microbiology and Virology, National Academy of Sciences of Ukraine,
Kyiv, D0368, Ukraine

⁴Kurnakov Institute of General and Inorganic Chemistry, Russian Academy of Sciences, Moscow, 119991, Russia
antonpopovleonid@gmail.com, ao_ermakovy@rambler.ru, taisia.shekunova@yandex.ru, carotene@igic.ras.ru,
beoluchi@yandex.ru, runetta05@mail.ru, nellipopovaran@gmail.com, a.baranchikov@yandex.ru, *van@igic.ras.ru

PACS 68.65.k, 81.20.n, 82.70.Dd, 82.50.Hp, 87.17.Ec

DOI 10.17586/2220-8054-2019-10-1-92-101

In this study, photochromic PVP-stabilized tungsten oxide nanoparticles (WO_{3-x} NPs) were shown to exhibit a dose-dependent cytotoxic effect on mouse fibroblasts *in vitro*. WO_{3-x} NPs reduce viability and proliferative activity of the cells *via* induction of intracellular oxidative stress leading to apoptosis and cell death. WO_{3-x} NPs modulate the mRNA expression of a wide range of genes responsible for oxidative stress and the cell redox-system.

Keywords: tungsten oxide nanoparticles, cytotoxicity, apoptosis, fibroblasts.

Received: 3 January 2019

Revised: 22 January 2019

1. Introduction

Metal oxide-based nanomaterials are widely used in biomedical applications as radioprotectors, radiosensitizers, photosensitizers, contrast agents, etc. One of the most promising X-ray contrast agents is nanocrystalline tungsten oxide (WO_{3-x}) [1–5]. In recent years, WO_{3-x} NPs have also been widely employed in antibacterial coatings or biosensors [6, 7]. Due to the specific physical and chemical properties of WO_{3-x} NPs, such as high surface energy and surface-to-volume ratio, quantum confinement effects and local plasmon resonance effects, they can be used in photothermal cancer therapy [8, 9]. Sharker *et al.* synthesized dopamine-conjugated hyaluronic acid-coated WO_3 nanoparticles (WO_3 -HA) which demonstrated quite efficient photothermal conversion with time-dependent tumor-specific accumulation [10]. Zhou *et al.* used tungsten oxide nanorods for effective photothermal therapy and CT imaging of the tumor model *in vivo* [11]. Liu *et al.* used PEGylated WO_{3-x} nanoparticles as photothermal agents under near-IR laser irradiation (980 nm, $0.5 \text{ W}\cdot\text{cm}^{-2}$). Additionally, PEGylated WO_{3-x} nanoparticles were shown to be effective CT imaging contrast agent on a tumor-bearing mouse model [12]. Liu *et al.* used ultrasmall WO_{3-x} @ γ -poly-L-glutamic acid (WO_{3-x} @ γ -PGA) nanoparticles with good photoacoustic and photothermal properties for effective photothermal-enhanced chemodynamic therapy [13]. AbuMousa demonstrated enhancement of photocatalytic activity of nanostructured silver loaded tungsten oxide providing high anticancer efficiency under UV radiation [14].

The usage of tungsten oxide in advanced therapeutic compositions requires an in-depth systematic study of their cytotoxicity including detailed investigation of molecular mechanisms of WO_{3-x} NPs action on mammalian cells. Here, we analyzed the cytotoxicity of PVP-stabilized WO_{3-x} nanoparticles using the mouse fibroblasts NCTC L929 cell line and provided the first report on the molecular mechanisms of WO_{3-x} nanoparticles' cytotoxic action.

2. Materials and methods

2.1. Synthesis and characterization of tungsten oxide nanoparticles

Ultrasmall hydrated tungsten oxide nanoparticles were synthesized by hydrothermal processing of tungstic acid in the presence of polyvinylpyrrolidone (PVP K-30, average mol. wt. 40,000) acting as template, stabilizer and growth regulator. Tungstic acid was prepared by ion-exchange method using sodium tungstate (Na_2WO_4) solution and strongly acidic cation exchange resin (Amberlite®IR120). Briefly, ion exchange resin (in hydrogen form)

was swelled in water and loaded into the glass column (filling volume 200 ml). Then, 100 ml of 0.05 M sodium tungstate solution was passed through the column dropwise, 4 g of PVP was added to the obtained eluent; the solution was transferred to the flask and stirred for 4 h under reflux. During heating a clear sol of hydrated WO_{3-x} was formed, as shown by the appearance of UV-absorption band at 325 nm and Tyndall cone observation. For cytotoxicity study, WO_{3-x} sol was diluted to prepare 0.1 – 25.0 mg/ml colloid solutions.

Comprehensive analysis of WO_{3-x} nanoparticles was performed as described elsewhere [15].

2.2. Investigation of WO_{3-x} photochromic properties

To analyze the photochromic properties of the PVP-stabilized WO_{3-x} sol, it was subjected to UV exposure (BLX-E312 chamber) for 10 min: then the absorption spectra of the irradiated sol were analyzed using an OceanOptics QE65000 spectrometer for every 10 seconds during 10 min. After that, the sample was subjected to UV exposure for the second time. Such procedure (cycle) was repeated 10 times. The volume of the sol was 2 ml, the sol was diluted by 50 fold, *i.e.* the WO_{3-x} concentration was about 0.0006 M. The temperature of the cuvette compartment was maintained at 37 °C.

2.3. Cell culture

In vitro experiments were performed using a mouse fibroblast NTCT L929 cell line. The cells were cultivated in a DMEM/F12 (1:1) medium containing 10 % of fetal bovine serum (FBS), 50 $\mu\text{g}/\text{mL}$ of penicillin, 50 $\mu\text{g}/\text{mL}$ of streptomycin and 1 % of L-glutamine. The cells were cultivated at 37 °C in a humid atmosphere containing 95 % air and 5 % CO_2 . The cells were seeded with the density of 30,000 – 35,000 per cm^2 . Fetal bovine serum (FBS), penicillin, streptomycin, Dulbecco's Modified Eagle Medium (DMEM), F12 medium, L-glutamine, trypsin/versene solution were purchased from PanEco and Biosintez, Russia. Six hours after cells attachment, the medium was replaced by a medium containing different concentrations of WO_{3-x} NPs. In the control experiments, the cells were cultured without WO_{3-x} NPs.

2.4. MTT assay

Determination of mitochondrial and cytoplasmic dehydrogenase activity in living cells was performed using the MTT assay, which is based on the reduction of a colorless tetrazolium salt (3-citiation[4,5-dimethylthiazol-2-yl]-2,5-diphenyltetrazolium bromide, MTT). 24, 48 and 72 h after cell incubation with WO_{3-x} NPs a standard MTT assay was performed.

2.5. Analysis of proliferative activity

Cells were seeded in 24 well plates. After incubation for 6 hours, WO_{3-x} NPs were added to the cells at various concentrations (1 – 15 mg/ml). After 24, 48 and 72 hours cells were counted using Clone Select Imager (Molecular Device, USA).

2.6. Live/Dead viability assay

To evaluate the cytotoxic effects of the WO_{3-x} NPs, a Live/Dead Viability Kit (Invitrogen, Life Technologies) was used. Cells attached to the 96-well plate were processed according to the manufacturer's protocol, and visualized 25 minutes after adding the dye with an Axiovert 200 fluorescence-light microscope (Carl Zeiss, Germany) and recorded by a Canon A620 digital camera (Canon, USA). The green signal (SYTO 9 $\lambda = 485/498$ nm) characterized live cells and the red signal (propidium iodide $\lambda = 535/617$ nm) characterized dead cells. For each cell group, four fields in each well were examined.

2.7. PCR-RT

In order to extract mRNAs a kit with magnetic particles was used, according to the manufacturer's protocol (Sileks, Russia). Reverse transcription was performed by a Sileks kit (Russia) using oligodT primer according to the manufacturers protocol. The produced cDNAs served as a real-time PCR matrix. The amplification was performed on a CFX-96 amplifier (BioRad, USA) or an ABI 7500 Fast Real-Time PCR System (Applied Biosystems, USA). We determined the expression of 96 genes responsible for key cell processes (Table 1).

TABLE 1. Selected gene groups for PCR-RT analysis

Description	Symbol	Description	Symbol
glutathione peroxidase 1	<i>Gpx1</i>	interleukin 22	<i>Il22</i>
glutathione peroxidase 2	<i>Gpx2</i>	alsin Rho guanine nucleotide exchange factor	<i>Als2</i>
glutathione peroxidase 3	<i>Gpx3</i>	apolipoprotein E	<i>ApoE</i>
glutathione peroxidase 4	<i>Gpx4</i>	chemokine (C-C motif)	<i>Ccl5</i>
glutathione peroxidase 5	<i>Gpx5</i>	excision repair cross-complementing rodent repair deficiency complementation group 2	<i>Ercc2</i>
glutathione peroxidase 6	<i>Gpx6</i>	excision repair cross-complementing rodent repair deficiency, complementation group 6	<i>Ercc6</i>
glutathione peroxidase 7	<i>Gpx7</i>	ferritin heavy polypeptide 1	<i>Fth1</i>
glutathione S-transferase kappa 1	<i>Gstk1</i>	glutamate-cysteine ligase, catalytic subunit	<i>Gclc</i>
glutathione S-transferase, pi 1	<i>Gstp1</i>	glutamate-cysteine ligase, modifier subunit	<i>Gclm</i>
EH-domain containing 2	<i>Ehd2</i>	glutathione synthetase	<i>Gss</i>
peroxiredoxin 1	<i>Prdx1</i>	heme oxygenase 1	<i>Hmox1</i>
peroxiredoxin 2	<i>Prdx2</i>	heat shock protein 90 alpha (cytosolic), class B member 1	<i>Hspa1a</i>
peroxiredoxin 3	<i>Prdx3</i>	isocitrate dehydrogenase 1 (NADP+), soluble	<i>Idh1</i>
peroxiredoxin 4	<i>Prdx4</i>	keratin 1	<i>Krt1,</i>
peroxiredoxin 5	<i>Prdx5</i>	myeloperoxidase	<i>Mpo</i>
peroxiredoxin 6	<i>Prdx6</i>	NAD(P)H dehydrogenase, quinone 1	<i>Nqo1</i>
adenomatous polyposis coli	<i>Apc</i>	Parkinson disease (autosomal recessive, early onset) 7	<i>Park7</i>
catalase	<i>Cat</i>	prion protein	<i>Prnp</i>
cathepsin B	<i>Ctsb</i>	proteasome (prosome, macropain) subunit, beta type 5	<i>Psm5</i>
dual oxidase 1	<i>Duox1</i>	sequestosome 1	<i>Sqstm1</i>
eosinophil peroxidase	<i>Epx</i>	thioredoxin 1	<i>Txn1</i>
lactoperoxidase	<i>Lpo</i>	thioredoxin interacting protein	<i>Txnip</i>
myeloperoxidase	<i>Mpo</i>	uncoupling protein 3 (mitochondrial, proton carrier)	<i>Ucp3</i>
prostaglandin-endoperoxide synthase 1	<i>Ptgs1</i>	xeroderma pigmentosum, complementation group A	<i>Xpa</i>
prostaglandin-endoperoxide synthase 2	<i>Ptgs2</i>	ataxia telangiectasia and Rad3 related	<i>Atr</i>
recombination activating gene 2	<i>Rag2</i>	cytoglobin	<i>Cygb</i>

erine (or cysteine) peptidase inhibitor, clade B, member 1b	<i>Serp1b1b</i>	dynamin 2	<i>Dnm2</i>
thyroid peroxidase	<i>Tpo</i>	Fanconi anemia, complementation group C	<i>Fancc</i>
albumin	<i>Alb</i>	intraflagellar transport 172	<i>Ift172</i> ,
glutathione reductase	<i>Gsr</i>	myoglobin	<i>Mb</i>
sulfiredoxin 1 homolog (S. cerevisiae)	<i>Srxn1</i>	neuroglobin	<i>Ngb</i>
thioredoxin reductase 1	<i>Txnrd1</i>	solute carrier family 38, member 1	<i>Slc38a1</i>
thioredoxin reductase 2	<i>Txnrd2</i>	vimentin	<i>Vim</i>
thioredoxin reductase 3	<i>Txnrd3</i>	beta-2 microglobulin	<i>B2m</i>
superoxide dismutase 1, soluble	<i>Sod1</i>	heat shock protein 90 alpha (cytosolic), class B member 1	<i>Hsp90ab1</i>
superoxide dismutase 3, extracellular	<i>Sod3</i>	actin, beta	<i>Actb</i>
superoxide dismutase 2, mitochondrial	<i>Sod2</i>	glyceraldehyde-3-phosphate dehydrogenase	<i>Gapdh</i>
copper chaperone for superoxide dismutase	<i>Ccs</i>	glucuronidase, beta	<i>Gusb</i>
cytochrome b-245, alpha polypeptide	<i>Cyba</i>	mVPA1	<i>mVPA1</i>
neutrophil cytosolic factor 1	<i>Ncf1</i>		
neutrophil cytosolic factor 2	<i>Ncf2</i>		
nitric oxide synthase 2, inducible	<i>Nos2</i>		
NADPH oxidase 1	<i>Nox1</i>		
NADPH oxidase 4	<i>Nox4</i>		
NADPH oxidase activator 1	<i>Noxa1</i>		
NADPH oxidase organizer 1	<i>Noxol1</i>		
RecQ protein-like 4	<i>Recql4</i>		
stearoyl-Coenzyme A desaturase 1	<i>Scd1</i>		
uncoupling protein 2 (mitochondrial, proton carrier)	<i>Ucp2</i>		
aldehyde oxidase 1	<i>Aox1</i>		
flavin containing monooxygenase 2	<i>Fmo2</i>		
interleukin 19	<i>Il19</i>		

The analyzed genes were selected from <http://www.sabiosciences.com> database for PCR profiling of different biological processes. The level of gene transcription was normalized by the levels of expression of housekeeping genes β -actin, *B2m* (beta-2 microglobulin), *Hsp90ab1* (heat shock protein 90 alpha (cytosolic), class B member 1), *gapdh* (glyceraldehyde-3-phosphate dehydrogenase) and *Gusb* (glucuronidase, beta). Each measurement was repeated twice (internal repetition) and averaged for 2 independent samples. The obtained expression data were analyzed using <http://www.sabiosciences.com> online services, mayday-2.14 software (Center for Bioinformatics Tubingen, Germany) and the Genesis software.

2.8. Statistical analysis

The experiments were conducted in 3 or 4 repetitions. Experimental results were compared with the control. Statistical analysis was performed using the methods of variation statistics. We determined the mean values and the standard deviation of the mean. The significance of the difference between the groups was determined by Student t-test. The obtained data were processed using GraphPad 6.0 and Microsoft Excel 2007 software.

3. Results and discussion

The synthesized WO_{3-x} sol possesses good photochromic properties – it turns blue under UV radiation, and in the absence of the UV light it gradually becomes colorless. A detailed study of the sol's photochromic properties regeneration showed the changes in the sol's discolouration rate during the repeated UV exposure. Thus, after the first irradiation (cycle 1), the sol become almost completely colorless in 10 min (Fig. 1(a)). In turn, after the fifth and tenth irradiation (cycles 5 and 10, respectively) the sol remained light blue (Fig. 1(b,c)). It is also worth noting that the absorption coefficient of the WO_{3-x} sol after each irradiation cycle changed. To determine the possible influence of polyvinylpyrrolidone stabilizer, we conducted a control experiment with an individual PVP solution prepared in a similar way. The concentration of the solution was 0.03 mol/L. Fig. 1(d,e) show that the PVP solution is stable under UV light, irrespective of the number of cycles.

Analysis of the dehydrogenase activity *via* MTT assay after 24 and 72 hours of incubation with tungsten oxide nanoparticles showed a dose-dependent viability decrease (Fig. 2). In particular, viability of mouse fibroblasts was significantly reduced after 24 hours of culturing with WO_{3-x} NPs (5 – 15 mg/ml). Analysis of cell viability after 72 hours of culturing also showed a significant decrease in the dehydrogenase activity for all the studied concentrations of WO_{3-x} nanoparticles (1 – 15 mg/ml). Such decrease indicates disturbances in the functioning of mitochondria. Considering the ability of WO_{3-x} NPs to generate ROS and free radicals [10], we can suggest that oxidative stress in the cell was developed.

Analysis of the proliferative activity of the cells revealed an inhibitory effect of WO_{3-x} nanoparticles (Fig. 3). Low concentrations of WO_{3-x} nanoparticles (1 and 2.5 mg/ml) did not significantly reduce the proliferative activity of the cells (Fig. 3(b)). However, even a 5 mg/ml concentration of WO_{3-x} nanoparticles led to a 50 % inhibition of proliferative activity, resulting in the change of cell confluence. Higher concentrations of WO_{3-x} nanoparticles (10 and 15 mg/ml) resulted in more than 70 % inhibition of proliferative activity (Fig. 3(c)). Upon 72 hours incubation with higher concentrations of WO_{3-x} nanoparticles, the appearance of the cells also changed significantly. After 72 hours, almost all the cells detached from the substrate, acquired a rounded shape, losing the characteristic spreading (Figure 3a).

We analyzed the number of dead cells after incubation with WO_{3-x} nanoparticles using fluorescent dyes (Syto 9/propidium iodide) (Fig. 4). This analysis did not reveal the presence of dead cells after 24 hours of cultivation with 1 to 10 mg/ml of WO_{3-x} nanoparticles. Meanwhile, higher concentration of WO_{3-x} nanoparticles (15 mg/ml) led to the appearance of dead cells. After 72 hours of incubation, 5, 10 and 15 mg/ml concentrations of WO_{3-x} nanoparticles resulted in a significant proportion of dead cells. A significant reduction in the number of the cells indicated both an inhibitory effect on the proliferation of the cell culture and their detachment from the substrate.

We carried out gene expression analysis of the effect of tungsten oxide nanoparticles on cellular components. PCR RT method was used to analyze mRNA expression of 96 genes responsible for the development of oxidative stress response (Fig. 5). The data obtained indicated that WO_{3-x} nanoparticles led to changes in the transcriptional activity of genes associated with the development and protection against oxidative stress. The action of WO_{3-x} nanoparticles was found to be dose- and time-dependent. Thus, WO_{3-x} nanoparticles (1 mg/ml) after 24 hours incubation activated transcription of the glutathione peroxidase (*GPx*) genes (*Gpx* 1 – 3, *Gpx* 5 – 7 and *Gstk1*) and some other peroxidase genes (*Epx*, *Lpo*, *Mpo*, *Rag2*, *Serp1nb1b* and *Tpo*). There was also an increase in the transcriptional activity of a few genes associated with reactive oxygen species (ROS) metabolism (*Cyba*, *Nos2*, *Nox4*, *Il22*), six genes associated with oxidative stress response (*Ercc2*, *Hspa1a*, *Krt1*, *Txn1* and *Xpa*) and one gene of the oxygen transporters group (*Ngb*). After 72 h, a significant activation of gene expression took place, but with a different pattern. Thus, in the glutathione peroxidases and peroxiredoxins (*TPx*) cluster, an increased level

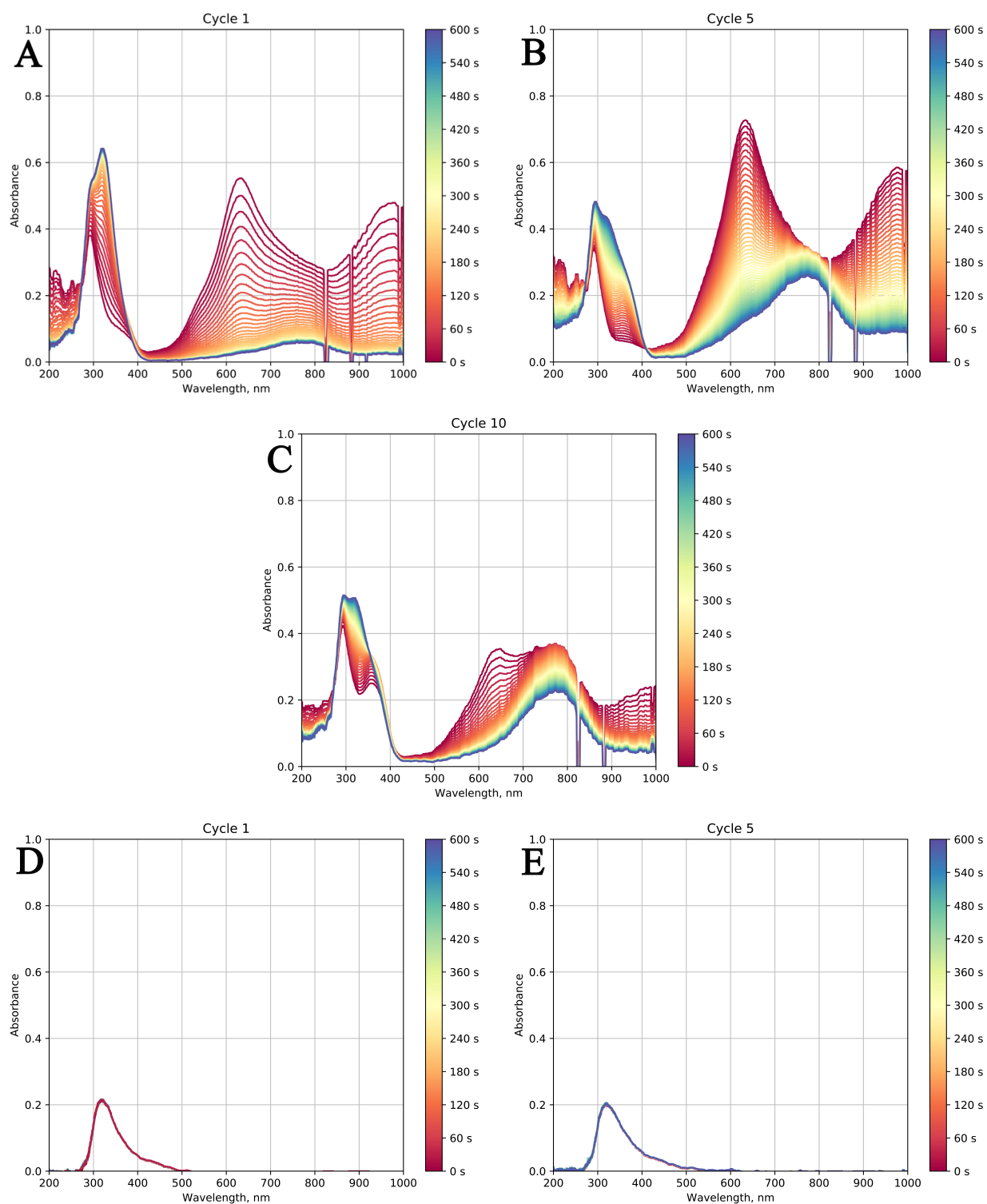


FIG. 1. Absorption spectra of the sol at the first, fifth and tenth irradiation cycle, respectively (A–C), absorption spectra of the PVP solution during the first and fifth cycle (D–E)

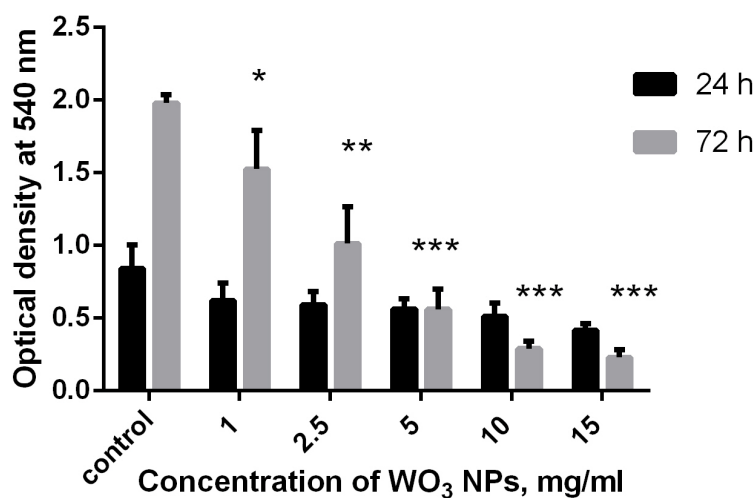


FIG. 2. Results of MTT assay 24 and 72 h after incubation of NTCT L929 cells with WO_{3-x} nanoparticles. Data are presented as mean \pm sd ($yEr\pm$), $n = 3$. * - $p \leq 0.05$, ** - $p \leq 0.001$, *** - $p \leq 0.0001$ according to Mann-Whitney U-test

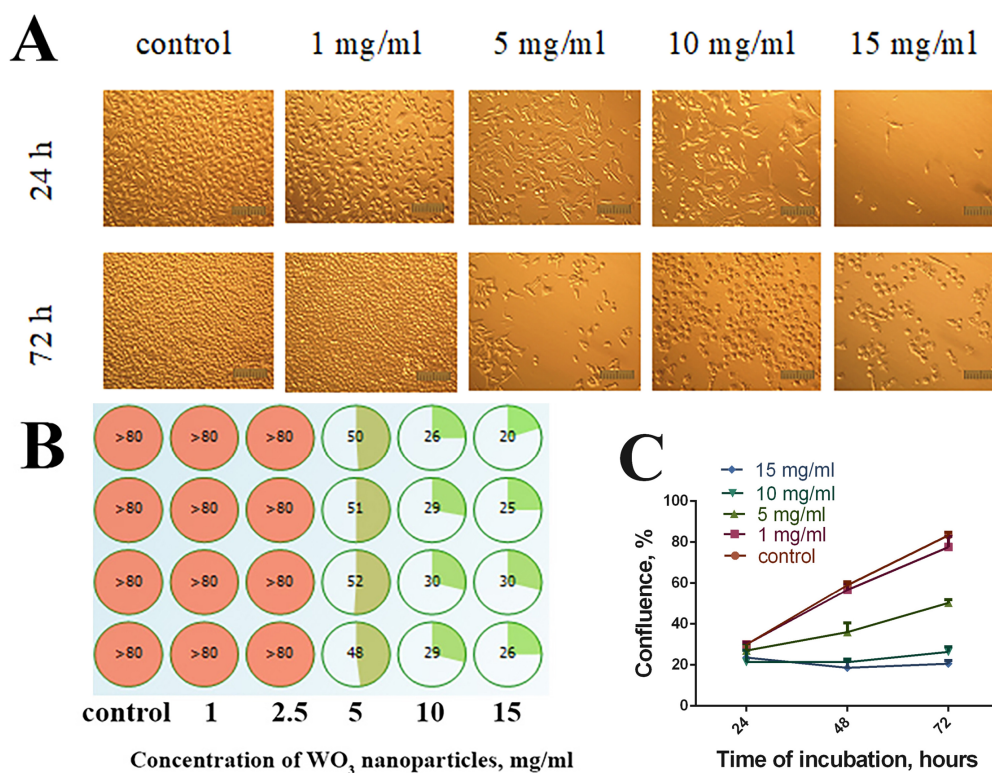


FIG. 3. Microphotographs of NCTC L929 cells after 24 and 72 h incubation with WO_{3-x} nanoparticles (1 – 15 mg/ml) (A). Confluence of NCTC L929 cells after 72 h of incubation with WO_{3-x} nanoparticles (1 – 15 mg/ml) (B). Growth curve of NCTC L929 cells after 3 day incubation (C). Cells were plated in 96 well plates and left overnight. Then WO_{3-x} nanoparticles (1 – 15 mg/ml) were added and after 24, 48 and 72 h cells confluence was analyzed

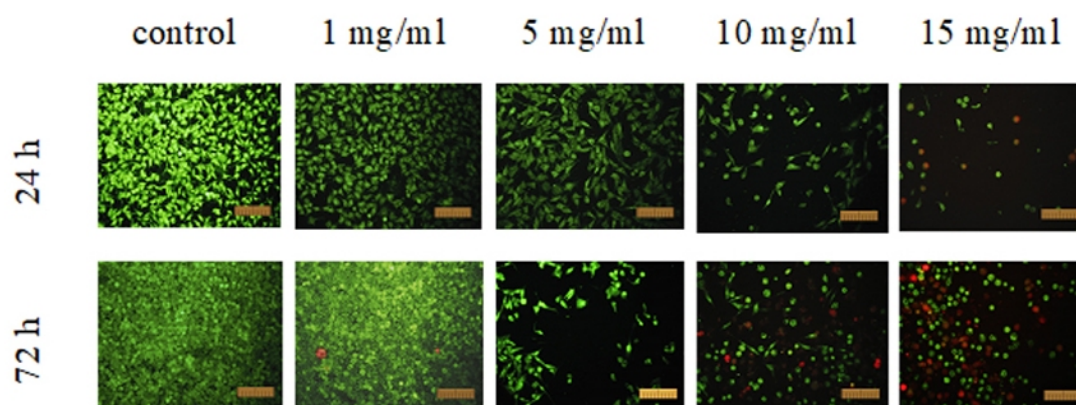


FIG. 4. Microphotographs of NCTC L929 cells after 24 and 72 h incubation with WO_{3-x} nanoparticles (1 – 15 mg/ml). Cells were plated in 96 well plates and left overnight. Then WO_{3-x} nanoparticles (1 – 15 mg/ml) were added and after 24 and 72 h cells were stained with L-7007 LIVE/DEAD kit

of transcription of only 3 genes (*Gpx2*, *Gpx3* and *Ehd2*) was recorded, and the expression level of some genes of this group was reduced compared to the control (*Gpx5*, *Gpx6* and *Gstk1*). During this period, an increase in the expression of genes of other peroxidases (*Apc*, *Cat*, *Duox1*, *Lpo*, *Ptgs2*, *Serpin1b* and *Tpo*) occurred. In contrast to the 24-hour incubation period, after 72 hours incubation, NCTCT L929 cells showed increased transcription of 2 other antioxidant genes (*Alb* and *Txnrd2*), and in the cluster of other superoxide metabolism genes 7 genes were up-regulated - *Cyba*, *Nox1*, *Noxa1*, *Recq14*, *Scd1*, *Aox1* and *Il19*.

Compared to 24 h incubation, an increase in the transcription of a larger number of genes (*Als2*, *Apoe*, *Ccl5*, *Ercc6*, *Ercc2*, *Gclc*, *Sqstm1*, *Txn1*, *Txnip*, and *Ucp3*) occurred in the oxidative stress responsive genes cluster. In the group of oxygen transporters, there was a total activation of the expression of all genes, except for *Vim*. WO_{3-x} nanoparticles at the concentration of 10 mg/ml led to an increase in the transcriptional activity of genes involved in the development of oxidative stress. Meanwhile, the transcriptional expression patterns were very similar to those recorded for 1 mg/ml concentration after 72 hours of incubation. At the same time, in some clusters, a significant decrease in the expression of some genes was observed (*Gpx2*, *Gstp1*, *Ehd2*, *Prdx1*, *Prdx2*, *Prdx3*, *Cat*, *Serpin1b*, *Gsr*, *Sod3*, *Txnrd1*, *Txnrd3*, *Noxo1*, *Scd1*, *Ucp2*, *Gclc*, *Gcl*, *Im*, *Txnrd3*, *Noxo1*, *Scd1*, *Ucp2*, *Gclc*, *Gcl*, *Im*, *Txnrd3*, *Noxo1*, *Scd1*, *Ucp2*, *Gclc*, *Gcl*, *Cygb*, *Fance*, *Vim*). After 72 hours of cell incubation with 10 mg/ml WO_{3-x} concentration, up-regulation of the maximum number of genes was observed. Thus, in peroxiredoxins group (*TPx*) and other antioxidants, all studied genes were upregulated, as well as 70 % genes in the oxidative stress responsive cluster. Despite this, expression of some genes was down-regulated (*Gpx2*, *Gpx3*, *Gpx5*, *Gpx6*, *Gstk1*, *Epx*, *Mpo*, *Rag2*, *Ncf1*, *Nos2*, *Noxo1*, *Fmo2*, *Hspala*, *Krt1* and *Ngb*). This suggests that WO_{3-x} nanoparticles have a pronounced pro-oxidant activity. Our results showed that WO_{3-x} nanoparticles are able to significantly modulate both pro- and antioxidant gene expression. Firstly, WO_{3-x} nanoparticles activated the glutathione peroxidases and peroxiredoxins after 24 h even at low concentrations (1 mg/ml). Higher concentration of WO_{3-x} nanoparticles (10 mg/ml) led to the activation of the transcriptional activity of other antioxidant protection genes and genes responsible for ROS metabolism.

4. Conclusions

PVP-stabilized tungsten oxide nanoparticles provide dose- and time-dependent inhibition of the mouse fibroblasts proliferative activity due to the induction of strong oxidative stress leading to cell death. The intermediate concentration of WO_{3-x} nanoparticles (5 mg/ml) showed significant inhibition of proliferation, while higher concentrations (10 and 15 mg/ml) resulted in the development of apoptosis and cell death. WO_{3-x} concentrations less than 2.5 mg/ml did not cause an increased cell death and did not significantly affect cell metabolism. The obtained data indicate that WO_{3-x} nanoparticles may have a potential toxic effect on mammalian cells.

Acknowledgements

This study was funded by Russian Science Foundation (project 18-73-10150).

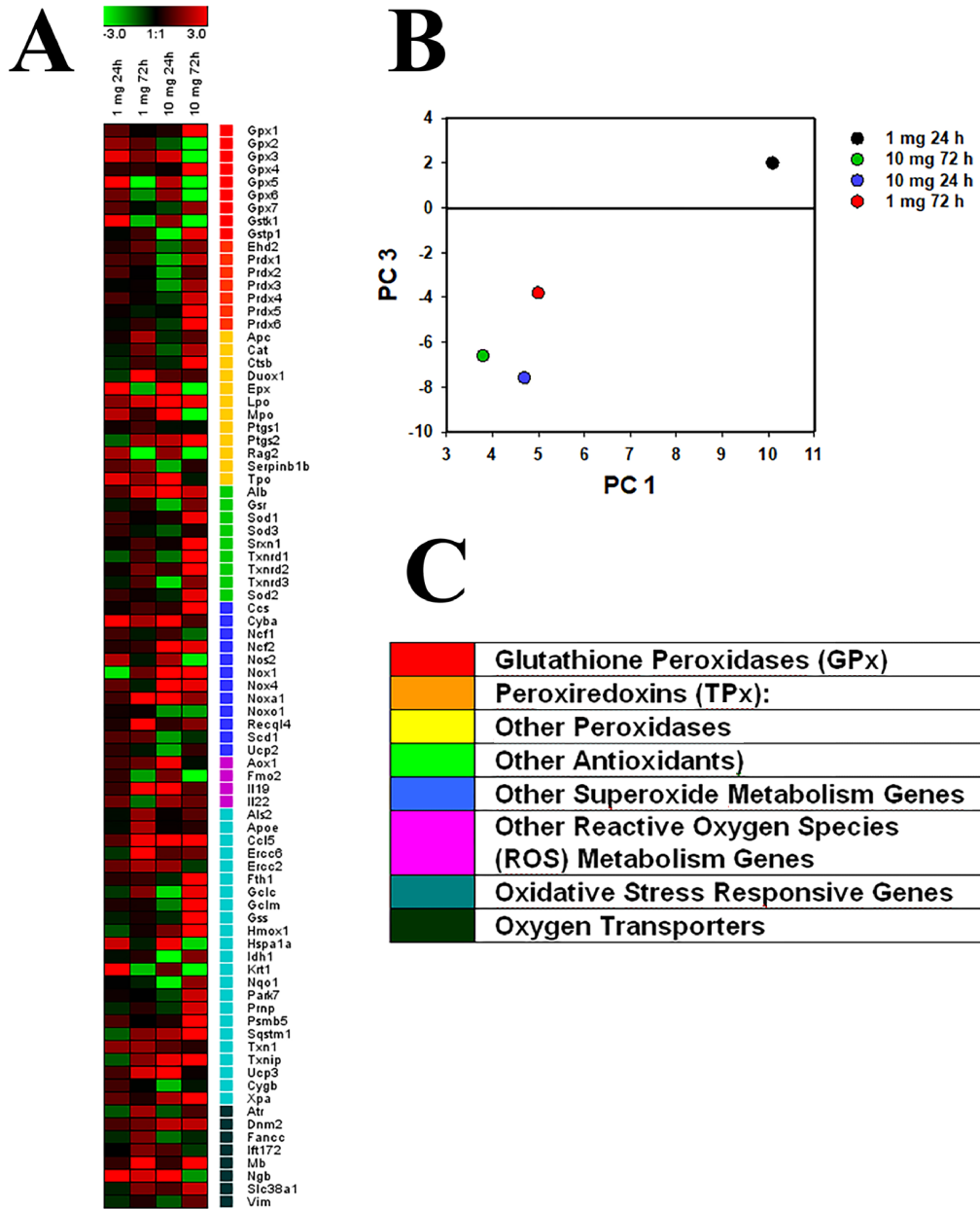


FIG. 5. Heat map of gene expression in NCTC L929 cells treated with WO_{3-x} nanoparticles (1 and 10 mg/ml) after 24 and 72 h of incubation (A). The intensity scale of the standardized expression values ranges from -3 (green: low expression) to $+3$ (red: high expression, with 1:1 intensity value (black) representing the control (non-treated)). Principal component analysis (PCA) of qRT-PCR data from different concentration of WO_{3-x} nanoparticles (B). Cluster groups of genes and their functionality (C)

References

- [1] Firouzi M., Poursalehi R., et al. Chitosan coated tungsten trioxide nanoparticles as a contrast agent for X-ray computed tomography. *Int. J. Biol. Macromol.*, 2017, **98**, P. 479–485.
- [2] Popov A.L., Savintseva I.V., et al. Cytotoxicity analysis of gadolinium doped cerium oxide nanoparticles on human mesenchymal stem cells. *Nanosyst. Phys. Chem. Math.*, 2018, **9** (3), P. 430–438.
- [3] Popov A.L., Shcherbakov A.B., et al. Cerium dioxide nanoparticles as third-generation enzymes (Nanozymes). *Nanosyst. Phys. Chem. Math.*, 2017, **8** (6), P. 760–781.
- [4] Popova N.R., Popov A.L., Shcherbakov A.B., Ivanov V.K. Layer-by-layer capsules as smart delivery systems of CeO₂ nanoparticle-based theranostic agents. *Nanosyst. Phys. Chem. Math.*, 2017, **8** (2), P. 282–289.
- [5] Popov A.L., Popova N.R., et al. Cerium oxide nanoparticles stimulate proliferation of primary mouse embryonic fibroblasts *in vitro*. *Mater. Sci. Eng., C*, 2016, **68**, P. 406–413.
- [6] Hosseini F., Rasuli R., Jafarian V. Immobilized WO₃ nano-particles on graphene oxide as a photo-induced antibacterial agent against UV resistant *Bacillus Pumilus*. *J. Phys. D: Appl. Phys.*, 2018, **51** (14), 145403.
- [7] Hariharan V., Radhakrishnan S., et al. Synthesis of polyethylene glycol (PEG) assisted tungsten oxide (WO₃) nanoparticles for L-dopa bio-sensing applications. *Talanta*, 2011, **85** (4), P. 2166–2174.
- [8] Deng K., Hou Z., et al. Enhanced Antitumor Efficacy by 808 nm Laser-Induced Synergistic Photothermal and Photodynamic Therapy Based on a Indocyanine-Green-Attached W₁₈O₄₉ Nanostructure. *Adv. Funct. Mater.*, 2015, **25** (47), P. 7280–7290.
- [9] Chen Z., Wang Q., et al. Ultrathin PEGylated W18O49 nanowires as a new 980 nm-laser-driven photothermal agent for efficient ablation of cancer cells *in vivo*. *Adv. Mater.*, 2013, **25** (14), P. 2095–2100.
- [10] Sharker S.Md., Kim S.M., et al. Functionalized biocompatible WO₃ nanoparticles for triggered and targeted *in vitro* and *in vivo* photothermal therapy. *J. Control. Release*, 2015, **217**, P. 211–220.
- [11] Zhou Z., Kong B., et al. Tungsten Oxide Nanorods: An Efficient Nanoplatform for Tumor CT Imaging and Photothermal Therapy. *Sci. Rep.*, 2014, **4**, 3653.
- [12] Liu J., Han J., et al. *In vivo* near-infrared photothermal therapy and computed tomography imaging of cancer cells using novel tungsten-based theranostic probe. *Nanoscale*, 2014, **6** (11), P. 5770–5776.
- [13] Liu P., Wang Y., et al. Ultrasmall WO_{3-x}@ γ -poly-L-glutamic Acid Nanoparticles as a Photoacoustic Imaging and Effective Photothermal-Enhanced Chemodynamic Therapy Agent for Cancer. *ACS Appl. Mater. Interfaces*, 2018, **10** (45), P. 38833–3884.
- [14] AbuMousa R.A., Baig U., et al. Photo-catalytic Killing of HeLa Cancer Cells Using Facile Synthesized Pure and Ag Loaded WO₃ Nanoparticles. *Sci. Rep.*, 2018, **8**, 15224.
- [15] Popov A., Zholobak N., et al. Photo-induced toxicity of tungsten oxide photochromic nanoparticles. *J. Photochem. Photobiol. B*, 2018, **178**, P. 395–403.

Direct synthesis of hydrogenated graphene via hydrocarbon decomposition in plasmas

M. B. Shavelkina, R. H. Amirov

Joint Institute for High Temperatures of Russian Academy of Sciences, Izhorskaya st. 13 Bd. 2, Moscow, 125412, Russia

mshavelkina@gmail.com, amirovravil@yahoo.com

PACS 52.75.Hn, 52.77.Fv, 61.46.Fg, 68.37.Hk

DOI 10.17586/2220-8054-2019-10-1-102-106

We study graphene synthesis in a plasma-jet reactor. Graphene is obtained via decomposition of hydrocarbons in the plasma produced in the DC plasma torch. The products of synthesis are characterized using the following methods: electron microscopy, Raman spectroscopy, X-ray diffraction and X-ray photoelectron spectroscopy, thermal analysis and express-gravimetry. We make the conclusion that, at the few-layer graphene samples, their hydrogenation takes place. The maximal hydrogen-to-carbon ratio was 1:4.

Keywords: Synthesis, graphane, plasma jet, hydrocarbons.

Received: 2 November 2018

Revised: 11 December 2018

1. Introduction

Graphene is a single layer of carbon atoms arranged in a hexagonal lattice and graphane is the hydrogenated graphene where each carbon atom is covalently connected with the hydrogen atom in the CH stoichiometry [1]. Here, the sp^3 -hybridized carbon atoms shift up or down from the planes; according to the calculations in [1], it is an energy-profitable system. The theoretically proposed models of the graphane structure are only partly confirmed theoretically [2]. In the conditions of wide investigations of potential graphane applications to the particular problems in various fields of technology, science, and industry, primarily for the hydrogen storage [1] or in precise devices [3] or solar batteries [4], the search for optimal graphene synthetic methods becomes especially urgent.

Recently, hydrogenated graphene structures were obtained, with the different hydrogen-to carbon stoichiometry depending on the production method. The methods based on application of low or high pressure the hydrogen containing gas medium result in lower sample saturation by hydrogen than the liquid-phase methods based on the modified Birch method [5–9]. Authors [10] used the scaled electrochemical approach to obtain the hydrogenated graphene from the solvated NR (4+) graphite. Yet, currently, totally hydrogenated graphene is still not synthesized. Even in order to obtain the graphene with various hydrogenation degree, at least two or more stages are required. At the first stage, the initial material, graphene, is obtained using one of the known methods: adhesive tape, CVD, Hummers' method, or on the SiC surface. At the second stage, the hydrogenation itself proceeds by means of physical or chemical methods. In liquid-phase approaches, an additional stage of refinement from the undesirable medium admixtures, i.e. atoms, molecules, small atomic clusters, is needed.

2. Experimental setup and procedure

Earlier, we investigated the possibility of synthesizing free graphene by means of high-power plasma torch at the pressure of 150 – 710 Torr [11, 12]. Analysis of the processes in the carbon nucleation zone of the plasma jet generated by the plasma torch indicates high concentration of the atomic hydrogen and of the C_6H_6 -like compounds; these substances, according to [13–16], might promote the graphene formation. Additionally, it is common knowledge that application of the DC plasma torches makes it possible to synthesize high-quality pure carbon nanomaterials from inexpensive precursors [17], thus reducing the requirements to the carbon source, its cost and the final product cost. Authors [18–20] show that, with application of the plasma torches, high purity graphene might be obtained with controlled electronic properties.

The present work is aimed at experimental search to plasma-assisted synthesis of graphene with the attached hydrogen atoms. The plasma jets used here is the same one as in the work [21]. We performed decomposition of hydrocarbons in the thermal plasma jet up to the carbon vapor formation. Then we rapidly cooled the decomposition products of hydrocarbons in a vacuum chamber with the subsequent nucleation of solid carbon. We received synthesized products on the collector. Simultaneous input of the precursors (methane, propane-butane, acetylene) and the plasma-forming gas (helium) into the discharge gap of the plasma torch is an advantage of such method.

Here, we might independently vary the component ratio in the plasma jet within wide ranges. Besides, the extending anode channel – the constructive peculiarity of the plasma torch – makes it possible to widely vary the rate of the vapor-gas flow cooling, to change its geometry, and, in general, to control the process efficiency [22].

Table 1 presents the parameters of experiments on the hydrogenated graphene synthesis. The synthesis process duration equals to 6 min and is governed by the quantity of specimens required to investigate their properties. Total output of the carbon sediment collected on the target varies from 6 g to 10 g (99 wt. %).

TABLE 1. Experimental conditions

Power (kW)	Current (A)	Voltage (V)	Gas pressure (Torr)	Helium flow rate (g·s ⁻¹)	Propane-butane flow rate (g·s ⁻¹)	Methane flow rate (g·s ⁻¹)	Acetylene flow rate (g·s ⁻¹)
22–36	350–400	60–90	150, 350, 710	0.75–0.9	0.11–0.30	0.15–0.37	0.05–0.16

We measured the temperature in the zone of carbon vapor condensation and formation of graphene and graphite by the chromel-alumel thermocouple. Depending on the experimental conditions, the temperature on the collector surface was varied from 500 – 700 °C. This temperature range is optimal to obtain the hydrogenated graphene [23].

The samples synthesized in the plasma jet volume were characterized by means of the standard methods of graphene materials investigation [7, 24, 25]. To provide the most accurate identification of the samples, we used a method of a scanning electron microscopy (SEM) with a Hitachi S5500 microscope in the DF-STEM, BF-STEM and SE modes and a Raman spectroscopy study (Nectra Spectra, a laser with a wavelength of 532 nm). To quantitatively investigate the element composition and the electron state of the atoms, we used the X-ray photoelectron spectroscopy (XRPS) – the measurements were performed at the room temperature by means of the Theta Probe (ThermoFisher Scientific, GB) spectrometer: we took the Al K- α emission without using the system of the surface charging neutralization. To determine the element composition, we applied the vario MICRO cube express-gravimetry method. The phase composition of the synthesized samples was investigated by the thermal methods (thermogravimetry and differentially-scanning calorimetry), under linear heating with a rate of 10 K/min, under argon atmosphere, by means of the Netzsch (STA 409, PC Luxx) device. The X-ray structure analysis was performed using the standard technique and the DRON-2 facility (CuK α -emission). We obtained the X-ray diffraction spectra from the basic surfaces of the samples.

3. Results of experiments

The electron microscopy results confirm the possibility of graphene hydrogenation at its synthesis. Fig. 1 shows the typical SEM images of the hydrogenated graphene structures obtained via decomposition of methane and acetylene in the helium plasma at 350 Torr and at the maximal consumption (0.16 – 0.37 g/s), Tab. 1. In morphology, these structures are identical with the structures synthesized, with plasma application, in the experiments [20]. The samples represent the disoriented flakes, differing in the edge morphology and the lateral sizes (with sufficient scattering – from below 3 nm to above 1.5 μ m). The X-ray analysis of the flakes shows that the spectrum of a typical sample contains two weak halos. The first of them is in the Bragg angle range $2\theta = 11 - 120$ and can belong to any hydrocarbon phase. The maximum intensity of this halo corresponds to the interplanar distance $d = 0.7694$ nm. The second halo is located in the area of angles $2\theta = 24 - 280$. The maximum intensity of this halo corresponds to the interplanar spacing $d = 0.3401$ nm. Study of morphology shows that the sample surface is wavy. Fig. 1 shows that the areas with swelling (covering not only the surface layer but also the next ones) rise above the waves. The swelling has a rhomboid shape which, as a rule, forms when a gas fills the layered structures. The rhomb angle equals to 120 ° – typical for the crystal structure rather than for amorphous carbon. The swellings on the graphene surface are distributed irregularly. That very swelling effect was previously observed when studying the morphology of the pyrolytic graphite surface after the impact by the hydrogen flow [26].

The thermal sample analysis data concerning the hydrogen output are in agreement with the results obtained earlier in the works on the hydrogen desorption from both graphite [27] and graphene [24]. Fig. 2 shows an example of thermogram of the samples synthesized via the methane decomposition in the helium plasma at

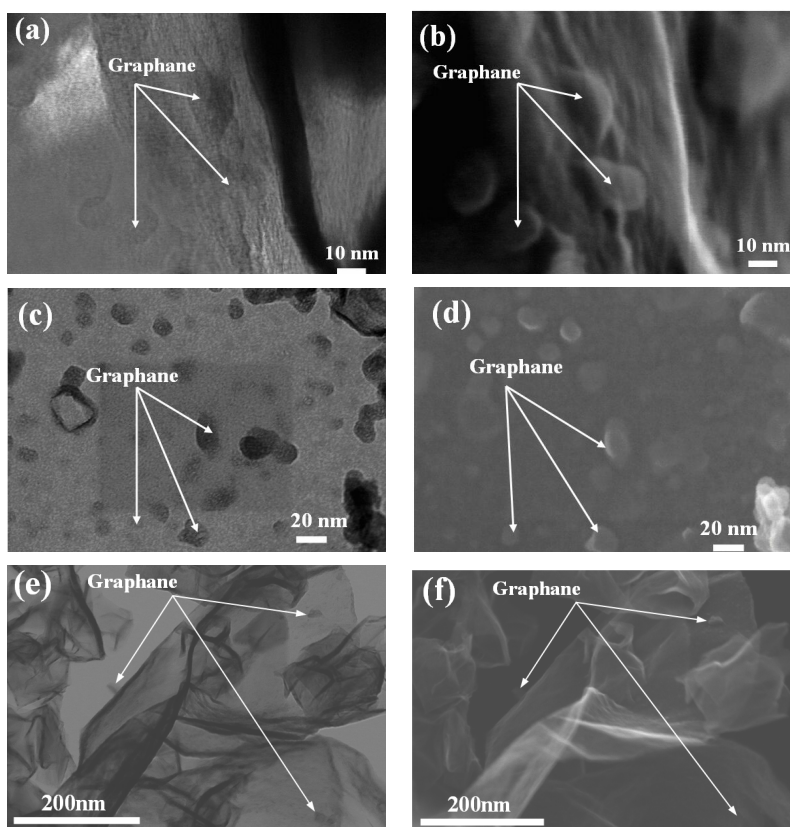


FIG. 1. (a) BF-STEM of the sample obtained via the propanebutane mixture decomposition in helium plasma at 350 Torr; (b) SEM of the sample obtained via the propanebutane mixture decomposition in helium plasma at 350 Torr; (c) SEM of the sample obtained via the acetylene decomposition in the helium plasma at 350 Torr; (d) BF-STEM of the sample obtained via the acetylene decomposition in helium plasma at 350 Torr; (e) SEM of the sample obtained via the methane decomposition in the helium plasma at 710 Torr; (f) BF-STEM of the sample obtained via the methane decomposition in helium plasma at 710 Torr

pressure of 710 Torr. Analysis of the thermogram shows that the content of the graphane component in the obtained hydrogenated material is above 60 wt. %. Here, intensive mass decrease begins at 300 °C and continues up to above 1000 °C. In the desorption curves, two desorption peaks are observed. Depending on the precursor type, the maximum falls on the temperature ranges of 300 – 400 °C and 800 – 900 °C.

The XPS spectra also confirmed obtaining of graphane. Fig. 3 shows the high-resolution C1s spectra for the specimen obtained via the propane-butane mixture decomposition in the helium plasma at 710 Torr and the highly-oriented pyrolytic graphite (HOPG) measured at two angles against the normal to the surface. The spectra differ in the width of the main peak because of the specimen non-uniformity caused by the presence of the different size particles and the defects which is consistent with the work [28]. The difference in the spectra within the lower binding energy region indicates different conductivity caused, possibly, by the presence of the C–H bonds – this fact is in agreement with results [24].

By means of the direct express-gravimetry method, we determine the C:H content ratio in the samples. The minimal quantity of the hydrogen atoms per a single carbon atom equals to 0.017. This value was obtained when methane was used as the precursor. At the propane-butane mixture decomposition (with the flow rate of 0.37 g/s), in the helium plasma (710 Torr), with variation of the gas flow velocities, we obtained the hydrogen-to-carbon ratio of 1:4. The Raman-spectroscopic investigation of the samples also confirmed formation of graphane. Fig. 4 shows the Raman-spectrum of the samples synthesized from the propane-butane mixture in the helium plasma at different temperature on the collector surface [29]. These results respect to the Raman-spectrum of the single-layer graphane obtained via mechanical exfoliation (the adhesive tape) [24]. In Fig. 4, the D, G, and 2D peaks move up to 1337 cm^{-1} , 1569 cm^{-1} , and 2659 cm^{-1} , respectively. For all the spectra, the D line is present – due to the

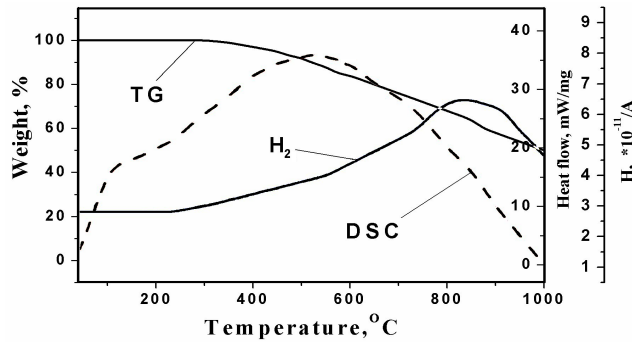


FIG. 2. Thermal analysis, in the inert medium, of the sample obtained via the methane decomposition in helium plasma at 710 Torr. The G is the sample mass variation, the DSC – variation of the sample heat release under the linear heating, H – the hydrogen output

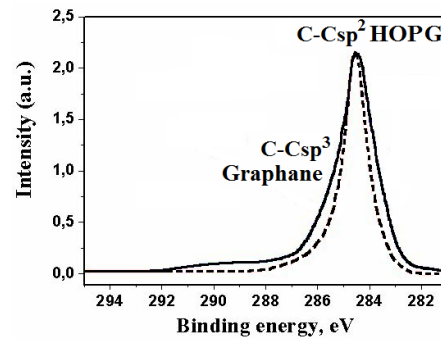


FIG. 3. Comparison of the C 1s photoelectron spectra of the sample and of the HOPG measured at the various angles against the normal to the sample surface

morphology peculiarity of the structures, flakes with the fold edges. Certain discrepancy with the literary data is caused by application of the different lasers for excitement of the spectra – this fact is confirmed by the analysis in [30]. Figure 4 shows a typical spectrum of the hydrogenated graphene [31–34]. Note that the intensity shift of the breathing modes to the higher frequencies takes place; respectively, the D, G, and 2D peaks move up to 1350 cm^{-1} , 1580 cm^{-1} , and 2690 cm^{-1} . Analysis of shape of the 2D peaks shows that the samples are two-layered. According to [35], the highest possibility of hydrogenation with respect to that, vary the bilayer graphene.

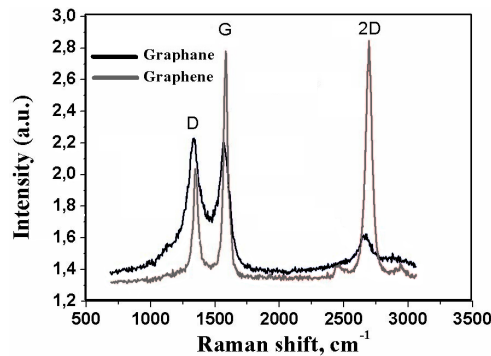


FIG. 4. Raman spectra of the samples obtained via the propanebutane mixture decomposition in helium plasma at 350 Torr

Measurements of the electrical conductivity of synthesized hydrogenated graphene from $10 - 50\text{ }^{\circ}\text{C}$ using the classical four-probe method for bulk materials correlate with the data of [7] and correspond to the classical temperature dependence for a semiconductor. The band gap energy (equal to 0.22 eV) confirms their semiconductor-like character.

4. Conclusions

We demonstrate the possibility of synthesizing hydrogenated graphene structures in plasma jets. Their characterization by Raman spectroscopy, the XPS, the express-gravimetry and the thermal analysis methods shows that their properties are close to the properties of the hydrogenated single-layered graphene, both on the substrates and in the liquid media. We state the correlation between the degree of hydrogenation and the synthesis conditions. The hydrogen content depends on the synthesis conditions.

Acknowledgements

This work was financially supported by the Russian Fond of Basic Research (Grant No. 18-08-00040).

References

- [1] Sofo J.O., Chaudhari A.S., Barber G.D. Graphane: A two-dimensional hydrocarbon. *Phys. Rev. B*, 2007, **75**, P. 153401.
- [2] Chernozatonskii L.A., Artyukh A.A., Kvashnin D.G. Formation of graphene quantum dots by “Planting” hydrogen atoms at a graphene nanoribbon. *JETP Lett.*, 2012, **95**, P. 266–270.
- [3] Huang L.F., Zeng Z. Lattice dynamics and disorder-induced contraction in functionalized graphene. *J. Appl. Phys.*, 2013, **113**, P. 083524.
- [4] Gao H., Wang L., et al. Band gap tuning of hydrogenated graphene: H coverage and configuration dependence. *J. Phys. Chem. C*, 2011, **115**, P. 3236–3242.
- [5] Pumera M., Wong C.H. Graphane and hydrogenated graphene. *Chem. Soc. Rev.*, 2013, **42**, P. 5987–5995.
- [6] Zhou C., Chen S., et al. Graphene’s cousin: the present and future of graphane. *Nanoscale Res. Lett.*, 2014, **9**, P. 26.
- [7] Jones J.D., Mahajan K.K., et al. Formation of graphane and partially hydrogenated graphene by electron irradiation of adsorbates on graphene. *Carbon*, 2010, **48**, P. 2335–2340.
- [8] Smith D., Howie R.T., et al. Hydrogenation of graphene by reaction at high pressure and high temperature. *ACS Nano*, 2015, **9**, P. 8279–8283.
- [9] Eng A.Y., Poh H.L., et al. Searching for magnetism in hydrogenated graphene: using highly hydrogenated graphene prepared via birch reduction of graphite oxides. *ACS Nano*, 2013, **7**, P. 5930–5939.
- [10] Abdelkader A.M., Patten H.V., et al. Electrochemical exfoliation of graphite in quaternary ammonium-based deep eutectic solvents: a route for the mass production of graphane. *Nanoscale*, 2015, **7**, P. 11386–11392.
- [11] Shavelkina M.B., Amirov R.H., Ivanov P.P., Filimonova E.A. Conversion of hydrocarbons in the plasma jet to produce carbon nanostructures. *Proceedings of the Workshop on Magneto-Plasma Aerodynamics*, Moscow, Russia, 5–7 April 2017, P. 92–93.
- [12] Amirov R., Shavelkina M., et al. Direct synthesis of porous multilayer graphene materials using thermal plasma at low pressure. *J. of Nanomaterials*, 2015, **2015**, P. 724508.
- [13] Back M.H. Mechanism of the pyrolysis of acetylene. *Can. J. of Chem.*, 1971, **49**, P. 2199–2204.
- [14] Tsyganov D., Bundaleska N., et al. On the plasma-based growth of ‘flowing’ graphene sheets at atmospheric pressure conditions. *Plasma Sources Sci. Technol.*, 2016, **25**, P. 015013.
- [15] Norinaga K., Deutschmann O. Detailed kinetic modeling of gas-phase reactions in the chemical vapor deposition of carbon from light hydrocarbons. *Ind. Eng. Chem. Res.*, 2007, **46**, P. 3547–3557.
- [16] Khalilov U., Bogaerts A., Neyts E.C. Microscopic mechanisms of vertical graphene and carbon nanotube cap nucleation from hydrocarbon growth precursors. *Nanoscale*, 2014, **6**, P. 9206–9214.
- [17] Keidar M., Shashurin A., et al. Arc plasma synthesis of carbon nanostructures: where is the frontier? *J. Phys. D: Appl. Phys.*, 2011, **44**, 174006.
- [18] Wang Q., Wang X., Chai Z., Hu W. Low-temperature plasma synthesis of carbon nanotubes and graphene based materials and their fuel cell applications. *Chem. Soc. Rev.*, 2013, **42**, P. 8821–8834.
- [19] Kim J., Suh J.S. Size-controllable and low-cost fabrication of graphene quantum dots using thermal plasma jet. *ACS Nano*, 2014, **8**, P. 4190–4196.
- [20] Kim J., Heo S.B., Gu G.H., Suh J.S. Fabrication of graphene flakes composed of multi-layer graphene sheets using a thermal plasma jet system. *Nanotechnology*, 2010, **21**, P. 095601.
- [21] Amirov R., Isakaev E., Shavelkina M., Shatalova T. Synthesis of carbon nanotubes by high current divergent anode-channel plasma torch. *J. Phys.: Conf. Ser.*, 2014, **550**, P. 012023.
- [22] Isakaev E.Kh., Sinkevich O.A., et al. Thermal fluxes in a generator of low temperature plasma with a divergent channel of the outlet electrode. *High Temperature*, 2011, **6**, P. 797–802.
- [23] Tozzini V., Pellegrini V. Prospects for hydrogen storage in graphene. ArXiv:1207.5703, 2012. URL: <https://arxiv.org/abs/1207.5703>.
- [24] Elias D.C., Nair R.R., et al. Control of graphene’s properties by reversible hydrogenation: evidence for graphane. *Science*, 2009, **323**, P. 610–613.
- [25] Sahin H., Leenaerts O., Singh S.K., Peeters F.M. Graphane. *Wiley Interdiscip. Rev. Comput. Mol. Sci.*, 2015, **5**, P. 255–272.
- [26] Scheffler M., Haberer D., et al. Probing local hydrogen impurities in quasi-free-standing graphene. *ACS Nano*, 2012, **6**, P. 10590–10597.
- [27] Denisov E.A., Kompaniets T.N., Kurdyumov A.A., Mazaev S.N. Atomic hydrogen interaction with various graphite types. *J. Plasma Devices and Operations*, 1998, **6**, P. 265–269.
- [28] Barinov A., Malcioglu O.B., et al. Initial Stages of Oxidation on Graphitic Surfaces: Photoemission Study and Density Functional Theory Calculations *J. Phys. Chem. C*, 2009, **113**, P. 9009–9013.
- [29] Shavelkina M.B., Amirov R.H., Shatalova T.B. The effect of reactor geometry on the synthesis of graphene materials in plasma jets. *J. of Phys.: Conf. Ser.*, 2017, **857**, P. 012040.
- [30] Ferrari A.C. Raman spectroscopy of graphene and graphite: disorder, electron-phonon coupling, doping and nonadiabatic effects. *Solid State Commun.*, 2007, **143**, P. 47–57.
- [31] Ferrari A.C., Meyer C., et al. Raman spectrum of graphene and graphene layers. *Phys. Rev. Lett.*, 2006, **97**, P. 187401.
- [32] Jorio A., Dresselhaus M.S., Saito R., Dresselhaus G. *Raman Spectroscopy in Graphene Related System*, Wiley-VCH: Germany, 2011.
- [33] Son J., Lee S., et al. Hydrogenated monolayer graphene with reversible and tunable wide band gap and its field-effect transistor. *Nature Comm.*, 2016, **7**, P. 13261.
- [34] Cancado L.G., Jorio A., et al. Quantifying defects in graphene via raman spectroscopy at different excitation energies. *Nano Lett.*, 2011, **11**, P. 3190–3196.
- [35] Nechaev Y.S., Veziroglu T.N. Thermodynamic aspects of the stability of the grapheme/graphane/hydrogen systems, relevance to the hydrogen on-board storage problem. *Adv. Mat. Phys. Chem.*, 2013, **3**, P. 255–280.



NANOSYSTEMS:

PHYSICS, CHEMISTRY, MATHEMATICS

INFORMATION FOR AUTHORS

The journal publishes research articles and reviews, and also short scientific papers (letters) which are unpublished and have not been accepted for publication in other magazines. Articles should be submitted in English. All articles are reviewed, then if necessary come back to the author to completion.

The journal is indexed in Web of Science Core Collection (Emerging Sources Citation Index), Chemical Abstract Service of the American Chemical Society, Zentralblatt MATH and in Russian Scientific Citation Index.

Author should submit the following materials:

1. Article file in English, containing article title, the initials and the surname of the authors, Institute (University), postal address, the electronic address, the summary, keywords, MSC or PACS index, article text, the list of references.
2. Files with illustrations, files with tables.
3. The covering letter in English containing the article information (article name, MSC or PACS index, keywords, the summary, the literature) and about all authors (the surname, names, the full name of places of work, the mailing address with the postal code, contact phone number with a city code, the electronic address).
4. The expert judgement on possibility of publication of the article in open press (for authors from Russia).

Authors can submit a paper and the corresponding files to the following addresses: nanojournal.ifmo@gmail.com, popov1955@gmail.com.

Text requirements

Articles should be prepared with using of text editors MS Word or LaTeX (preferable). It is necessary to submit source file (LaTeX) and a pdf copy. In the name of files the English alphabet is used. The recommended size of short communications (letters) is 4-6 pages, research articles– 6-15 pages, reviews – 30 pages.

Recommendations for text in MS Word:

Formulas should be written using Math Type. Figures and tables with captions should be inserted in the text. Additionally, authors present separate files for all figures and Word files of tables.

Recommendations for text in LaTeX:

Please, use standard LaTeX without macros and additional style files. The list of references should be included in the main LaTeX file. Source LaTeX file of the paper with the corresponding pdf file and files of figures should be submitted.

References in the article text are given in square brackets. The list of references should be prepared in accordance with the following samples:

- [1] Surname N. *Book Title*. Nauka Publishing House, Saint Petersburg, 2000, 281 pp.
- [2] Surname N., Surname N. Paper title. *Journal Name*, 2010, **1** (5), P. 17-23.
- [3] Surname N., Surname N. Lecture title. In: Abstracts/Proceedings of the Conference, Place and Date, 2000, P. 17-23.
- [4] Surname N., Surname N. Paper title, 2000, URL: <http://books.ifmo.ru/ntv>.
- [5] Surname N., Surname N. Patent Name. Patent No. 11111, 2010, Bul. No. 33, 5 pp.
- [6] Surname N., Surname N. Thesis Title. Thesis for full doctor degree in math. and physics, Saint Petersburg, 2000, 105 pp.

Requirements to illustrations

Illustrations should be submitted as separate black-and-white files. Formats of files – jpeg, eps, tiff.



NANOSYSTEMS:

PHYSICS, CHEMISTRY, MATHEMATICS

Журнал зарегистрирован

Федеральной службой по надзору в сфере связи, информационных технологий и массовых коммуникаций

(свидетельство ПИ № ФС 77 - 49048 от 22.03.2012 г.)

ISSN 2220-8054

Учредитель: федеральное государственное автономное образовательное учреждение высшего образования

«Санкт-Петербургский национальный исследовательский университет информационных технологий, механики и оптики»

Издатель: федеральное государственное автономное образовательное учреждение высшего образования

«Санкт-Петербургский национальный исследовательский университет информационных технологий, механики и оптики»

Отпечатано в Учреждении «Университетские телекоммуникации»

Адрес: 197101, Санкт-Петербург, Кронверкский пр., 49

Подписка на журнал НФХМ

На второе полугодие 2019 года подписка осуществляется через

ОАО Агентство «Роспечать»

Подписной индекс 57385 в каталоге «Издания органов научно-технической информации»